Analysis and Control of Multimode Combustion Switching Sequence

by

Sandro Patrick Nüesch

A dissertation submitted in partial fulfillment
of the requirements for the degree of
Doctor of Philosophy
(Mechanical Engineering)
in The University of Michigan
2015

Doctoral Committee:
Professor Anna G. Stefanopoulou, Chair
Professor Andre L. Boehman
Professor Ilya V. Kolmanovsky
Research Scientist Jason B. Martz

Everything should be made as simple as possible,
but not simpler.
— Albert Einstein

To my family for their never-ending support.

Acknowledgments

This dissertation and its underlying research could not have been done without the collaboration and support of countless people. First and foremost I want to thank Prof. Stefanopoulou. A little bit less than four years ago, in February 2012, she gave me the great opportunity to write my Master's thesis in the Powertrain Control Laboratory (PCL). After a brief detour working on fuel cells and diesel engines, I began my work in the HCCI group with the task to develop a vehicle model and think about drive cycle simulations. This work carried me further than I expected and the associated model ended up being a helpful tool to determine the fuel economy of our engine. When Prof. Stefanopoulou suggested to continue my research in form of a Ph.D. thesis as part of the ACCESS project, I had to accept. Since then she was always available to provide helpful advice, guidance and support. I also want to thank the other members of my dissertation committee, Prof. Andre Boehman, Prof. Ilya Kolmanovsky and Dr. Jason Martz, for their valuable remarks and fruitful discussions.

Every start is difficult. Many times I was required to rely on the more experienced members of the PCL for advice. I want to highlight Patrick Gorzelic, who, despite his extremely busy schedule, was always approachable to share with me his wisdom on combustion mode switches, his control strategy and his experimental data. I also want to thank the other PCL-HCCI old-timers who moved on to different tasks: Erik Hellström, Jacob Larimore and Shyam Jade. In terms of batteries and HEVs I was able to count on Jason Siegel's and Youngki Kim's expertise and want to thank them too. I also want to thank the other current and former members of the PCL I enjoyed working with: Niket Prakash, Huan Lian, Rasoul Salehi, Yi Chen, Shima Nazari, Shankar Mohan, Xinfan Lin and Michael Hand.

Besides the PCL I want to thank other current and former researchers in the Walter E. Lay Automotive Laboratory, or the University of Michigan in general, for their collaboration and support: John Hoard, Galen Fisher, Stani Bohac, Robert Middleton, Prasad Shingne, Xiaowu Zhang, Vasileios Triantopoulos and many more. I also

want to thank Kathie Wolney for all her work behind the scenes, who I could rely on to help with administrative issues, from car rentals to travel reimbursements.

I also want to thank the great systems engineering group at Robert Bosch in Farmington Hills, which provided me a more industrial view on my research. Special thanks goes to Jeff Sterniak, who helped me tremendously, from vehicles over engines to TWCs. Especially during my first two years I must have asked him dozens of questions and he patiently replied to all my emails. I also want to thank Li Jiang and Jason Schwanke, who guided me during my Ph.D. and internship. They both provided me with great ideas and inputs for my research. I also very much enjoyed working with the other members of the ESN team: Michael Mosburger, Nikolay Livshiz, Julien Vanier, Kyle Davidson, Kivanc Temel, Oliver Miersch-Wiemers, Hakan Yilmaz and others.

To wrap up the professional part of my acknowledgments, I want to thank the U.S. Department of Energy and the U.S. taxpayers for providing the funds that supported the ACCESS project.

However, moving through a Ph.D. not only requires professional, scientific and financial assistance. I am lucky to have great friends and family in Switzerland, Europe and the United States, that prepared, supported or simply bared with me for the last three years. First of all I want to thank Mallory Maynard, my girlfriend, who stood by my side the entire time. Already in summer 2012, she helped me by error-checking my application essay to the University of Michigan. Now, about three years later, she proofread my dissertation (I hope my English proficiency has improved in the mean time). Year-in and year-out, despite my long working hours, she has been a great friend and persistent supporter. I am grateful for all the amazing times we enjoy together, either traveling, biking, running, swimming, and so on, many of which she introduced me to. Thank you and I love you!

I also want to thank Mallory's parents, Gerald and Heather Maynard, who from the start welcomed me in their home for family events. I want to thank the other great people and friends from all over the world, that I was lucky to meet in Ann Arbor: Ryan Miller, Philipp Schiffmann, Pauline Malo, Avani Kamath, Tobias Albrecht, Michael Kalchauer, Priyanka Desai, Fabrice Laye, Sameer Sathaye, Julie Prinet, Delphine Rolland, Justin Hodges, Preeti Abraham, Thomas Juhl, Rafael de Juan Astray, Martin Lichtl and many more. I want to thank my friends from my time at ETH Zurich, with whom I spent endless hours studying in the ML building, playing cards and drinking coffee in the Tannenbar, enjoying beers in the bQm or partying in the Stutz^2: Andreas Marti, Nathalie Zatti, Raphael Heierli, Klemens Vogel, Domenica

Brütsch and Michael Baumann. Thanks to Satoshi Segawa and Carlo Possenti, for working with me on my first engineering project, when planning our photovoltaic plant on the roof of the school. I also want to thank other friends from Kanti Baden: Manuel Gugger, Ramon Mägert, Eric Funk, Manuel Peder and Jenny Weilenmann. I want to thank my brother Olivier Nüesch for all the great times we shared over the years. I enjoy our funny discussions and appreciate his continuously great inputs for movies, books, shows and music.

This work would not have been possible without the teachers that prepared me along the way. And after about 21 years of school I have had my fair share of them. Since elementary school I have had the privilege to study under dedicated and motivating teachers, professors and supervisors. From ETH Zurich I would like to highlight Prof. Lino Guzzella and Dr. Christopher Onder for teaching me about engines and controls. Thanks to Christian Dülk and Divesh Bhatia from Daimler. From Kantonsschule Baden I want to thank Dr. Hans-Rudolf Scheebeli, who provided me with the best preparation imaginable for my engineering studies, and also Thomas Notter and Martin Speck for their great classes. I would also like to thank Urs Bilgerig and Sandra Wild from Bezirksschule Spreitenbach and Annemarie Kühn from Primarschule Killwangen.

Finally, I want to thank my parents, Stephan and Rose-Marie Nüesch. Without them this whole endeavor would not have been possible. For the last 28 years they taught me the value of studying, learning and hard work. They always provided me with the means to pursue and achieve my goals. They continue to support me in my decisions, even if this means me moving across the Atlantic ocean. I appreciate all the small and big things they did for me and I dedicate this dissertation to them.

GO BLUE!

Sandro Nüesch, Nov. 2015

Table of Contents

List of Tables

Table

List of Figures

Figure

List of Appendices

Appendix

List of Acronyms

Acronym	
ACCESS	Advanced combustion concepts - enabling systems and solutions
AFR	Air-fuel ratio
AT	Automatic transmission
ATAC	Active thermo-atmosphere combustion
BMEP	Brake mean effective pressure
BSFC	Brake specific fuel consumption
CA50	Crank angle of 50% mass fraction burned
CAFE	Corporate average fuel economy
CAI	Controlled autoignition
CIHC	Compression ignited homogeneous charge
COV	Coefficient of variance
CV	Cyclic variability
CVT	Continuously variable transmission
DCT	Dual clutch transmission
DI	Direct injection
DOE	Department of Energy
DP	Dynamic programming
ECMS	Equivalent consumption minimization strategy
ECU	Engine control unit
eEGR	External EGR
EGR	Exhaust gas recirculation
EPA	Environmental Protection Agency
EV	Electric vehicle
Ext	Supervisory strategy: Extended stay
FCV	Fuel cell vehicle
FFVA	Fully flexible valve actuation

FiD	Depletion strategy: Fill and deplete
FTP	Federal Test Procedure
GDI	Gasoline direct injection
HCCI	Homogeneous charge compression ignition
HEV	Hybrid electric vehicle
HF	High feature
HWFET	Highway fuel economy test
ISC	Idle speed controller
ISG	Integrated starter/generator
LEV	Low emission vehicle
LiP	Supervisory strategy: Linear prediction
LNT	Lean NO_x trap
LQ	Linear quadratic
LQG	Linear quadratic gaussian
LTC	Low temperature combustion
Max	Supervisory strategy: Maximum stay
MIMI	Multiple injection and multiple ignition
MIMO	Multi-input multi-output
MM	Multimode
MPC	Model predictive control
MPG	Miles per gallon
MT	Manual transmission
NA	Naturally aspirated
NEDC	New european drive cycle
NeF	Depletion strategy: Never fill
NHTSA	National Highway Traffic Safety Administration
NMEP	Net mean effective pressure
NoO	Depletion strategy: No oxygen storage dynamics
NoP	Supervisory strategy: No prediction
NSFC	Net specific fuel consumption
NVO	Negative valve overlap
Opt	Supervisory strategy: Optimal stay
OSC	Oxygen storage capacity
PeP	Supervisory strategy: Perfect prediction
PHEV	Plug-in hybrid electric vehicle
PI	Proportional-integral

PID	Proportional-integral-differential
RCCI	Reactivity controlled compression ignition
RMS	Root mean square
RPM	Revolutions per minute
SACI	Spark assisted compression ignition
SA-HCCI	Spark assisted HCCI
SCR	Selective catalytic reduction
SI	Spark ignition
SISO	Single-input single-output
Sml	Case study: Small HCCI regime with small OSC
Str	Case study: Stratified HCCI-SI switch
SOC	State of charge
SOI	Start of injection
SULEV	Super ultra-low emission vehicle
TDC	Top dead center
TS	Toyota-Soken
TWC	Three-way catalytic converter
UDDS	Urban dynamometer driving schedule
VCR	Variable compression ratio
VVT	Variable valve timing

List of Symbols

Symbol

A	Area
C	Oxygen storage capacity
F	Force
H	Prediction horizon / heating value
I	Current
J	Equivalent power consumption
K	Controller parameters
M	Current combustion mode
P	Power
Q	Battery cell capacity
$\dot{Q}$	Heat flow
R	Desired combustion regime
T	Torque
U	Voltage (also heat transfer coefficient)
V	Volume
X	Set of admissible controls
c	Heat capacity
d	Mode switch penalty
e	Tracking error
f	Map / function
g	Acceleration of gravity / gear
h	Prediction history (also heat transfer coefficient)
i	Set of combustion mode states / index
j	Number of time steps
k	Current time step
l	Clutch state
m	Mass

$\dot{m}$	Mass flow
n	Number
$\dot{n}$	Molar flow
r	Radius
s	Distance
t	Time
u	Command
v	Velocity
x	Optimization argument
Θ	Relative oxygen storage capacity
Φ	Magic tire formula
α	Equivalence factor (also heat capacity / heat transfer coefficient)
γ	Gear ratio
δ	Drivetrain state
ϵ	Driver state (also volume fraction)
ζ	Battery resistance
η	Efficiency
θ	Inertia
ϑ	Temperature
λ	Relative air-fuel ratio
μ	Friction coefficient / policy
ξ	Battery state-of-charge (also temperature penalty)
ρ	Density
σ	Slip
τ	Time constant / delay
ψ	Time constant
ω	Rotational speed

Abstract

Highly dilute, low temperature combustion technologies, such as homogeneous charge compression ignition (HCCI), show significant improvements in internal combustion engine fuel efficiency and engine-out NO_x emissions. These improvements, however, occur at limited operating range and conventional spark ignition (SI) combustion is still required to fulfill the driver's high torque demands. In consequence, such multimode engines involve discrete switches between the two distinct combustion modes. Such switches unfortunately require a finite amount of time, during which they exhibit penalties in efficiency.

Along with its challenges, the design of such a novel system offers new degrees of freedom in terms of engine and aftertreatment specifications. Prior assessments of this technology were based on optimistic assumptions and neglected switching dynamics. Furthermore, emissions and driveability were not fully addressed. To this end, a comprehensive simulation framework, which accounts for above-mentioned penalties and incorporates interactions between multimode engine, driveline, and three-way catalyst (TWC), has been developed.

Experimental data was used to parameterize a novel mode switch model, formulated as finite-state machine. This model was combined with supervisory controller designs, which made the switching decision. The associated drive cycle results were analyzed and it was seen that mode switches have significant influence on overall fuel economy, and the issue of drivability needs to be addressed within the supervisory strategy.

After expanding the analysis to address emissions assuming a TWC, it was shown that, in practice, HCCI operation requires the depletion of the TWC's oxygen storage capacity (OSC). For large OSCs the resulting lean-rich cycling nullifies HCCI's original efficiency benefits. In addition, future emissions standards are still unlikely to be fulfilled, deeming a system consisting of such a multimode engine and TWC with generous OSC unfavorable.

In view of these difficulties, the modeling framework was extended to a mild

hybrid electric vehicle (HEV) allowing a prolonged operation in HCCI mode with associated fuel economy benefits during city driving. Further analysis on how to reduce NO_x while maintaining fuel economy resulted in a counterintuitive suggestion. It was deemed beneficial to constrain the HCCI operation to a small region, exhibiting lowest NO_x, while reducing instead of increasing the OSC.

Chapter 1

Introduction

1.1 Background

Over the last forty years, the vehicle fleet in the U.S. has undergone dramatic changes. As shown in Fig. 1.1, compared to 1975 standards, fuel economy[1] increased by more than 80% with a simultaneous increase in horsepower. At the same time, vehicles became significantly more luxurious and safe while maintaining close to constant weight. One important reason for these improvements in fuel economy is the implementation of the Corporate Average Fuel Economy (CAFE) standards in 1975. From 1985 to 2010, the CAFE standards remained constant, as shown in Fig. 1.2. However, recent legislation has implemented more stringent goals for the automotive industry. Based on these new standards, the projected annual increase in fuel economy of a passenger car lies in average at 3.8-3.9% from 2017-2021, and at 4.7% from 2022-2025 [6].

[1] Adjusted fuel economy is supposed to reflect real world driving and is approximately 25% higher than standard drive cycle values as presented by industry.

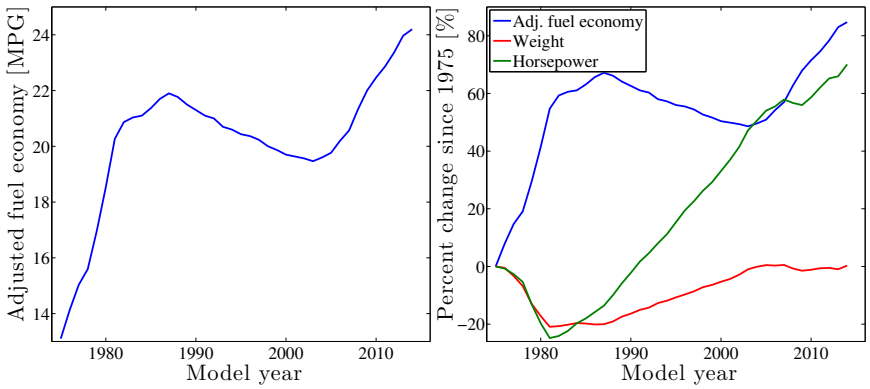

Figure 1.1: Fuel economy trends in the U.S. since implementation of CAFE standards. Left: Fleetwide average adjusted fuel economy of new vehicles. Right: Relative change in fuel economy, vehicle weight, and horsepower. Source: [5].

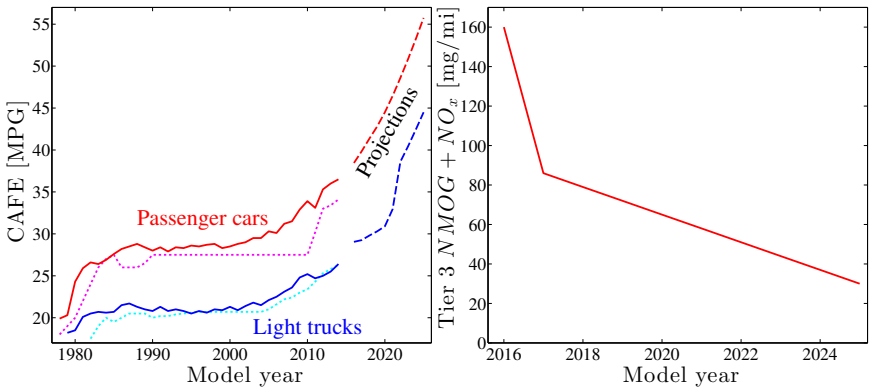

Figure 1.2: Fuel economy and emissions standards. Left: Past standards (dotted) and the respective CAFE (solid) for passenger cars (red) and light trucks (blue) [7] and projections of future CAFE (dashed) [6]. Right: Tier 3 fleet average FTP $NMOG+NO_x$ standards for passenger cars [8].

In addition to the demanded increase in fuel economy, the U.S. Environmental Protection Agency (EPA) is phasing in its Tier 3 emissions standards, once again increasing its restriction on harmful exhaust gases. Among other restrictions, combined fleet average NO_x and $NMOG$ for passenger cars will be reduced from 2016-2025 by over 80%, as shown in Fig. 1.2.

As described in [9], while zero-emissions technologies such as electric vehicles (EV) and fuel cell vehicles (FCV) potentially show dramatic improvements in terms of fuel economy and emissions, they require more time to significantly penetrate the market. Plug-in hybrid electric vehicles (PHEV) and EV rely on large batteries, which are currently still too expensive for mainstream application. In addition, FCV and EV require infrastructural changes, e.g., new type of fueling and charging stations, respectively. However, as seen in Figs. 1.1 and 1.2, the fuel economy standards are rising already and require short and mid-term improvements. Besides reducing the vehicle weight, the efficiency of the conventional powertrain needs to be improved. Several technologies are already available or will enter the market soon. Downsizing, turbocharging, exhaust gas recirculation (EGR), and variable valve lift increase engine efficiency. Start-stop technology, cylinder deactivation, and an increase in the number of gears result in more efficient engine operation. For the near future the EPA and the National Highway Traffic Safety Administration (NHTSA) [10] see potential for advanced spark ignited (SI) combustion technologies, which are currently still under development. In general, research is pursued on a vast number of different advanced combustion technologies.

Due to the increase in complexity and the interaction of several different technolo-

gies within the engine, one important aspect in future engine and vehicle technologies is the requirement of mode switching. This generally involves a supervisory controller making a choice between a discrete set of states. This could include shifting gears, deactivating individual cylinders, activating fuel cut-off, or shutting-off the engine. Often a switch between the different modes does not occur instantaneously and might result in a certain penalty, e.g., fuel efficiency or drivability, thereby creating a trade-off.

Many advanced combustion technologies, if individually implemented in a conventional powertrain, are not capable of fulfilling all engine torque or speed demands of a regular driver. One possible solution is the integration of several combustion modes in a multimode engine [11]. Based on engine operating condition a mode switch is performed between the different combustion modes. One advanced combustion mode with high potential is homogeneous charge compression ignition (HCCI) combustion. The fuel efficient HCCI mode is combined with regular SI combustion with the goal of an overall improvement in fuel economy. This work focuses on the mode switching in such a SI/HCCI multimode combustion engine.

1.2 Homogeneous Charge Compression Ignition

The two most common combustion modes in internal combustion engines (ICE), spark ignition (SI) gasoline combustion and direct injection (DI) diesel combustion, both show significant drawbacks. Conventional gasoline SI combustion is constrained to a fuel-air mixture relatively close to stoichiometry. Therefore it is required to operate throttled at part-load conditions, which leads to a strong reduction in efficiency. At the same time its high combustion temperature results in significant levels of engine-out NO_x emissions. However, the stoichiometric SI operation allows the use of a three-way catalytic converter (TWC), which enables an almost complete reduction of the harmful exhaust emissions. On the other hand, DI diesel combustion runs under lean conditions and unthrottled, thereby leading to significantly higher part-load efficiencies than SI. It is, however, subject to a trade-off between high NO_x and PM emissions. In addition, the excess air restricts the use of a TWC and requires more sophisticated exhaust aftertreatment systems. The advanced combustion technology HCCI attempts to offer the advantages of both types of combustion while also diminishing their drawbacks.

In HCCI combustion a lean homogeneous mixture of gasoline and air autoignites

through compression. This allows the engine to run unthrottled at part-load conditions, thereby offering high engine efficiency close to DI diesel levels. The autoignition combustion is inherently different from a regular flame-based process. HCCI combustion occurs almost instantaneously and is much closer to an explosion or engine knock than to regular SI or DI combustion. Besides the reduction of pumping losses the engine efficiency benefits from improved mixture properties and increased specific heat ratio [12] as well as a reduction in timing losses due to the rapid heat release [13]. The lack of a flame results in low temperature combustion (LTC). While levels of HC and CO can be increased [14], the low temperature leads to very low engine-out NO_x emissions. Therefore potentially only lower cost exhaust aftertreatment system for the other emissions might be required [11]. More information on HCCI combustion can be found in [15–17].

Since the early research on advanced combustion modes, HCCI was known under many names. In 1958, Alperstein et al. [18] premixed a small amount of fuel with air in a diesel engine, leading to improvements in efficiency. By conducting optical experiments in a two-stroke gasoline engine in 1979, Noguchi et al. [19] encountered a stable autoignition combustion without the presence of a flame but instead several ignition locations throughout the cylinder. The process showed improvements in fuel efficiency and HC emissions and they called it Toyota-Soken (TS). At the same time Onishi et al. [20] studied the autoignition process in lean gasoline engines. Active Thermo-Atmosphere Combustion (ATAC), as they called it, lead to reduced exhaust emissions and improved fuel efficiency. Based on these discoveries, Najt and Foster [21] studied the Compression Ignited Homogeneous Charge (CIHC) combustion process systematically in a four-stroke engine. They found that the kinetics of the autoignition process are sufficiently controllable by changing species concentrations and intake temperature. In 1989, Thring [22] first introduced the acronym HCCI and confirmed that by utilizing high intake temperatures and high levels of exhaust gas recirculation (EGR) the efficiency of a DI diesel engine is achievable.

1.2.1 HCCI Actuator Strategies

The start of HCCI combustion is mainly determined by temperature [23]. The cylinder charge needs to reach the right level of thermal energy to ignite at top dead center (TDC). The required amount of thermal energy is significantly larger than in the case of regular SI combustion. Several methods, which increase and regulate the charge temperature, have been discussed in the literature. The success of these

methods depends on the available and applied hardware. In the decades between its discovery and today, new types of technologies started penetrating the market, offering alternative ways to enable a stable autoignition process.

The early studies [21, 22] relied on intake air heating to achieve sufficiently high charge temperatures to allow autoignition. This method is very slow and not suitable for the highly dynamic combustion phasing control in a vehicle. Different groups [24, 25] accelerated the preparation of intake air temperature by using heat transfer between hot and cold air. In other studies [26, 27] variable compression ratio (VCR) was applied. Both methods incur, however, practical issues in the implementation. In [26] dual port injection was used to change the ratio of two different fuels and thereby obtaining a large variety in octane numbers. Dual-fuel operation, however, requires infrastructural and behavioral changes with regards to fueling.

The two most common methods to enable HCCI combustion nowadays rely on variable valve timing (VVT) technology: Recompression and rebreathing. By shifting the opening and closing timings of exhaust and intake valves, the amount of residual gas in the cylinder is increased ($\approx 40\% - 70\%$). This modified composition of the charge leads to increased temperature and thereby reactivity at intake valve closing and enables its succeeding autoignition around TDC. Willand et al. [28] introduced recompression HCCI by closing the exhaust valve early and opening the intake valve late, thereby creating a negative valve overlap (NVO). Increased NVO leads to more hot and reactive residuals and thereby earlier combustion phasing [29]. Song and Edwards [30] show that pilot fuel injection during the recompression event leads to chemical reactions, i.e., pyrolysis. Earlier start of injection (SOI) results in advanced combustion phasing.

On the other hand, rebreathing HCCI involves a secondary exhaust valve event during the intake stroke which leads to re-induction of exhaust gas. Law et al. [31] use fully flexible valve actuation (FFVA) for recompression and rebreathing of controlled autoignition (CAI) combustion, another alternative name for HCCI. Compared to regular cam phasing, FFVA technologies are much more complex and might lead to extra cost and packaging issues. They offer, however, the maximum level of flexibility and allow all kinds of valve actuation strategies. Other work on HCCI combustion phasing with FFVA was performed in [32–34]. Rebreathing and recompression with fixed cams and phasers are compared in a simulation study by Babajimopoulos et al. [35]. They conclude that, while recompression shows higher efficiency at lower loads, rebreathing leads to noticeably larger operating range. The work presented in this dissertation is focused on recompression HCCI combustion with VVT.

1.2.2 HCCI Combustion Control

One main difficulty in the implementation of HCCI combustion is its lack of a direct combustion trigger. In SI and DI combustion, ignition is directly linked to spark and injection timing, respectively. In HCCI combustion, however, the mixture needs to be prepared accurately before the compression stroke begins. Combustion phasing will only be at its designated reference if the right composition, temperature, and pressure are achieved. This has to be accomplished on a cycle-by-cycle basis under varying load and speed conditions. Different types of hardware, such as VVT, FFVA, or split injection, ask for different complexity in the control strategy and also add cost to the system. This makes the regulation of HCCI combustion phasing a challenging control problem, which has been discussed in a vast amount of literature. In the following, you will find a brief overview of different HCCI combustion control schemes.

Single-input single-output (SISO) control approaches are presented in [36–40]. Olsson et al. [36] use in-cylinder pressure sensors and heat release analysis to get feedback of the timing of 50% mass fraction burned (CA50). Individual PID regulators control load and CA50 using dual-fuel injection. Agrell et al. [37] control CA50 with PI regulators and two different valve strategies. In [38] the authors designate each of these two strategies to specific operating conditions. Shaver et al. [39] use LQR with VVT to track a desired peak pressure. Instead of in-cylinder pressure feedback Souder et al. [40] use microphones to obtain combustion phasing, which is regulated using a PID controller and an exhaust throttle.

Multi-input multi-output (MIMO) control strategies are described in [41–46]. Shaver et al. [47] apply the dynamic feedback linearization technique to control combustion phasing and peak pressure with the valve timings. Chiang and Stefanopoulou [41] use the LQG optimal control technique to track CA50 and air-fuel ratio (AFR) with rebreathing valve timing and an EGR valve. Killingsworth et al. [42] use extremum seeking to tune the parameters of their PID controller online. Bengtsson et al. [43] present a model predictive control (MPC) strategy where they control load and CA50 with valve timings and fuel amount while limiting pressure rise rates. Ravi et al. [44, 45] develop a model for pilot fuel injection during the recompression event and use it as additional input to manipulate combustion phasing. In [44] the authors apply this model in a MPC strategy and impose rate constraints on their valve actuation. The work is continued in [45], where a mid-ranging structure with two controllers is presented. The first controller uses pilot injection as a fast actuator for CA50 regulation. The second controller uses exhaust valve timing to return combustion phasing to its reference, generally in the middle of its range. Due to

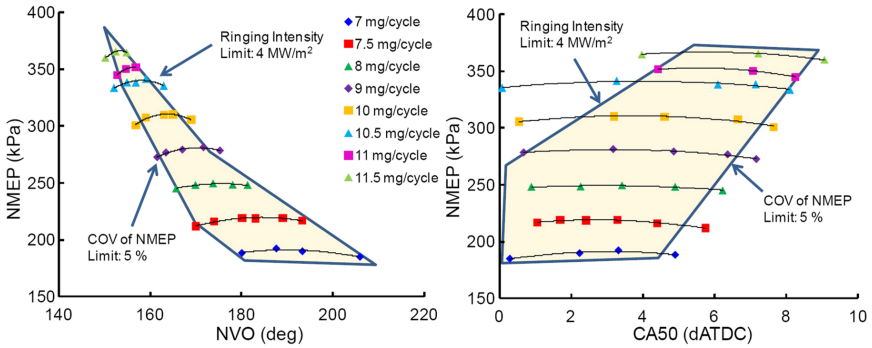

Figure 1.3: Feasible HCCI operating regime in terms of load versus NVO (left) and combustion phasing (right). (Source: Fig. 3 from [48])

its relative simplicity in hardware and computation this approach is feasible for production engines. However, without the benefit of model prediction during large load transitions the viable limits of combustion phasing might be violated. Jade et al. [46] solved this problem by introducing a reference governor to the mid-ranging structure.

As shown above, a plethora of literature is available on HCCI combustion control and the problem has been solved to a point in which HCCI combustion is theoretically implementable in a vehicle. Relatively inexpensive and available hardware, such as variable valve actuation and in-cylinder pressure sensors, can be used together with model-based feedback strategies to control fast transients in load and speed. The applied controllers are computationally efficient, which allows them to run in real time on current engine control units (ECU).

1.2.3 Operating Regime

HCCI combustion is limited to low and medium loads [22]. The operating regime of HCCI is presented in [48] and shown in Fig. 1.3 for varying load over NVO and combustion phasing. It can be seen that with larger NVO and advanced combustion phasing the extremely short combustion duration leads to very high pressure rise rates, audible noise (ringing), and eventually damage of the engine [49]. At a specific target combustion phasing, this effectively results in a limit at higher loads. In [50–52] boosting strategies are discussed with the goal of increasing dilution at higher loads, thereby mitigating ringing. In both [50, 52] it is concluded that, while the HCCI operating regime could be increased, mechanical supercharging is not an option due to high parasitic losses, which reduce overall brake efficiency.

At low loads, bulk-gas quenching leads to increased levels of engine-out CO and

HC emissions, as well as a significant reduction in combustion efficiency [53]. The effects of fuel reformation [54] and charge stratification [55] on the lower HCCI load limit were discussed. By using a multiple ignition and multiple injection (MIMI) strategy, Yun et al. [56] are able to extend the low load limit down to idle conditions.

In Fig. 1.3 it can be seen that late combustion and small NVO lead to a large coefficient of variance (COV) in load, a measure of combustion stability. In [31] it is noted that HCCI combustion shows better stability, i.e., lower cyclic variability (CV), than HCCI combustion. This, however, is only true for a very small range. To increase the HCCI operating range, Hellström et al. [57] investigated the nonlinear coupling between succeeding engine cycles due to the residual gas. Especially during transients in engine load and speed, it might be necessary to cross high CV regions. During large load transients, as could occur in a drive cycle, high CV might even lead to misfires. Jade et al. [58] augmented their control strategy from [46] with a CV model-based SOI controller. This strategy reduces CV and enables large load transients within the HCCI operating regime as fast as in SI combustion.

1.2.4 Spark-Assist

Depending on operating condition, the spark can be used as an additional measure to control the combustion phasing of HCCI [59]. This can be of interest during mode switches between SI and HCCI combustion [60, 61]. Another important advantage of Spark Assisted HCCI (SA-HCCI) or Spark Assisted Compression Ignition (SACI) is the enlargement of HCCI's operating range. Urushihara et al. [62] utilize the spark to promote autoignition of the remainder of the mixture, which allows lower pre-combustion temperatures. Kalian et al. [63] describe a propagating flame from the ignition time until the autoignition event. The flame consumes a portion of the cylinder charge and releases energy. The associated increase in temperature and pressure advances the autoignition of the remainder of the charge. In turn, the advanced combustion phasing leads to increased load. Due to the longer burn duration of the flame, SACI exhibits a reduced peak heat release rate at higher loads and thereby reduces ringing intensity. The result is an extension of the autoignition operating regime [64]. Lavoie et al. [65] show that spark has greater control authority at higher and medium compared to lower loads. Manofsky et al. [48] run stoichiometric SACI as an independent combustion mode between the HCCI ringing limit and the SI misfire limit. Polovina et al. [52] use external cold EGR to mitigate ringing at increased loads. It is stated that, despite generally lower efficiency than pure HCCI combustion, SACI

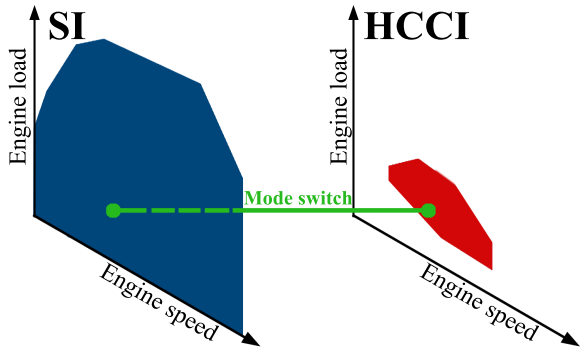

Figure 1.4: Sketch of SI and HCCI operating regimes, connected by combustion mode switch.

is a viable method to extend HCCI's operating regime. However, SACI combustion suffers from high cyclic variability [66–68]. Reuss et al. [66] distinguish between four combustion periods and identified their individual contributions to the cyclic variability. The authors conclude that, at the studied light load conditions, the early kernel growth period has the largest effect on combustion phasing. Daw et al. [67] present a model for the cyclic variability based on global kinetic rate parameters.

1.2.5 Combustion Mode Switches

For several reasons it might be required to switch between SI and HCCI combustion. However, SI and HCCI are two entirely different combustion modes. SI combustion relies on spark-induced flame propagation and operates at throttled stoichiometric conditions with low amounts of residuals and high combustion temperatures. In contrast, HCCI combustion is autoignition-based with several ignition zones throughout the cylinder. It runs unthrottled and at lean conditions with a large fraction of internal residuals. A combustion mode switch from SI to HCCI or back, as illustrated in Fig. 1.4, has to occur with as little torque fluctuations as possible to remain unnoticed by the driver. In addition, misfires and high pressure rise rates need to be avoided. Therefore, a combustion mode switch between the two modes is a very challenging controls task. A vast amount of literature about SI/HCCI combustion mode switching is available. However, there is a large spread in applied hardware and pursued control strategies.

Due to the differences mentioned above, SI and HCCI require significantly distinct valve timings and lifts. In [61, 69–74] a FFVA system is employed which allows for great flexibility in valve manipulation. The requirement of a FFVA, however, may add

prohibitive hardware cost to the system. Commonly available hardware, which allows flexibility in valve actuation, is a VVT system with two-stage cam profile switching Such a system is applied in [75–83]. While operating in SI and HCCI mode the valve lifts are high and low, respectively. Sometime in the course of the mode switch the lifts are changed, which occurs nearly instantaneously. Such a system theoretically allows a mode switch within one engine cycle.

A majority of the presented control strategies rely on open-loop actuator calibration [61, 69, 72, 73, 75–80]. Cairns and Blaxill [77] present a mode switch in experiments on a four-cylinder engine, however, with significant fluctuations in torque. To avoid calibration effort and to improve robustness of the design against aging and changing environmental conditions, some approaches rely on model-based feedback control [74,81–84]. However, not many closed-loop mode switch controllers have been validated experimentally.

Widd et al. [74] compare a PI regulator to a state-feedback controller on a single-cylinder engine with FFVA. Yang and Zhu [84] apply LQ control in simulation to track intake manifold pressure using the throttle. In addition, spark-assist is employed for stabilization. Ravi et al. [81] switch the cams from high to low lift in SI mode and start phasing the cams open loop at a fixed rate. The increasing amount of internal EGR will eventually lead to autoignition and a transition cycle between SI and HCCI mode. During this engine cycle, the authors apply a state-feedback and model-based feedforward controller for SOI to track the desired combustion phasing. After this cycle, control is switched to regular HCCI. A validation of the controller on a single-cylinder engine was performed. Gorzelic et al. [82] present a control oriented SI/HCCI mode switch model, based on the HCCI model in [46]. In the associated strategy, discussed in detail in [85], the mode switch and the cam switch occur simultaneously. The following dissertation focuses on the mode switch strategy from [85] using a two-stage cam switching mechanism. However, the presented methodology is applicable to a wide variety of strategies and hardware.

Control of combustion mode switches between SI and HCCI has not yet reached the same maturity as the control of the nominal HCCI mode. While several control strategies are being pursued, many are either based on more sophisticated hardware, like FFVA, or rely strongly on calibration. In general, it can be seen that combustion mode switches do not occur instantaneously and require a certain amount of time, e.g., due to airpath or actuator dynamics. Furthermore, a situation is likely, during which the engine operates in HCCI combustion when the driver requests a load outside the feasible HCCI operating regime. The HCCI load controller can only

track the load all the way up or down to the boundary of the HCCI regime. A mode switch to SI combustion is then required before tracking of the load command can be continued. Therefore, during a drive cycle, the switches need to be scheduled and executed in a way that maximizes the residence time in the HCCI combustion mode, while also avoiding jerks in load and other drivability issues. In addition, operation under non-optimal conditions during the combustion mode switches leads to reduced combustion efficiency or increased pumping losses, and also incurs a fuel penalty. Therefore, to result in a net fuel economy benefit, the accumulated HCCI efficiency gains need to overcompensate for the mode switching penalties. This is only achieved if the residence time in HCCI combustion is long enough.

1.2.6 Multimode Combustion Concept & Drive Cycle Fuel Economy

As mentioned above, due to the limited operating regime of HCCI it is not possible to fulfill all the load and speed demands of a driver during regular vehicle operation. Thring [22] suggested the multimode combustion engine as a solution of this problem. Such an engine generally operates in nominal SI mode and switches to the beneficial HCCI combustion, if current load and speed conditions are located within its feasible regime. So far, vehicles utilizing such engines have not reached the stage of production. In 2009 [86] General Motors demonstrated a prototype vehicle using a SI/HCCI multimode engine. In 2014 [1] the ACCESS project developed a prototype vehicle applying a multimode engine based on SI and SACI combustion modes. Neither of those vehicles were officially tested and the fuel economy results are not publicly available. In general, the performance in terms of fuel economy and emissions of such a vehicle still needs to be assessed in drive cycle simulations. The focus of most published simulation results lies on the potential improvement in fuel economy of the SI/HCCI multimode engine compared to a nominal SI-only engine.

In [11, 12, 87–89] steady-state fuel efficiency maps of SI and HCCI combustion are applied in vehicle simulations. Zhao et al. [87] generate their maps based on engine data and achieve an improvement in fuel economy of approximately 5% for the New European Driving Cycle (NEDC). Cairns and Blaxill [12] apply a validated engine simulation to develop and analyze HCCI steady-state data. The authors predict a total fuel economy benefit of 10% for the NEDC. Kulzer et al. [11] discuss multimode combustion and compare different valve timing and injection strategies. Based on data from a single-cylinder engine with FFVA, a fuel economy benefit of 12% during

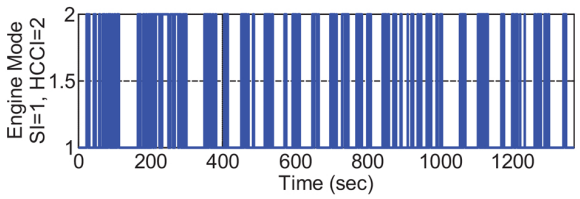

Figure 1.5: Instantaneous combustion mode switches during a city drive cycle based on vehicle and engine simulation. (Source: Fig. 23 from [88])

the NEDC compared to direct injected SI combustion is achieved. In addition, they simulate different supervisory control strategies which command a switch back to SI if the temperature of the three-way catalyst decreases to a lower threshold. Ortiz-Soto et al. [88] use a detailed engine model to generate their maps and they show improvements between 7-21% depending on the drive cycle and 23% residence time in HCCI during the FTP75 drive cycle[2]. As can be seen in Fig. 1.5, it is briefly noted that some visitations of the HCCI regime might actually be too short to allow for a mode switch. Wheeler et al. [89] apply a similar approach resulting in a fuel economy improvement of 20% over the FTP75 drive cycle. Of the publications listed above, [11, 87, 89] take into account engine cold start. However, all the mentioned publications assume instantaneous switches between SI and HCCI maps and thereby neglect mode switching penalties and dynamics.

Hybrid electric vehicles (HEV) are increasingly penetrating U.S. and European markets. Besides fuel savings due to start-stop and regenerative braking strategies, the coupling of a multimode engine with an electric machine leads to an additional degree of freedom in engine operation. This extra degree of freedom results in increased flexibility when optimizing the operating point of the engine and can therefore increase fuel economy benefits. Delorme et al. [90] perform a simulation study to investigate the drive cycle fuel economy of different hybridization levels (micro, mild, power-split, plug-in). In particular, the authors study the extra fuel economy benefit of using a SI/HCCI multimode combustion engine instead of a conventional SI engine in the hybrid powertrain. It is concluded that, while all configurations benefit from the use of HCCI, the conventional powertrain with a fuel economy increase of 15% for the FTP75 drive cycle gains the most. In fact they claim that, the higher the level of hybridization, the smaller the benefit from using a multimode engine. Lawler et al. [91] introduce a rule-based supervisory strategy which utilizes HCCI in a parallel hybrid powertrain. In a fuel economy assessment over the UDDS drive

[2]See Appendix A for an overview of different EPA drive cycles.

cycle they present an improvement of 17% due to the use of multimode combustion in a conventional and an improvement of 18.4% in a mild parallel hybrid powertrain. Similar work was done in [92, 93]. However, also none of these publications considers combustion mode switching and associated penalties, neither in their simulation nor in their supervisory control strategies.

1.3 Dissertation Contributions

The key contributions of this dissertation are described in the following section together with the corresponding conference and journal publications. The first novelty is the introduction of a vehicle model incorporating a multimode combustion engine, which emulates the properties and dynamics of combustion mode switches over the course of a drive cycle. As discussed in the previous section, several other researchers [11, 12, 87–91] conducted simulation studies and attempted to predict the drive cycle fuel economy of a SI/HCCI multimode engine. However, none of those publications accounted for the switches between the two modes, and the associated dynamics and penalties. To account for this, a basic integration of a finite-state combustion mode switch model into a vehicle simulation was presented by the author in [94]. This model was refined in [95] to distinguish between different periods of the mode switch, e.g., cam phasing, cam switch, etc., and to capture mode switches to SACI combustion. The model was parameterized with mode switch experiments, shown in [96], and embedded within the overall vehicle dynamics, described in [97]. The finite-state model, developed over the course of this work, represents a computationally efficient way to capture the properties of combustion mode switches during vehicle-level simulations.

In a second contribution, the system model was applied to quantify the influence of the mode switch dynamics and fuel penalties on the drive cycle performance. The author discussed the impact of such switches on fuel economy in [96]. It was shown that frequent mode switches and their associated penalties add up over the course of a drive cycle and lead to a significant reduction of the modest HCCI benefits. Furthermore, in HCCI mode, the engine's load is very limited. Therefore, if the driver requests high torque, the engine is required to switch back to SI combustion before being able to respond. The corresponding mode switch delays could therefore lead to potential drivability problems. In [97] a trade-off was discussed between ignoring the driver's torque demand, leading to longer residence time in HCCI mode and higher

fuel economy, and the increasing delay in engine response. In conclusion, combustion mode switches can have strong impact on fuel economy and drivability, and therefore need to be accounted for in the design of the engine system and the mode switch control strategy, as well as the supervisory controller. This is especially important if the size of the HCCI regime is very limited, leading to a high frequency of mode switches and short residence times in HCCI.

The third contribution of this work is an analysis of supervisory control strategies and the decision, when to perform a mode switch. The predictability of engine torque over very short time horizon was discussed in [98]. It was seen that a visitation of the HCCI regime needs to be of the order of 0.8-1.2 s to be beneficial for overall fuel economy. Therefore, different receding horizon prediction methods were tested on engine data from chassis dynamometer experiments in terms of their accuracy in predicting HCCI entry and exit events. It was seen that, while the methods were not very accurate, they were still capable of distinguishing very short from very long visitations. These findings were implemented in supervisory control strategies and presented in [97]. It was seen that a simple linear prediction is able to better anticipate HCCI visitations, and prepare mode switches accordingly. This leads to a higher fraction of beneficial HCCI residences and a lower impact on drivability. In addition, results from an optimal mode switching strategy, based on dynamic programming and prior drive cycle knowledge, are shown for benchmarking purposes. It was seen that under those conditions, drivability issues can be avoided while fuel economy is slightly improved.

One major focus of attention was an analysis of the interaction between the SI/HCCI multimode engine and a three-way catalyst (TWC) exhaust aftertreatment system. Very low engine-out NO_x emissions is one of the main advantages of HCCI combustion. This potentially allows the use of relatively inexpensive TWCs. Under lean HCCI conditions with a relative AFR >1.25, the NO_x concentration is <25 ppm and remains untreated while CO and HC are removed. Under stoichiometric SI conditions, the TWC is fully functional and converts all three species. However, this statement neglects the oxygen storage dynamics within the TWC. Lean operation fills up the oxygen storage, thereby making the TWC incapable of converting NO_x. Back at stoichiometry, the TWC's oxygen storage needs to be depleted to restore its NO_x conversion efficiency. The depletion is achieved by operating the engine rich, thereby leading to poor engine efficiency. A simulation framework was presented [99] and published [2], which takes into account this dynamic oxygen storage behavior. It was shown that a TWC-based aftertreatment system with generous oxygen storage

exhibits significant fuel penalties. Therefore, such a TWC system with large oxygen storage is deemed unsuitable for operation with a SI/HCCI multimode engine. This finding prompted HCCI-SI mode switching studies by collaborating researchers [85] that achieve the rich condition already during the switch with the goal to expedite the restoration of the TWC's conversion efficiency while reducing breakthroughs in NO_x.

An additional contribution considers the integration of a multimode engine in a mild HEV with 48 V-system. Depending on the drive cycle, the torque assist from the electric motor enables significantly longer HCCI residence times. While such systems have been studied by other researchers [90, 91], the dynamics of mode switches were not considered. In [100] the author introduced different SI/HCCI HEV supervisory control strategies, which connect the mode switching decision to the HEV control strategy. It was seen that drive cycles with low load requirements and a vast number of regenerative braking events, e.g., the FTP75, exhibit synergies between the multimode engine and the HEV. These synergies lead to significant improvements in fuel economy, even without specifically incorporating the battery's state-of-charge (SOC) into the mode switching decision. On the other hand, with higher load demands and less battery regeneration, as seen during the HWFET, HCCI operation can lead to a decrease in fuel economy if SOC is not considered.

As a final contribution, in [101] and [102] the author considered the sizing of the TWC aftertreatment system in a mild HEV with a SI/HCCI multimode engine. Due to longer residence times in HCCI, the depletion of the TWC's oxygen-storage is not as harmful on fuel economy as in the non-HEV case. In turn, the prolonged use of HCCI leads to significant amounts of tailpipe NO_x emissions. To resolve this issue, the combination of two potential hardware modifications was evaluated. First, instead of the original TWC with generous oxygen storage capacity, a small storage is assumed. This reduces the amount of fuel required to deplete it. Second, the size of the feasible HCCI regime is reduced to the area where NO_x emissions are extremely low, therefore not requiring aftertreatment. It was seen that such a system has the potential to achieve the same or higher fuel economy than the original configuration, but with a significant reduction in NO_x emissions. This is counterintuitive to prior presumptions, which stated that a higher fuel economy and better emissions can be achieved with a larger HCCI regime and a larger OSC.

In summary, the six contributions of this dissertation are as follows:

1. A finite-state combustion mode switch model for drive cycle simulations is introduced. (Chapter 2)
2. The model is applied to analyze the impact of combustion mode switches on

fuel economy and drivability. (Chapter 3)
3. The potential of short-term torque prediction in a supervisory control strategy are tested. (Chapter 3)
4. It is shown that the interaction between multimode combustion and TWC can result in prohibitive fuel penalties. (Chapter 4)
5. Synergies between multimode combustion and mild HEVs are discussed. (Chapter 5)
6. A hardware modification is suggested, in which a small HCCI regime is combined with a small oxygen storage, to achieve similar fuel economy with lower emissions. (Chapter 5)

A majority of this research work was conducted as part of the ACCESS (Advanced Combustion Concepts - Enabling Systems and Solutions) project [103] and funded by the U.S. Department of Energy. The goal of this project was to develop strategies that enable the use of advanced combustion modes in light-duty vehicles. The target was a 25% reduction in drive cycle fuel economy compared to a naturally aspirated, conventional SI baseline engine while meeting SULEV emissions requirements. Findings of this dissertation were highlighted in the 2014 DOE Annual Merit Review [104] as well as the 2015 National Research Council Report [105].

1.4 Dissertation Outline

In Chapter 2, the longitudinal vehicle and driver model is presented and validated. Chapter 3 discusses the finite-state combustion mode switch model and analyzes its influence on drive cycle fuel economy and vehicle drivability. In addition, different short-term load prediction methods are discussed. Chapter 4 presents an analysis of the system based on a SI/HCCI combustion engine and three-way catalytic converter. In Chapter 5 the integration of a multimode engine in a mild hybrid electric vehicle is discussed. Finally, Chapter 6 contains conclusions and future work. A flow diagram of the dissertation is shown in Fig. 1.6.

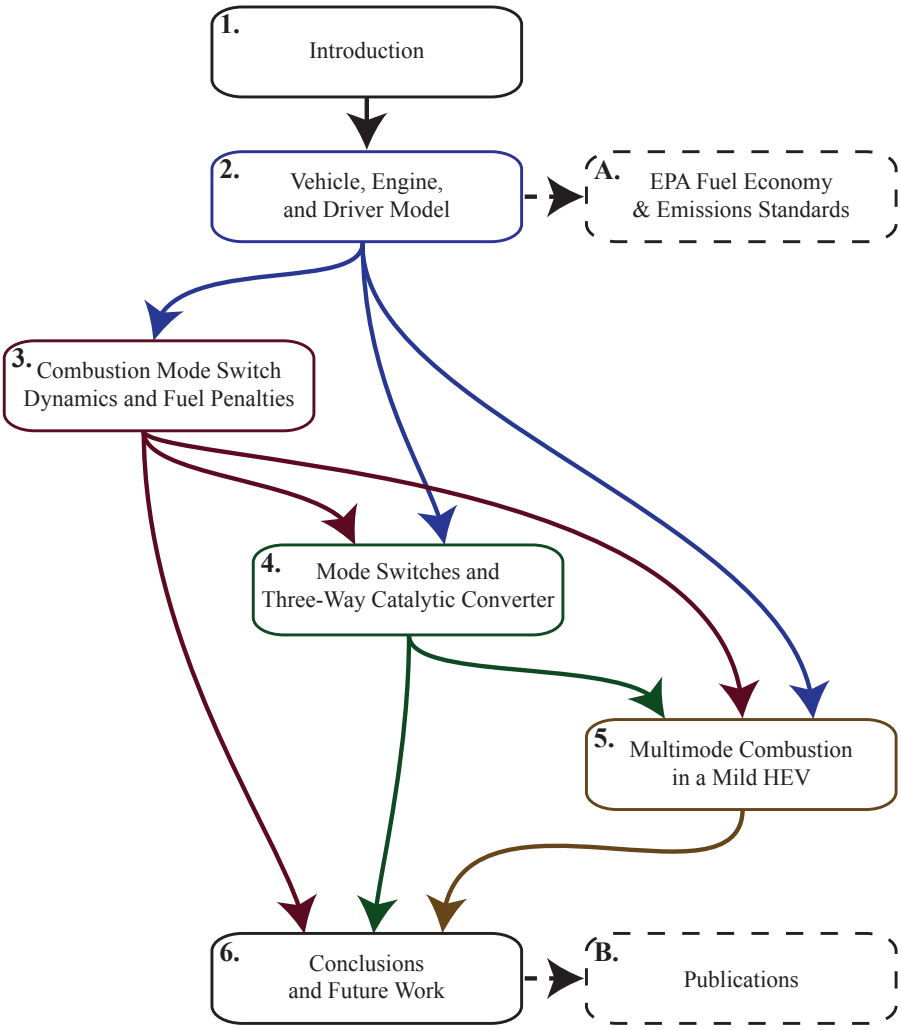

Figure 1.6: Flow diagram of the dissertation. Arrows show how chapters 1-6 are interconnected. Dotted lines point to corresponding appendices A and B.

Chapter 2
Vehicle, Engine, and Driver Model

A vehicle model is required to translate the reference velocity of the drive cycle into engine speed and load. Dynamic models have been used for decades to analyze vehicle behavior and controller design, with a vast amount of literature available, e.g., [106–109]. Little work has been done on the integration of multimode combustion engines in vehicle simulations, e.g., [11, 88]. However, combustion mode switches were assumed to be instantaneous without any impact on engine torque. Therefore, it would also be possible to run vehicle and combustion simulations separately. In this dissertation, combustion mode switches are penalized, i.e., incur a fuel penalty and require a certain duration. The vehicle model, applied to analyze the impact of such mode switches on vehicle performance, is described in this chapter. Note that this chapter is only concerned with the baseline model for the conventional powertrain, applying standard SI combustion. Models for combustion mode switches, aftertreatment, and hybrid electric system are described in the following chapters.

The vehicle used in this dissertation is a stock Cadillac CTS, model year 2009, with 6-gear manual transmission, Fig. 2.1. The baseline engine of this vehicle is a naturally aspirated (NA) 3.6 L GM HF V6, which runs standard SI combustion. While a vehicle's longitudinal dynamics are widely published, this chapter also describes the implementation of a longitudinal driver model in detail, including the dynamics during gear shifting and vehicle launch. The model is realized in MATLAB / Simulink / Stateflow and was first introduced in [94]. It consists of equations for vehicle and driveline dynamics, which are shown in Sec. 2.1. The engine model is based on steady-state maps and described in Sec. 2.2. Lower level engine control tasks, e.g., engine idle, are located in the model of the engine control unit (ECU) and shown in Sec. 2.3. The driver model is responsible for following the reference velocity and shifting the gears, and its details are presented in Sec. 2.4. Finally, the vehicle model is validated in Sec. 2.5 by comparing its results to chassis dynamometer measurements.

Figure 2.1: Picture of the Cadillac CTS vehicle used in the ACCESS project [1].

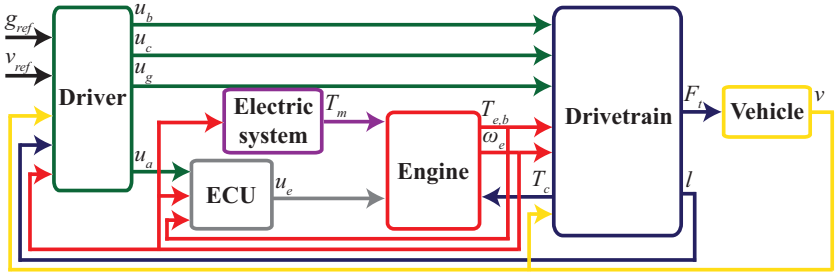

Figure 2.2: Top-level block diagram of the longitudinal model of the conventional vehicle.

2.1 Vehicle & Driveline Model

In the following section the longitudinal vehicle and driveline model is explained. It consists of the main state equations for velocity v, rotational speed of the driven and non-driven wheels, $\omega_{w,d}$ and $\omega_{w,n}$, respectively, and engine speed ω_e. A schematic representation of the forces acting on the vehicle can be found in Fig. 2.3. The model distinguishes between open and locked clutch, is thereby a hybrid system in which different sets of state equations are activated depending on the state of the clutch. The block diagram of the vehicle model can be seen in Fig. 2.4. Its parameters are listed in Table 2.1.

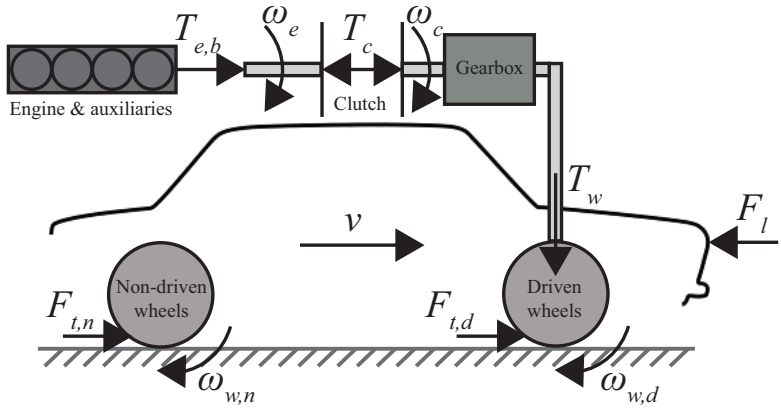

Figure 2.3: Schematic representation of the forces acting on the vehicle in motion.

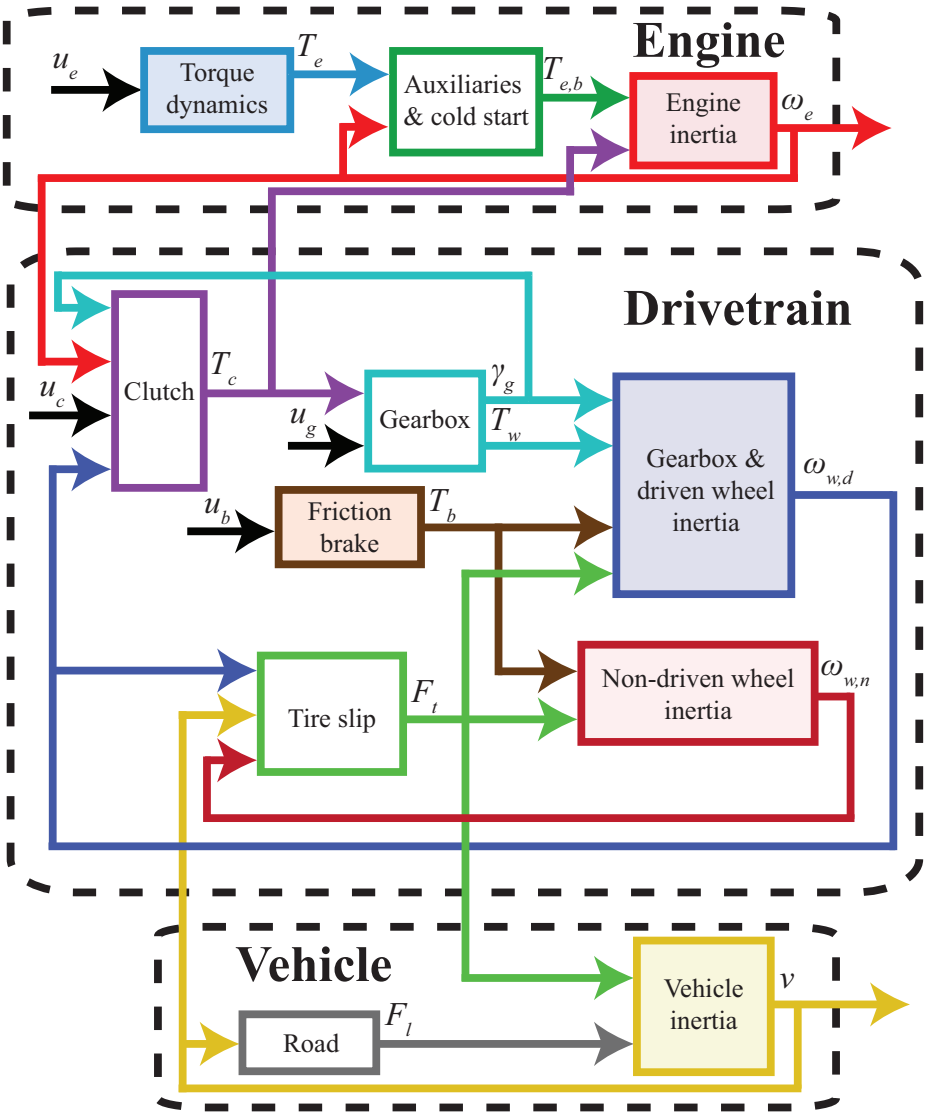

Figure 2.4: Block diagram of the vehicle model.

2.1.1 Road and Tires

The road load F_l is calculated as:

$$F_l = F_a + F_r. \tag{2.1}$$

Rolling resistance F_r and aerodynamic drag F_a are calculated as described in [107, 109, 110]:

$$F_a = \frac{1}{2}\rho_a \mu_a A_f v^2 \tag{2.2}$$

$$F_r = m_v g(\mu_{r,0} + \mu_{r,1} v) \tag{2.3}$$

with aerodynamic and rolling resistance coefficients μ_a, $\mu_{r,0}$ and $\mu_{r,1}$, respectively, the frontal area A_f, and acceleration of gravity g. Note that the model does not include any forces due to elevation changes or due to driving in reverse gear.

The tire slip σ_t is calculated as follows:

$$\sigma_t = 1 - \begin{cases} 1 & \omega_w = 0 \text{ or } v = 0 \\ \frac{v}{\omega_w \cdot r_t} & \omega_w \cdot r_t - v \geq 0 \\ \frac{\omega_w \cdot r_t}{v} & \omega_w \cdot r_t < 0 \end{cases} \tag{2.4}$$

with tire radius r_t and rotational speed of the wheel ω_w. Note the associated subscripts d and n for driven and non-driven wheels, respectively. The tire forces for the driven and non-driven tires $F_{t,d}$ and $F_{t,n}$, respectively, follow as

$$F_{t,d} = n_{w,d} \cdot \text{sign}(\omega_{w,d} \cdot r_t - v) \cdot \Phi(\sigma_{t,d}) \tag{2.5}$$

$$F_{t,n} = n_{w,n} \cdot \text{sign}(\omega_{w,n} \cdot r_t - v) \cdot \Phi(\sigma_{t,n}) \tag{2.6}$$

with the number of driven and non-driven wheels $n_{w,d}$ and $n_{w,n}$, respectively, and the relationship $\Phi(\sigma_t)$ based on the Magic tire formula presented in [111]. The total number of wheels is $n_w = n_{w,d} + n_{w,n}$.

2.1.2 Vehicle Dynamics

The state equation for vehicle speed v follows from Newton's first law:

$$m_v \frac{d}{dt} v = F_{t,d} + F_{t,n} - F_l. \tag{2.7}$$

2.1.3 Gearbox and Brakes

The driver command u_g determines the gear ratio γ_g. Together with final drive ratio γ_{fdr} the total gear ratio γ is computed.

$$\gamma = \gamma_{fdr} \cdot \gamma_g(u_g) \tag{2.8}$$

The total torque acting on all driven wheels is denoted T_w and is equal to the output torque of the gearbox. As described in [107] the gearbox was modeled with the Willans approach. Power losses reduce or increase T_w with respect to the direction of

the power flow:

$$T_w = \gamma \cdot \begin{cases} \eta_g \cdot T_c & T_{e,b} \geq 0 \\ \frac{1}{\eta_g} \cdot T_c & T_{e,b} < 0 \end{cases} \tag{2.9}$$

with engine brake torque $T_{e,b}$ and gearbox efficiency η_g.

The friction brake torque T_b was modeled as a first order element, similar to [112]:

$$\tau_b \frac{d}{dt} T_b = u_b \cdot T_{b,max} - T_b \tag{2.10}$$

with brake time constant τ_b, brake pedal position u_b, and maximum transmittable torque $T_{b,max}$.

2.1.4 Driveline Dynamics

Therefore the dynamics of the driveline can be derived from conservation of momentum:

$$(\theta_g \gamma^2 + n_{w,d}\theta_w) \frac{d}{dt} \omega_{w,d} = T_w - n_{w,d} \cdot T_b - r_t \cdot F_{t,d} \tag{2.11}$$

$$n_{w,n}\theta_w \frac{d}{dt} \omega_{w,n} = -n_{w,n} \cdot T_b - r_t \cdot F_{t,n} \tag{2.12}$$

with the combined gearbox and drive axis inertia θ_g and the inertia of a wheel θ_w.

2.1.5 Clutch

The rotational speed of the gearbox-side of the clutch is denoted ω_c:

$$\omega_c = \gamma \cdot \omega_{w,d}. \tag{2.13}$$

By using the binary state l the vehicle model distinguishes between locked clutch, $l = 1$, the main drivetrain mode, and slipping clutch, $l = 0$, used for vehicle standstill, launch, and up- and downshifts. The deciding clutch logic is inspired by [113]. The sign of the clutch torque T_c is determined by the clutch slip σ_c:

$$\sigma_c = \omega_e - \omega_c. \tag{2.14}$$

Based on clutch pedal position u_c and the maximum static friction torque, i.e., friction limit, $T_{c,max}$, the currently transmittable static friction torque $T_{c,s}$ is calculated:

$$T_{c,s} = (1 - u_c) \cdot T_{c,max}. \tag{2.15}$$

By neglecting tire slip and by combining (2.7), (2.11), and (2.12) the required friction torque to lock the clutch $T_{c,req}$ follows as:

$$T_{c,req} = \frac{(\theta_g \gamma^2 + n_w \theta_w + m_v r_t^2) \cdot T_{e,b} + \theta_e \gamma n_w T_b - r_t F_l}{\theta_g \gamma^2 + n_w \theta_w + m_v r_t^2 + \gamma^2 \eta_g \theta_e}. \tag{2.16}$$

The clutch locks and unlocks during the next time step k based on the applied clutch pedal position and the slipping speed:

$$l(k+1) = \begin{cases} 0 & l(k) = 0 \text{ (unlocked) and } (|T_{c,req}| > T_{c,s} \text{ or } \sigma_c \neq 0) \\ 1 & l(k) = 0 \text{ (unlocked) and } |T_{c,req}| \leq T_{c,s} \text{ and } \sigma_c = 0 \\ 1 & l(k) = 1 \text{ (locked) and } |T_{c,req}| \leq T_{c,s} \\ 0 & l(k) = 1 \text{ (locked) and } |T_{c,req} > T_{c,s}. \end{cases} \tag{2.17}$$

For a slipping clutch the absolute value of the clutch torque is given by the kinetic friction torque $T_{c,k}$, based on static friction torque $T_{c,s}$ and the ratio between static and kinetic friction coefficient:

$$T_{c,k} = \left(\frac{\mu_{c,k}}{\mu_{c,s}} \right) \cdot T_{c,s}. \tag{2.18}$$

Therefore the transmitted clutch torque T_c follows as

$$T_c = \begin{cases} T_{e,b} & l = 1 \\ T_{c,k} & l = 0. \end{cases} \tag{2.19}$$

2.1.6 Engine Speed Dynamics

Finally, the differential equation for engine speed ω_e follows from conservation of momentum,

$$\theta_e \frac{d}{dt} \omega_e = T_{e,b} - T_c \tag{2.20}$$

with engine inertia θ_e.

Table 2.1: Vehicle model parameters for Cadillac CTS

Name	**Symbol**	**Value**
Aerodynamic resistance coefficient	μ_a	0.276
Rolling resistance coefficient	μ_f	0.0075
Rotational resistance coefficient	μ_r	$4.8\,{}^{\mathrm{Ns}}/_{\mathrm{m}}$
Frontal area	A_f	$2.19\,\mathrm{m}^2$
Density of air	ρ_a	$1.225\,{}^{\mathrm{kg}}/_{\mathrm{m}^3}$
Vehicle mass (curb + passenger)	m_v	$1725\,\mathrm{kg} + 136\,\mathrm{kg}$
Acceleration of gravity	g	$9.807\,{}^{\mathrm{kgm}}/_{\mathrm{s}^2}$
Tire radius	r_t	$0.347\,\mathrm{m}$
Number of driven wheels	$n_{w,d}$	2
Number of non-driven wheels	$n_{w,n}$	2
Gear ratios (1st - 6th)	γ_g	{4.5, 2.75, 1.76, 1.32, 1, 0.78}
Final drive ratio	γ_{fdr}	3.42
Gearbox efficiency	η_g	0.96
Brake time constant	τ_b	$0.25\,\mathrm{s}$
Static tire friction coefficient	μ_b	0.7
Maximum brake torque ($\frac{\mu_b m_v g}{4}$)	$T_{b,max}$	$3.2 \cdot 10^3\,\mathrm{Nm}$
Maximum clutch torque	$T_{c,max}$	$500\,\mathrm{Nm}$
Ratio of clutch friction coefficients	$\frac{\mu_k}{\mu_s}$	0.5
Gearbox and drive axis inertia	θ_g	$0.05\,\mathrm{kgm}^2$
Wheel mass	m_w	$10.9\,\mathrm{kg}$
Wheel inertia ($m_w r_t^2$)	θ_w	$1.308\,\mathrm{kgm}^2$
Engine inertia	θ_e	$0.134\,\mathrm{kgm}^2$
Minimum velocity for tire slip	$v_{min,t}$	$0.28\,{}^{\mathrm{m}}/_{\mathrm{s}}$

2.1.7 Discrete Drivetrain States

The state equations (2.7), (2.11), (2.12), and (2.20) depend on the state of the clutch. In addition, tire slip is neglected for velocities below $v_{min,t}$. Therefore the discrete state δ is introduced, describing the current drivetrain mode: $\delta = 1$ represents locked clutch, $\delta = 2$ unlocked clutch while considering tire slip, and $\delta = 3$ unlocked clutch while neglecting tire slip. (2.21) takes care of the transition to a different drivetrain mode at the next time step k.

$$\delta(k+1) = \begin{cases} 1 & l(k) = 1 \\ 2 & l(k) = 0 \text{ and } v(k) \geq v_{min,t} \\ 3 & l(k) = 0 \text{ and } v(k) < v_{min,t} \end{cases} \tag{2.21}$$

The second drivetrain mode, $\delta = 2$, for the unlocked clutch and tire slip, is the most general representation of the system with the maximum number of states.

In case of $\delta = 1$, the clutch is locked and the algebraic relationship

$$\omega_e \equiv \omega_c \tag{2.22}$$

can be used to simplify (2.11) and (2.20):

$$\left((\theta_g + \theta_e) \cdot \gamma^2 + n_{w,d}\theta_w\right) \frac{d}{dt}\omega_{w,d} = T_w - n_{w,d} \cdot T_b - r_t \cdot F_{t,d}. \tag{2.23}$$

In case of $\delta = 3$, tire slip is neglected,

$$v \equiv r_t \cdot \omega_{w,d} \equiv r_t \cdot \omega_{w,n} \tag{2.24}$$

which simplifies (2.7), (2.11), and (2.12):

$$\left(\frac{\theta_g\gamma^2 + n_w\theta_w}{r_t^2} + m_v\right) \frac{d}{dt}v = \frac{T_w - n_w \cdot T_b}{r_t} - F_l. \tag{2.25}$$

2.2 Engine Model

In the following section the engine part of the model is described in detail. It consists of simple torque dynamics and assumptions for penalties due to auxiliaries and engine cold start. The values for the engine model can be found in Table 2.2.

2.2.1 Fuel Efficiency Maps & Engine Torque Dynamics

The engine fuel flow $\dot{m}_f$ is computed as a function of engine torque T_e and speed ω_e, using a steady-state map of fuel flow $f_{f,SI}$:

$$\dot{m}_f = f_{f,SI}(\omega_e, T_e). \tag{2.26}$$

The efficiency maps of the two engines used in this dissertation are depicted in Fig. 2.5 in terms of brake specific fuel consumption (BSFC).

The torque limitations of the SI combustion mode $T_{max,SI}(\omega_e)$, $T_{min,SI}(\omega_e)$ are functions of engine speed. The overall maximum and minimum torques of the engine

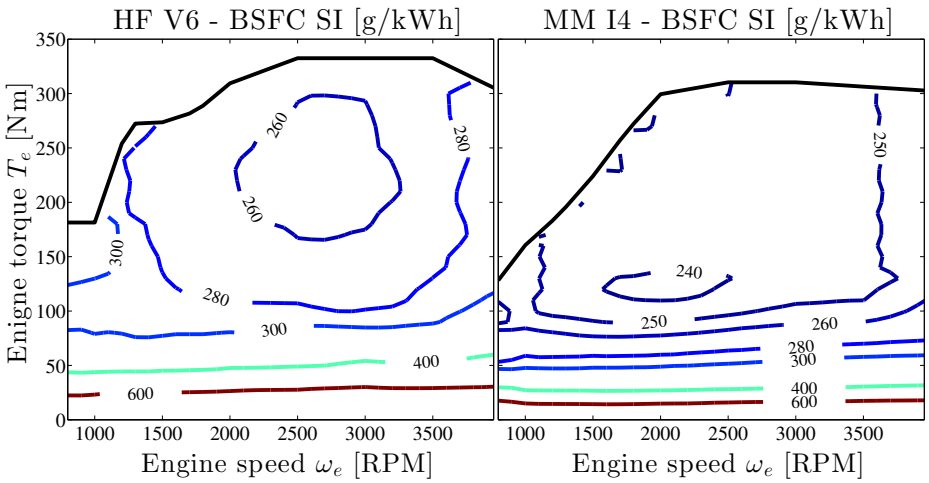

Figure 2.5: BSFC Maps of HF V6 engine (left) and MM I4 engine (right) for SI combustion.

are denoted $\hat{T}_{max}$ and $\hat{T}_{min}$, respectively.

$$\hat{T}_{max} = \max_{\omega_e} \; T_{max,SI}(\omega_e) \tag{2.27}$$

$$\hat{T}_{min} = \min_{\omega_e} \; T_{min,SI}(\omega_e) \tag{2.28}$$

The engine torque response is modeled as a first-order system with time constant τ_e and commanded torque by the ECU u_e as input:

$$\tau_e \frac{d}{dt} T_e = u_e - T_e. \tag{2.29}$$

Throttle snap measurements of the 2.0 L engine were used to identify the time constant of the intake manifold dynamics. The throttle was stepped from wide open to almost fully closed. The intake manifold pressure p_{im} was modeled as a first-order system with time constant $\tau_e = 0.09\,\text{s}$. The engine torque was simply assumed to be proportional to p_{im}. An individual throttle snap is shown in Fig. 2.6. Due to the sampling time it is not exactly clear when the step occurred. However, it can be seen that this first-order system reproduces the dynamics reasonably well.

2.2.2 Alternator

Besides the torque for the driveline the engine is required to provide power for the electric auxiliaries, which draw current from the 12 V-battery system. Reference [114] suggests a constant electric load to charge the battery P_{al}, which is implemented here

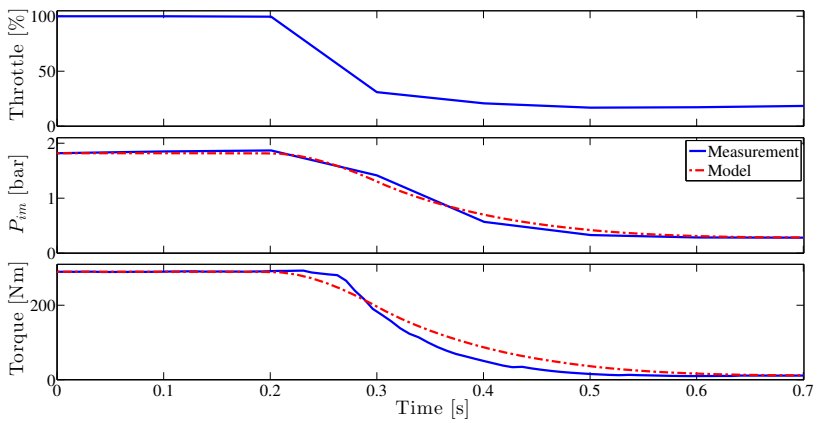

Figure 2.6: Throttle snap measurement (solid blue) and model (dashed red). Top: Throttle. Center: Intake manifold pressure. Bottom: Engine torque.

with $P_{al} = 1250\,\mathrm{W}$. It is assumed that at engine idle the battery is not being charged and that the load is reduced to $P_{al,idle} = 600\,\mathrm{W}$. In this dissertation, instead of a regular alternator, the engine provides this power via belt-driven integrated starter-generator (ISG). The reason for this choice is the analysis in Chap. 5, where the model is extended to a mild HEV. In that particular case, the electric machine will also be used for start/stop operation and regenerative braking.

The torque response of the ISG T_m is modeled as first-order system with time constant $\tau_m = 0.0043\,\mathrm{s}$ and ISG torque command u_m as input:

$$\tau_m \frac{d}{dt} T_m = u_m - T_m. \tag{2.30}$$

The ISG's torque is defined such that a positive and negative torque represents torque assist and battery charging, respectively. The applied efficiency map of the ISG f_m is based on experimental data and provides the ISG's electric power $P_{m,el}$ as a function of ISG speed ω_m and mechanical power P_m,

$$\omega_m = \omega_e \cdot \gamma_b \tag{2.31}$$

$$P_m = T_m \cdot \omega_m \tag{2.32}$$

with belt-ratio $\gamma_b = 2.5$. Therefore, the torque command sent to the ISG to maintain the auxiliary electric load follows as:

$$u_m = -\frac{f_m^{-1}(\omega_m, P_{al})}{\omega_m}. \tag{2.33}$$

Table 2.2: Engine model parameters

Name	**Symbol**	**Value**	
		HF V6	MM I4
Engine time constant	τ_e	0.09 s	
Electric auxiliary load	P_{al}	1.25 kW	
(at idle)	$P_{al,idle}$	600 W	
Belt ratio	γ_b	2.5	
Power steering	$P_{ps,1}$	100 W	
	$\omega_{ps,1}$	1000 RPM	
	a_{ps}	0.1 W/RPM	
Maximum engine torque	$\hat{T}_{max}$	333 Nm	310 Nm
Minimum engine torque	$\hat{T}_{min}$	-72 Nm	-31 Nm
Engine temp. time constant (heating)	ψ_{heat}	15 s	
(cooling, engine on)	$\psi_{cool,on}$	125 s	
(cooling, engine off)	$\psi_{cool,off}$	60 s	
Temperature penalty (fuel)	ξ_f	1.2	
(friction torque)	ξ_T	1.3	
Engine thermal capacity	α_e	108 kJ/K	

2.2.3 Power Steering

Based on [115] and [116] the loss due to the power steering can be assumed to be an affine function of engine speed:

$$P_{ps} = P_{ps,1} + a_{ps} \cdot (\omega_e - \omega_{ps,1}). \tag{2.34}$$

It is further assumed that at idle condition, power steering is not being used. The associated load on the engine follows as:

$$T_{ps} = \frac{P_{ps}}{\omega_e}. \tag{2.35}$$

2.2.4 Exhaust Gas Temperature and Cold Start

The methodology introduced by Gao et al. [117] is applied in this dissertation to estimate the dynamics of the engine's exhaust gas temperature $\vartheta_{g,e}$ from a steady-state map. These map only consider the nominal operating conditions of SI combustion and neglects special cases, e.g., to heat up the aftertreatment system.

$$\bar{\vartheta}_{g,e} = f_{\vartheta,SI}(T_e, \omega_e). \tag{2.36}$$

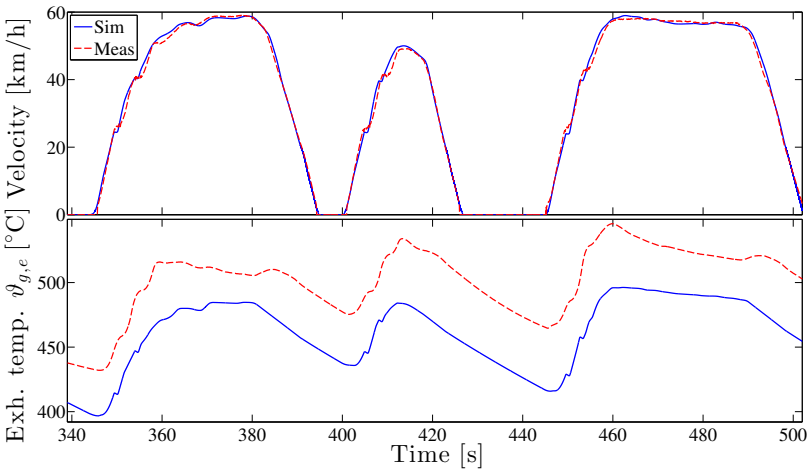

Figure 2.7: Comparison between simulated (solid blue) and measured (dashed red) engine exhaust temperature during exemplary time period of the third phase of the FTP75 cycle. Top: Velocity. Bottom: Temperature.

The map's output $\bar{\vartheta}_{g,e}$ is a forcing term used in case-sensitive first-order filters, finally resulting in temperature $\vartheta_{g,e}$. The associated time constants are ψ_{heat}, $\psi_{cool,on}$, and $\psi_{cool,off}$, depending if the engine is being heated or cooled and on or off, respectively. Parameter $\psi_{cool,on}$ was determined using engine cool-down experiments. The other parameters were chosen based on [117] and such that they matched the chassis dynamometer measurements, shown in Fig. 2.7.

The engine exhaust temperature together with the emissions will be used in Chapters 4 and 5 where the dynamics of the TWC are analyzed. However, the applied methodology is also able to approximate the process of warming-up the engine, as seen during the first phase of the FTP75 driving cycle. The temperature state of the engine is described by variable I_{warm}. A lower value of I_{warm} results in a reduction of the forcing term $\bar{\vartheta}_{g,e}$ relative to the map value. Also, during cold start the engine is subjected to a fuel penalty and additional engine friction torque T_{wu}:

$$T_{wu} = T_e \cdot \begin{cases} (1 - I_{warm}) \cdot (\xi_T - 1) & T_e > 0 \\ 0 & \text{else} \end{cases} \tag{2.37}$$

$$\dot{m}_f = f_{f,SI}(\omega_e, T_e) \cdot (I_{warm} + \xi_f(1 - I_{warm}))\,. \tag{2.38}$$

The reference velocity of first and third phase of the FTP75 are exactly the same. Therefore the measurements taken on the chassis dynamometer were used to find the associated penalties ξ_f and ξ_T as well as the engine's thermal capacity α_e.

Table 2.3: ECU model parameters

Name	**Symbol**	**Value**	
		HF V6	MM I4
Idle speed controller	$K_{p,idle}$	1.3	1.4
	$K_{i,idle}$	2.46	2.42
	$K_{d,idle}$	0.079	0.079
(filter constant)	N_{idle}	100	
	T_{idle}	11.4 Nm	9.6 Nm

2.2.5 Brake Engine Torque

The above introduced additional torque variables are used to calculate the brake engine torque $T_{e,b}$:

$$T_{e,b} = T_e + \gamma_b T_m - T_{ps} - T_{wu}. \tag{2.39}$$

2.3 ECU Model

The ECU model is located between driver and driveline models. Its main task is the computation of the torque command u_e, which is sent to the engine. The parameter values used in the ECU model can be found in Table 2.3.

2.3.1 Desired Torque

The ECU uses the accelerator pedal position u_a to determine a desired torque by the driver T_{des}. In real ECUs often a nonlinear mapping is applied, based on pedal position and engine speed. The maps are calibrated with the subjective feeling of the driver in mind, which is not an issue here. In addition, the torque maps vary from engine to engine and they lead to additional nonlinearities, which need to be taken into account when designing the driver controller. For those reasons they were replaced with a linear relationship between the minimum and maximum torque the engine is able to provide, $\hat{T}_{min}$ and $\hat{T}_{max}$, respectively:

$$T_{des} = u_a \cdot (\hat{T}_{max} - \hat{T}_{min}) + \hat{T}_{min}. \tag{2.40}$$

2.3.2 Idle Speed Controller

To avoid engine stall, the engine speed ω_e is not allowed to drop below the engine idle speed ω_{idle}. For that reason an idle speed controller (ISC) is implemented. To meet emissions regulations, it is important during cold start to heat up the three-way catalyst (TWC) in a short amount of time. One possible strategy to increase the exhaust temperature is retarding the spark timing. Efficiency penalties associated with such strategies are accounted for in Sec. 2.2.4. In addition it is assumed that the idle speed is increased to ω_{cat} for a short amount of time while the TWC temperature $\vartheta_{b,1}$ is below a certain threshold. This leads to the actual reference idle speed $\omega_{ref,idle}$ which the ISC needs to track:

$$\omega_{ref,idle} = \begin{cases} \omega_{cat} & \vartheta_{b,1} < 350\,^{\circ}\mathrm{C} \\ \omega_{idle} & \text{else.} \end{cases} \tag{2.41}$$

A finite state machine governs the use of the ISC. In general, the ISC is inactive and the desired torque by the driver T_{des} is fed through to engine command $T_{cmd,1}$. However, as soon as the accelerator pedal is released and $\omega_e < \omega_{ref,idle}$, the ISC takes over and holds ω_e constant. The ISC will remain active until the driver presses the accelerator pedal, T_{des} increases to $T_{des} > T_{cmd,1}$.

In the following paragraph, the design of the ISC is presented. The standard equilibrium condition for the ISC to be active is at vehicle standstill with the clutch pedal fully pressed and the engine running at idle speed ω_{idle}:

$$v_o = 0 \tag{2.42}$$

$$\omega_{e,o} = \omega_{idle} \tag{2.43}$$

$$u_{c,o} = 1 \Rightarrow T_{c,o} = 0 \tag{2.44}$$

Tire slip is irrelevant, therefore the drivetrain mode is $\delta = 3$. At low engine speeds the electric load is modeled as constant power $P_{al,idle}$. Applying the efficiency map of the ISG the mechanical power from the motor is approximated as:

$$P_{m,idle} = -f_m^{-1}(\omega_m, P_{al,idle}) \approx -802\,\mathrm{W}. \tag{2.45}$$

Therefore the equilibrium condition for engine torque follows as:

$$T_{e,b,o} = 0 \Rightarrow T_{e,o} = -\gamma_b T_{m,o} = -\frac{P_{m,idle}}{\omega_{e,o}} \tag{2.46}$$

$$u_{e,o} = T_{e,o}. \tag{2.47}$$

The linearization of the alternator torque leads to

$$\delta T_m = -\frac{P_{m,idle}}{\omega_{e,o}^2}\delta\omega_e \tag{2.48}$$

and the linearized state equations follow as

$$\delta\dot{T}_e = -\frac{1}{\tau_e}\delta T_e + \frac{1}{\tau_e}\delta u_e \tag{2.49}$$

$$\delta\dot{\omega}_e = \frac{1}{\theta_e}\delta T_e - \frac{P_{m,idle}}{\theta_e\omega_{e,o}^2}\delta\omega_e. \tag{2.50}$$

The state space representation looks as follows:

$$\mathbf{x} = \begin{pmatrix} \delta T_e \\ \delta\omega_e \end{pmatrix},\ \mathbf{A}_{idle} = \begin{bmatrix} -\frac{1}{\tau_e} & 0 \\ \frac{1}{\theta_e} & -\frac{P_{m,idle}}{\theta_e\omega_{e,o}^2} \end{bmatrix},\ \mathbf{B}_{idle} = \begin{bmatrix} \frac{1}{\tau_e} \\ 0 \end{bmatrix},\ \mathbf{C}_{idle} = \begin{bmatrix} 0 & 1 \end{bmatrix} \tag{2.51}$$

$$\dot{\mathbf{x}} = \mathbf{A}_{idle}\cdot\mathbf{x} + \mathbf{B}_{idle}\cdot\delta u_e \tag{2.52}$$

$$\delta\omega_e = \mathbf{C}_{idle}\cdot\mathbf{x}. \tag{2.53}$$

The eigenvalues of the linearized system are

$$p_{idle} = \left\{ -\frac{1}{\tau_e}\ ,\ -\frac{P_{m,idle}}{\theta_e\omega_{e,o}^2} \right\} \tag{2.54}$$

and as can be seen, the system is unstable due to the constant electric load at idle conditions. Note that $P_{m,idle}$ is negative. The comparison of the open-loop step response of the linearization to response the nonlinear model is shown in Fig. 2.8. The responses are very similar up to $\omega_e = 900\,\mathrm{RPM}$, where the electric load increases and the nonlinear system is stabilized.

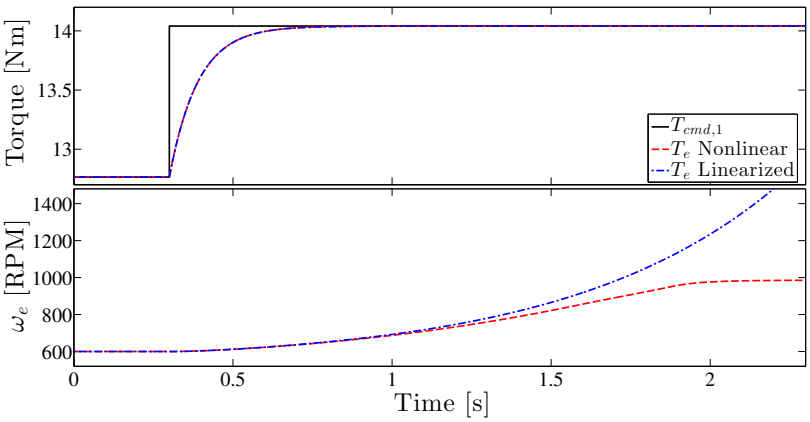

Figure 2.8: Open-loop responses of the nonlinear (dashed red) and the linearized (dash-dotted blue) systems at engine idle to a step in torque command. Top: Engine torque T_e with command $T_{cmd,1}$ (solid black). Bottom: Engine speed ω_e.

A PID controller C_{idle} was tuned to stabilize the system

$$T_{cmd,1} = C_{idle} \cdot (\omega_{ref,idle} - \omega_e) + T_{idle} \tag{2.55}$$

$$C_{idle}(s) = K_{p,idle} + \frac{1}{s} K_{i,idle} + s \cdot K_{d,idle} \tag{2.56}$$

resulting in a phase margin of 118° at 8.18 $^{\text{rad}}/_{\text{s}}$. In Fig. 2.9 the closed-loop responses of linearized and nonlinear model are compared during a step in reference engine speed $\omega_{ref,idle}$. The nonlinear and the linearized systems respond almost exactly the same, with a very fast convergence and acceptable overshoot. As can be seen, the torque command looks very aggressive, is then, however, significantly dampened by the engine torque dynamics from (2.29).

2.3.3 Torque Command

An engine is not always capable of delivering the maximum and minimum torque $\hat{T}_{max}$, $\hat{T}_{min}$, respectively. The engine torque command from the driver or ISC is saturated at the two limits $T_{max,SI}$ and $T_{min,SI}$. Therefore, for a conventional engine the torque command u_e is defined as:

$$u_e = \begin{cases} T_{max,SI} & T_{cmd,1} > T_{max,SI} \\ T_{min,SI} & T_{cmd,1} < T_{min,SI} \\ T_{cmd,1} & \text{else.} \end{cases} \tag{2.57}$$

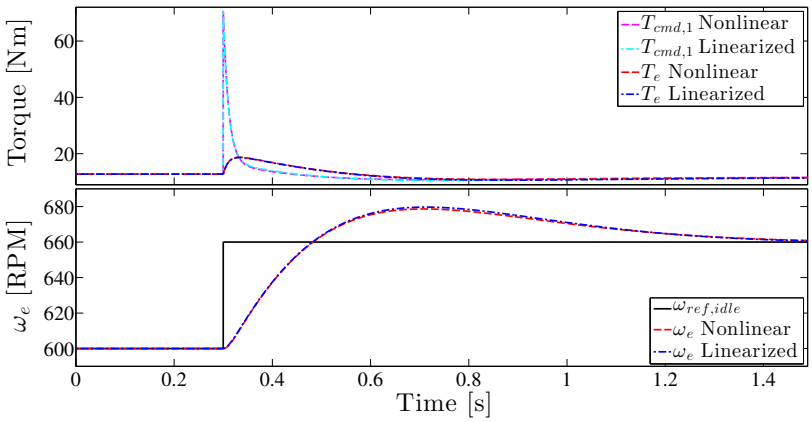

Figure 2.9: Closed-loop responses of the nonlinear (dashed red) and the linearized (dash-dotted blue) systems to a step in reference idle speed. Top: Engine torque T_e and command $T_{cmd,1}$ for the nonlinear (dashed magenta) and the linearized (dash-dotted cyan) system. Bottom: Engine speed ω_e with reference $\omega_{ref,idle}$ (solid black).

Modifications associated with multimode combustion operation are discussed in Sec. 3.4.

2.3.4 Fuel Cut-Off

During strong vehicle decelerations it can be beneficial to stop the engine fuel injection, therefore transmitting high negative torque T_{fc}, which is a function of ω_e. This strategy is denoted fuel cut-off. The binary command u_{fc} is used to activate a fuel cut-off and is in reality often calibrated based on several inputs, e.g., u_a, u_b, v, l, u_c, etc. If fuel cut-off is activated, the state equation for engine torque (2.29) needs to be replaced with

$$T_e = T_{fc} = f_{fc}(\omega_e). \tag{2.58}$$

For this vehicle, however, it was seen that fuel cut-off events occurred only rarely during the drive cycle measurements and it is not straightforward to reproduce them. Therefore, this functionality was generally not activated. In case of multimode operation, however, it can be beneficial to use fuel cut-off during mode switches, as discussed in Sec. 3.4.

2.4 Driver Model

The driver model's main responsibility is to follow the reference velocity v_{ref}, specified by the drive cycle, by tracking the error e, using acceleration and brake pedal positions, u_a and u_b, respectively.

$$e = v_{ref} - v \tag{2.59}$$

It is assumed that the driver has a preview of the reference velocity v_{pv} of 1 s. Based on this preview the acceleration $\dot{v}_{pv}$ is computed. Both values are used for gain-scheduling and vehicle launch.

$$v_{pv}(t) = v_{ref}(t + 1\,\mathrm{s}) \tag{2.60}$$

$$\dot{v}_{pv} = \frac{v_{pv} - v_{ref}}{1\,\mathrm{s}} \tag{2.61}$$

While it would also be possible to select the gear u_g depending on engine load and speed, in this paper the gear follows a predetermined shift schedule g_{ref}. The clutch pedal position u_c connects the engine with the rest of the drivetrain. As explained above, the drivetrain model distinguishes between locked and slipping clutch. To achieve a realistic load behavior it is required to accurately shift gears and to drive with slipping clutch during vehicle launches and stops. Therefore the driver model is divided into three discrete states ϵ.

The state machine coordinating the three modes is shown in Fig. 2.10. The driver mode $\epsilon = 1$ is the primary mode and responsible for velocity control at locked clutch condition. The other two modes are active while the clutch is slipping. If the engine speed ω_e drops below a threshold $\omega_{e,min}$, the mode is switched to $\epsilon = 2$, which controls vehicle halt, standstill, and launch. On the other hand, if a gear shift is requested, $g_{ref} \neq u_g$, the mode is changed to $\epsilon = 3$, which conducts the up- and downshifts. The modes are switched back to $\epsilon = 1$ when the clutch locks, $l = 1$, after the shifts are completed. In the following sections the different modes are described in detail. The associated parameters can be found in Table 2.4.

2.4.1 Driver Mode $\epsilon = 1$, Locked

The driver mode $\epsilon = 1$ is responsible for vehicle control at locked clutch condition. To tune the controller the nonlinear vehicle model is linearized around a constant velocity v_o with a specific gear selection $u_{g,o}$. Generally, the drivetrain mode is locked, $l = 1$,

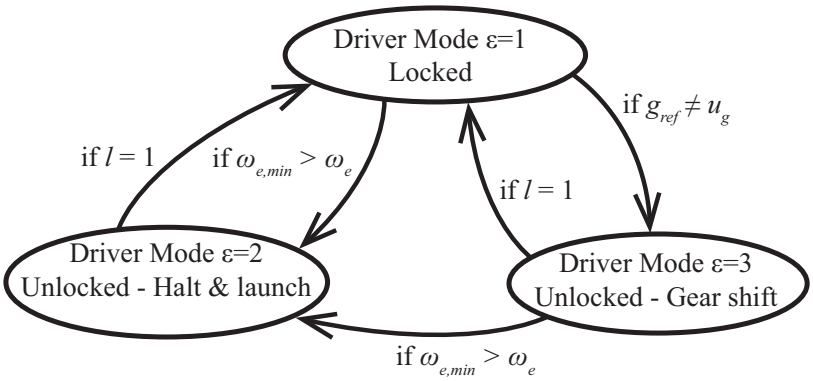

Figure 2.10: State machine for the three driver modes ϵ.

with fully released brake and clutch pedals, $u_{b,o} = u_{c,o} = 0$. Tire slip is neglected, which leads to the following equilibrium condition:

$$\gamma_o = \gamma_g(u_{g,o}) \cdot \gamma_{fdr} \tag{2.62}$$

$$T_{e,b,o} = \frac{1}{\gamma_o} \cdot T_{w,o} = \frac{r_w}{\gamma_o} \cdot F_{l,o} = \frac{r_w}{\gamma_o} \left(\frac{1}{2} \rho_a A_f \mu_a v_o^2 + m_v g(\mu_{r,0} + v_o \mu_{r,1}) + m_v g \right) \tag{2.63}$$

$$\omega_{e,o} = \gamma_o \cdot \omega_{w,o} = \gamma_o \frac{v_{v,o}}{r_w} \tag{2.64}$$

$$\omega_{m,o} = \gamma_b \cdot \omega_{e,o} \tag{2.65}$$

$$T_{ps,o} = \frac{P_{ps,o}}{\omega_{e,o}} = \frac{P_{ps,1} + a_{ps} \cdot (\omega_{e,o} - \omega_{ps,1})}{\omega_{e,o}} \tag{2.66}$$

$$T_{m,o} = \frac{P_{m,o}}{\omega_{m,o}} = -\frac{f_m^{-1}(\omega_{m,o}, P_{al,o})}{\omega_{e,o}} \tag{2.67}$$

$$T_{des,o} = u_{e,o} = T_{e,o} = T_{e,b,o} + T_{ps,o} - \gamma_b T_{m,o} \tag{2.68}$$

$$u_{a,o} = \frac{\hat{T}_{max} - T_{des,o}}{\hat{T}_{max} - \hat{T}_{min}}. \tag{2.69}$$

The linearization of the road load F_l leads to

$$\delta F_l = (\rho_a A_f \mu_a v_o + \mu_{r,1} m_v g) \cdot \delta v \tag{2.70}$$

and the linearized auxiliary loads are

$$\delta T_{ps} = \underbrace{\left(-\frac{P_{ps,o}}{\omega_{e,o}^2} + \frac{a_{ps}}{\omega_{e,o}}\right)}_{=a_{ps,1}} \delta\omega_e \tag{2.71}$$

$$\delta T_m = \underbrace{\left(-\frac{P_{m,o}}{\omega_{m,o}^2} + \frac{a_m}{\omega_{m,o}}\right)}_{=a_{m,1}} \delta\omega_m \tag{2.72}$$

where a_m is the slope of f_m^{-1} at the associated equilibrium:

$$a_m = \frac{d}{d\omega_m} f_m^{-1}(\omega_m, P_{al})|_{\omega_m=\omega_{m,o}}. \tag{2.73}$$

The rotational inertia of the driveline can be summarized as

$$\theta_1 = (\theta_e + \theta_g)\gamma_o^2 + \theta_w(n_{w,d} + n_{w,n}) + m_v r_t^2. \tag{2.74}$$

The linearized state equations for the vehicle under locked clutch condition follow as

$$\delta\dot{T}_e = -\frac{1}{\tau_e}\delta T_e + \frac{\hat{T}_{max} - \hat{T}_{min}}{\tau_e}\delta u_a \tag{2.75}$$

$$\delta\dot{\omega}_w = \frac{\gamma_o\eta_g}{\theta_1}\delta T_e - \frac{1}{\theta_1}\left(r_t(\rho_a A_f \mu_a v_o + \mu_{r,1} m_v g) - (a_{m,1}\gamma_b^2 - a_{ps,1})\gamma_o^2\eta_g\right)\delta\omega_w \tag{2.76}$$

with the associated state space representation:

$$\mathbf{A}_{drive} = \begin{bmatrix} -\frac{1}{\tau_e} & 0 \\ \frac{\gamma_o\eta_g}{\theta_1} & -\frac{1}{\theta_1}\left(r_t(\rho_a A_f \mu_a v_o + \mu_{r,1} m_v g) - (a_{m,1}\gamma_b^2 - a_{ps,1})\gamma_o^2\eta_g\right) \end{bmatrix}, \tag{2.77}$$

$$\mathbf{x} = \begin{bmatrix} \delta T_e \\ \delta\omega_e \end{bmatrix}, \mathbf{B}_{drive} = \begin{bmatrix} \frac{\hat{T}_{max} - \hat{T}_{min}}{\tau_e} \\ 0 \end{bmatrix}, \mathbf{C}_{drive} = \begin{bmatrix} 0 & r_w \end{bmatrix} \tag{2.78}$$

$$\dot{\mathbf{x}} = \mathbf{A}_{drive} \cdot \mathbf{x} + \mathbf{B}_{drive} \cdot \delta u_a \tag{2.79}$$

$$\delta v = \mathbf{C}_{drive} \cdot \mathbf{x}. \tag{2.80}$$

The poles of the linearized system are

$$p_{drive} = \left\{-\frac{1}{\tau_e}\ ,\ -\frac{1}{\theta_1}\left(r_t(\rho_a A_f \mu_a v_o + \mu_{r,1} m_v g) - (a_{m,1}\gamma_b^2 - a_{ps,1})\gamma_o^2\eta_g\right)\right\} \tag{2.81}$$

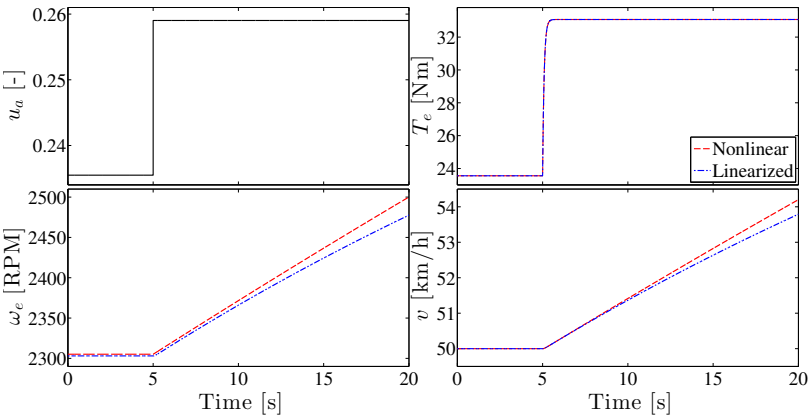

Figure 2.11: Open-loop responses of the nonlinear (dashed red) and the linearized (dash-dotted blue) systems to a step in accelerator pedal position. Top left: Pedal position u_a. Top right: Engine torque T_e. Bottom left: Engine speed ω_e. Bottom right: Velocity v.

and as can be seen the stability of the system depends on the local slopes of the motor efficiency map and the road load. Therefore the stability varies with operating condition. By sweeping the equilibrium point over reasonable velocities and gears it was seen that the system is asymptotically stable for a majority of cases. The associated pole varies from -0.057 to 0.082 and is therefore always relatively slow, even when unstable. The system becomes unstable at low velocities and gears due to the shape of f_m^{-1}. However, this does not significantly impact its overall behavior. The linearized and the nonlinear systems are compared in Fig. 2.11 during a step in pedal position u_a and as can be seen they show very similar responses.

The vehicle is controlled based on gain-scheduled PI controllers due to the following reasons. First of all, the vehicle system is nonlinear and its dynamics depend on operating condition, mainly gear selection and velocity. Second of all, during normal driving it is generally not too difficult for the driver to remain within the tolerance limits of the drive cycle. However, during short periods of very high acceleration, when the gear shifts act as disturbance, the driver needs to be more aggressive to be able to stay within bounds. For the moderate phase a controller with lower crossover frequency is acceptable. Here the PI controller $C_{drive,mod}$ was tuned to result in a phase margin of 65° at $1\,^{\mathrm{rad}}/_{\mathrm{s}}$. For aggressive accelerations the controller $C_{drive,agg}$ was tuned to a phase margin of 65° at $2.2\,^{\mathrm{rad}}/_{\mathrm{s}}$.

The closed-loop response of the system is shown in Fig. 2.12. As can be seen both controllers show a similar and acceptable overshoot. As expected the controller $C_{drive,agg}$ converges significantly faster, utilizes, however, much higher torque. Note

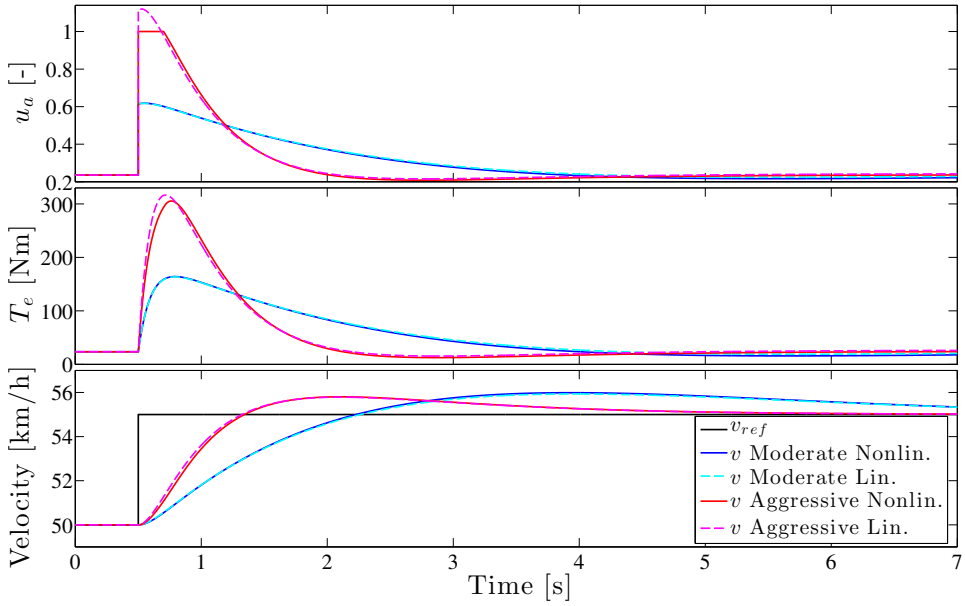

Figure 2.12: Closed-loop responses of the nonlinear (solid) and the linearized (dashed) systems to a step in reference velocity using the controllers $C_{drive,mod}$ (blue) and $C_{drive,agg}$ (red). Top: Acceleration pedal position u_a. Center: Engine torque T_e. Bottom: Velocity v with reference v_{ref} (solid black).

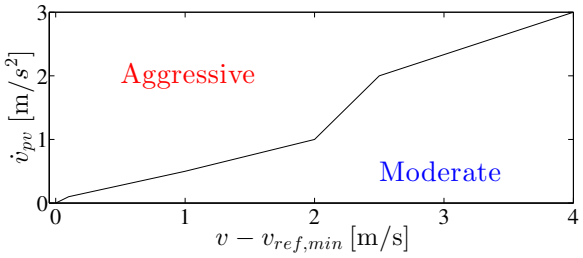

Figure 2.13: Decision to use an aggressive or moderate driver controller $C_{drive,agg}$ and $C_{drive,mod}$, respectively.

that in the nonlinear model u_a saturates at 0 and 1 using anti-reset windup. But as can be seen this only has little influence on the overall response of the system due to the dynamics in engine torque.

A logic is implemented which selects the appropriate set of controller gains. In general the moderate controller is used. However, as shown in Fig. 2.13, in situations with high acceleration $\dot{v}_{pv}$ or if the velocity get close to its lower tolerance limit $v_{ref,min}$, it is switched to the aggressive gains.

As shown in Fig. 2.14 the controller parameters $K_{p,drive}$ and $K_{i,drive}$ were tuned

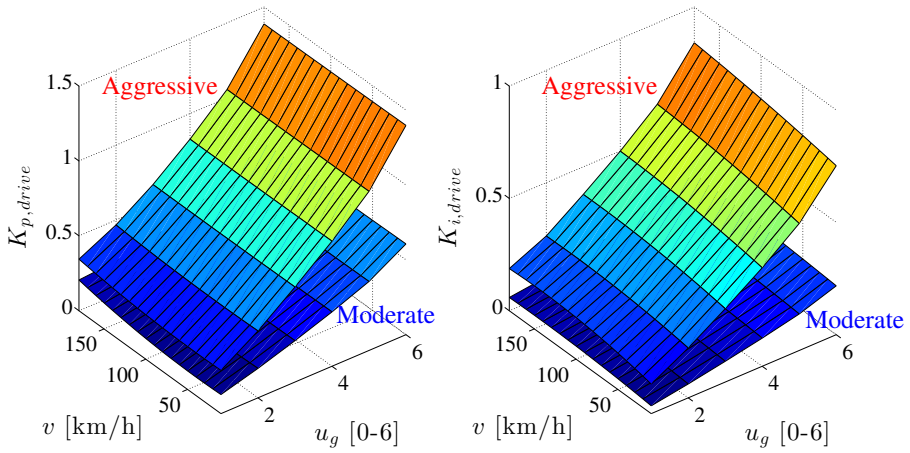

Figure 2.14: Gains of driver controllers $C_{drive,agg}$ and $C_{drive,mod}$ scheduled as a function of velocity v and gear u_g to result in constant phase margin and crossover frequency. Left: $K_{p,drive}$. Right: $K_{i,drive}$.

at a variety of gears u_g and velocities v:

$$u_a = C_{drive} \cdot e \tag{2.82}$$

$$C_{drive}(s) = K_{p,drive}(v, u_g) + \frac{1}{s} K_{i,drive}(v, u_g). \tag{2.83}$$

Controller C_{drive} is saturated between (-1,1) with anti-reset windup and used to compute u_a (positive output) and u_b (negative output):

$$u_a = \max\{\mathrm{C}_{drive} \cdot e, 0\} \tag{2.84}$$

$$u_b = \max\{-\mathrm{C}_{drive} \cdot e, 0\}. \tag{2.85}$$

2.4.2 Driver Mode $\epsilon = 2$, Unlocked - Halt & Launch

Driver mode $\epsilon = 2$ controls the vehicle while the clutch is slipping during halt, standstill, and launch. A state machine is used to distinguish between those different driving scenarios, shown in Fig. 2.15. For low engine speeds the no-kill condition must be fulfilled, i.e., one must avoid engine stall. During deceleration and standstill this is mainly achieved by the ISC within the ECU model, see Sec. 2.3, while the acceleration pedal is released $u_a = 0$. However, during acceleration phases the driver needs to control acceleration and clutch pedals accordingly. Overall, two situations are distinguished. Either the transmission is in Neutral, $u_g = 0$, or a gear is engaged,

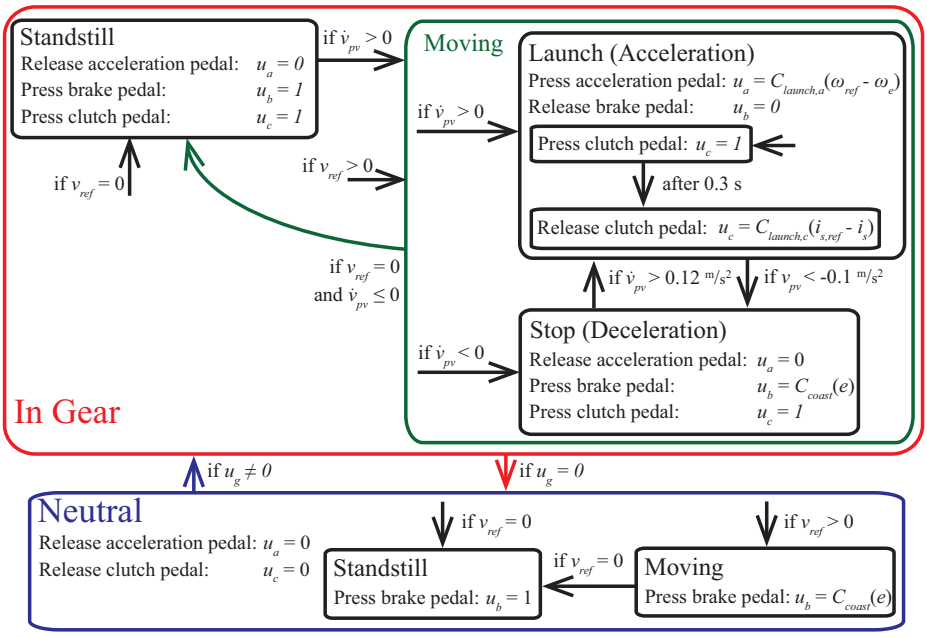

Figure 2.15: State machine for the driver mode $\epsilon = 2$.

$u_g \neq 0$. Furthermore, a distinction is made between vehicle standstill and motion, i.e., launch and stop. The transition between those different driver sub-states is managed by the finite-state machine, shown in Fig. 2.15.

Neutral $u_g = 0$

If the gearbox is in Neutral, the engine is disconnected from the driveline. Therefore the clutch is allowed to be locked and the associated pedal can be released, $u_c = 0$. Concurrently, the acceleration pedal is released, $u_a = 0$, while the ISC regulates engine speed, see (2.55). If a non-zero reference velocity v_{ref} is requested and the vehicle is coasting, the only active controller output is the brake pedal u_b, output of PI controller C_{coast}:

$$C_{coast}(s) = K_{p,coast} + \frac{1}{s} K_{i,coast} \tag{2.86}$$

$$u_b = \max\{-C_{coast} \cdot e, 0\}. \tag{2.87}$$

If a standstill is requested, $v_{ref} = 0$, the brake is fully engaged, $u_b = 1$.

In Gear $u_g \neq 0$

If a gear is engaged, the clutch pedal u_c is required to prevent the engine from stalling. During vehicle standstill, again, the acceleration pedal is released, $u_a = 0$, while both brake and clutch pedal a fully pressed, $u_b = u_c = 1$.

Launch As soon as a vehicle acceleration is requested, $\dot{v}_{pv} > 0$, the brake is released and u_a and u_c need to be coordinated. Representative launch conditions are

$$v_o = 4\,{}^{\mathrm{km}}\!/_{\mathrm{h}}\ ,\ \omega_{e,o} = 900\,\mathrm{RPM}\ ,\ u_{g,o} = 1 \tag{2.88}$$

with the clutch unlocked. The equations to compute the equilibrium conditions are similar to the ones above, except for

$$\omega_{c,o} = \gamma_o \cdot \omega_{w,o} \tag{2.89}$$

$$T_{c,k,o} = \frac{1}{\gamma_o} \cdot T_{w,o} \tag{2.90}$$

$$u_{c,o} = 1 - \left(\frac{\mu_{c,k}}{\mu_{c,s}}\right)^{-1} \cdot \frac{T_{c,k,o}}{T_{c,max}} \tag{2.91}$$

$$T_{des,o} = u_{e,o} = T_{e,o} = T_{ps,o} - \gamma_b T_{m,o}. \tag{2.92}$$

The rotational inertia from vehicle to gearbox can be summarized to

$$\theta_2 = \theta_g \gamma_o^2 + \theta_w (n_{w,d} + n_{w,n}) + m_v r_w^2. \tag{2.93}$$

The linearization of road load and auxiliary loads is shown in (2.70), (2.71), and (2.72), respectively. Linearization of the clutch friction torque leads to

$$\delta T_{c,k} = -\left(\frac{\mu_{c,k}}{\mu_{c,s}}\right) \cdot T_{c,max} \cdot \delta u_c. \tag{2.94}$$

This results in the following, linearized state equations:

$$\delta \dot{T}_e = -\frac{1}{\tau_e}\delta T_e + \frac{\hat{T}_{max} - \hat{T}_{min}}{\tau_e}\delta u_a \tag{2.95}$$

$$\delta \dot{\omega}_e = \frac{1}{\theta_e}\delta T_e + \frac{a_{m,1}\gamma_b^2 - a_{ps,1}}{\theta_e}\delta \omega_e + \left(\frac{\mu_{c,k}}{\mu_{c,s}}\right) \cdot \frac{T_{c,max}}{\theta_e}\delta u_c \tag{2.96}$$

$$\delta \dot{\omega}_w = -\frac{r_t(\rho_a A_f \mu_a v_{v,o} + \mu_{r,1} m_v g)}{\theta_2}\delta \omega_w - \left(\frac{\mu_{c,k}}{\mu_{c,s}}\right) \cdot \frac{\gamma_0 \eta_g T_{c,max}}{\theta_2}\delta u_c. \tag{2.97}$$

The state-space representation is chosen such that $\delta\omega_e$ and i_c are the outputs:

$$\mathbf{x} = \begin{bmatrix} \delta T_e \\ \delta\omega_e \\ \delta\omega_w \end{bmatrix}, \mathbf{A}_{launch} = \begin{bmatrix} -\frac{1}{\tau_e} & 0 & 0 \\ \frac{1}{\theta_e} & \frac{a_{m,1}\gamma_b^2 - a_{ps,1}}{\theta_e} & 0 \\ 0 & 0 & -\frac{r_t(\rho_a A_f \mu_a v_{v,o} + \mu_{r,1} m_v g)}{\theta_2} \end{bmatrix}, \quad (2.98)$$

$$\mathbf{B}_{launch} = \begin{bmatrix} \frac{\hat{T}_{max} - \hat{T}_{min}}{\tau_e} & 0 \\ 0 & \left(\frac{\mu_{c,k}}{\mu_{c,s}}\right) \cdot \frac{T_{c,max}}{\tau_e} \\ 0 & -\left(\frac{\mu_{c,k}}{\mu_{c,s}}\right) \cdot \frac{\gamma_0 \eta_g T_{c,max}}{\theta_2} \end{bmatrix}, \mathbf{C}_{launch} = \begin{bmatrix} 0 & 1 & 0 \\ 0 & 1 & -\gamma_o \end{bmatrix}. \quad (2.99)$$

$$\dot{\mathbf{x}} = \mathbf{A}_{launch} \cdot \mathbf{x} + \mathbf{B}_{launch} \cdot \begin{bmatrix} \delta u_a \\ \delta u_c \end{bmatrix} \quad (2.100)$$

$$\begin{bmatrix} \delta\omega_e \\ i_c \end{bmatrix} = \mathbf{C}_{launch} \cdot \mathbf{x}. \quad (2.101)$$

The eigenvalues are

$$p_{launch} = \left\{ -\frac{1}{\tau_e}, \frac{a_{m,1}\gamma_b^2 - a_{ps,1}}{\theta_e}, -\frac{r_t(\rho_a A_f \mu_a v_o + \mu_{r,1} m_v g)}{\theta_2} \right\}. \quad (2.102)$$

The system is unstable due to the shape of f_m^{-1}. The responses of the system during steps in u_a and u_c are shown in Fig. 2.16. As can be seen the engine speed is very sensitive to both control inputs, while velocity only changes little during the step in u_c. Two SISO controllers are applied to control the vehicle launch. The velocity needs to be increased by reducing u_c, which in turn leads to a drop in ω_e. As can be seen in $\mathbf{C}_{launch}$, both v and ω_e will effect clutch slip i_c and make it decrease. The controller in the outer loop uses the clutch pedal u_c to control and reduce clutch slip i_c to 0, enabling the clutch to lock. Meanwhile the engine speed ω_e is held with u_a by the controller in the inner loop. To design the controller the two loops are closed sequentially. The inner loop only consists of the engine and its state-space representation looks as follows:

$$\mathbf{x} = \begin{bmatrix} \delta T_e \\ \delta\omega_e \end{bmatrix}, \mathbf{A}_{launch,a} = \begin{bmatrix} -\frac{1}{\tau_e} & 0 \\ \frac{1}{\theta_e} & \frac{a_{m,1}\gamma_b^2 - a_{ps,1}}{\theta_e} \end{bmatrix}, \quad (2.103)$$

$$\mathbf{B}_{launch,a} = \begin{bmatrix} \frac{\hat{T}_{max} - \hat{T}_{min}}{\tau_e} \\ 0 \end{bmatrix}, \mathbf{C}_{launch,a} = \begin{bmatrix} 0 & 1 \end{bmatrix} \quad (2.104)$$

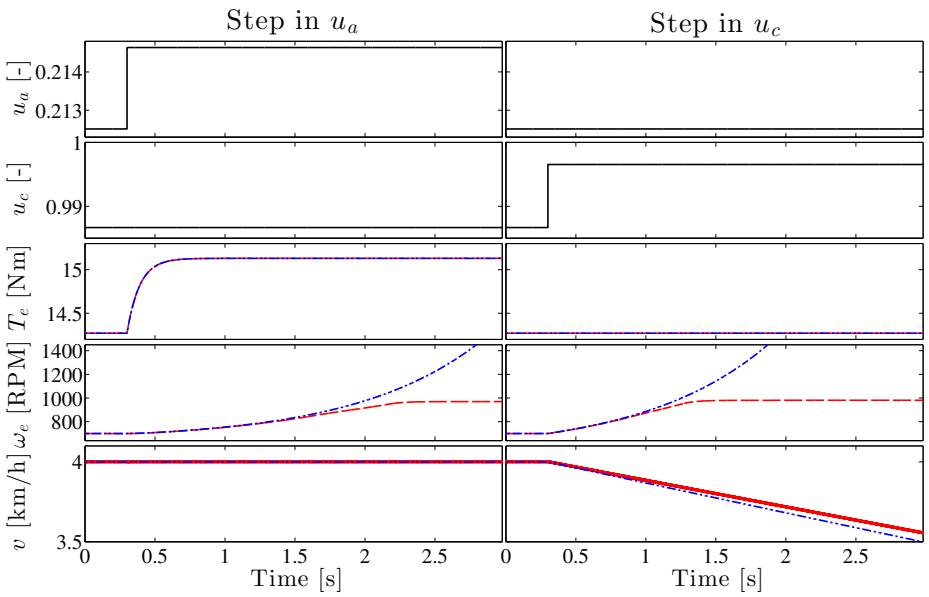

Figure 2.16: Open-loop responses of the nonlinear (dashed red) and the linearized (dash-dotted blue) systems to a step in accelerator pedal (left) and clutch pedal (right). Top: Accelerator pedal u_a. Second row: Clutch pedal u_c. Third row: Engine torque T_e. Fourth row: Engine speed ω_e. Bottom: Velocity v.

$$\dot{\mathbf{x}} = \mathbf{A}_{launch,a} \cdot \mathbf{x} + \mathbf{B}_{launch,a} \cdot \delta u_a \tag{2.105}$$

$$\delta\omega_e = \mathbf{C}_{launch,a} \cdot \mathbf{x}. \tag{2.106}$$

The system is stabilized with the PID controller $C_{launch,a}$ leading to a phase margin of 50° at 28.7 $^{\text{rad}}/_{\text{s}}$:

$$u_a = C_{launch,a} \cdot (\omega_{e,ref} - \omega_e) \tag{2.107}$$

$$C_{launch,a}(s) = K_{p,launch,a} + \frac{1}{s} K_{i,launch,a} + s \cdot K_{d,launch,a}. \tag{2.108}$$

The step response of the system, with $C_{launch,a}$ in the loop, is shown in Fig. 2.17. As can be seen, the controller is relatively aggressive, which is necessary, since it has to reject disturbances induced by the outer loop and u_c as fast as possible.

The transfer function from u_c to i_c is calculated with $C_{launch,a}$ in the loop.

$$G_1(s) = \frac{\delta T_e}{\delta\omega_e} = -\frac{\hat{T}_{max} - \hat{T}_{min}}{\tau_e \cdot s + 1} C_{launch,a}(s) \tag{2.109}$$

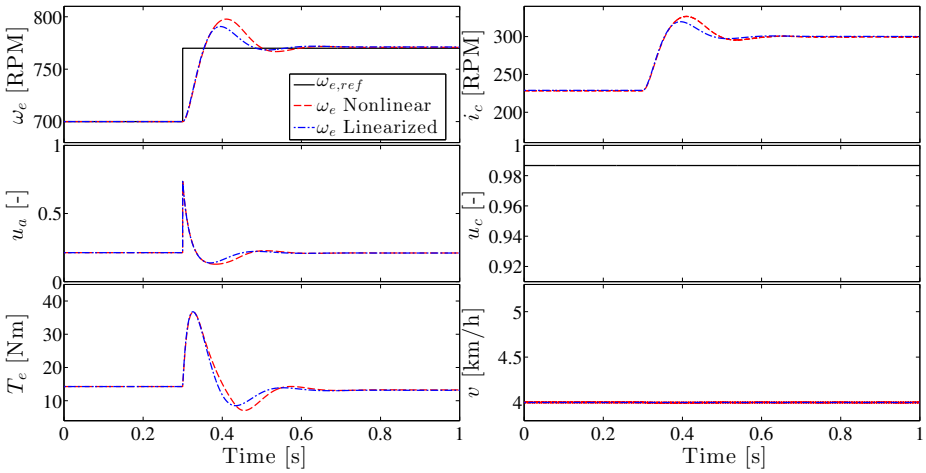

Figure 2.17: Closed-loop response of the nonlinear (dashed red) and the linearized (dash-dotted blue) systems to a step in reference engine speed. Top left: Engine speed ω_e with reference $\omega_{e,ref}$ (black solid). Top right: Clutch slip i_c. Center left: Accelerator pedal u_a. Center right: Clutch pedal u_c. Bottom left: Engine torque T_e. Bottom right: Velocity v.

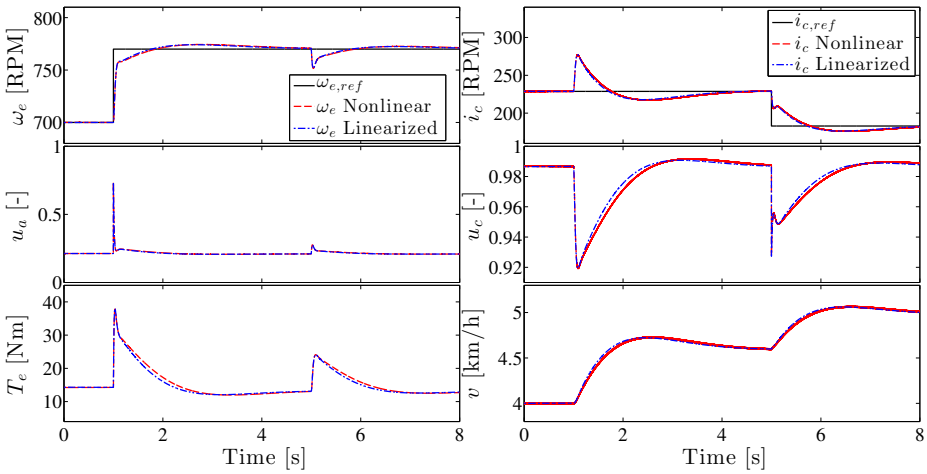

Figure 2.18: Closed-loop response of the nonlinear (dashed red) and the linearized (dash-dotted blue) systems to steps in reference engine and clutch slip speed, respectively. Top left: Engine speed ω_e with reference $\omega_{e,ref}$ (solid black). Top right: Clutch slip i_c with reference $i_{c,ref}$ (solid black). Center left: Accelerator pedal u_a. Center right: Clutch pedal u_c. Bottom left: Engine torque T_e. Bottom right: Velocity v.

Therefore the closed-loop transfer function from u_c to ω_e is

$$s\delta\omega_e = \left(\frac{1}{\theta_e}G_1(s) + \frac{a_{m,1}\gamma_b^2 - a_{ps,1}}{\theta_e}\right)\delta\omega_e + \left(\frac{\mu_{c,k}}{\mu_{c,s}}\right)\cdot\frac{T_{c,max}}{\theta_e}\delta u_c \tag{2.110}$$

$$\Leftrightarrow G_2(s) = \frac{\delta\omega_e}{\delta u_c} = \left(\frac{\mu_{c,k}}{\mu_{c,s}}\right)\cdot\frac{T_{c,max}}{\theta_e s - G_1(s) - a_{m,1}\gamma_b^2 + a_{ps,1}}. \tag{2.111}$$

The first-order open-loop transfer function from u_c to ω_w is simply

$$G_3(s) = \frac{\delta\omega_w}{\delta u_c} = -\left(\frac{\mu_{c,k}}{\mu_{c,s}}\right) \cdot \frac{\gamma_o \eta_g T_{c,max}}{\theta_2 s + r_t(\rho_a A_f \mu_a v_o + \mu_{r,1} m_v g)}. \tag{2.112}$$

From this follows the open-loop transfer function for the entire system:

$$\delta i_c(s) = \delta\omega_e(s) - \gamma_o \cdot \delta\omega_w(s) = (G_2(s) - \gamma_o \cdot G_3(s))\, \delta u_c. \tag{2.113}$$

The PI controller $C_{launch,c}$, resulting in a phase margin of 90° at $4\,^{\mathrm{rad}}/_{\mathrm{s}}$,

$$\delta u_c = C_{launch,c} \cdot (i_{c,ref} - i_c) \tag{2.114}$$

$$C_{launch,c}(s) = K_{p,launch,c} + \frac{1}{s} K_{i,launch,c} \tag{2.115}$$

is used to track the reference clutch slip $i_{c,ref}$. The step response of the closed-loop system is shown in Fig. 2.18. As can be seen, ω_e and i_c can be controlled independently.

Since the maximum engine torque at low engine speeds is relatively small, it is useful to ramp up the reference engine speed $\omega_{e,ref}$ during the launch, to increase robustness against the influence of u_c. While the priority of the launch controller is to reduce the clutch slip without stalling the engine, it is also important to follow the reference velocity v_{ref}. Both goals are achieved by using v_{ref} and $\omega_{e,ref}$ to calculate the associated $i_{c,ref}$:

$$i_{c,ref} = \omega_{e,ref} - \frac{\gamma}{r_t} v_{ref}. \tag{2.116}$$

Eventually, $i_c = 0$, i.e., $\omega_e = \omega_c$, will be reached, the clutch will lock and the driver mode will change to $\epsilon = 1$.

A complete launch using the full model is shown in Fig. 2.19. As can be seen, due to the preview v_{pv} the reference engine speed $\omega_{e,ref}$ is ramped up a fraction of a second before the vehicle launch is demanded. Immediately after v_{ref} changes, the controller $C_{launch,c}$ is used to track the reference clutch slip $i_{c,ref}$. This leads to launch of the vehicle. As can be seen, both pedal positions, u_a and u_c, are moved simultaneously, resulting in increasing engine speed and velocity. It is highlighted where $v > v_{min,t}$ and the tire slip is activated, $\delta = 3 \to 2$. Eventually i_c drops below a threshold at which u_c is quickly ramped down, leading to a drop in engine speed and fast increase in clutch torque $T_{c,s}$. This in turn leads to lock-up of the clutch, $\delta = 2 \to 1$. It can be seen that in the example presented here, throughout the launch $T_{c,s} > |T_{c,req}|$ and therefore the static friction torque is high enough to lock the clutch. During more

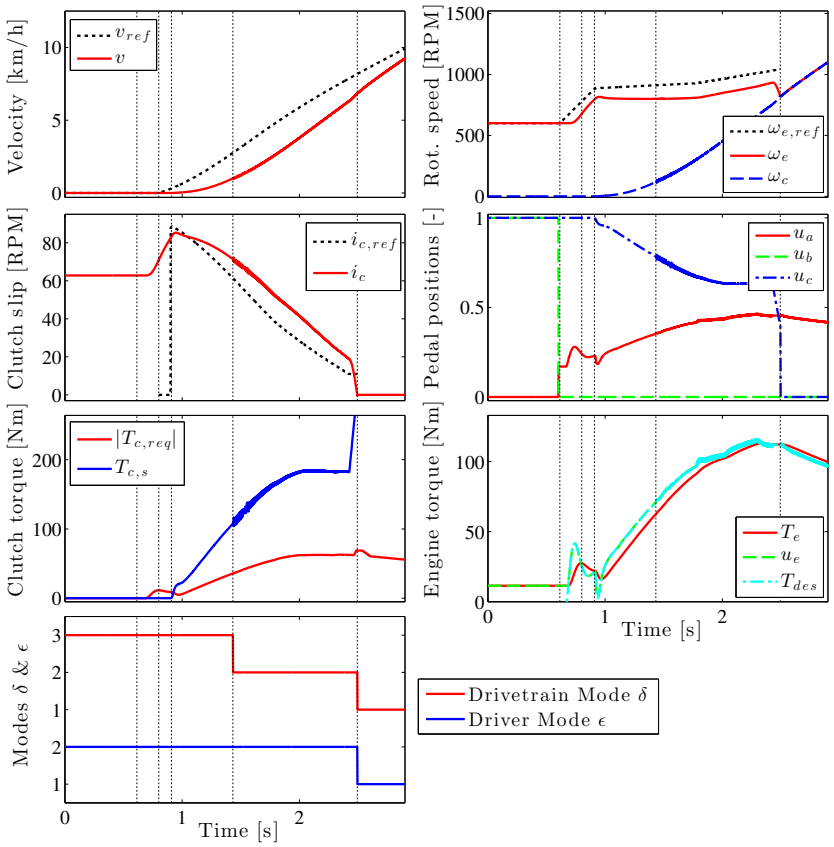

Figure 2.19: Exemplary launch of the complete, nonlinear model during the FTP75 drive cycle.

aggressive accelerations, however, this might not be the case and the last quick release of the clutch pedal can be used to ensures high friction torque. As soon as the clutch locks the driver mode switches, $\epsilon = 2 \rightarrow 1$.

Stop If a vehicle deceleration is requested, $\dot{v}_{pv} < 0$, the acceleration pedal is released and the clutch pedal pressed, $u_a = 0$ and $u_c = 1$, respectively. The brake pedal tracks velocity with PI controller C_{coast}, see (2.86), (2.87).

2.4.3 Driver Mode $\epsilon = 3$, Unlocked - Gear Shift

Driver mode $\epsilon = 3$ is responsible for up- and downshifts. One shift is divided into four different phases, similar to the description in [106]. A state machine is used to transition through those phases, shown in Fig. 2.20.

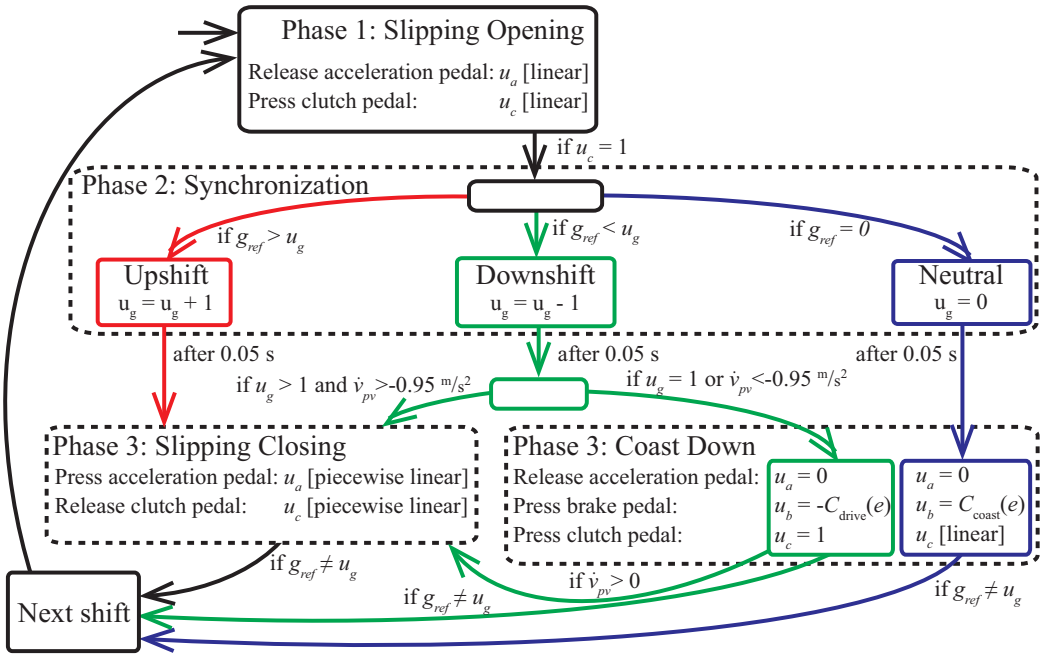

Figure 2.20: State machine for the driver mode $\epsilon = 3$.

Slipping Opening

Initially the clutch is engaged. As soon as g_{ref} requests a gear shift the slipping-opening phase starts, denoted as time $t_{gs,1}$. The acceleration pedal u_a is released and u_c pressed using linear feedforward trajectories:

$$u_c = K_{gs,1} \cdot (t - t_{gs,1}) \tag{2.117}$$

$$u_a = u_a(t_{gs,1}) \cdot (1 - K_{gs,1} \cdot K_{gs,2}(t - t_{gs,1}))\,. \tag{2.118}$$

At some point during this phase the clutch disengages and drivetrain mode δ switches from locked to unlocked.

Synchronization

As soon as the clutch pedal is fully released, $u_c = 1$, the synchronization phase begins. The gear is changed depending if an up- or a downshift or a shift to Neutral is

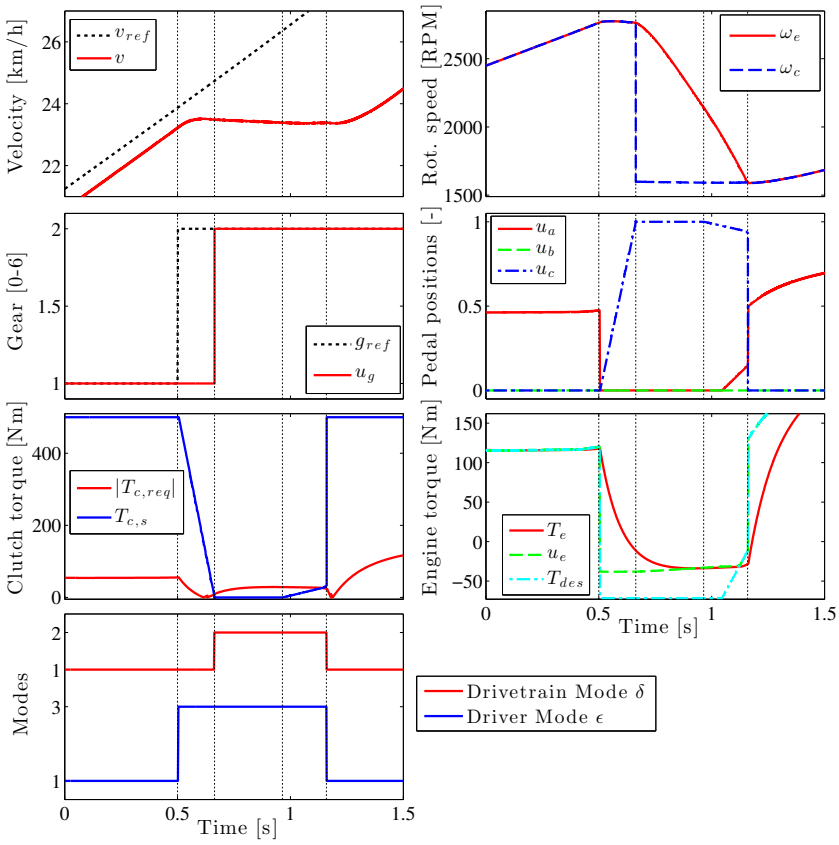

Figure 2.21: Exemplary gear shift of the complete, nonlinear model during FTP75 drive cycle.

requested. k denotes the current time step.

$$u_g(k+1) = \begin{cases} u_g(k)+1 & g_{ref} > u_g(k) \\ u_g(k)-1 & 0 < g_{ref} < u_g(k) \\ 0 & g_{ref} = 0 \end{cases} \tag{2.119}$$

Meanwhile the inputs are held constant at $u_c = 1$ and $u_a = 0$.

Slipping Closing

After the gear change the slipping closing phase begins, denoted as time $t_{gs,2}$. During an upshift both u_a and u_c are controlled using feedforward trajectories to regulate

Table 2.4: Driver model parameters

Name	**Symbol**	**Value**	
		HF V6	MM I4
Coast $\epsilon = \{2, 3\}$	Kp_{coast}	0.6	
	$K_{i,coast}$	0.8	
Launch $\epsilon = 2$	$Kp_{launch,a}$	0.023	0.027
	$K_{i,launch,a}$	0.0113	0.0134
	$K_{d,launch,a}$	$4.79 \cdot 10^{-4}$	$5.57 \cdot 10^{-4}$
	$K_{p,launch,c}$	0.0124	0.0125
	$K_{i,launch,c}$	0.0148	0.0146
Gear shift $\epsilon = 3$	$K_{gs,1}$	$6.3\,1/\mathrm{s}$	
	$K_{gs,2}$	1.5	
	$K_{gs,3}$	$1.3\,1/\mathrm{s}$	
	$K_{gs,4}$	$0.3\,1/\mathrm{s}$	
	$K_{gs,5}$	$1\,1/\mathrm{s}$	
	$\Delta t_{gs,1}$	0.33 s	
	$\Delta t_{gs,2}$	0.25 s	
	$\Delta t_{gs,3}$	0.18 s	

engine and vehicle speed:

$$u_a = \begin{cases} 0 & t < t_{gs,2} + \Delta t_{gs,1} \text{ and } \omega_e > \omega_c \\ K_{gs,3} \cdot (t - (t_{gs,2} + \Delta t_{gs,1})) & \text{else} \end{cases} \tag{2.120}$$

$$u_c = \begin{cases} 1 & t - t_{gs,2} < \Delta t_{gs,2} \\ 1 - K_{gs,4} \cdot (t - (t_{gs,2} + \Delta t_{gs,2})) & \Delta t_{gs,2} \leq t - t_{gs,2} < \Delta t_{gs,2} + \Delta t_{gs,3} \\ 1 - K_{gs,4} \Delta t_{gs,2} \ldots & \\ -K_{gs,5} \left(t - (t_{gs,2} + \Delta t_{gs,2} + \Delta t_{gs,3})\right) & \text{else.} \end{cases} \tag{2.121}$$

Eventually the clutch will lock up, $l = 1$, and therefore the driver mode will switch back to $\epsilon = 1$. During a downshift similar trajectories are used:

$$u_a = K_{gs,3} \cdot (t - t_{gs,2}) \tag{2.122}$$

$$u_c = 1 - K_{gs,5}(t - t_{gs,2}). \tag{2.123}$$

However, while generally upshifts occur one gear at a time to avoid large drops in engine speed, during downshifts gears are often skipped. In such cases, before u_a and u_c are moved, (2.119) is repeated until the final gear is reached.

If the gear is changed to Neutral or a downshift occurs during a steep deceleration, $\dot{v}_{pv} < -0.95\,\mathrm{m/s^2}$, a coast-down is assumed. Therefore acceleration and clutch pedals are released, $u_a = u_c = 0$, and the brake pedal is used to regulate velocity with PI controllers C_{coast}, (2.86), (2.87), and C_{drive}, (2.82), (2.83). If the vehicle continues the coast-down, eventually $\omega_e < \omega_{e,min}$ and the driver mode transitions to $\epsilon = 2$.

An exemplary upshift with the full vehicle model is presented in Fig. 2.21. As can be seen, as soon as g_{ref} changes, the gear shift mode is entered, $\epsilon = 1 \rightarrow 3$, u_a is fully released and u_c ramped up. Eventually $T_{c,s} < |T_{c,req}|$ and the clutch unlocks, $\delta = 1 \rightarrow 2$. The gear is changed and after a time delay of 0.05 s both u_a and u_c are moved again. Meanwhile ω_e approaches ω_c, due to the negative engine torque and the increasing clutch friction. Eventually the clutch slip will be zero and $T_{c,s} > |T_{c,req}|$, which will lead to lock-up of the clutch and return to the regular driver mode, $\delta = 3 \rightarrow 1$.

2.5 Model Validation & Analysis

The vehicle and driver model is validated by comparing the quantitative results as well as the qualitative behavior to chassis dynamometer measurements that were acquired within the ACCESS project. Experimental results from the FTP75, the HWFET, and the US06 drive cycle were available for the Cadillac CTS model year 2009 baseline vehicle equipped with the original HFV6 3.6 L engine.

2.5.1 Quantitative Validation

The fuel economy results as well as the accuracy of the driver to track the reference velocity are used for quantitative validation. Furthermore, the cumulated errors between engine torque, speed, and fuel are compared. Finally, the frequently visited engine operating conditions are analyzed.

Table 2.5: Model validation using different fuel economy results.

Drive cycle	**Bag**	**ECU**		**Meas. & map**		**Sim.**	
FTP75	17.89	18.32	(+2.4%)	18.62	(+4.1%)	17.98	(+0.5%)
Phase 1	19.01	18.46	(-2.9%)	18.97	(-0.2%)	17.91	(-5.8%)
Phase 2	16.18	16.85	(+4.1%)	17.22	(+6.4%)	16.68	(+3.1%)
Phase 3	21.15	21.52	(+1.8%)	21.66	(+2.4%)	21.15	(-0.0%)
HWFET	34.40	32.56	(-5.3%)	32.45	(-5.7%)	31.17	(-9.4%)
US06	20.89	22.19	(+6.2%)	21.31	(+2.0%)	21.83	(+4.5%)

Fuel Economy & Velocity Tracking

The different fuel economy results are listed in Tab. 2.5 and shown in a histogram in Fig. 2.5. The chassis dynamometer results are used for three different fuel economy values. First, the result from the emissions bag analysis is available and shown in the first column. Since this value is supposed to be the most accurate and official one, it is used as baseline. The second column contains the fuel economy based on the ECU-internal calculations, which rely on the commanded fuel injection. The third column shows the fuel economy based on measured engine speed and load trajectories applied to the BSFC map of the HF V6 3.6 L. All those values are compared to the fuel economy result of the simulation.

As can be seen, all the presented values lie within a window of ±10% for the four drive cycles, which is the accuracy that can be expected. In most cases the results are in fact significantly closer to each other and within a margin of 5%. The first phase of the FTP75 drive cycle shows a difference of 5.8%. This phase includes the engine cold start, modeled using a simplified model, which might explain the discrepancy. The overall largest error occurred during the HWFET. However, as can be seen, only the bag emissions result is significantly different, both ECU and map based values are closer. In general, it can be seen that there are noticeable differences between the bag emissions results and the ECU calculations.

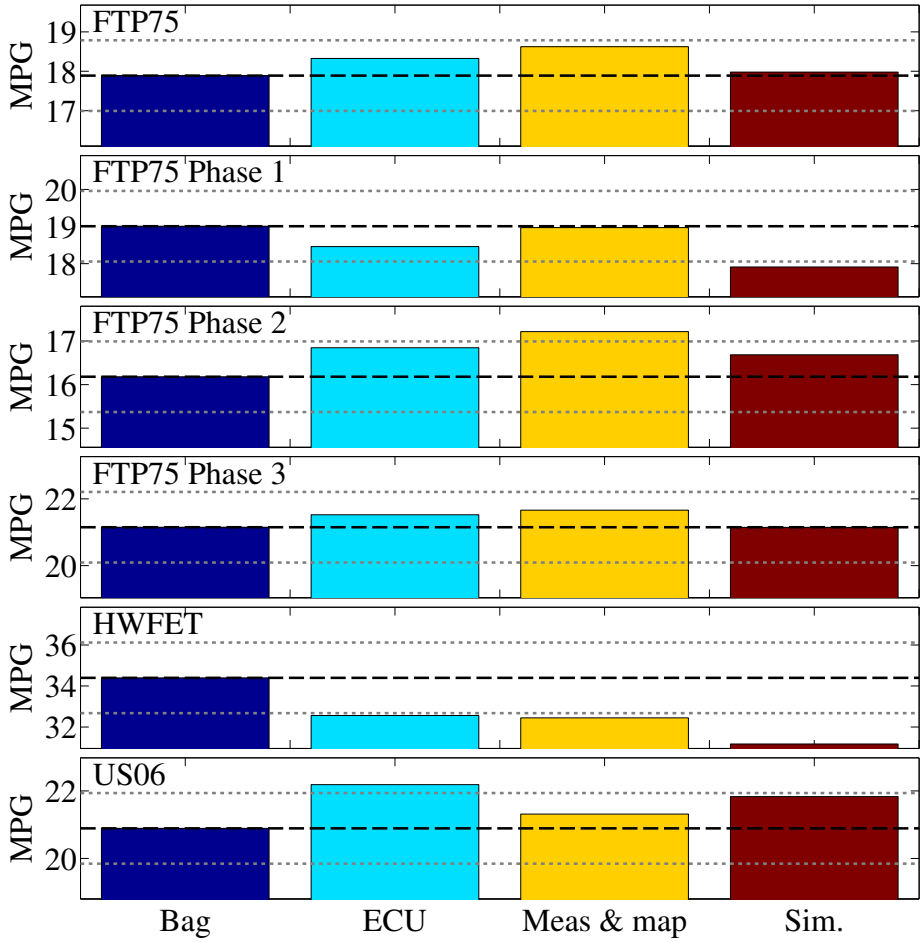

Figure 2.22: Model validation using different fuel economy results. Same values as in Tab. 2.5.

The ability to track the reference velocity of both the real and the simulated driver are compared in Tab. 2.6. It lists the average velocity difference:

$$\bar{v} = \frac{1}{t_f} \int_0^{t_f} |v_{ref} - v| dt \tag{2.124}$$

with t_f being the duration of the associated drive cycle. As can be seen, the modeled driver is able to track the reference velocity more accurately. The difference is relatively small with exception of the HWFET. However, it must be noted that the HWFET velocity data is quantized, which might lead to an erroneous calculation of $\bar{v}$.

Table 2.6: Mean driver error $\bar{v}$ in $\frac{m}{s}$.

Drive cycle	Measurement	Simulation
FTP75	0.23	0.19
HWFET	0.31	0.09
US06	0.44	0.30

Frequently Visited Engine Conditions

The engine load and speed trajectories for measurements and simulations were analyzed in terms of their visitation frequency at each load/speed condition, plotted in Fig. 2.23. Note that the load is expressed in brake mean effective pressure (BMEP). The maps show several interesting features of driver behavior. Starting at engine idle, generally a highly frequented point, the vehicle launches by increasing load and speed. While both simulation and measurements show similar launch behavior, the real driver generally lets engine speed drop when releasing the clutch pedal. The launch control strategy, introduced above, avoids this to ensure a robust launch. In addition, the driver model shows very little variability between different vehicle launches and all the load/speed trajectories lie close to each other, while the real driver exhibits a much larger spread. Both real driver and model exhibit similar high frequency areas and short excursion to higher loads and speeds. As can be seen, the measurements show drops in engine load below the minimum limit. These occurrences represent fuel cut-off operation, which is not activated in the simulation. Qualitatively, the plots based on the simulation results look very similar to the ones based on the measurements.

Accumulated Error

The simulation is validated in more detail by directly comparing engine load and speed trajectories to the chassis dynamometer measurements. The accumulated error of load and speed is calculated as follows:

$$e_T(t) = \frac{1}{\bar{T}_{e,meas}} \int_0^t (T_{e,meas} - T_{e,sim}) dt \tag{2.125}$$

$$e_\omega(t) = \frac{1}{\bar{\omega}_{e,meas}} \int_0^t (\omega_{e,meas} - \omega_{e,sim}) dt. \tag{2.126}$$

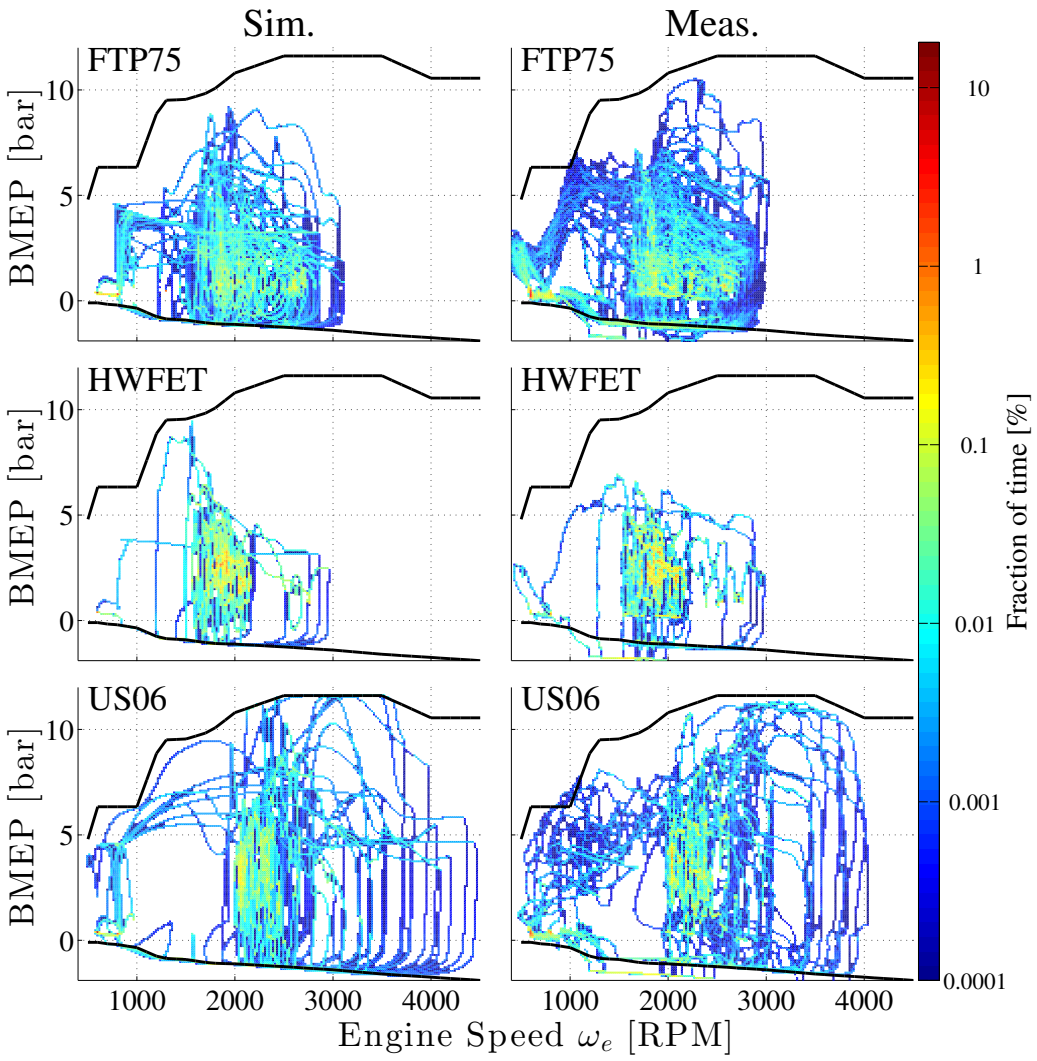

Figure 2.23: Maps of frequently visited engine load/speed conditions in terms of time for simulations and measurements, left and right respectively. The visitation time is color-coded on a logarithmic scale from blue (low frequency) to red (high frequency). Top: FTP75. Center: HWFET. Bottom: US06.

They are normalized using the mean measured torque and speed, $\bar{T}_{e,meas} = 50\,\text{Nm}$ and $\bar{\omega}_{e,meas} = 1800\,\text{RPM}$, respectively, for all drive cycles. Note that not the absolute error is used since shifting, acceleration, and braking events might be shifted in time, therefore leading to large temporary discrepancies. Those errors, however, do not have an actual impact on fuel economy or performance. By retaining the sign, the average difference between measurements and simulations is calculated. The errors e_T and e_ω are shown in Fig. 2.24. As can be expected, the errors in engine speed are small since this value is generally well-determined by gear schedule and reference velocity. The errors in load are significantly larger, especially during the US06 cycle.

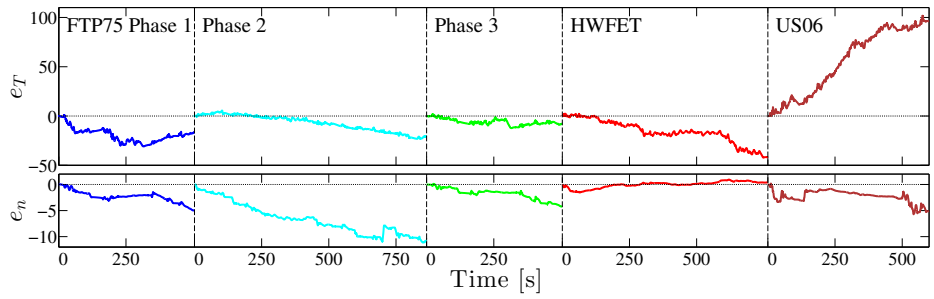

Figure 2.24: Accumulated error for engine torque e_T (top) and speed e_ω (bottom) for the individual drive cycles.

This is the only drive cycle in which the measured load is on average greater than the simulated one. This matches the results from Tab. 2.5, where only the values for the US06 based on measured trajectories and BSFC map show lower fuel economy than the simulation. The US06 cycle requires aggressive driving and results in fast engine dynamics. In this simplified engine model such dynamics cannot be reproduced perfectly. Therefore, considering the circumstances, the accuracy in torque response is still relatively good. To verify this, the qualitative behavior of the system is discussed in the next section. However, as will be seen in the next chapters, the US06 cycle leads to poor usage of the HCCI regime anyway, and therefore small modeling errors do not have a great effect on the associated results.

2.5.2 Qualitative Validation

In the following sections the trajectories of measurements and simulations during different exemplary driving situations are qualitatively compared.

Drive

In Fig. 2.25 trajectories are depicted for driving situations during FTP75, HWFET, and US06 drive cycles, respectively, that do not include launches or shifts. The plots show velocity v, engine torque T_e, engine speed ω_e, and fuel flow $\dot{m}_f$. Note that the vehicle velocity data from the HWFET was quantized. The right hand side of the figures shows phase plots of engine load in BMEP over engine speed. This establishes a connection between the trajectories and the maps shown in Fig. 2.23. Due to the underlying physics and the fact that the drive cycle does not include elevation changes, both measurements and simulations exhibit spiral motions of load over speed. It can be confirmed that the driver model generally tracks the reference ve-

locity more accurately than the real driver, leading to larger excursions in torque. Especially during the HWFET and the US06 cycles the simulation attempts to follow each acceleration of the reference velocity, thereby utilizing the entire load range. This could be addressed by having the driver model track the velocity measurement instead of the official drive cycle reference trajectory. Then, however, the result of the simulation would depend on corresponding driver, instead of being solely relying on the models parameterization. Finally, it can be seen how the engine data temporarily drops below the minimum torque line, due to fuel cut-off events.

Launch

Three vehicle launch situations which include at least one upshift during FTP75, HWFET, and US06 drive cycles, respectively, are presented in Fig. 2.26. It can be seen that the real driver is able to anticipate the change in reference velocity and launches the vehicle slightly beforehand. The measured engine speed exhibits a large drop during vehicle acceleration, which points to a fast release of the clutch pedal. This matches the distribution frequently visited conditions from Fig. 2.23. As explained in the sections above, to improve robustness the driver model increases the engine speed slightly before releasing the clutch. In addition, the real driver seems to require higher load during the launches, which was also seen in Fig. 2.23. The third case demands very high acceleration. Here the real driver pressed the acceleration pedal earlier, leading, however, to large overshoot in engine speed.

Since the velocity profiles are not exactly the same and due to a certain degree of freedom for the real driver, the gears change at slightly different times. Nevertheless it can be seen that the load/speed behavior during and after the shifts matches well.

Coast

A vehicle coasting and braking event during the FTP75 drive cycle is depicted in Fig. 2.27. It can be seen that the load drops when the driver releases the acceleration pedal and shifts to Neutral. With decreasing velocity, engine load follows the minimum torque limit until engine speed approaches idle condition. At this point the idle speed controller takes over and increases torque to keep engine speed constant.

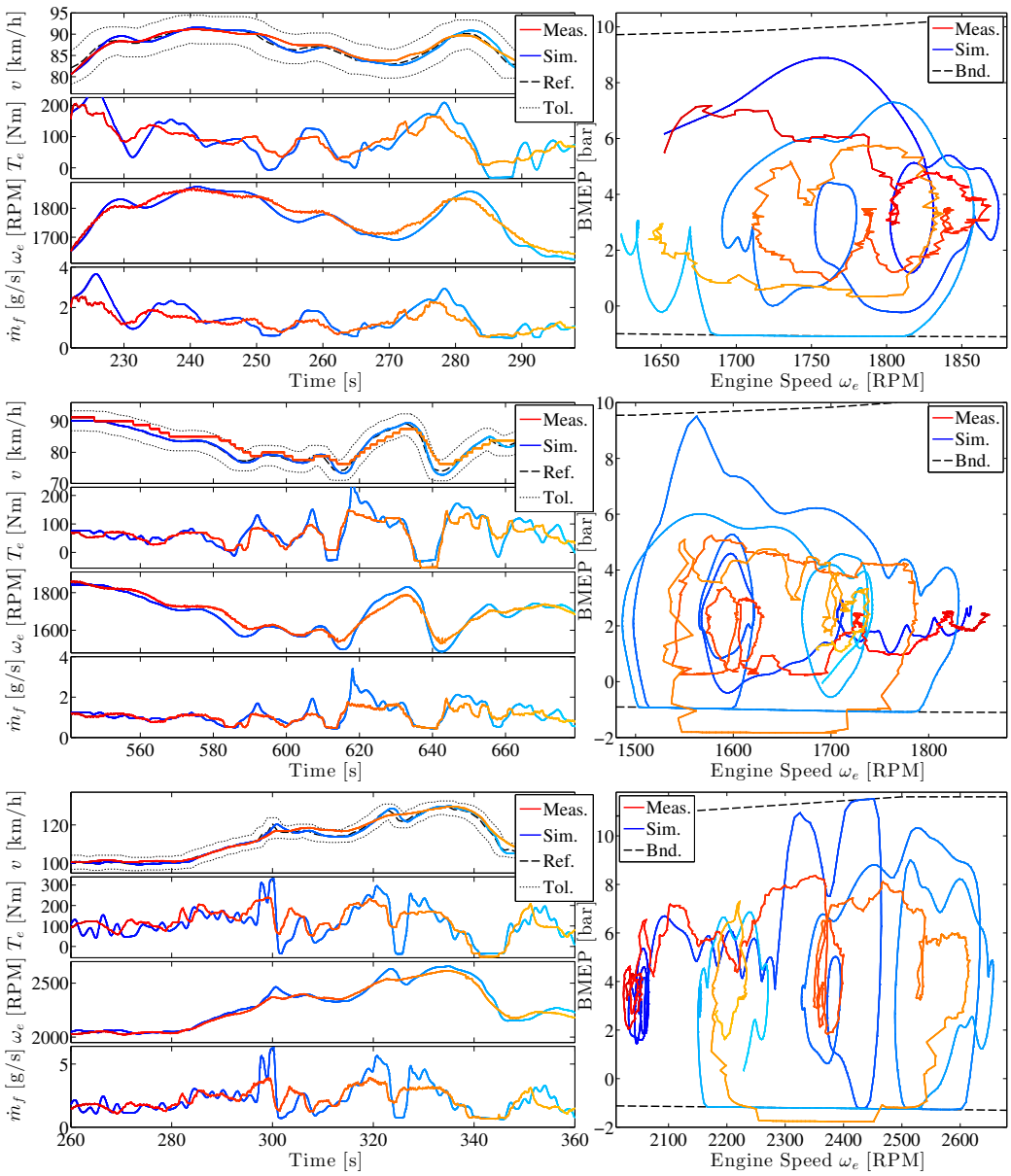

Figure 2.25: Three exemplary driving situations during FTP75 (top), HWFET (center), and US06 (bottom) comparing measurement (red) to simulation (blue) results. Depicted are trajectories of velocity, engine torque and speed, and fuel flow. The right side shows phase plot of engine load over speed. The color changes from dark (beginning) to bright (end).

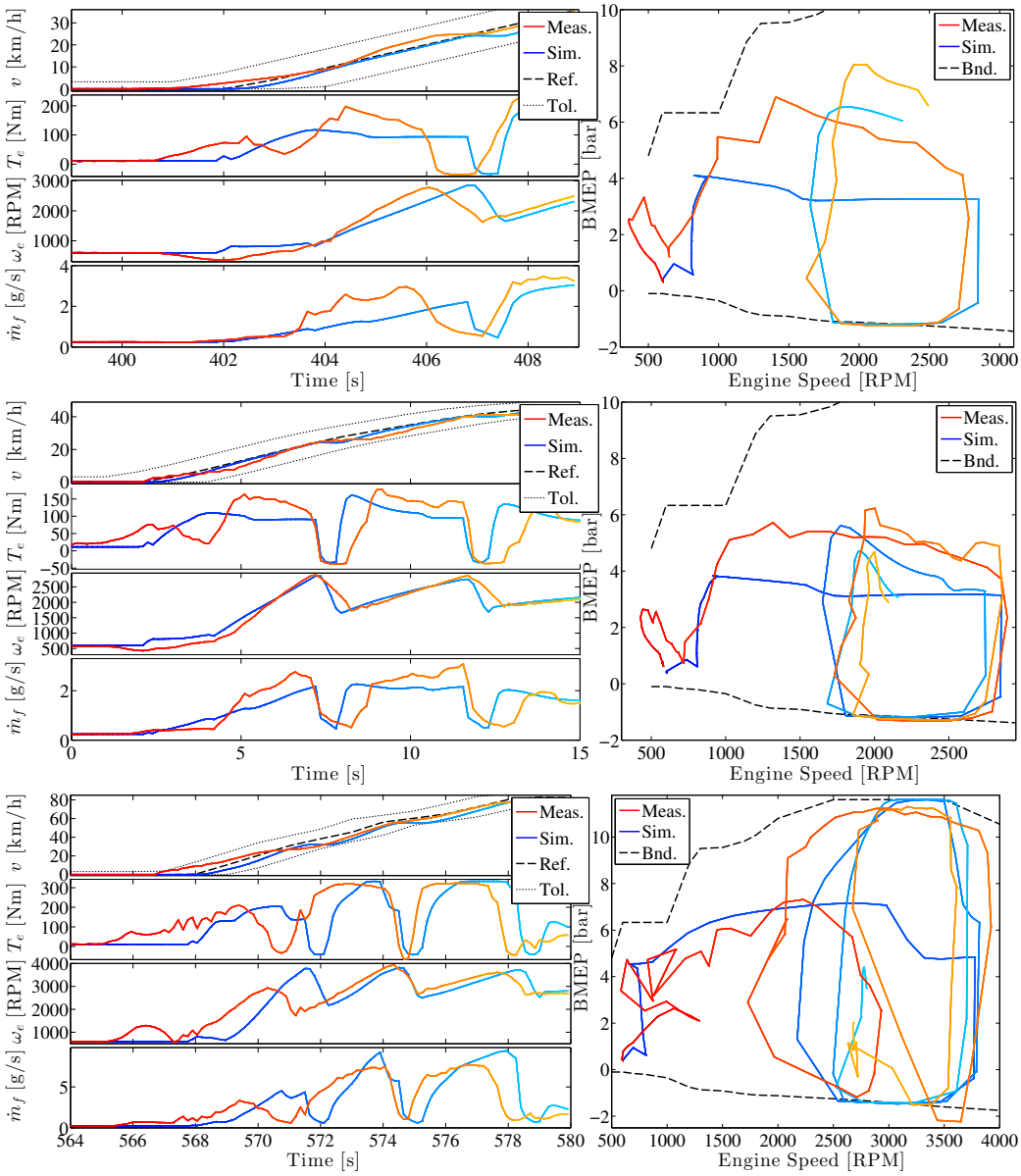

Figure 2.26: Three exemplary launch situations during FTP75 (top), HWFET (center), and US06 (bottom) comparing measurement (red) to simulation (blue) results. Depicted are trajectories of velocity, engine torque and speed, and fuel flow. The right side shows phase plot of engine load over speed. The color changes from dark (beginning) to bright (end).

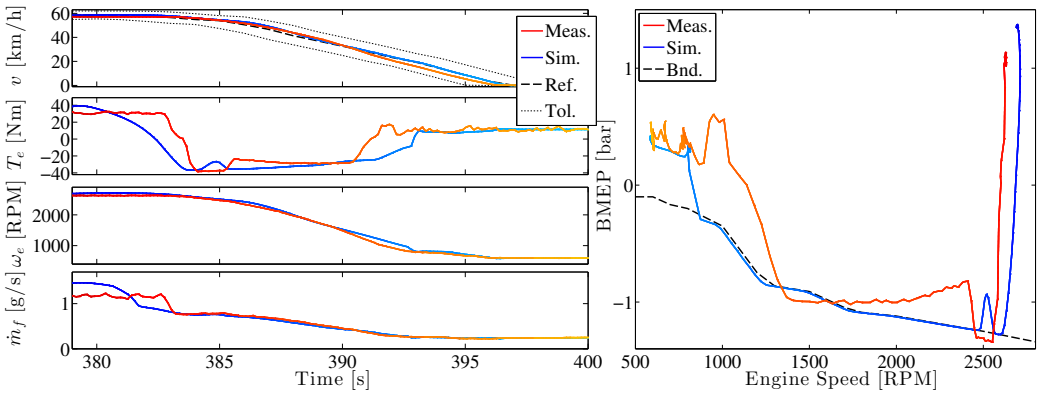

Figure 2.27: Exemplary coast situation during the FTP75 comparing measurement (red) to simulation (blue) results. Depicted are trajectories of velocity, engine torque and speed, and fuel flow. The right side shows phase plot of engine load over speed. The color changes from dark (beginning) to bright (end).

2.6 Summary

This chapter presents a model for the longitudinal dynamics of a vehicle with manual transmission, suitable for drive cycle simulations and fuel economy evaluations. The drivetrain model has four dynamic states: velocity, engine speed as well as speeds of driven and non-driven wheels. The engine's efficiency is described by steady-state maps and its torque response is modeled as a first-order system. A methodology is included to describe the engine's cold start behavior as well as exhaust temperature dynamics. Losses due to a constant electric load and power steering are assumed.

Besides the common drivetrain dynamics, the model includes a detailed driver model based on PI controllers. The controller's gains are scheduled based on a preview of the reference velocity of 1 s. The driver model reproduces the dynamics during launch and gear shifts, when the vehicle is operated with a slipping clutch.

The model is parameterized for a Cadillac CTS 2009 and validated with chassis dynamometer measurements. The simulation is developed in the MATLAB / Simulink / Stateflow environment.

Throughout this dissertation this vehicle model is extended in several ways. In Chap. 3 the engine model is modified to incorporate dynamics and penalties due to combustion mode switching. The vehicle system is extended in Chap. 4 to include oxygen storage and temperature dynamics of the three-way catalyst aftertreatment system. Finally, in Chap. 5 the alternator is used as a starter-generator to simulate a mild HEV.

Chapter 3

Combustion Mode Switch Dynamics and Fuel Penalties

The majority of the contributions presented in following chapter have been published in [96]:

International Journal of Engine Research

online, May 2015, *Accounting for Combustion Mode Switch Dynamics and Fuel Penalties in Drive Cycle Fuel Economy*

S. Nüesch, P. Gorzelic, L. Jiang, J. Sterniak, and A.G. Stefanopoulou.

It entails a methodology to analyze the drive cycle fuel economy of a vehicle equipped with a multimode combustion engine by employing a finite-state mode switching model. The structure and parameterization of the model were chosen to represent a SI/HCCI multimode engine, utilizing commercial cam phasers and two-step cam profile switching. The influence of fuel penalties on fuel economy was quantified by comparing the results of the model with the assumption of instantaneous mode switches. A distinction was introduced between beneficial and harmful mode switches, based on their individual fuel economy benefits. The numerical results shown here, however, are based on the final parameterization and integration of the combustion mode switch model, as presented in [97] and [100].

Furthermore, based on [97], three supervisory control strategies are discussed, applying different levels of short-term engine load and speed prediction, respectively. This includes a case study during which the driver is being temporarily ignored to extend the residence time in HCCI combustion. A second case study shows alternative drive cycle results, which assume gear shifting without any fluctuations in torque.

3.1 Multimode Engine Data and Operating Regimes

The engine predominantly used in this dissertation is a downsized and turbocharged 2.0 L I4, specifications listed in Table 3.1. The downsized design was altered to a multimode combustion engine by increasing compression ratio and reinforcement of reciprocating components. Furthermore two-step cam profile switching and electric cam phasing for recompression or NVO were added. "These modifications and the associated combustion control strategy enable lean naturally aspirated (NA) HCCI in the low-load regime, which is generally characterized by an improvement in BSFC compared to regular SI mode and very low engine-out NO_x emissions. More details on the engine design and specifications can be found in [89].

The favorable regime for HCCI combustion within the SI engine map is shown in Fig. 3.1-a. In Fig. 3.1-b the improvement in BSFC of HCCI over SI mode is depicted. At low loads HCCI combustion results in over 25% lower BSFC than SI; at the ringing limit the decrease in BSFC is between 5-10%. The relative air-fuel ratio (AFR) is shown in Fig. 3.1-c and the reduction in engine-out NO_x compared to SI combustion with external exhaust gas recirculation (EGR) in Fig. 3.1-d. The HCCI NO_x emissions lie between 4-281 ppm, which relates to a reduction of 55.3-99.4%. The limits of the HCCI operating regime are determined in experiments based on engine-out NO_x, ringing intensity (Fig. 3.1-e), and combustion stability." [96] The maximum and minimum feasible engine speed in HCCI combustion are denoted $\omega_{max,HCCI}$ and $\omega_{min,HCCI}$, respectively. As can be seen in Fig. 3.1 the load limits of the HCCI regime are functions of engine speed and are referred to as $T_{min,HCCI}(\omega_e)$ and $T_{max,HCCI}(\omega_e)$.

As discussed in the previous chapter, "interpolation of steady-state experimental data of the BSFC maps for SI and HCCI combustion mode is used to compute engine torque T_e and fuel consumption $\dot{m}_f$ from engine speed ω_e and pedal position u_a. Penalties in fuel consumption associated with transient phenomena on engine level, which are faster than the drive cycle dynamics, e.g., manifold filling dynamics etc., are

Table 3.1: Engine specifications

Number of cylinders	4
Displacement	2.0 L
Compression ratio	11.7:1
Bore / stroke	86 mm / 86 mm
Con. rod length	145.5 mm
High / low cam lift	10 mm / 4mm

neglected, to study the influence of the combustion mode switches. Ignoring manifold filling dynamics is a standard approach for fuel economy assessments of SI combustion engines. The airpath dynamics of NA HCCI are negligible since combustion is directly controlled by the fuel. In addition, reasonable speed and load transitions in the HCCI mode can be controlled as well as in SI mode, as shown in [46]. Note that this excludes the dynamics connected to combustion mode switching, which will be discussed in Sec. 3.3." [96]

Throughout this dissertation the following notation is used. At every time step, it is tested if T_e and ω_e lie inside the feasible boundaries for HCCI combustion, as

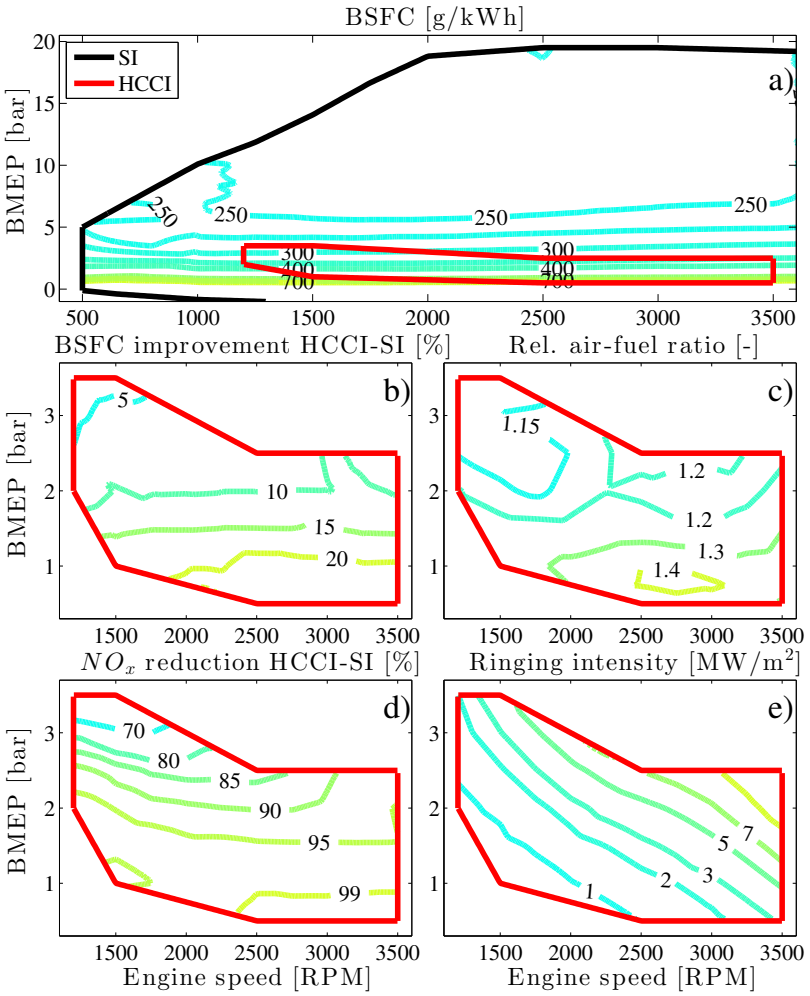

Figure 3.1: Data taken on the 2.0 L I4 multimode combustion engine. Top: Operating regime of lean NA HCCI with ultra-low NO_x (red, solid). Below: Maps of the improvement in BSFC and engine-out NO_x by using HCCI compared to SI combustion, relative air-fuel ratio, and ringing intensity. [96]

described by function f_R:

$$f_R(\omega_e, T, T_{min}, T_{max}) = \begin{cases} \text{HCCI} & T_{min} \leq T \leq T_{max} \text{ and } \omega_{min,HCCI} \leq \omega_e \leq \omega_{max,HCCI} \\ \text{SI} & \text{else} \end{cases} \tag{3.1}$$

$$R_{act} = f_R(\omega_e, T_e, T_{min,HCCI}, T_{max,HCC}). \tag{3.2}$$

A time period, during which $R_{act} = \text{HCCI}$, is called a visitation of the HCCI operating regime. In addition, it can also be tested if the desired torque by the driver T_{des} lies within the regime:

$$R_{des} = f_R(\omega_e, T_{des}, T_{min,HCCI}, T_{max,HCC}). \tag{3.3}$$

However, R_{act} only considers the feasibility of a combustion mode, not if a mode switch is conducted nor if the engine is operated in the associated mode. Actual operation in HCCI combustion is referred to as residence. This distinction is important since a visitation is determined only by engine speed and load condition. Due to constraints posed by the mode switch dynamics, fuel penalties, aftertreatment system etc., not every visitation of the HCCI regime might allow for a residence in HCCI mode.

3.2 Instantaneous Combustion Mode Switches

"In this section, combustion mode switches between SI and HCCI combustion are assumed to occur instantaneously and without fuel penalties due to mode switching. In other words, each visitation of the HCCI combustion regime is also a residence in HCCI mode. Therefore, the results in this section provide the maximum use of HCCI for a specific drive cycle and the maximum potential gain in fuel economy without the influence of the mode switching losses." [96]

$$M = R_{act} = f_R(T_e, T_{min,HCCI}, T_{max,HCCI}) \tag{3.4}$$

The computation of the fuel flow from (2.26) is therefore extended as follows:

$$\dot{m}_f = \begin{cases} f_{f,SI}(\omega_e, T_e) & R_{act} = \text{SI} \\ f_{f,HCCI}(\omega_e, T_e) & R_{act} = \text{HCCI}. \end{cases} \tag{3.5}$$

Functions $f_{f,SI}$ and $f_{f,HCCI}$ are fuel flow maps, varying with engine speed and torque for nominal SI and HCCI combustion, respectively. Note that the engine exhaust temperature and cold start calculations, described in Sec. 2.2.4, are still valid. During the engine cold start, e.g., the first approximately 300 s of the FTP75 drive cycle, the engine temperature is too low to allow a switch to HCCI combustion mode. Therefore $I_{warm} \geq 0.95$ is used as an additional constraint when deciding to switch to HCCI.

3.2.1 Engine Operation

The frequency with which engine load/speed conditions are visited during simulation of the FTP75, HWFET, and US06 drive cycles is shown in Fig. 3.2. "The plots on the left depict the fraction of time; the plots on the right show the fraction of fuel consumed at each operating point on the engine map for a particular drive cycle. A brighter color represents more frequent visits of the particular load/speed point. An increase in load leads to a higher power which correlates to an increase in fuel consumption. Therefore, analyzing the engine operation in terms of fuel consumption instead of time is expected to shift the important points towards higher loads, which is reproduced in the figure. For FTP75 and the US06, both including several vehicle launches, a loop-like structure can be identified, always beginning at vehicle rest with idle condition (800 RPM). During acceleration of the vehicle, first the engine load, then speed increases. During vehicle braking the operation returns to idle, with the engine load remaining close to its lower limit.

In the legend of each plot the total fraction of time and fuel is listed for both combustion modes. As can be seen in the top row of plots, the frequently visited area during the FTP75 is spread out over a large load/speed regime. Even though the feasible regime of HCCI is very limited, the engine operates at those lower loads for a significant amount of time (20%), fuel (18%), and distance (28%). Note that the first phase of the FTP75 includes a warm-up period of approximately 5 min, during which the engine exclusively operates in SI mode since the low temperature does not allow a mode switch to HCCI. In case of the HWFET the usage of HCCI in terms of time also lies at 20%, but decreases in terms of fuel to 13%. The area of frequently visited points lies above the HCCI regime, around 5 bar BMEP, which could be handled by expanding the lean HCCI regime to stoichiometric spark-assisted HCCI (SACI) [95]. Similar for the US06 cycle. Here the values drop even further to 7% and 3% respectively. It can also be seen that, with the transmission and the shift schedule used for these simulations, the engine barley operates at engine speeds higher than 2800 RPM

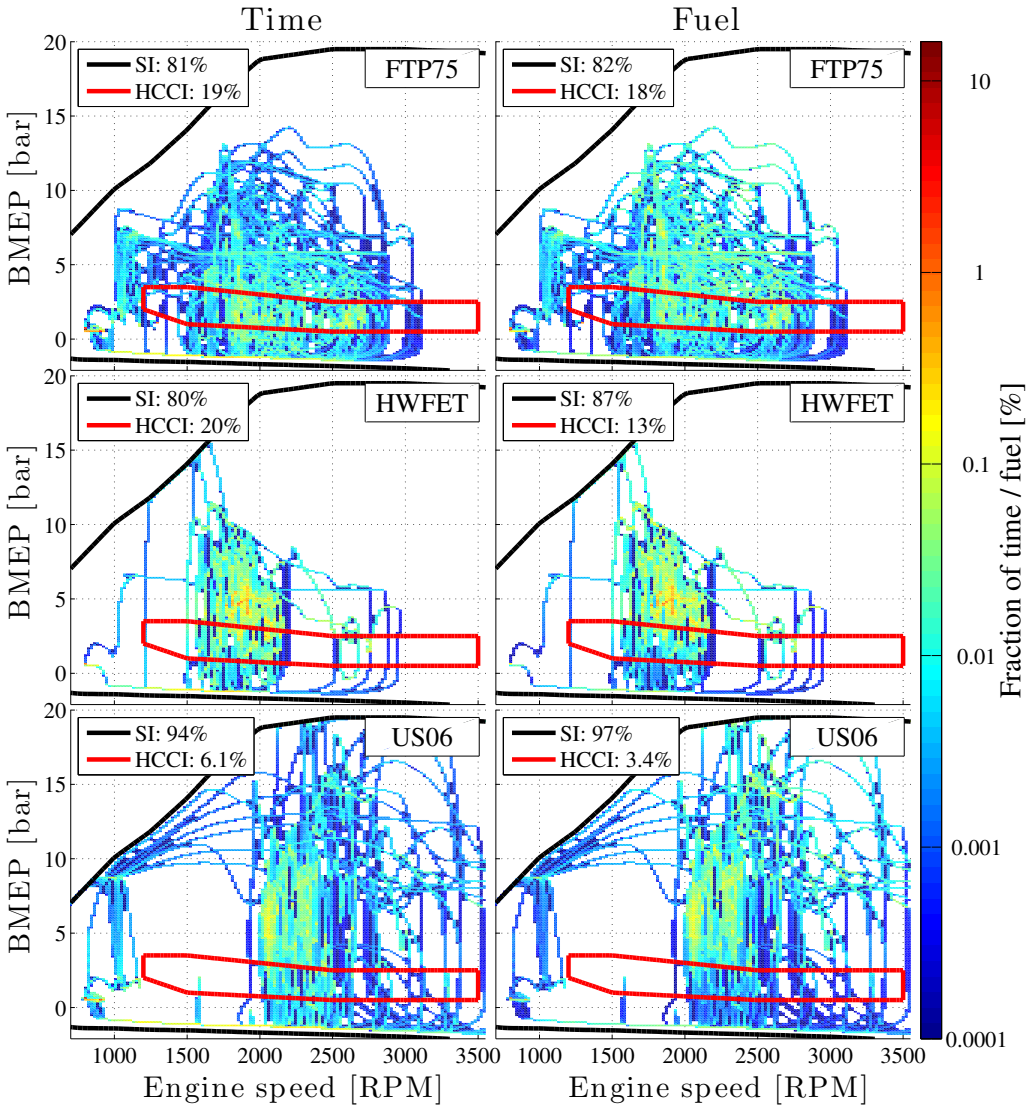

Figure 3.2: Maps of frequently visited engine load/speed points of the 2.0 L I4 multi-mode engine during FTP75 (top), HWFET (middle), and US06 (bottom) drive cycles. Left plots show distribution according to time, right ones according to fuel consumption. The feasible regime of HCCI (red) is highlighted. Instantaneous combustion mode switches are assumed for the fuel consumption calculation.

and lower than 1500 RPM, except when idling." [96]

3.2.2 Fuel Economy Results and HCCI Visitations

The fuel economy results for FTP75, HWFET, US06, and other drive cycles are shown in Table 3.2. It can be seen that, assuming instantaneous switches, the improvement in fuel economy due to the use of HCCI lies at 3.1% for the FTP75, at 1.4% for

Table 3.2: Drive cycle fuel economy in MPG for SI-only engine and assuming instantaneous mode switches.

Drive Cycle	**SI-only** [MPG]	**SI/HCCI inst.** [MPG]	
FTP75	23.9	24.6	(+3.09%)
HWFET	38.6	39.2	(+1.44%)
US06	25.6	25.7	(+0.39%)
NEDC	21.1	23.9	(+3.61%)
MODE1015	17.7	18.0	(+1.91%)

the HWFET, and 0.4% for the US06. The improvement in the case of the US06 cycle is only marginal. Furthermore, simulation of this aggressive drive cycle requires engine dynamics that are not modeled here. Therefore results for the US06 drive cycle need to be treated with caution. In general, the fuel economy improvements shown in Table 3.2 "are substantially smaller than the ones reported in previous papers. Those analyses utilized models, which show significantly larger HCCI operating regimes and higher engine efficiency improvements than presented here.[1] In addition, some neglect engine warm-up and apply an optimized gear schedule. Note that this fuel economy improvement heavily depends on the particular engine design. Certain hardware aspects, such as compression ratio, are subject to a trade-off between SI, HCCI, and overall combustion efficiency. However, the focus of this dissertation is not the fuel economy improvement of HCCI over SI mode, but the incorporation of the mode switch penalties." [96]

As can be seen in Fig. 3.3, despite the fact that during the FTP75 around 20% of time and fuel are spent in the HCCI regime, the durations of the individual visitations of HCCI regime are very short. "In total, engine speed and load enter the feasible combustion regime of HCCI 160 times and the average duration is 41 engine cycles. Around 38% of the visitations are shorter than 10 cycles and more than 70% of the visitations are shorter than 45 cycles. During the HWFET drive cycle the number of visitations in the HCCI regime is 63 with an average duration of 39 cycles. The US06 cycle exhibits 71 HCCI visitations with an average duration of 10 cycles. The time to prepare and perform a mode switch from SI to nominal HCCI conditions and vice versa lies around 6 to 8 engine cycles, limited by cam phasing actuator and air path dynamics. Therefore, the durations of many visitations of the HCCI regime are comparable to the time required to actually conduct the mode switches. A su-

[1]Load regimes (BMEP): Fig. 3.1: 1-3 bar, [89]: 1-8 bar, [12]: 1-5 bar, [88]: 1-4 bar

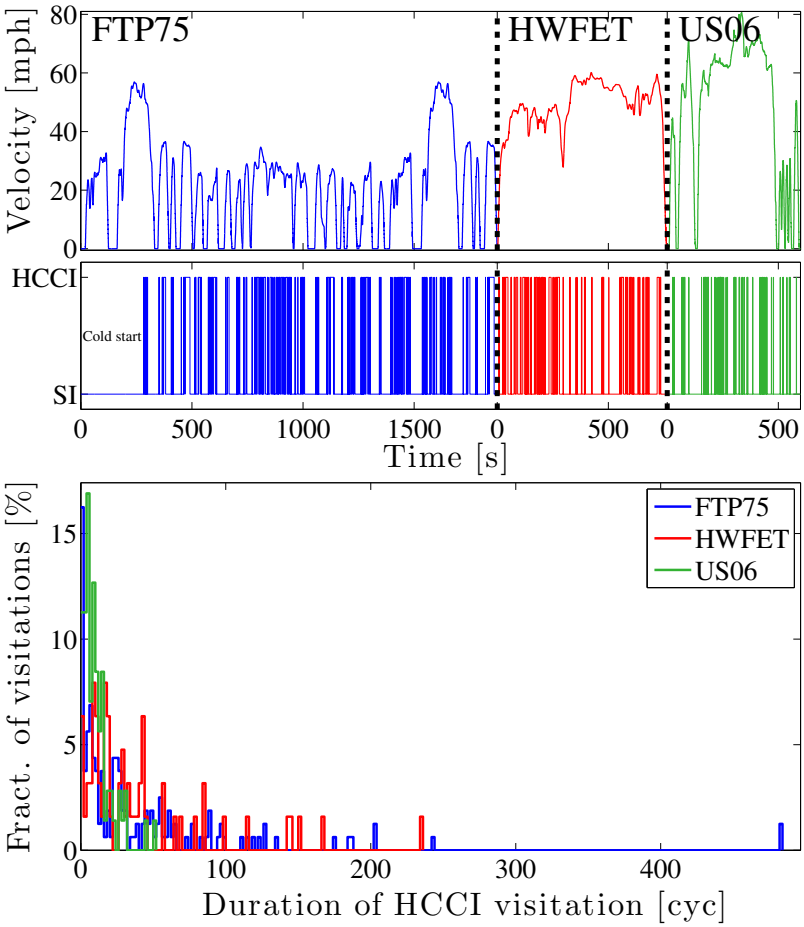

Figure 3.3: Duration of visitations of the feasible HCCI regime during FTP75 (blue), HWFET (red), and US06 (green) drive cycles. Top: Velocity profile. Middle: Visitations. Bottom: Distribution of fraction of visitations in HCCI for different durations. The first 5 min of the FTP75 drive cycle include the engine cold start.

pervisory strategy is required to decide which visitations are long enough to allow a switch to HCCI mode. In addition, with such short visitations, instantaneous mode switches cannot be assumed and the mode switch dynamics have to be taken into account." [96] They are discussed in Sect. 3.3.

3.2.3 Analysis of HCCI Regime Visitations

"The individual visitations in the HCCI load regime were analyzed to better understand the engine load and speed transients within the HCCI regime and any salient characteristics that lead to the distribution shown in Fig. 3.3. The actual engine torque dynamics depend on several aspects, such as driver behavior, engine control strategy, combustion mode, etc. The vehicle simulation results are used to get a gen-

eral idea of the characteristics. Figure 3.4 depicts every individual visitation of the HCCI regime during the FTP75 and the HWFET drive cycles. The different visitations are color-coded by duration and separated by the direction they enter and exit the HCCI load regime. As can be seen in the figure, more than 70% and more than 50% of all visitations during the FTP75 and the HWFET drive cycle, respectively, belong to crossings of the load regime, i.e., one of the two categories, in which the HCCI regime is entered from SI at the lower load boundary and left at the upper one, or vice versa. All the remaining visitations are turns, which enter from the same boundary as the exit. The engine speed dynamics are significantly slower than the engine torque ones. In addition, HCCI offers a substantially larger range in engine speed than in torque, relative to the entire engine operating regime. For these reasons changes in engine speed are only very rarely responsible for mode switches.

The longest visitations of the HCCI regime last for 200 to 240 engine cycles. However, such long visitations do not occur often. The median (Q_2) and the third quartile (Q_3) show the average duration of the visitations of each case. The crossings are in general very short with the Q_2 around 16 engine cycles and Q_3 smaller than 50 engine cycles.

As mentioned above, the employed vehicle model consists of a manual transmission following a predefined gear schedule. The applied shift schedules for the 6-speed transmissions include 48 and 5 upshifts for the FTP75 and the HWFET, respectively. During each gear shift the driver model releases the accelerator pedal, presses the clutch, and the engine load reduces rapidly to zero. If before the shift the engine torque lies above the HCCI load limit, the release of the accelerator pedal will result in a very short crossing of the HCCI regime from top to bottom. Then the gear is changed, and the load increases again sharply. In case of an upshift the final engine load after the gear shift is generally going to be higher than before, vice versa for a downshift. Moreover, the driver model might demand additional torque to regain vehicle velocity. Therefore, after the shifts the engine load is often going to cross the HCCI regime from bottom to top in a very short amount of time." [96] Of the 160 visitations of the HCCI regime during the FTP75 drive cycle, 25 (16%) are such short crossings due to upshifts. However, the actual impact of the upshifts on mode switching might be smaller. Of the 48 upshifts occurring during the FTP75 cycle, 41 take place under hot engine conditions. Of those, only 13 upshifts occur at initial engine torque and speed conditions close to or in the HCCI regime. And of those, an abrupt end of a longer visitation due to such an upshift occurs only twice. Therefore the impact of those upshifts on mode switching and fuel economy can in this case

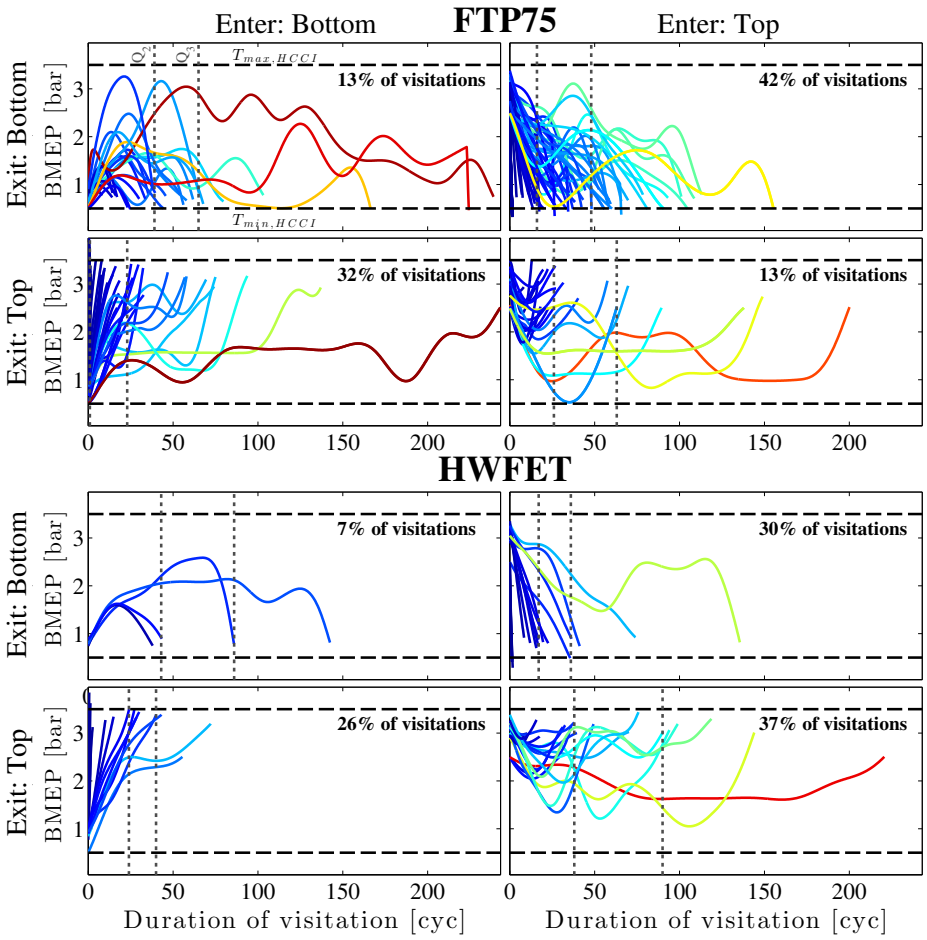

Figure 3.4: Plots of load trajectories over engine cycles of each individual visitation in the HCCI regime. Top four plots: FTP75; Bottom four plots: HWFET; Left: Visitations that enter the HCCI regime from the bottom; Right: Visitations that enter the HCCI regime from the top; Top: Visitations that exit the HCCI regime through the bottom; Bottom: Visitations that exit the HCCI regime through the top. The numbers in the top right corner of each plot represent the fraction of visitations that belongs to the associated category. The color represents the duration of the visitation. The vertical grey lines represent second and third quartile of the durations of the visitations. [96]

expected to be small. To explore this further, a case study assuming instantaneous shifts in gear ratio is presented in Sec. 3.5. More details on the driver model can be found in Chap. 2.

"The attempt of a switch to HCCI during such a short crossing would neither be possible nor reasonable, due to the duration of the switch and the potential penalty in fuel it incurs. On the other hand, if the engine load is initially located within the HCCI limits, the current visitation is going to be interrupted. Upcoming gear

shifts cannot be forecasted and it is not possible to eliminate the switches due to gear changes altogether. It should be noted that a long visitation of HCCI might occur both for crossings and for turns. Although those long visitations are rare, they are largely responsible for the overall fuel economy benefit. For that reason a supervisory control strategy needs to distinguish the very short visitations from the long ones as quickly as possible in order to lead to successful mode switches, beneficial residence in HCCI mode, and increased fuel economy. In addition, modifications in the transmission hardware would be possible to avoid interruption of visitations of the HCCI regime. While a manual transmission with a larger number of gears only leads to more gear changes and therefore shorter visitations, dual-clutch transmissions (DCT) or continuously variable transmissions (CVT) are potential alternatives, that would allow changes in transmission ratio without sharp transitions in engine load and might lead to in average longer continuous visitations of the HCCI regime." [96] Finally, in an automatic transmission (AT) it would be possible to combine the control of gear shifting and mode switching to optimize fuel economy and drivability.

3.3 Dynamics of Combustion Mode Switches

As shown in Sec. 3.2, residence times in the HCCI combustion regime during a standard drive cycle with manual transmission are in general very short, and for that reason, mode switching dynamics and associated fuel penalties cannot be neglected. In the following section the dynamics of a particular SI/HCCI mode switching strategy are discussed together with their simplified description by a finite-state machine. "Mode switches are very complex and consist of several stages with varying properties. A finite-state machine represents a computationally inexpensive way to reduce the complexity of this process while maintaining the essential characteristics, required by a supervisory control strategy. In addition, this way of modeling is flexible and can be modified easily for different mode switch control approaches." [96] This enables the use of this mode switch model for drive cycle fuel economy analysis, evaluation of different mode switch control strategies, as well as the development of supervisory controllers.

Both the structure and the parameterization of this model went through several iterations. The author first introduced it in [94]. It was refined in [95], with its parameters so far based on preliminary experimental and simulation results, as well as justified assumptions. In [96] open-loop combustion mode switch experiments

are shown with which the model was parameterized. The model used in [94–96] computed mode switches and resulting drive cycle fuel economy by post-processing engine torque and speed data. Therefore, the combustion mode switching did not have any implications on the actual engine torque behavior. In [97] the finite-state machine was integrated within the dynamics of the vehicle simulation. In addition, in [100] all the mode switching parameters were based on actual mode switch experiments. The experimental setup and data, from which the parameters were acquired, are explained in detail in [85]. Throughout this dissertation, the most recent and final version of the mode switching model was used, which will be the one described in this section.

"The mode switch between SI and HCCI has been investigated with different approaches and strategies in several papers. Due to their large manipulation range and response speed, fully flexible valve actuators (FFVA) [61, 69, 72–75, 118, 119] are typically used in combustion mode switches. In this dissertation, a two-step cam profile switching system with a fixed cam offset and intake/exhaust cam phasers is considered due to its low cost and potential wide spread use, similar to [80, 120, 121]. When a mode switch is commanded, a hydraulic actuator switches from one cam profile to another. By switching the valve lift from high to low the amount of trapped residuals increases and enables autoignition. Therefore one set of cams with long duration and high lift is suitable for SI operation while the other one, with short duration and low lift, is used for HCCI operation. Open-loop experimentation results are shown in [77–80], while [120–123] present simulation results." [96]

A detailed flowchart of the model is shown in Fig. 3.5. The model distinguishes between 12 finite states i. The currently active state is denoted M. The ordering of the states used in this dissertation, as shown in Fig. 3.5, represents a cam switch strategy. States $i \in (4-9)$ operate under low lift conditions and states $i \in (1-3, 10-12)$ are at high lift. Every switch can be divided into a pre- and a post-step switch phase. During the pre-phase of a SI-HCCI switch the cams are phased in SI combustion until preferable conditions for initialization of the cam switch are reached. After the cam switch the combustion changes abruptly to HCCI conditions. At each time step k, the amount of time since entering the current state $M(k)$ is denoted by state $\Delta t(k)$. Each of the finite states features two parameters. Parameter d_i represents the fuel penalty compared to nominal operation. Parameter Δt_i describes the required residence time in seconds or engine cycles until transition to another state is possible. "Open-loop experimental results from a SI-HCCI combustion mode switch on the 2.0 L I4 multimode combustion engine are shown in Fig. 3.6. A preliminary open-loop cam switch strategy was applied. The engine was operated at 2000 RPM and approximately

2.1 bar net mean effective pressure (NMEP) and the goal was a torque neutral switch. The fuel penalty is derived as the ratio between measured fuel efficiency, defined by net specific fuel consumption (NSFC), and the average value under SI conditions, shown in Fig. 3.6-h." [96] While the open-loop data from Fig. 3.6 was originally used for preliminary parameterization of the model, it is shown here only as illustration. In this dissertation the values for parameters Δt_i and d_i are based on SI-HCCI and HCCI-SI mode switching measurements applying the same strategy, however, with closed-loop control. The associated data was taken at similar conditions as shown in Fig. 3.6 and also at 1.8 bar and 3.2 bar NMEP. Additional information on those experiments, the applied closed-loop control strategy, and the determination of the fuel penalties can be found in [85]. The parameters of the model are shown in Fig. 3.5. As can be seen, constant parameters for most states have been assumed, i.e., they are not a function of speed and load. The exception is the residence time Δt_2, which is interpolated as a function of current engine load. To switch the cams at higher loads, different set points for valve timing are required. This results in longer durations at the top and shorter at the bottom of the HCCI regime to complete the phasing of the valves. As can be seen, the duration parameters which are based on hardware time constants are defined in seconds, while the ones which are based on the thermodynamic properties are defined in engine cycles. Therefore, this leads to a variation in overall mode switch properties for varying engine speeds. However, main reason for assuming most parameters constant over the HCCI load/speed regime is the sparseness of the required mode switch experimental data. In future work it is advised to experimentally map out the mode switching parameters in more detail and to validate the impact of mode switching using experimental drive cycle data. The reader must note that the numerical values of the mode switching parameters presented in this dissertation, represent the used cam switching strategy when applied with the associated hardware. For example, a faster VVT system would reduce the duration required for preparation. A different tracking strategy during this preparation might lead to a slightly different fuel penalty. As another example, the engine applied in this dissertation exhibited very advanced combustion phasing close to knock during the first HCCI engine cycles following the cam switch. However, other research studies report rapid drops in exhaust temperature and potential misfires. Finally, the amount of deposit formation in the engine might affect the combustion phasing during the switch, and therefore lead to different fuel penalties. However, the advantage of using a finite-state machine to describe the mode switch is the flexibility of this approach. Different strategies and hardware can be expressed by varying the order of states i

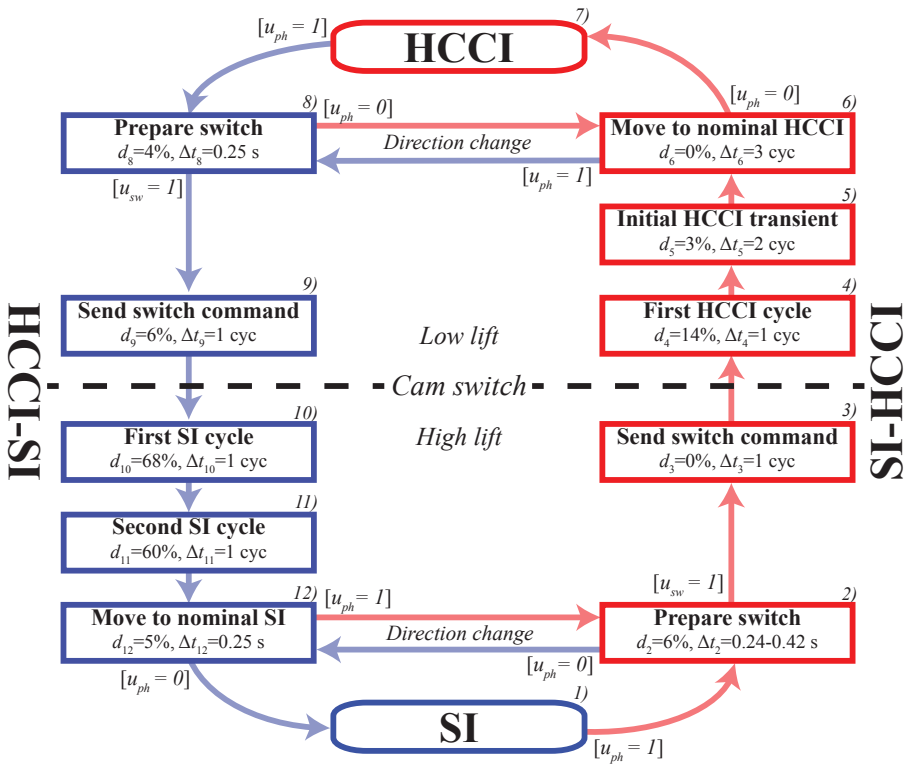

Figure 3.5: Finite-state model of the combustion mode switch between SI and HCCI describing a cam switching strategy. Blue paths lead to SI and red paths to HCCI. The black dashed horizontal line represents the cam switch. The finite states i are enumerated from 1 through 12. The model is subject to two control inputs u_{ph} and u_{sw}. Also shown are the parameters for fuel penalties d_i and durations Δt_i.

and with different durations Δt_i and penalties d_i.

Finally, the model consists of the following two control inputs:

- The input u_{ph} initiates a mode switch. If $u_{ph} = 1$, the cams are phased from their regular to the switching position. This process is reversed and the cams moved to their initial location if $u_{ph} = 0$.
- The second signal u_{sw} controls the actual cam switch command. If the cams are in position and $u_{sw} = 1$, the cam switch command is sent. This represents the point-of-no-return during the combustion mode switch.

The supervisory control strategies, described in Sec. 3.4, result in requested operating regimes, denoted R_{act}, R_{in}, $R_{out,1}$, and $R_{out,2}$. R_{act} and R_{in} are responsible for the switch to HCCI, $R_{out,1}$ and $R_{out,2}$ for the switch to SI. The fuel flow calculation from

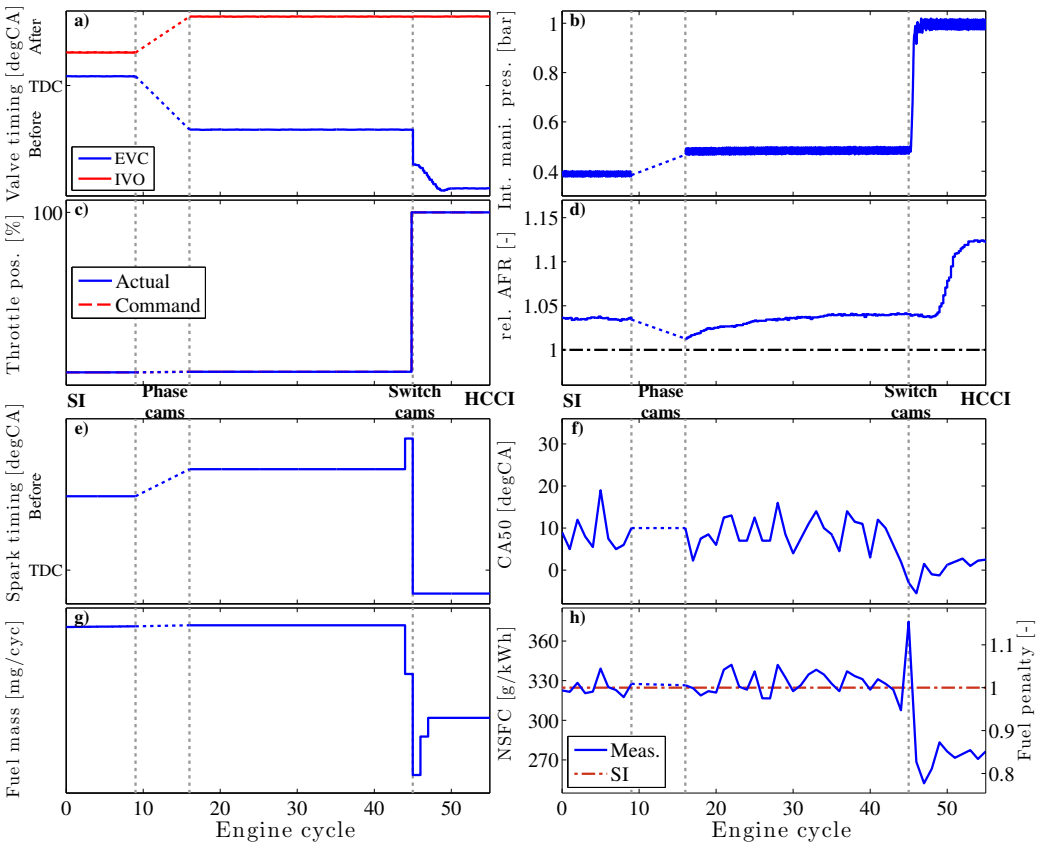

Figure 3.6: Experimental data from SI-HCCI combustion mode switch, performed at 2000 RPM and approximately 2 bar NMEP. Locations of cam phasing and cam switch are represented by grey dashed vertical lines. Data during cam phasing is not shown. Subplot g) shows commanded fuel mass to fuel injector, which is used to determine the fuel efficiency in subplot h). [96]

equation (3.5) is extended to incorporate the fuel penalty parameters:

$$\dot{m}_f = \begin{cases} f_{f,SI}(\omega_e, T_e) & M = 1 \\ f_{f,HCCI}(\omega_e, T_e) & M = 7 \\ f_{f,SI}(\omega_e, T_e) \cdot (1 + d_i) & M \in (2, 3, 10 - 12) \\ f_{f,HCCI}(\omega_e, T_e) \cdot (1 + d_i) & M \in (4 - 6, 8, 9). \end{cases} \tag{3.6}$$

The following two sections describe the mode switches in more details together with equations (3.7)-(3.15), which are used to translate those inputs into appropriate control actions u_{ph} and u_{sw}.

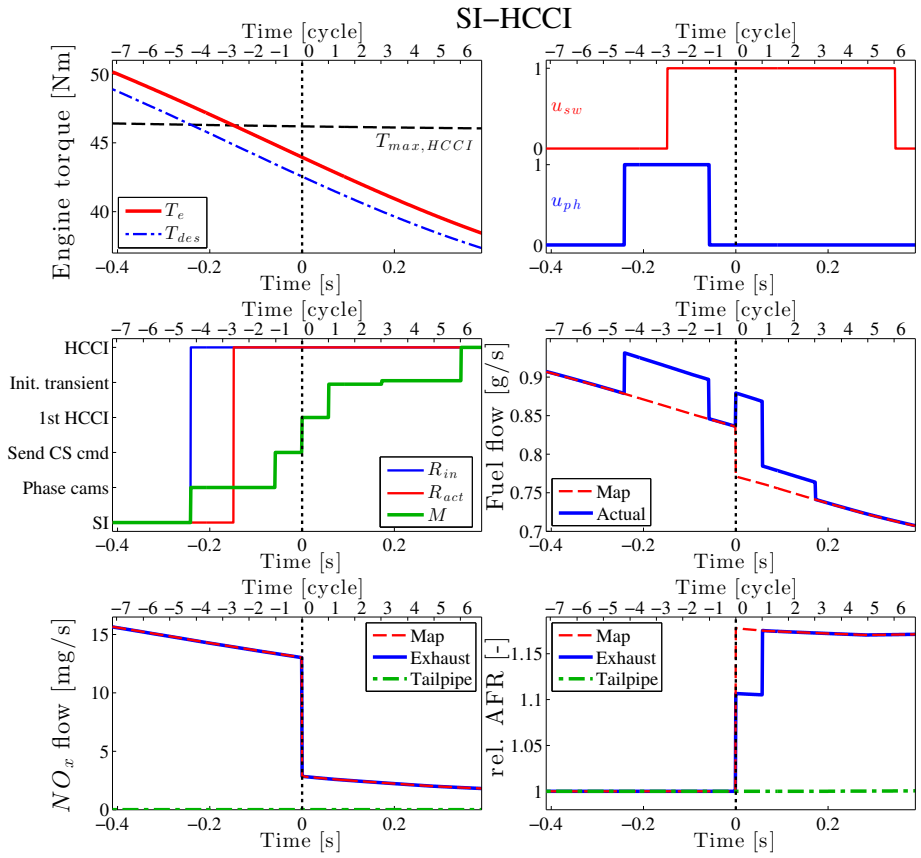

Figure 3.7: Exemplary SI-HCCI mode switch during simulation of the FTP75 drive cycle. The variables are plotted over time (bottom-axis) and engine cycles (top-axis). Engine speed is 2500 RPM.

3.3.1 SI-HCCI Mode Switch

The following section discusses the different stages during the SI-HCCI mode switching process, the choice of the parameters, and the associated inputs. An exemplary SI-HCCI mode switch during a drive cycle simulation is shown in Fig. 3.7.

- The mode switch starts in **nominal SI mode** ($M = 1$), initialized by input R_{in}. R_{in} represents the combustion mode preferred by the supervisory control strategy. In case of Fig. 3.7, R_{in} is triggered by the desired engine torque T_{des} entering the HCCI regime at $t = -0.24\,\mathrm{s}$.

$$u_{ph} = \begin{cases} 1 & R_{in} = \mathrm{HCCI} \\ 0 & \text{else} \end{cases} \tag{3.7}$$

$$u_{sw} = 0 \tag{3.8}$$

- At this point the finite-state machine progresses to the **mode switch preparation** ($M = 2$). "Exhaust valve closing (EVC) timing is advanced and intake valve opening (IVO) timing is retarded to calibrated positions to adjust the thermodynamic conditions so that trapped residuals are anticipated to be sufficient to ensure subsequent autoignition after the abrupt switch of the cams. This phasing period also involves opening the throttle and adjusting fuel quantity to maintain constant load at a stoichiometric AFR to compensate for the valve timing disturbance to the air flow and load. In an optimized mode switch strategy, coordination of the cam phaser, throttle, and fuel quantity actuators would be carried out to minimize fuel penalty and accomplish the phasing in a short number of cycles, with the limiting factor being the speed of the cam phaser." [96] The applied control strategy and hardware resulted in a duration of $\Delta t_2 = 240 - 420\,\text{ms}$. At higher loads the switching set point for EVC timing is generally later, and therefore the cam phaser does not need to advance EVC timing that far, resulting in the shorter duration [85]. "The advanced EVC position leads to a shorter expansion stroke and therefore reduced fuel efficiency." [96] It was seen that the fuel penalty throughout the cam phasing period is approximately $d_3 = 6\%$.[2] At this point the mode switch is still controlled by R_{in}:

$$u_{ph} = \begin{cases} 0 & R_{act} = \text{SI and } R_{in} = \text{SI} \\ 1 & \text{else.} \end{cases} \tag{3.9}$$

  If a mode switch is cancelled in this state, the phasing has to be reversed to SI.

- When the cams are sufficiently close to their target switching location and if allowed by the current engine conditions R_{act}, the **cam switch command** u_{sw} is sent ($M = 3$), shown in Fig. 3.7 at $t = -1\,\text{cycle}$:

$$u_{sw} = \begin{cases} 1 & R_{act} = \text{HCCI and } R_{in} = \text{HCCI} \\ 0 & \text{else.} \end{cases} \tag{3.10}$$

  For the mode switch experiment in Fig. 3.6, where the intake cams are switched

[2] "The strategy, employed in the mode switch experiment of Fig. 3.6, was to switch the intake cams to low lift prior to the exhaust cams, as opposed to switching both cam sets simultaneously. The intake cam switch is performed during the initial preparation phase over a short interval given the speed of the two-step cam switching actuator. Therefore the structure of the finite-state model remains the same whether the intake cams are switched prior to or simultaneously with the exhaust cams. However, the absolute values of actuator commands and fuel penalties may change. The intake cam switch to low lift has been experimentally determined to negligibly impact the cylinder breathing and fuel economy for a significant range of intake valve timings with exhaust valve closing after top dead center, and so the fuel penalty is unchanged during the preparation period." [96]

prior to the exhaust cams, this phase is defined by the exhaust cam switch command only. Due to the time required for signal processing and physical dynamics of the two-step cam switching actuator, the duration from sending the cam switch command to the mechanism actually switching lies between 60 to 90 ms, leading to the delay $\Delta t_3 = 1$ engine cycle between the command and the switch. "However, after sending the command the cam switch has to be performed, which means it is impossible to directly return to SI in case R_{in} changes. In the mode switch experiments, presented in Fig. 3.6, the delay period between cam phasing and cam switching, engine cycles 16 to 45, was exaggerated to prevent transients associated with the non-optimized cam phasing profile from obscuring the results during the cam switch. As can be seen in Fig. 3.6-g, on the last SI engine cycle (44 s) the fuel is reduced while engine torque remains almost constant. The valve timings are placed in a more advantageous position to extract expansion work, which leads to increased fuel efficiency. This effect may vary with hardware. Here, a fuel penalty of $d_3 = 0\%$, i.e., regular SI efficiency, was chosen." [96]

- After the two-step cam switching actuator delay finishes, the cam switch occurs and the system transitions to the **first HCCI cycle** ($M = 4$). The cam switch "is the key event to increase trapped residuals and enable autoignition. In this configuration it is assumed that immediately after the cams are switched autoignition starts. As can be noticed in Fig. 3.6-g and h at engine cycle 45, the first HCCI cycle immediately following the cam switch exhibits a drop in load and fuel. Early combustion phasing during the first HCCI cycle leads to negative piston work and heat losses, imposing a large fuel penalty" [96] of $d_4 = 14\%$.

- During the **initial HCCI transient** ($M = 5$) "exhaust temperature drops rapidly. EVC timing needs to be advanced to avoid misfires. After the first HCCI cycle the fuel efficiency soon approaches the steady-state HCCI value. In the case of the experiment in Fig. 3.6, at engine cycles 46 to 51, this was about 85% of the nominal SI penalty." [96] The fuel penalty during this phase was chosen $d_5 = 3\%$ compared to nominal HCCI fuel flow. "It is necessary to control combustion through this transient phase and wait until more stable thermodynamic conditions are reached before a mode switch to SI mode can be initiated." [96] This required duration is chosen to be $\Delta t_5 = 2$ engine cycles.

- Once the conditions are **close to nominal HCCI** ($M = 6$) "the strong temperature transients passed, which allows a cancellation of the mode switch to switch back to

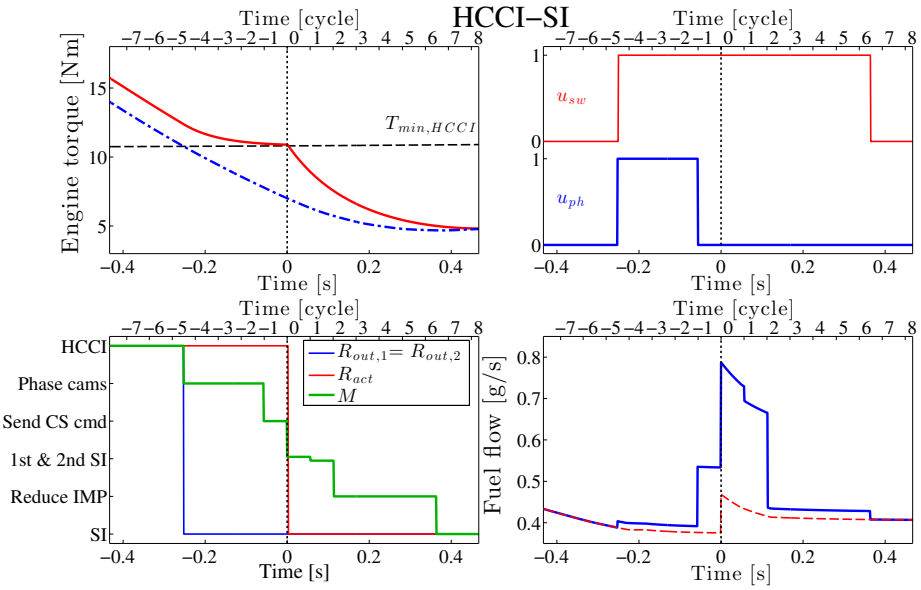

Figure 3.8: Exemplary HCCI-SI mode switch during simulation of the FTP75 drive cycle. The variables are plotted over time (bottom-axis) and engine cycles (top-axis). Engine speed is 2500 RPM.

SI combustion" [96], if required by inputs $R_{out,1}$ and $R_{out,2}$:

$$u_{ph} = \begin{cases} 1 & R_{out,1} = \text{SI or } R_{out,2} = \text{SI} \\ 0 & \text{else.} \end{cases} \tag{3.11}$$

In this phase the fuel efficiency is equal to nominal HCCI $d_6 = 0\%$ and the required duration to reach nominal HCCI is $\Delta t_6 = 3$ cycles.

3.3.2 HCCI-SI Mode Switch

"Similar to the SI-HCCI direction the backwards mode switch needs to be modeled to account for its dynamics and fuel penalties, despite statements in previous papers. Preliminary combustion mode switch simulations with the commercially speed-limited cam phaser and lift switching hardware show that, while the SI-HCCI direction poses a more difficult combustion control problem, specifically, the HCCI-SI direction is challenged by the air path control. Based on its dynamics the intake manifold pressure requires a certain amount of time to reach nominal SI condition. In that period both stoichiometric AFR and the specified torque need to be maintained with limited actuator authority. Papers [61, 69, 75, 78–80, 118] show differences between SI-HCCI and HCCI-SI switching directions. Based on their hardware in [118] it is claimed

that a switch from HCCI to SI is much easier to accomplish than the other direction. According to them, except for lower wall temperatures slowing down the flame after HCCI, the SI combustion is generally independent of the previous cycle. Also [69] explains that the SI-HCCI direction is more difficult since the conditions have to be controlled precisely to attain successful autoignition. On the other hand, in [79] potential difficulties with misfiring and torque fluctuations in the HCCI-SI direction are shown." [96] In this dissertation, however, due to the constraints posed by the air path and the applied hardware, it was seen that the HCCI-SI direction leads to higher fuel penalties than the forward direction.

An exemplary HCCI-SI mode switch during a drive cycle simulation is shown in Fig. 3.8. The associated states of the finite-state model during the HCCI-SI switch are as follows.

- In **nominal HCCI** ($M = 7$) the cams are prepared for the switch back to SI mode, if demanded by any of the inputs $R_{out,1}$ or $R_{out,2}$. In case of Fig. 3.8 this is due to T_{des} exiting the HCCI regime at $t = -0.25\,\mathrm{s}$.

$$u_{ph} = \begin{cases} 1 & R_{out,1} = \text{SI or } R_{out,2} = \text{SI} \\ 0 & \text{else} \end{cases} \tag{3.12}$$

- "Similar to the associated phase of the other switching direction the cam switch has to be **prepared** ($M = 8$) by moving the actuators to the right locations. Before the cam switch command is sent it is still possible to cancel the mode switch to SI, and move back to HCCI, if speed and load conditions remain in the feasible range of HCCI combustion." [96] Also, similar to the other mode switch direction the cams remain under prepared conditions until both $R_{out,1}$ and $R_{out,2}$ demand SI mode:

$$u_{ph} = \begin{cases} 0 & R_{out,1} = \text{HCCI and } R_{out,2} = \text{HCCI} \\ 1 & \text{else} \end{cases} \tag{3.13}$$

$$u_{sw} = \begin{cases} 1 & R_{out,1} = \text{SI and } R_{out,2} = \text{SI} \\ 0 & \text{else.} \end{cases} \tag{3.14}$$

  Due to the actuator dynamics it is seen to require $\Delta t_8 = 250\,\mathrm{ms}$ to phase the cams with a fuel penalty $d_8 = 4\%$ compared to nominal HCCI.

- The **cam switch command** ($M = 9$) is sent, requiring a processing time of $\Delta t_9 = 1$ engine cycle, as discussed above. The switch of the exhaust cam advances exhaust

valve opening (EVO) timing into the expansion stroke, resulting in a fuel penalty $d_9 = 14\%$.

- Immediately after the cam switch to high lift the engine exhibits the **first SI cycle** ($M = 10$). "Similar to the strategy described in [79], the throttle is closed right away. However, due to the system dynamics, some time is required for the intake manifold pressure to decrease. In order to compensate for the increased air mass additional fuel is required." [96] The engine is operated rich to enable the three-way catalyst to reduce the increased levels of NO_x, resulting in a relatively high fuel efficiency penalty $d_{10} = 68\%$ for $\Delta t_{10} = 1$ engine cycle.

- While still under rich conditions, during the following **second SI cycle** ($M = 11$) the injected fuel amount is slightly reduced since intake manifold pressure decreased, resulting in $d_{11} = 60\%$ and $\Delta t_{11} = 1$ cycle.

- During the final mode switch stage the **intake manifold pressure is reduced** ($M = 12$) until the target pressure is reached. This phase is assumed to be close to a reverse of the preparation phase of the SI-HCCI direction. Here it can be decided to operate at stoichiometry and return to nominal SI mode ($M = 1$) or alternatively change the switching direction:

$$u_{ph} = \begin{cases} 1 & R_{in} = \text{HCCI} \\ 0 & \text{else.} \end{cases} \tag{3.15}$$

  A duration of $\Delta t_{12} = 250\,\text{ms}$ is chosen until the cams are phased back to their regular SI positions, with a fuel penalty of $d_{12} = 5\%$, slightly higher than for the other direction, due to earlier EVC timing.

3.4 Supervisory Strategies

In the following section, three different supervisory control strategies are introduced, which translate engine and vehicle conditions into desired operating regimes R_{in}, $R_{out,1}$, and $R_{out,2}$. In addition, they determine the definition of the actual engine torque command u_e based on the desired torque by the driver T_{des}. Those strategies have been described previously in [97]. In case of the first strategy, the mode switch decision depends only on the current engine operating conditions. The second strategy applies a prediction in engine torque and speed to anticipate the switch. The

hypothetical third strategy is similar to the second one, however, assumes perfect knowledge of future engine torque and speed trajectories.

3.4.1 Engine Torque Command

The variable u_e represents the engine torque command. Its computation is part of the ECU model, described in Sec. 2.3. While in SI mode, specifically at high cam lift conditions, i.e., the lower half of Fig. 3.5, $M \in (1-3, 10-12)$, the entire SI torque range is available and the engine load can be commanded unconstrained. However, in HCCI, specifically as long as the cams are in low lift, i.e., the upper half of Fig. 3.5, $M \in (4-9)$, the torque is limited to HCCI's operating regime. For that reason the definition of u_e is extended here, introducing function f_{sat}:

$$f_{sat}(T, M) = \begin{cases} T_{max,HCCI} & T \geq T_{max,HCCI} \text{ and } M \in (4-9) \\ T_{min,HCCI} & T \leq T_{min,HCCI} \text{ and } M \in (4-9) \\ T_{des} & \text{else.} \end{cases} \tag{3.16}$$

Therefore, the engine command u_e, based on desired load T_{des}, is saturated such as:

$$u_e = f_{sat}(T_{des}, M). \tag{3.17}$$

This implementation has two underlying assumptions. First, it is assumed that, if in the HCCI regime, the mode switch controller is able to track the load command during the mode switch and the resulting switch is approximately torque neutral. The cam switching strategy from [85] seems to offer these properties. However, if this assumption proves to be inaccurate when actually implementing the strategy in the vehicle, engine torque would have to be parameterized and penalized for each state of the finite-state mode switch model, similar to fuel efficiency. Second, it is assumed that a mode switch can be conducted everywhere within the HCCI regime. However, close to the limits, e.g., at high ringing conditions, mode switching properties might be compromised. If this is the case, during the switch additional torque constraints are required. Note that the definitions connected to the idle speed controller, as described in Sec. 2.3, are omitted here for simplicity. They are, however, still required in the actual implementation.

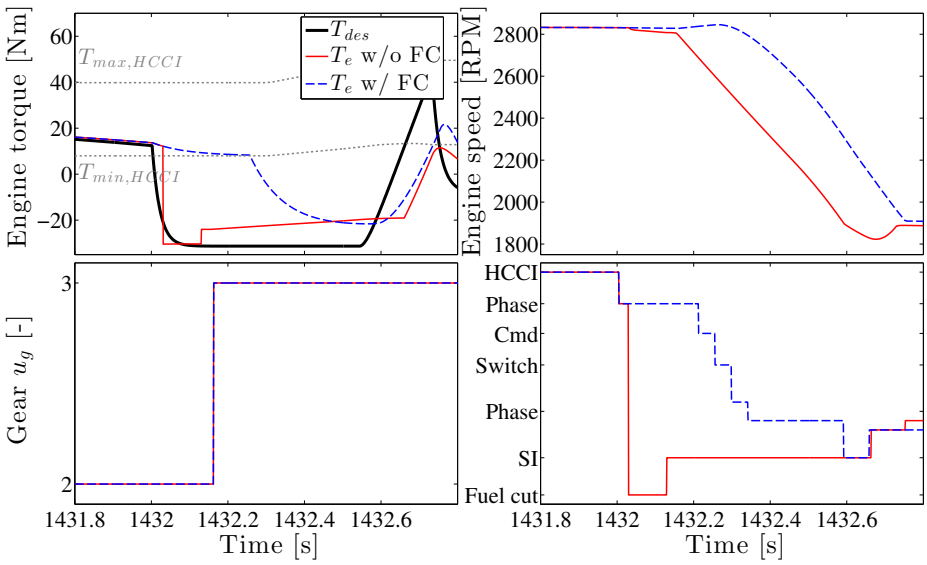

Figure 3.9: Exemplary HCCI-SI mode switch during simulation of FTP75 drive cycle to compare a strategy without (blue) and with (red) fuel cut-off (FC). The switch occurs due to a gear change. The desired engine torque in black and the HCCI limits in grey. Top left: Engine torque. Top right: Engine speed. Bottom left: Gear. Bottom right: Combustion mode M.

3.4.2 Fuel Cut-Off

The general fuel cut-off operation is described in Sec. 2.3. In addition, it is assumed that at any point during a mode switch or in HCCI operation, it is possible to cut-off fuel for a short period of time and to re-initiate combustion again in SI mode. Of course, due to the engine's friction this results in a large and rapid drop in torque. However, if the driver requests negative engine torque, e.g., to brake the vehicle or during a gear change, delaying the torque response, while the mode switch is being prepared, might be intolerable. An exemplary HCCI-SI mode switch during a gear shift is shown in Fig. 3.9. In this dissertation this strategy of cutting fuel is occasionally used to quickly return to SI combustion, e.g., if the driver pushes the brake or clutch pedal and therefore desires negative engine torque.

3.4.3 Strategy 1: No Prediction (*NoP*)

"The first strategy *NoP* is solely based on the current actual and desired combustion regimes, R_{act} and R_{des}, respectively. It prepares the SI-HCCI mode switch once T_{des} enters the HCCI regime. The cams are switched to low lift as soon as the valves reach their switching positions and T_e enters the HCCI regime. Conversely, in the

HCCI-SI direction the mode switch is prepared when T_{des} exits the HCCI regime. If by the time the valves reach their switching position, T_{des} still lies outside the HCCI boundaries, the cam switch to high lift is initiated. Therefore the following variables are equal:

$$R_{in} = R_{out,1} = R_{out,2} = R_{des}. \tag{3.18}$$

Since this strategy only acts based on the current engine operating conditions, a time delay is incurred upon entering the HCCI regime until the mode switch to HCCI combustion is completed. This therefore reduces the potential residence time in the beneficial HCCI combustion. The opposite is the case during the switch from HCCI to SI combustion, where the residence in HCCI mode is prolonged. However, this is done by temporarily saturating the load command T_{cmd} at the HCCI load boundary, leading to potential drivability issues. Finally, it is likely that some visitations of the HCCI operating regimes are very short. Therefore this strategy might allow mode switches, which are actually harmful for overall fuel economy, since short visitations cannot be predicted." [97]

3.4.4 Strategy 2: Predict by Linear Extrapolation (*LiP*)

"To mitigate the two potential problems of the first control strategy, in the strategy *LiP* the controller attempts to predict the short-term behavior of engine load and speed. The prediction is used to anticipate entries and exits of the feasible HCCI regime, thereby preparing the mode switches beforehand and mitigating associated delays. In addition, mode switches during very short visitations of the HCCI operating regime can be prevented. In [98] different prediction methods were tested on drive cycle measurements and they exhibited poor accuracy in predicting the duration of future visitations of the HCCI regime. However, they were able to correctly identify very short and very long durations, which is applied in this strategy. The prediction method used here utilizes linear least squares to the h most recent values of desired load and engine speed,

$$\mathbf{T}^k_{hist} = \left(T^{k-h}_{des}, \ldots, T^{k-2}_{des}, T^{k-1}_{des}, T^{k}_{des}\right)^{\mathrm{T}} \tag{3.19}$$

$$\boldsymbol{\omega}^k_{hist} = \left(\omega^{k-h}_{e}, \ldots, \omega^{k-2}_{e}, \omega^{k-1}_{e}, \omega^{k}_{e}\right)^{\mathrm{T}} \tag{3.20}$$

using $t_s \cdot h = 0.5\,\mathrm{s}$ with sampling time t_s. The more recent values are weighted more heavily by applying

$$\mathbf{W} = \mathrm{diag}\left(e^{-35\cdot h\cdot t_s}, e^{-35\cdot (h-1)\cdot t_s}, \ldots, e^{-35\cdot t_s}, 1\right). \tag{3.21}$$

The slopes f_T and f_ω for linear polynomial extrapolations of desired engine torque and speed, respectively, are found by

$$\mathbf{A} = -t_s \cdot (h, h-1, \ldots, 0)^{\mathrm{T}} \tag{3.22}$$
$$\mathrm{A}^* = \mathbf{A}^{\mathrm{T}} \cdot \mathbf{W} \cdot \mathbf{A} \tag{3.23}$$
$$\mathbf{b}^* = \mathbf{A}^{\mathrm{T}} \cdot \mathbf{W} \tag{3.24}$$

$$\mathbf{T}_{des}^k = T_{des}^k \cdot (1, \ldots, 1)^{\mathrm{T}} \tag{3.25}$$
$$\boldsymbol{\omega}_e^k = \omega_e^k \cdot (1, \ldots, 1)^{\mathrm{T}} \tag{3.26}$$
$$f_T = \frac{1}{\mathrm{A}^*} \cdot \mathbf{b}^* \cdot (\mathbf{T}_{hist}^k - \mathbf{T}_{des}^k) \tag{3.27}$$
$$f_\omega = \frac{1}{\mathrm{A}^*} \cdot \mathbf{b}^* \cdot (\boldsymbol{\omega}_{hist}^k - \boldsymbol{\omega}_{des}^k). \tag{3.28}$$

Desired engine load and speed are predicted over a horizon H with $t_s \cdot H = 1.5\,\mathrm{s}$, leading to vectors

$$\hat{\mathbf{T}}_{des}^k = \mathbf{T}_{des}^k + f_T \cdot t_s \cdot (1, \ldots, H)^{\mathrm{T}} \tag{3.29}$$
$$= \left(\hat{T}_{des}^{k+1}, \hat{T}_{des}^{k+2}, ..., \hat{T}_{des}^{k+H}\right)^{\mathrm{T}} \tag{3.30}$$
$$\hat{\boldsymbol{\omega}}_e^k = \boldsymbol{\omega}_e^k + f_\omega \cdot t_s \cdot (1, \ldots, H)^{\mathrm{T}} \tag{3.31}$$
$$= \left(\hat{\omega}_e^{k+1}, \hat{\omega}_e^{k+2}, ..., \hat{\omega}_e^{k+H}\right)^{\mathrm{T}}. \tag{3.32}$$

To predict the actual engine torque, the discrete time first order engine dynamics are used

$$\hat{T}_e^{k+i} = \left(1 - \frac{t_s}{\tau_e}\right)^{i-1} + \frac{t_s}{\tau_e} \cdot \sum_{j=1}^{i} \left(1 - \frac{t_s}{\tau_e}\right)^{i-1-j} \cdot \hat{T}_{des}^{k+j} \tag{3.33}$$
$$\text{with } i = 1, ..., H$$

leading to the prediction of actual engine torque

$$\hat{\mathbf{T}}_e^k = \left(\hat{T}_e^{k+1}, ...\hat{T}_e^{k+H-1}, \hat{T}_e^{k+H}\right)^{\mathrm{T}}. \tag{3.34}$$

From prediction vectors $\hat{\mathbf{T}}_{des}^k$, $\hat{\mathbf{T}}_e^k$, and $\hat{\boldsymbol{\omega}}_e^k$ the crossing times of the HCCI operating regime can be calculate. The predicted duration until entry of the HCCI regime is denoted τ_{entry}:

$$j_{entry} = \min\left(i \in (1, H) \mid f_R(\hat{\omega}_e^{k+i}, \hat{T}_e^{k+i}, T_{min,HCCI}^{k+1}, T_{max,HCCI}^{k+1}) = \mathrm{HCCI}\right) \tag{3.35}$$

$$\tau_{entry} = j_{entry} \cdot t_s. \tag{3.36}$$

The predicted durations until actual torque and desired torque exit the HCCI regime are denoted $\tau_{exit,act}$ and $\tau_{exit,des}$, respectively:

$$j_{exit,act} = \max\left(i \in (1, H) \mid f_R(\hat{\omega}_e^{k+i}, \hat{T}_e^{k+i}, T_{min,HCCI}^{k+1}, T_{max,HCCI}^{k+1}) = \mathrm{HCCI}\right) \tag{3.37}$$

$$\tau_{exit,act} = j_{exit,act} \cdot t_s \tag{3.38}$$

$$j_{exit,des} = \max\left(i \in (1, H) \mid f_R(\hat{\omega}_e^{k+i}, \hat{T}_{des}^{k+i}, T_{min,HCCI}^{k+1}, T_{max,HCCI}^{k+1}) = \mathrm{HCCI}\right) \tag{3.39}$$

$$\tau_{exit,des} = j_{exit,des} \cdot t_s. \tag{3.40}$$

The potential visitation duration of the HCCI regime is defined as τ_{visit}:

$$\tau_{visit} = \tau_{exit,act} - \tau_{entry}. \tag{3.41}$$

These durations are used to schedule the combustion mode switches. In SI combustion the mode switch to HCCI mode is prepared as soon as τ_{entry} is smaller than the time requirement to phase the cams. Due to the constraints of the variable valve actuation it requires approximately 250 ms to phase the cams from nominal SI to switching conditions. In addition, it requires about one engine cycle to process the cam switching command." [97] However, this command can already be sent beforehand to reduce the overall switching duration, leading to the following conditions for R_{in}:

$$R_{in} = \begin{cases} \mathrm{HCCI} & \tau_{entry} < 250\,\mathrm{ms} - \frac{4\pi}{\omega_e} \text{ and } \tau_{visit} > 350\,\mathrm{ms} \\ \mathrm{SI} & \text{else.} \end{cases} \tag{3.42}$$

In HCCI combustion the mode switch is prepared in a way that allows a cam switch as soon as T_{des} exits the feasible regime.

$$R_{out,1} = \begin{cases} \text{SI} & \tau_{exit,des} < 200\,\text{ms} - \frac{4\pi}{\omega_e} \\ \text{HCCI} & \text{else} \end{cases} \tag{3.43}$$

$$R_{out,2} = f_R(\omega_e, T_{des}, T_{min,HCCI}, T_{max,HCCI}) \tag{3.44}$$

3.4.5 Strategy 3: Perfect Prediction (*PeP*)

The two supervisory strategies are compared to the best possible case, referred to as strategy *PeP*, in which perfect knowledge of the actual and desired torque and engine speed trajectories in a SI-only engine is assumed:

$$\hat{\mathbf{T}}_{des}^{k} = \left(T_{des,SI}^{k+1}, \ldots, T_{des,SI}^{k+H-1}, T_{des,SI}^{k+H}\right)^{\mathrm{T}} \tag{3.45}$$

$$\hat{\mathbf{T}}_{e}^{k} = \left(T_{e,SI}^{k+1}, \ldots, T_{e,SI}^{k+H-1}, T_{e,SI}^{k+H}\right)^{\mathrm{T}} \tag{3.46}$$

$$\hat{\boldsymbol{\omega}}_{e}^{k} = \left(\omega_{e,SI}^{k+1}, \ldots, \omega_{e,SI}^{k+H-1}, \omega_{e,SI}^{k+H}\right)^{\mathrm{T}}. \tag{3.47}$$

Note that all these trajectories will still differ from the multimode engine results, since they are not subject to the mode switching delays. However, they still allow a very accurate prediction of τ_{entry}, $\tau_{exit,act}$, and $\tau_{exit,des}$, since generally deviations between T_{des} and $T_{des,SI}$ are small.

In addition, an optimal switching policy $\mu^*(t)$ is determined by applying dynamic programming (DP) on a simplified mode switch model over the entire drive cycles. The mode switch model is reduced to two states, SI and HCCI, switching within a single time step. At each time t, $\mu^*(t)$ determines if a mode switch from SI to HCCI is beneficial. The drive cycle simulation results, sampled at a frequency of 100 Hz and assuming instantaneous mode switches, are used as basis of the DP calculation. Therefore, every visitation of the HCCI regime and associated fuel flows are known. At every time step during which HCCI operation is feasible, the penalty due to mode

switching is lumped together:

$$m_{SI-HCCI} = \dot{m}_{f,SI} \cdot (d_2 - 1)\Delta t_2 \ldots + \dot{m}_{f,HCCI} \cdot \left((d_4 - 1)\frac{4\pi\Delta t_4}{\omega_e} + (d_5 - 1)\frac{4\pi\Delta t_5}{\omega_e} \right) \tag{3.48}$$

$$m_{HCCI-SI} = \dot{m}_{f,HCCI} \cdot (d_8 - 1)\Delta t_8 \ldots + \dot{m}_{f,SI} \cdot \left((d_{10} - 1)\frac{4\pi\Delta t_{10}}{\omega_e} + (d_{11} - 1)\frac{4\pi\Delta t_{11}}{\omega_e} + (d_{12} - 1)\Delta t_{12} \right). \tag{3.49}$$

The resulting policy $\mu^*(t)$ denotes, which HCCI visitations result beneficial for fuel economy. Therefore, instead of equations (3.42) and (3.43), due to the perfect knowledge of engine speed and load trajectories as well as fuel efficiency of each HCCI visitations, mode switches in both directions with R_{in} and $R_{out,1}$ can be timed perfectly to maximize fuel economy and minimize deviations in engine torque:

$$R_{in} = \begin{cases} \text{HCCI} & \tau_{entry} < \Delta t_2 - \frac{4\pi\Delta t_3}{\omega_e} \text{ and } \mu^*(t + \tau_{entry}) = \text{HCCI} \\ \text{SI} & \text{else} \end{cases} \tag{3.50}$$

$$R_{out,1} = \begin{cases} \text{SI} & \tau_{exit,des} < \Delta t_8 - \frac{4\pi\Delta t_9}{\omega_e} \\ \text{HCCI} & \text{else.} \end{cases} \tag{3.51}$$

3.5 Penalized Combustion Mode Switches

In the following section penalized mode switches, i.e., applying the finite-state mode switch model from Sect. 3.3, are analyzed in terms of their influence on fuel economy and drivability. Drivability is a concern, since HCCI's load limitations and the resulting saturation in engine torque, as described by (3.17), might lead to a delayed torque response. "Drivability is a subjective measure of vehicle performance as perceived by the driver. Attempts to find an objective drivability measure can be found in [124–126]. A potential measure to quantify the impact of independent events such as mode switches might be jerk, i.e., the derivative of the vehicle's longitudinal acceleration." [97]

Three supervisory strategies, without prediction, with linear extrapolation, and with perfect prediction, all described in Sect. 3.4, are used to analyze the impact of the mode switch dynamics.

3.5.1 Exemplary Mode Switches

"Exemplary SI-HCCI and HCCI-SI mode switches are shown in Figs. 3.10 and 3.11, respectively. As can be seen in Fig. 3.10, the strategies relying on prediction are able to anticipate the upcoming entry of the feasible HCCI regime and prepare the mode switch accordingly. Therefore the cam switch command is sent as soon as the regime is entered. Strategy *NoP*, on the other hand, starts preparation slightly later, thereby reducing the available time spent in the HCCI regime. The effect of the torque saturation at the HCCI boundary during the HCCI-SI mode switch can be seen in Fig. 3.11. Strategy *NoP* initiates the mode switch much later than the other strategies, leading to a longer torque saturation in HCCI mode and resulting in a vehicle jerk motion. However, no effect on velocity is visible. Strategies *LiP* and *PeP*, due to their prediction of the exit event, are able to send the cam switch command as soon as the desired torque exits the HCCI regime. Therefore the disturbance in torque is mitigated and jerk reduced." [97]

3.5.2 Drive Cycle Results

The **fuel economy results** for the FTP75, HWFET, and US06 drive cycles are shown in Fig. 3.12 and Table 3.3. The influence of incorporating the mode switching dynamics can be clearly seen by comparing the results for the three supervisory strategies to the instantaneous case. As discussed in Sec. 3.2, multimode combustion assuming instantaneous switches leads to efficiency improvements of 3% (FTP75), 1.5% (HWFET), and 0.4% (US06). If the penalties and delays are included and applying the supervisor without any prediction *NoP*, the fuel economy benefits drop to 2% (FTP75), 0.6% (HWFET), and -0.2% (US06). Therefore, due to these switches the benefit from using multimode combustion is reduced by 30% and 50% during the FTP75 and HWFET, respectively, and the marginal gain during the US06 vanishes completely. Furthermore, it can be seen that incorporating the simple prediction of supervisor *LiP* leads to almost identical fuel economy. Perfect prediction *PeP*, on the other hand, does result in a visible improvement in fuel economy compared to the *NoP* case, as seen during the US06, where it at least achieves a neutral fuel economy result.

The **fraction of time** spent in the HCCI combustion modes (i.e., at low cam lift) is also shown in Fig. 3.12. As can be seen, the *NoP* strategy results in the longest total residence time in HCCI combustion, even longer than if instantaneous mode

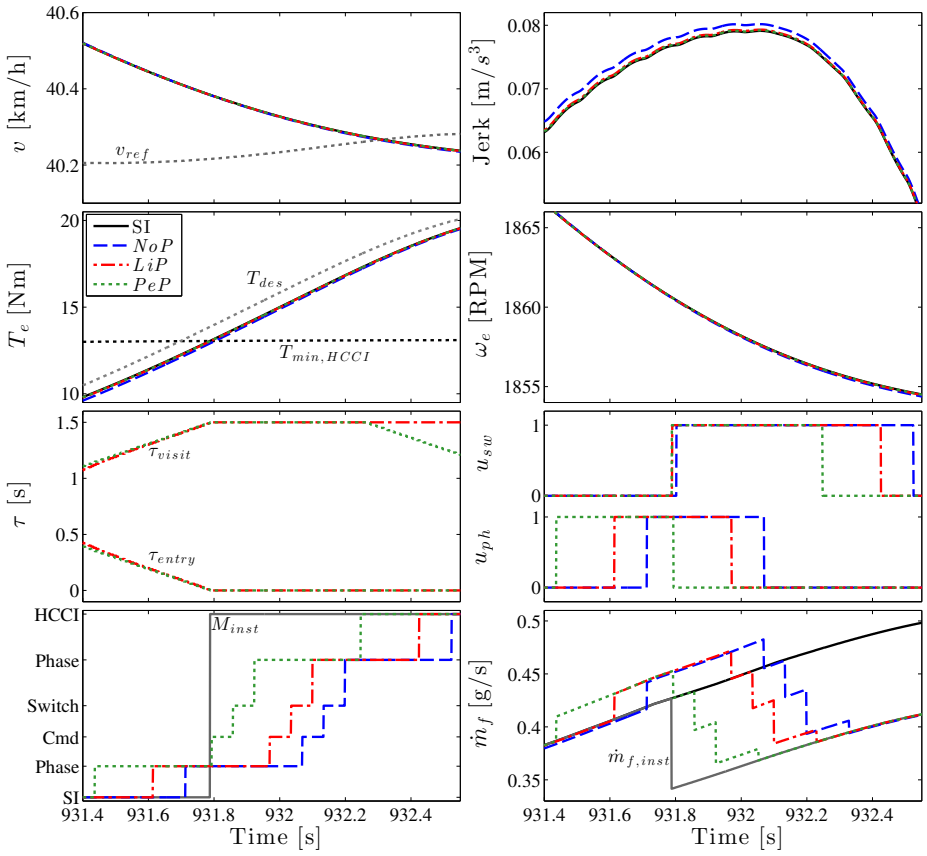

Figure 3.10: Exemplary SI-HCCI mode switch during the FTP75 drive cycle. SI-only (solid black) and strategies *NoP* without any prediction (dashed blue), *LiP* with linear extrapolation (dash-dotted red), and *PeP* with perfect prediction (dotted green). M_{inst} and $\dot{m}_{f,inst}$ are results assuming instantaneous mode switches.

Table 3.3: Drive cycle fuel economy in MPG for SI-only and multimode engine, assuming instantaneous and penalized mode switches.

Drive Cycle		FTP75		HWFET		US06	
SI-only		23.90		38.64		25.56	
SI/HCCI	Inst.	24.64	(+3.09%)	39.20	(+1.44%)	25.70	(+0.39%)
	NoP	24.40	(+2.06%)	38.88	(+0.63%)	25.50	(-0.23%)
	LiP	24.40	(+2.08%)	38.88	(+0.62%)	25.52	(-0.14%)
	PeP	24.45	(+2.27%)	38.96	(+0.83%)	25.57	(+0.05%)

switches are assumed. This is due to the load saturations at the HCCI limits. Instantaneous switches would have already reached nominal SI mode while the penalized mode switches are delayed due to the cam phasor dynamics. More details on the time spent in the different modes can be seen in Table 3.4. During FTP75 and HWFET

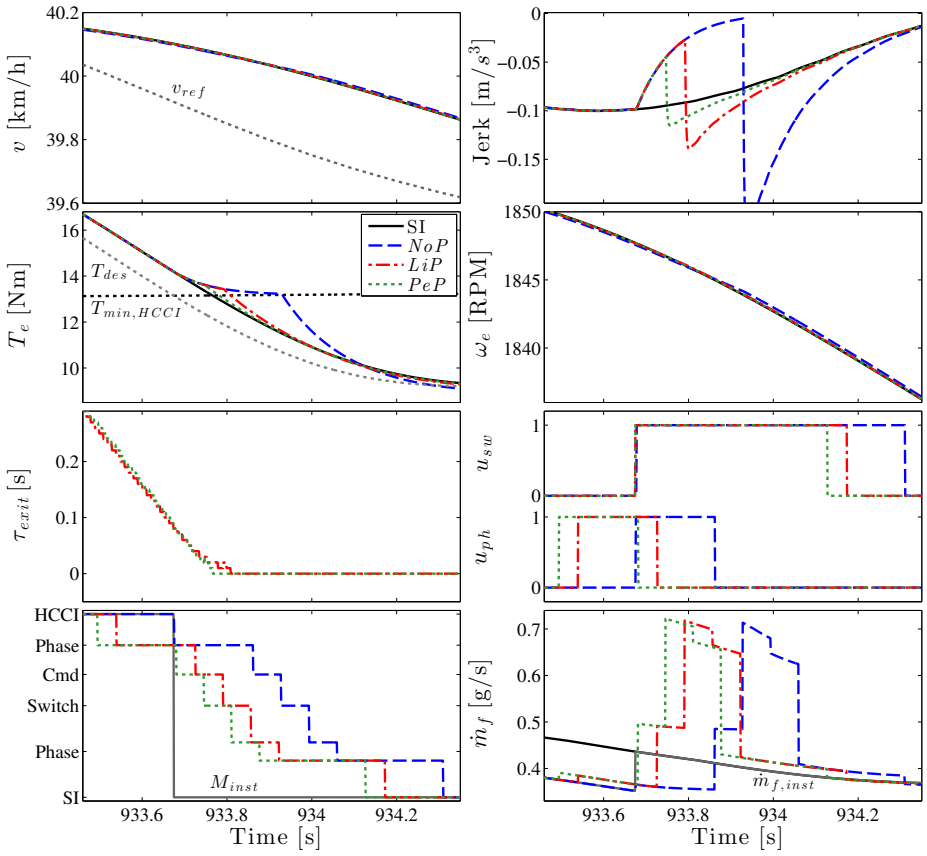

Figure 3.11: Exemplary HCCI-SI mode switch during the FTP75 drive cycle. SI-only in solid black and strategies *NoP* without any prediction (dashed blue), *LiP* with linear extrapolation (dash-dotted red), and *PeP* with perfect prediction (dotted green). M_{inst} and $\dot{m}_{f,inst}$ are results assuming instantaneous mode switches.

cycles the engine operates approximately 75% of time in nominal SI mode.[3] Approximately 15% of time is spent at nominal HCCI conditions. Therefore, the roughly 10% of time remaining is spent during mode switching, specifically phasing the valve timings to prepare for the cam switches. The situation is significantly different in case of the US06 drive cycle. Here, the time spent in nominal HCCI mode is only 2% and therefore even lower than what is required to switch between the modes. As can be seen in Fig. 3.12, perfect prediction *PeP* results in a significant reduction in time spent in HCCI mode due to the following reasons. First, the mode switches are timed very accurately and therefore engine torque is not being saturated at HCCI's limits. Second, short residences in HCCI mode are avoided, if they do not result in a net fuel economy benefit. In case of the US06, this prior knowledge leads to negligible HCCI

[3]This includes an engine cold start phase of approximately 5 min during the FTP75 and periods of engine idle.

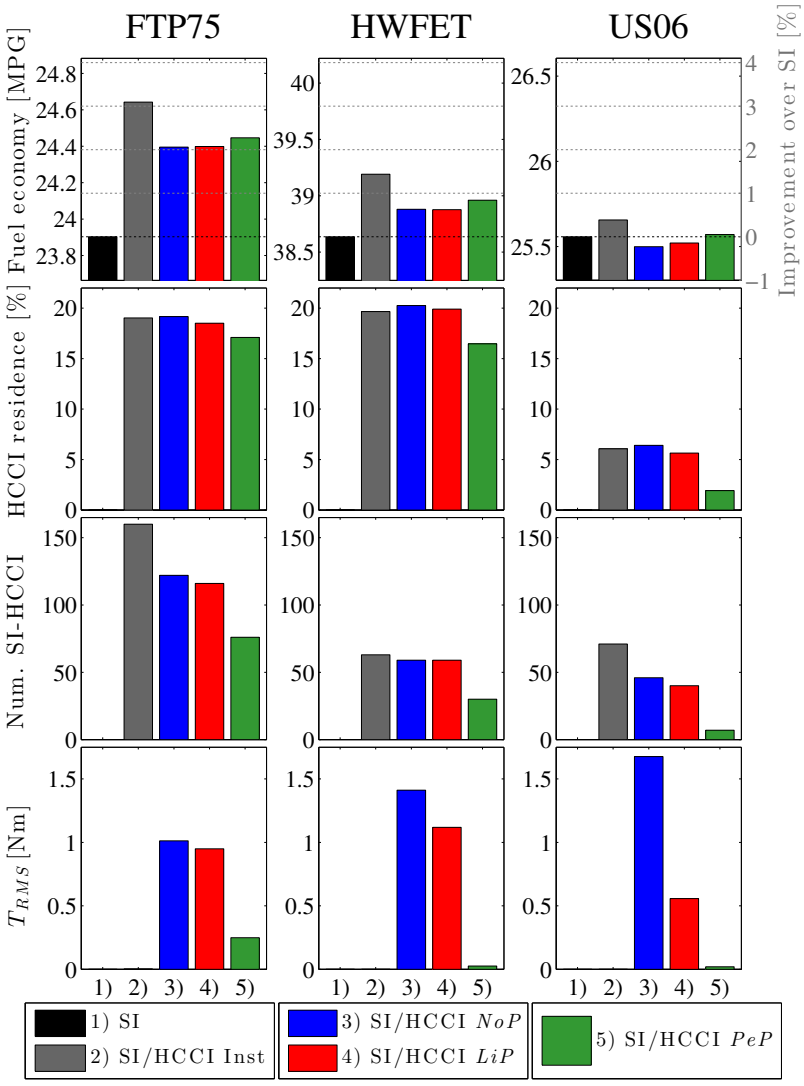

Figure 3.12: Drive cycle simulation results for the different strategies during the FTP75 (left column), HWFET (center column), and US06 (right column) drive cycles. SI-only (black), instantaneous switches (grey) and strategies *NoP* without any prediction (blue), *LiP* with linear extrapolation (red), and *PeP* with perfect prediction (green). Top row: Fuel economy in MPG. Second row: Total residence time in HCCI mode relative to duration of drive cycle. Third row: Number of cam switches in SI-HCCI direction. Bottom row: Torque deviation in RMS error.

operation.

Furthermore, Fig. 3.12 shows the **number of mode switches** from SI to HCCI, specifically cam switches from high to low lift in case of the penalized mode switches.[4] As can be seen, the FTP75 drive cycle exhibits more than double the number of mode

[4]The unnecessary preparation of a mode switch without switching the cams, i.e., an attempt, does not count as mode switch.

Table 3.4: Use of different sets of modes M in percentage time and fuel, when applying the mode switch model and NoP strategy.

Drive Cycle		FTP75	HWFET	US06
SI		75.9%	74.6%	87.0%
HCCI		15.4%	15.5%	2.4%
SI-HCCI	Pre	2.4%	2.2%	3.3%
	Post	2.1%	2.8%	2.0%
HCCI-SI	Pre	1.6%	1.9%	2.0%
	Post	2.6%	2.9%	3.4%

switches than the other drive cycles. Also, if instantaneous mode switches are assumed the number of mode switches is significantly higher. As discussed in Sec. 3.2, this is due to a large number very short visitations of the HCCI regime, which are too brief to allow for a mode switch. Many of these visitations occur during rapid accelerations of the vehicle and during gear changes. However, those unused short visitations do not accumulate to a significant duration, as can be seen when comparing the residence times in HCCI of instantaneous with penalized mode switches. During the HWFET drive cycle there is no substantial difference between the number of instantaneous and penalized mode switches.

The differences between the supervisory strategies NoP and LiP are minor for most of the prior aspects of the drive cycle results. However, as discussed above, besides fuel economy the multimode combustion operation can also influence the engine's **torque response**. Here the impact of the strategies on the overall torque response is measured as root-mean-square (RMS) error T_{RMS} between the torque T_e of the associated simulation run and the torque result $T_{e,SI}$, based on the conventional SI engine without any mode switching. A larger T_{RMS} is interpreted as a greater deviation from the desired engine torque and therefore as a reduction in drivability.

$$T_{RMS} = \sqrt{\frac{1}{t_f}\int_0^{t_f}(T_{e,SI} - T_e)^2 dt} \tag{3.52}$$

with t_f the duration of the associated drive cycle. Indeed, as can be seen in Fig. 3.12 the strategies applying prediction exhibit a reduction in T_{RMS}. During the FTP75 the LiP strategy only results in a relatively small improvement in drivability. The strategies allow to prepare the HCCI-SI mode switches beforehand to minimize periods under torque saturations. In addition, some short residences can be avoided.

However, the strategy is still subjected to interruptions due to gear shifts and the associated fuel cut-off events, as discussed in Sec. 3.4. The impact of shifts in a manual transmission are explored further in Sec. 3.5.4. As can be seen in case of the HWFET cycle, while the *LiP* results in some improvement, it requires perfect prediction *PeP* to avoid all the unnecessary HCCI visitations and prepare the mode switches optimally. Finally, during the US06 cycle already incorporating the extrapolation from the *LiP* strategy results in a great improvement since all the very short visitations of the HCCI regime can be predicted and avoided. Overall, however, even in case of strategy *NoP* relatively mild amplitudes of vehicle jerk were experienced and velocity was barely affected.

3.5.3 Beneficial and Harmful Mode Switches

In this dissertation, a mode switch cycle is defined as a series of transitions in M, which starts and ends in SI mode ($M = 1$). If this mode switch cycle only includes the preparation of the cam switch, $i \in (1, 12)$, it is defined as an attempt. Otherwise, if a cam switch from high to low lift is conducted, it is a switch. To better understand the impact of the different supervisory control strategies and the mode switch dynamics on fuel economy, each mode switch cycle j is analyzed individually. For every mode switch cycle the saved fuel, i.e., the difference between the SI-only and the multimode fuel use, is computed as

$$\Delta m_{f,j} = \int_{t_s^j}^{t_e^j} (\dot{m}_{f,SI} - \dot{m}_f)\, dt \tag{3.53}$$

with t_s^j and t_e^j as start and end of the mode switch cycle j, respectively. However, due to the fuel penalty, mode switch cycles require a certain amount of time s[emt in HCCI combustion mode to regain the invested fuel. In [98] it is shown that this duration is approximately 0.8-1.2 s. If the net fuel gain of a mode switch cycle is positive, it is denoted beneficial $m_{f,j}^+$, otherwise harmful $m_{f,j}^-$:

$$\Delta m_{f,j}^+ = \begin{cases} \Delta m_{f,j} & \Delta m_{f,j} > 0 \\ 0 & \text{else} \end{cases} \tag{3.54}$$

$$\Delta m_{f,j}^- = \begin{cases} \Delta m_{f,j} & \Delta m_{f,j} \leq 0 \\ 0 & \text{else.} \end{cases} \tag{3.55}$$

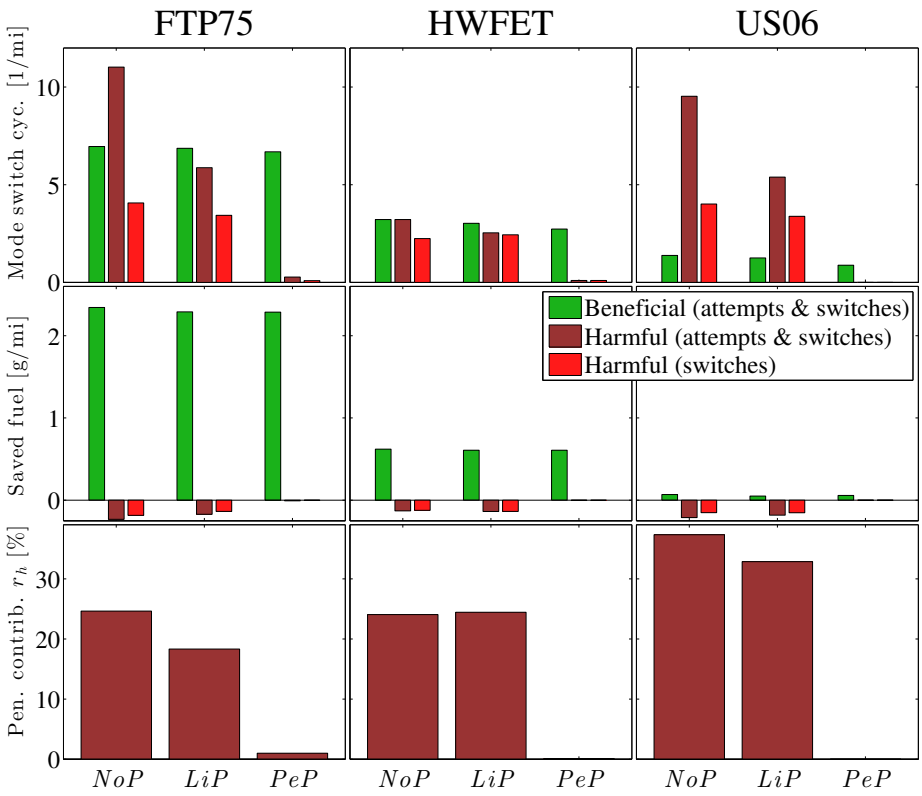

Figure 3.13: Analysis of drive cycle simulation results in terms of mode switch cycles for FTP75 (left), HWFET (center), and US06 (right) drive cycles and the three supervisory control strategies *NoP*, *LiP*, and *PeP*. Beneficial attempts and switches (green), harmful attempts and switches (dark red), and its subset harmful switches (light red). Top: Number of mode switches cycles per distance. Middle: Amount of saved fuel mass per distance. Bottom: Penalty contribution of harmful mode switch cycles.

The number of beneficial and harmful mode switch cycles for the different drive cycles and supervisory strategies are shown in Fig. 3.13. The effect of these mode switch cycles on fuel economy can be seen using the associated total fuel masses saved and misspent Δm_f^+ and Δm_f^-, respectively:

$$\Delta m_f^{+/-} = \sum_{j^{+/-}} \Delta m_{f,j}^{+/-}. \tag{3.56}$$

It follows that $m_{f,SI} - m_f \approx \Delta m_f^+ - \Delta m_f^-$.[5] This can be compared to an ideal gain

[5]This is approximately instead of exactly equal, since sometimes the mode switching dynamics alter the torque trajectories beyond the duration of the mode switch cycle, thereby also leading to small differences in fuel flow.

if instantaneous mode switches are assumed:

$$\Delta m_{f,id} = \int_0^{t_f} (\dot{m}_{f,SI} - \dot{m}_{f,inst})\, dt. \tag{3.57}$$

Therefore mode switching dynamics and penalties "lead to two kinds of losses of fuel economy compared to instantaneous mode switches. First, the harmful mode switch cycles lead to a loss $l_h = -\Delta m_f^-$, which can be minimized by eliminating those mode switches. A second loss is denoted $l_b = \Delta m_{f,id} - \Delta m_f^+$, with the subscript "b" because it refers to a loss occurring during beneficial mode switches. It represents the fuel that needs to be invested in order to use the HCCI combustion mode and the fact that mode switches require a certain amount of time." [96] The loss l_h could be slightly reduced using the predictive supervisory control strategies. However, l_b is significantly more difficult to attack. The ratio r_h, defined as

$$r_h = \frac{l_h}{l_h + l_b} \tag{3.58}$$

represents the penalty contribution, i.e., negative impact of those harmful switches on fuel economy compared to the instantaneous case. The larger r_h, the greater the potential of a supervisory controller to improve fuel economy by avoiding unnecessary switches. Sometimes, the hardware limitations such as delays and response of the valve timing can provide a natural way of avoiding short residence times, hence reducing the number of harmful mode switches. Since those harmful mode switch cycles are short, r_h is relatively small. As can be seen in Fig. 3.13, for the FTP75 and HWFET drive cycles and the strategies *NoP* and *LiP* the contribution r_h lies between 18-25%. The supervisor with perfect prediction *PeP* is able to reduce r_h to zero by avoiding all harmful residences. Therefore the difference in fuel economy between the penalized and the instantaneous case could be reduced by approximately 25%. This is the maximum fuel economy achievable for a given mode switching strategy. However, this result is still far away from the fuel economy assuming instantaneous switches. This remaining drop in fuel economy is due to extra fuel, simply required to use the advanced combustion mode. The total amount of fuel necessary for mode switches depends on the mode switch control strategy. A more efficient strategy could reduce the decrease in fuel economy compared to the instantaneous case.

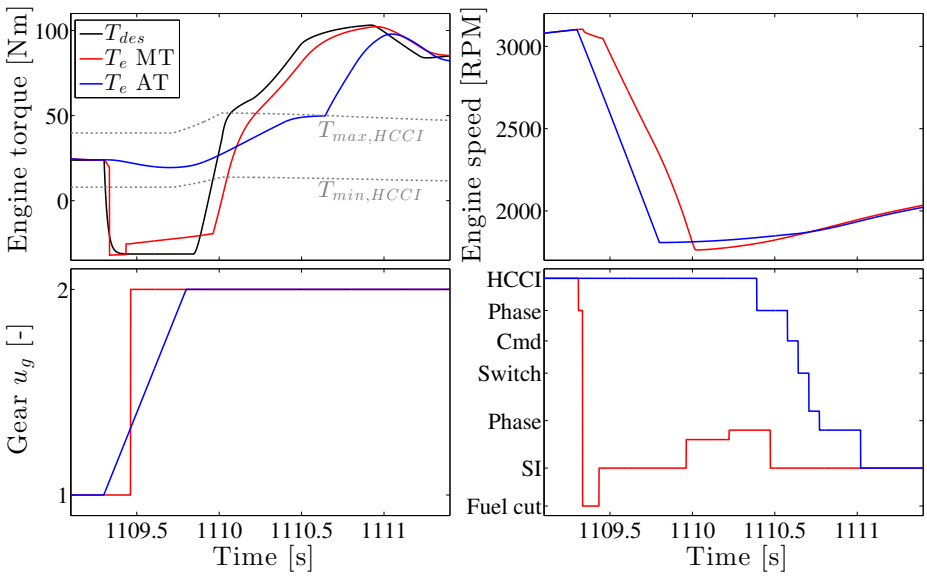

Figure 3.14: Exemplary gear shift during simulation of FTP75 drive cycle to compare the nominal manual transmission model (MT, red) and the simplified ramp in gear ratio (AT, blue). The desired engine torque in black and the HCCI limits in grey. Top left: Engine torque. Top right: Engine speed. Bottom left: Gear. Bottom right: Combustion mode M.

3.5.4 Case Study: "Automatic Transmission"

An engine connected to a manual transmission experiences fast changes in load during the gear changes, as seen in Fig. 3.14. As mentioned above, these transients might affect the operation in HCCI mode. For that reason, in this section smooth gear shifts are assumed, i.e., engine speed changes without having to de-clutch the engine, while the same gear ratios and the same shift schedule are applied as above. To emphasize, this is not understood as a model of an automatic transmissions. Such a model would require many additional parts such as torque converter, additional gears and clutches, and a supervisory controller for shifting. The goal here, however, is to just get a basic idea of the impact of the manual transmission on HCCI performance. The difference between the smooth and regular shifts in terms of resulting trajectories can be seen in Fig. 3.14. The regular shift leads to an abrupt drop in torque with fuel cut-off and the end of the associated HCCI residence. On the other hand, the smooth shift results in an extended residence in HCCI mode. However, eventually the changed gear ratio leads to higher engine torque demand, such that also the smooth case exits the HCCI residence.

The alternative drive cycle results for smooth gear shifting are shown in Fig. 3.15. Absolute results for fuel economy are slightly different from the ones in Fig. 3.12,

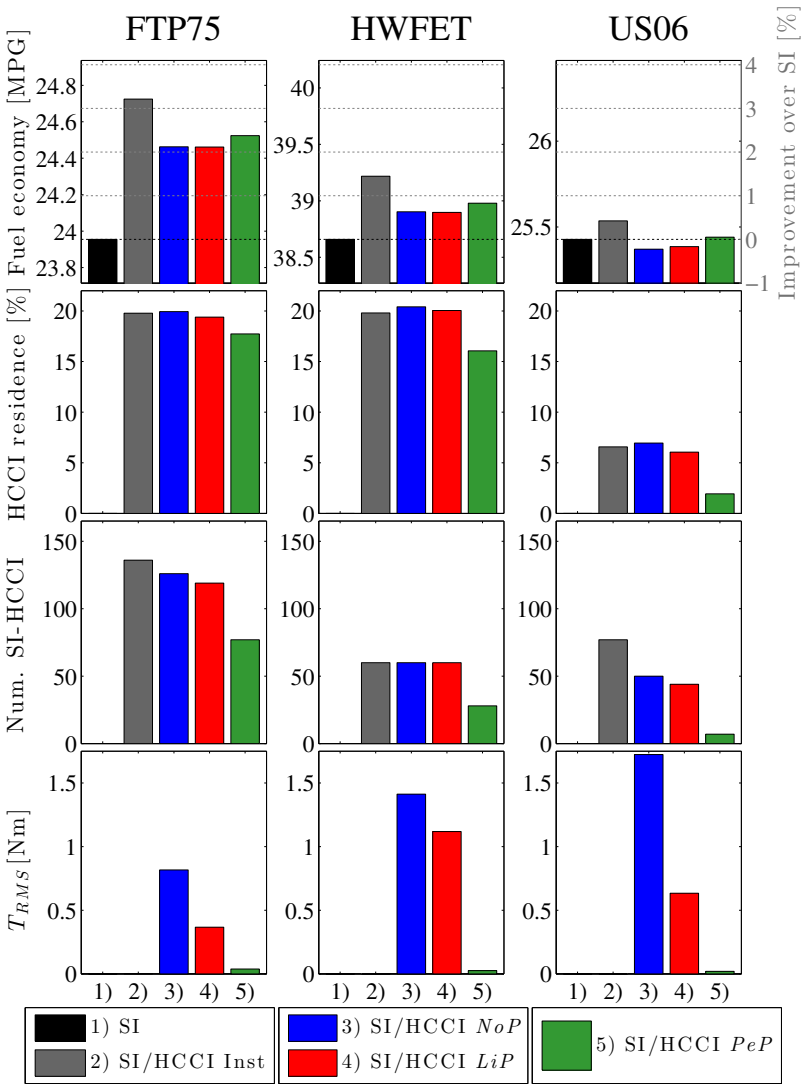

Figure 3.15: Drive cycle simulation results for the different strategies during the FTP75 (left column), HWFET (center column), and US06 (right column) drive cycles. Smooth gear shifting is assumed without fluctuations in engine torque to approximate an automatic transmission. SI-only (black), instantaneous switches (grey) and strategies *NoP* without any prediction (blue), *LiP* with linear extrapolation (red), and *PeP* with perfect prediction (green). Top row: Fuel economy in MPG. Second row: Total residence time in HCCI mode relative to duration of drive cycle. Third row: Number of cam switches in SI-HCCI direction. Bottom row: Torque deviation in RMS error.

since the driver is able to track the reference velocity without being disturbed by the gear shifts. However, here it is only focused on the relative performance of the different cases. As can be seen, fuel economy improvements as well as most other results are very similar to the ones presented above. One difference is a reduction in instantaneous mode switches. As mentioned above, with a manual transmission

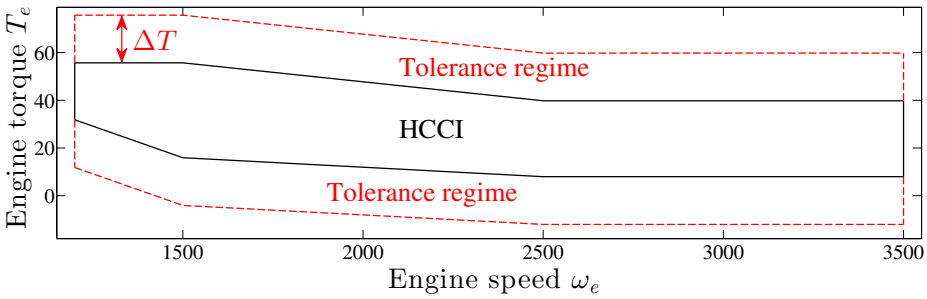

Figure 3.16: Boundary of the feasible operating regime of NA HCCI combustion (solid black). In HCCI combustion, the tolerance regime (dashed red) represents the load/speed conditions for which deviations between desired torque T_{des} and actual torque T_e are accepted for extended periods of time.

engine load crosses the HCCI regime very rapidly during the shifts. Such crossings are removed in case of smooth shifts. Furthermore, while in the regular case the gear changes interfere with the HCCI operation for supervisory strategies *NoP* and *LiP*, here the RMS errors in torque are significantly smaller and the *LiP* strategy is able predict the smoother torque profile more accurately.

3.5.5 Case Study: "Ignoring the Driver"

Since the occurrences of vehicle jerk in the cases without a tolerance band were acceptable, it may be possible to amplify HCCI's efficiency benefits by temporarily ignoring the driver's commands, thereby increasing HCCI's utilization. In this case study, which has been published in [97], a tolerance band with width ΔT is introduced above and below the HCCI regime, as can be seen in Fig. 3.16. Note that this study only concerns supervisors *NoP* and *LiP*. For strategy *PeP* the original results are shown without tolerance band, since the predicted load/speed trajectories are based on the SI-only case, which are not subject to the mode switching delays. Therefore, the larger ΔT, the greater the difference between T_{des} and $T_{des,SI}$, leading to inaccurate predictions.

$$\tilde{T}_{min,HCCI} = T_{min,HCCI} - \Delta T \tag{3.59}$$

$$\tilde{T}_{max,HCCI} = T_{max,HCCI} + \Delta T \tag{3.60}$$

While the HCCI entry conditions of the three strategies remain the same, the exit conditions are slightly modified. In case of the strategy *NoP*, instead of with equation

(3.18), $R_{out,2}$ is defined as:

$$R_{out,2} = \tilde{R}_{des} = f_R(T_{des}, \tilde{T}_{min,HCCI}, \tilde{T}_{max,HCCI}). \tag{3.61}$$

This leads to preparation of the cam switch, once the desired load T_{des} exits the HCCI regime. However, the cam switch command is not sent until T_{des} leaves the tolerance band.

In addition to this modification, in case of the predictive strategy *LiP* the computation of the predicted exit time $\tau_{exit,des}$, previously defined with equations (3.39), (3.40), is altered as well:

$$j_{exit,des} = \max\left(i \in (1, H) \mid f_R(\hat{\omega}_e^{k+i}, \hat{T}_{des}^{k+i}, \tilde{T}_{min,HCCI}^{k+1}, \tilde{T}_{max,HCCI}^{k+1}) = \text{HCCI}\right) \tag{3.62}$$

$$\tau_{exit,des} = j_{exit,des} \cdot t_s. \tag{3.63}$$

Doing so, the mode switch back to HCCI is not being prepared until T_{des} is predicted to exit the tolerance band soon. This avoids the fuel penalties from prolonged operation with prepared valve timings.

The width of the tolerance band ΔT is varied from 0 Nm to 20 Nm. The associated simulation results are shown in Fig. 3.17. As expected, with increasing tolerance band, fuel economy improvements relative to the SI-only case increase as well. The *LiP* strategy eventually even reaches the case assuming instantaneous switches. The reasons for this benefit are twofold. The larger tolerance band results in additional residence time in beneficial HCCI conditions. For the entire FTP75 drive cycle, residence time in HCCI mode increased by up to 20%. In addition, due to the tolerance band, short excursion from the operating regime do not necessarily lead to fuel expensive mode switches. Therefore, also the number in cam switches decreased by up to 32% for the two strategies. Together these two effects result in a dramatic increase in residence time in HCCI per cam switch, i.e., by up to 74% and 86% for strategies *NoP* and *LiP*, respectively.

Note that even for $\Delta T = 20$ Nm, the driver was able to follow the reference velocity without violating the velocity tolerance boundaries. However, with larger ΔT, time periods, during which the engine does not respond to changes in pedal position, become longer. This increasingly impacts drivability and T_{RMS}. The trade-off between fuel economy improvement and drivability can be seen in Fig. 3.18, split up into the three phases of the FTP75 cycle. By introducing a small band with $\Delta T = 1$ Nm to 5 Nm the fuel economy benefits are increased without greatly affecting drivability.

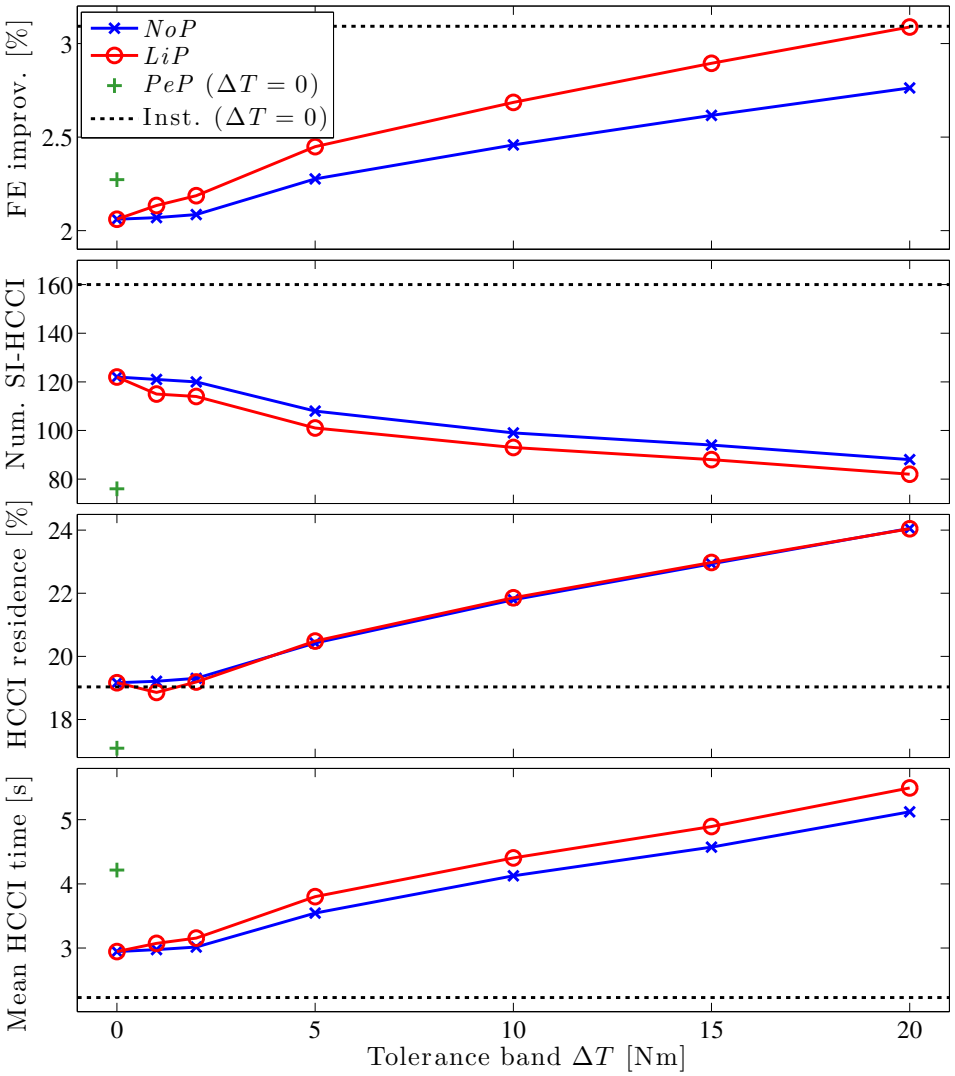

Figure 3.17: Simulation results for the FTP75 drive cycle with fuel economy improvements compared to a conventional SI engine versus width of the tolerance band ΔT. Strategy *NoP* without any prediction (red circles) and strategy *LiP* with linear extrapolation (blue crosses), compared with the fuel economy achieved by instantaneous mode switches (dashed black) and perfect prediction *PeP* (green pluses). Top: Fuel economy improvement compared to SI-only case. Second: Number of cam switches in SI-HCCI direction. Third: Total residence time in HCCI mode relative to duration of drive cycle phase. Bottom: Residence time in HCCI mode per SI-HCCI cam switch.

However, it can be seen that for larger ΔT the trade-off tends to plateau. Eventually, vehicle jerk and the slow engine response would become unacceptable for the driver. Overall, it can be seen that strategy *LiP* is slightly superior to *NoP* in a way that at same fuel economy, the impact on drivability is reduced. This is even amplified if perfect prediction is assumed, which at $\Delta T = 0\,\text{Nm}$ shows similar fuel economy, but

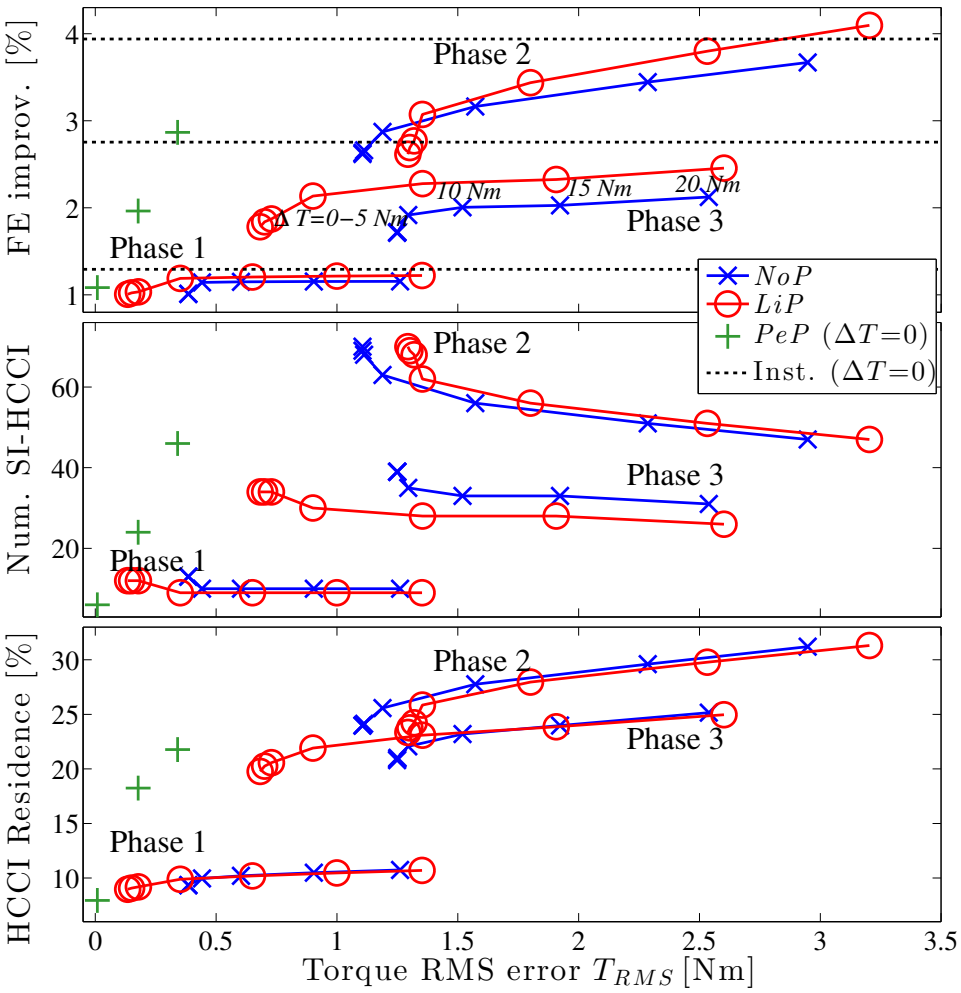

Figure 3.18: Simulation results for the three phases of the FTP75 drive cycle with fuel economy improvements compared to a conventional SI engine versus drivability as RMS torque error T_{RMS}. Strategy *NoP* without any prediction (red circles) and strategy *LiP* with linear extrapolation (blue crosses), compared with the fuel economy achieved by instantaneous mode switches (dashed black) and perfect prediction *PeP* (green pluses). Top: Fuel economy improvement compared to SI-only case. Center: Number of cam switches in SI-HCCI direction. Bottom: Total residence time in HCCI mode relative to duration of drive cycle phase.

at significantly reduced deviations in engine torque.

3.5.6 Sensitivity Analysis

In the following section, different model parameters are varied and their influence on FTP75 drive cycle fuel economy is discussed.

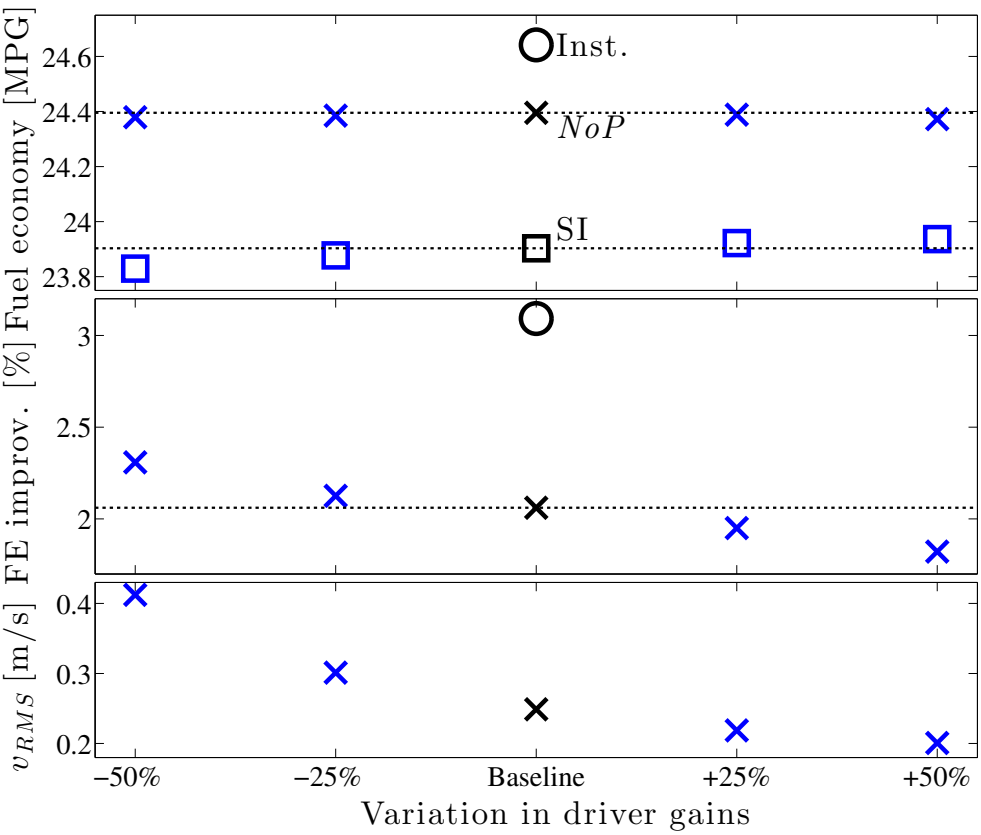

Figure 3.19: Influence of driver gains $K_{p,drive}$ and $K_{i,drive}$ on FTP75 fuel economy (top), fuel economy improvement over SI-only (middle), and RMS error in velocity tracking (bottom). The *NoP* supervisor strategy is used (cross) and compared with the instantaneous (circle) and the SI-only (square) cases. The baseline values are shown in black.

Driver Gains

First the driver behavior is varied by modifying gains $K_{p,drive}$ and $K_{i,drive}$, responsible for tracking the reference velocity v_{ref}. The gains are varied between -50% to +50% and the results are shown in Fig. 3.19. Besides the fuel economy results the accuracy of the reference tracking is shown, defined as RMS error v_{RMS}:

$$v_{RMS} = \sqrt{\frac{1}{t_f}\int_0^{t_f} (v - v_{ref})^2 \, dt}. \tag{3.64}$$

As expected, decreasing the driver gains results in a reduction in tracking accuracy. It must be noted that for the smallest gains the driver violates the drive cycle's velocity tolerances multiple times. However, as can be seen, the fuel economy is not very sensitive towards changes in driver response. While the SI-only fuel economy is in-

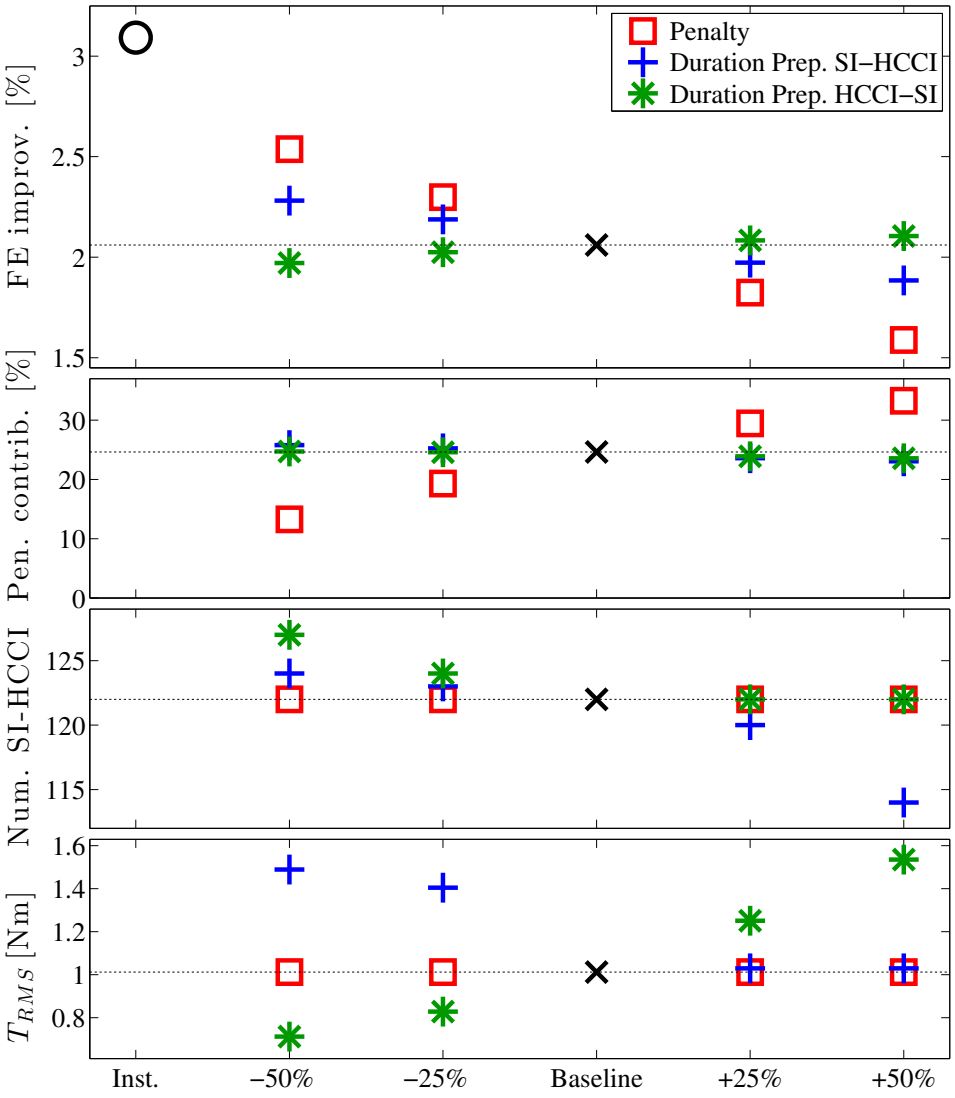

Figure 3.20: Influence of mode switch parameters on FTP75 fuel economy improvement over SI-only (top), penalty contribution of harmful mode switch cycles (second), number of SI-HCCI cam switches (third), and RMS error in engine torque (bottom). The *NoP* supervisor strategy is used and varied are fuel penalty parameters d_i (red square) as well as preparation durations during SI-HCCI switch Δt_2 (blue cross) and during HCCI-SI switch Δt_8 (green star). The baseline and instantaneous values are shown in black.

creasing with higher gains, the efficiency of the multimode strategy is fairly constant, resulting in a decreasing fuel economy improvement for increasing gains.

Mode Switch

Furthermore, different parameters of the combustion mode switch model are varied between ±50%, applying supervisory *NoP*. The results are shown in Fig. 3.20. The following parameters were altered: All fuel penalties d_i, the duration Δt_2 to prepare the cam switch during the SI-HCCI switch, and duration Δt_8 to prepare the switch in the other direction.

It is not surprising that fuel penalty parameters have the strongest influence on fuel economy. This can also be seen in terms of penalty contribution of harmful mode switch cycles. The higher the fuel penalty, the more important becomes the supervisory strategy to avoid short and harmful residences in HCCI mode. Of course, since the *NoP* strategy is applied, the number of mode switches and the error in torque are not affected by the penalty parameters. Of course this would change, if the *PeP* strategy is used.

The time requirement Δt_2 has a much smaller impact on fuel economy. Smaller values of Δt_2 lead to a benefit in fuel economy, since the mode switch to low lift can be conducted faster and the beneficial HCCI mode is reached sooner. Therefore, also the number of cam switches is directly affected. As can be seen, due to the additional mode switches, some of which result in a fuel cut-off, a decreasing Δt_2 can have an impact on torque response.

Finally, increasing the duration Δt_8 leads to longer periods, in which engine torque is being saturated at HCCI's limits. While this offers a small benefit in fuel economy it has, as expected, a very strong impact on the torque response. This is very similar to the effect discussed in the case study above about ignoring the driver.

3.6 Summary

This chapter discusses the influence of combustion mode switching on drive cycle fuel economy and drivability. A finite-state combustion mode switch model is described and integrated in a longitudinal vehicle model to simulate the FTP75, HWFET, and US06 drive cycles. The model is parameterized based on closed-loop mode switch experiments. Due to its restrictions in range, the gain in fuel economy by using HCCI in a multimode engine is limited, even if instantaneous mode switches are assumed. In this dissertation, improvements of up to 3.4% are shown, which is significantly below other results found in the literature.

With the presented methodology, the overall degradation of the achievable fuel

improvement by the use of HCCI due to the mode switch penalties is quantified. Further, if the driver requests a change in torque, which requires a mode switch from HCCI to SI mode, the torque response needs to be delayed until the mode switch is completed. Therefore, besides penalizing fuel economy, mode switches might also lead to a degradation in drivability.

The impact of these penalties is tested using three supervisory control strategies. The first only reacts on current engine speed and load conditions. The second applies linear extrapolation of engine speed and desired torque to anticipate entries and exits of the feasible HCCI combustion regime. The third strategy assumes perfect knowledge of the driver's desired torque and speed trajectories and in addition, the optimal mode switch policy is determined beforehand with dynamic programming. It is seen that while fuel economy improves with increasing prediction, the three strategies show still relatively similar fuel economy. However, more prediction also resulted in a significant drop in engine torque deviations.

A distinction is introduced between beneficial and harmful mode switches, based on their individual fuel economy benefits. It is observed that prediction results in a reduction of harmful mode switches and unnecessary mode switch preparations. However, the total penalty contribution of those harmful switches on overall fuel economy is relatively small. Even the perfect prediction strategy, which completely avoids harmful switches, is quite far from achieving the fuel economy, suggested by the instantaneous case. This shows that the impact of the supervisory control strategy is limited. As important as the supervisor is the fuel efficiency and duration of the actual mode switching strategy.

The work is extended in two case studies. The first study tested, how removing the fast torque dynamics during gear shifting affects the multimode performance. It was seen that the impact on fuel economy was only minor. The second case study introduced a tolerance regime around the HCCI regime. As long as the driver's desired torque torque is located within the tolerance regime, the actual engine torque saturates at the HCCI limit, thereby temporarily ignoring the driver's commands. It is seen that such a tolerance band with small width increases fuel economy by increasing time spent in the HCCI regime while avoiding mode switch fuel penalties due to short excursions. Conversely, the degradation of the torque response is still too small to show a significant impact on velocity.

Chapter 4

Mode Switches and Three-Way Catalytic Converter

The majority of the contributions presented in following chapter have been published in [2]:

Journal of Dynamic Systems, Measurement, and Control
Volume 137, Issue 5, May 2015, *"Fuel Economy of a Multimode Combustion Engine with Three-Way Catalytic Converter"*
S. Nüesch, A.G. Stefanopoulou, L. Jiang, and J. Sterniak.

In this chapter the efficiency benefits of a SI/HCCI multimode combustion engine are quantified, when emission constraints are to be met with a three-way catalytic converter (TWC). TWCs are the main technology used to control emissions from gasoline engines. However, generally they are not suited for the application in lean-burn direct injection engine systems. TWCs require stoichiometric conditions in order to reduce NO_x, HC, and CO simultaneously. In a lean environment selective catalyst reduction (SCR), lean NO_x catalysts (LNC) or passive NO_x adsorbers (PNA) can be used. However, the use of TWCs as aftertreatment system is desirable due to their wide distribution and relatively low cost compared to lean-burn aftertreatment systems [127, 128]. In contrast to lean-burn gasoline direct injection (GDI) combustion, HCCI combustion leads to very low engine-out NO_x emissions due to its low peak temperatures. Under lean HCCI conditions the TWC will still be able to convert CO and HC. In addition, TWCs have the ability to store a limited amount of O_2 to compensate for variations in dilution. If the TWC's oxygen storage capacity (OSC) is sufficiently large, a high NO_x conversion can be sustained for a certain amount of time while running lean HCCI. Conversely, if the OSC is filled the TWC needs to be depleted by running the engine rich which translates into a penalty in fuel economy.

It is difficult to make a judgment about the benefits of combining HCCI with a TWC. An investigation of the entire system is required, which needs to be based

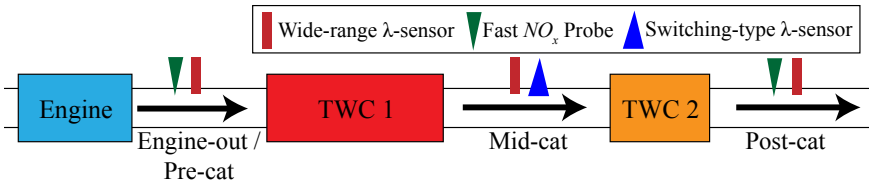

Figure 4.1: Hardware setup for aftertreatment experiments and control. [2]

on actual engine data, as well as consider combustion mode switches and the aftertreatment system. Therefore, this chapter describes a methodology to evaluate the impact of a TWC system on fuel economy within a SI/HCCI multimode concept, and provides insight on the suitability of such a system as an afterteatment measure to simultaneously enable high fuel economy and low emissions during a drive cycle.

The vehicle and multimode engine models are described in previous chapters. They are extended here to compute emissions and dilution during the combustion mode switches, based on steady-state maps. The models are combined with a phenomenological TWC model, focused on oxygen storage. The aftertreatment model is calibrated using combustion mode switch experiments from lean HCCI to rich spark-assisted compression ignition (SACI) and back. Different depletion strategies are compared in terms of their influence on drive cycle fuel economy and NO_x emissions.

Compared to [2] the results shown in this chapter are updated by applying the engine temperature dynamics from Chap. 2, and the combustion mode switch model and supervisory strategies from Chap. 3.

4.1 Aftertreatment Hardware & Overview

"The aftertreatment system consists of three Emitec prototype TWC substrates with the first two substrates housed together in one can and the third packaged as an underfloor catalyst. The close-coupled TWC substrates are based on Palladium (Pd) and Palladium/Rhodium (Pd/Rh), and the underfloor TWC is based on Palladium/Rhodium (Pd/Rh). The two catalysts each use a generous Cerium dioxide - Zirconia dioxide ($CeO_2 - ZrO_2$) oxygen storage. The hardware configuration is sketched in Fig. 4.1. The system is operated with two oxygen sensors (or λ-sensors). A wide-range sensor is located in front of the first catalyst and a switching-type sensor in between the two catalysts. The aftertreatment hardware is discussed in more detail in [129]." [2]

Figure 4.2 shows the block diagram of the mathematical model of the aftertreat-

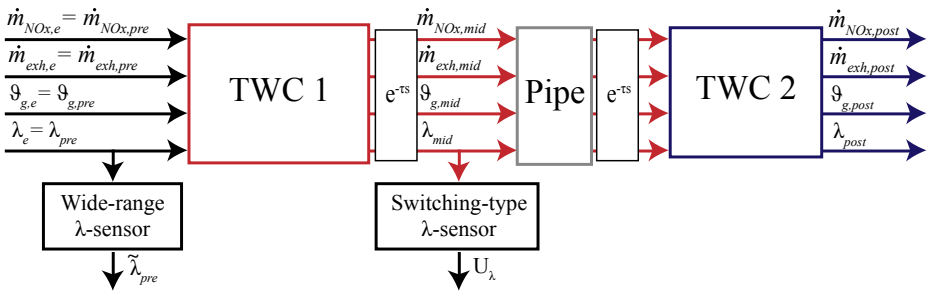

Figure 4.2: Block diagram of the system with the two TWCs and the two sensors.

ment system with the two connected TWC blocks. Inputs to the model are engine-out exhaust mass flow $\dot{m}_{exh,e}$, exhaust gas temperature $\vartheta_{g,e}$, relative air-fuel ratio (AFR) λ_e, and the exhaust gas composition. Exhaust mass flow $\dot{m}_{exh,e}$ is defined as:

$$\dot{m}_{exh,e} = \dot{m}_f \cdot (14.6 \cdot \lambda_e + 1). \tag{4.1}$$

The engine-out emissions mass flows (i.e., $\dot{m}_{NO_x,e}$, $\dot{m}_{HC,e}$, $\dot{m}_{CO,e}$) are based on steady-state load/speed maps, described in Sec. 4.2. The procedure from Heywood, chapter 4 [130] is applied to approximate the molar flows of the individual components of the exhaust gas (i.e., $\dot{n}_{NO_x,e}$, $\dot{n}_{HC,e}$, $\dot{n}_{CO,e}$, $\dot{n}_{O_2,e}$, etc.).

The heat transfer in the pipe between the two TWCs is modeled applying first-order dynamics, described in [131]. Since the first TWC is located close to the engine, the pre-cat values are equal to the associated engine-out ones. The transport delays τ, occurring inside TWC 1 as well as between TWC 1 and TWC 2, depend on ω_e and are chosen to be one and a half of an engine cycle, respectively, to match the experimental data. Also shown are the two sensors measuring λ_{pre} and λ_{mid}, resulting in $\tilde{\lambda}_{pre}$ and voltage U_λ, respectively.

4.2 Steady-State Experiments

In the following section steady-state experimental data is used to extend the engine model to compute engine-out emissions. The specifications of the multimode engine are described in Sec. 3.1 and its fuel efficiency maps for SI and HCCI combustion are shown in Fig. 3.1. Furthermore, the TWC's conversion efficiencies are discussed.

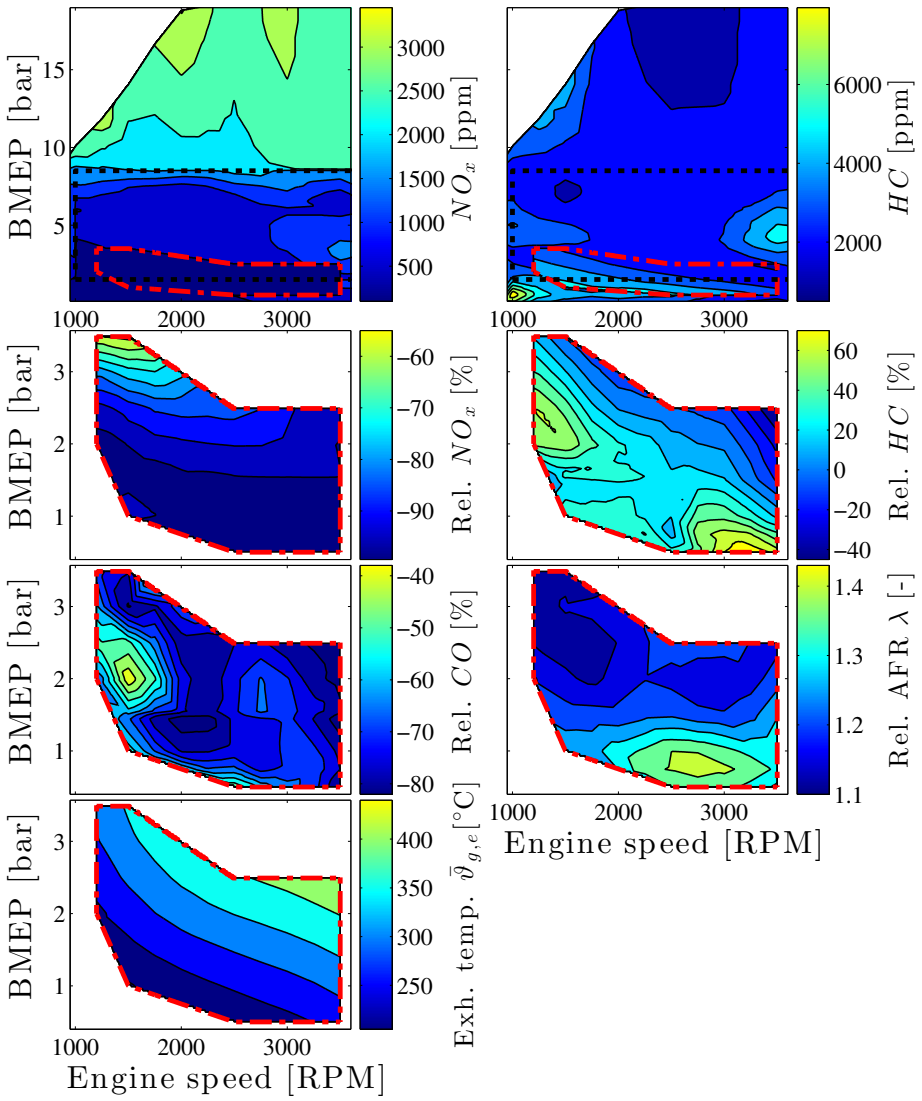

Figure 4.3: Maps of the multimode combustion engine based on steady-state experiments. Lean HCCI (dash-dotted red) and SI combined with eEGR (dotted black). Top: Engine-out NO_x (left) and HC emissions (right). Second and third: Relative improvements, i.e., (HCCI-SI)/HCCI, in NO_x (center left), HC (center right), and CO (bottom left) within the operating regime of HCCI compared to SI. Third right: Map of relative AFR λ. Bottom: Engine-out exhaust temperature. Associated fuel efficiency maps are shown in Fig. 3.1.

4.2.1 Emission Maps

Steady-state experimental data for relative AFR λ and engine-out emissions as functions of engine speed and load are depicted in Fig. 4.3. The maps are referred to as $f_{NO_x,SI}$, $f_{NO_x,HCCI}$, etc. As can be seen in Fig. 4.3, significant reduction in NO_x emissions can be noticed, especially in the lower half of the engine operating regime.

The HCCI regime overlaps with a region in which SI can be operated using external exhaust gas recirculation (eEGR). This strategy already results in a substantial decrease in NO_x emissions. Nevertheless, HCCI reduces these additionally by more than 95%. Furthermore, compared to SI mode operated with eEGR, HCCI results in a reduction in CO emissions between 40-80%. However, HC shows generally increased levels, up to 60% higher than in SI mode.

4.2.2 Rich Operation

Steady-state experimental data at varying dilution, shown in Fig. 4.4, was used to approximate the impact of rich operation on engine-out emissions and fuel efficiency.[1] Fuel efficiency drops rapidly under rich conditions [132]. Here this reduction is approximated by the inverse of the relative AFR. Therefore only the deficit in oxygen is considered and incomplete combustion and water shift losses are neglected. As can be seen in Fig. 4.4 this approximation is accurate enough for purposes here. The experimental data is used to find the associated parameters $d_{r,j}$ with $j = \{HC, CO, NO_x\}$. The integration of those parameters into the combustion mode switch model is described in Sec. 4.5.

4.2.3 Conversion Efficiencies

The conversion efficiencies of the TWCs were measured under steady-state operation at different dilutions and combustion modes, shown in Fig. 4.5. The engine was operated at 1800 RPM and between 1.6-3.1 bar BMEP. Similar to [133] S-shaped Wiebe

[1] During the transient experiments and the simulations in this dissertation engine AFR $\lambda = 0.9$ is the most rich operating condition used.

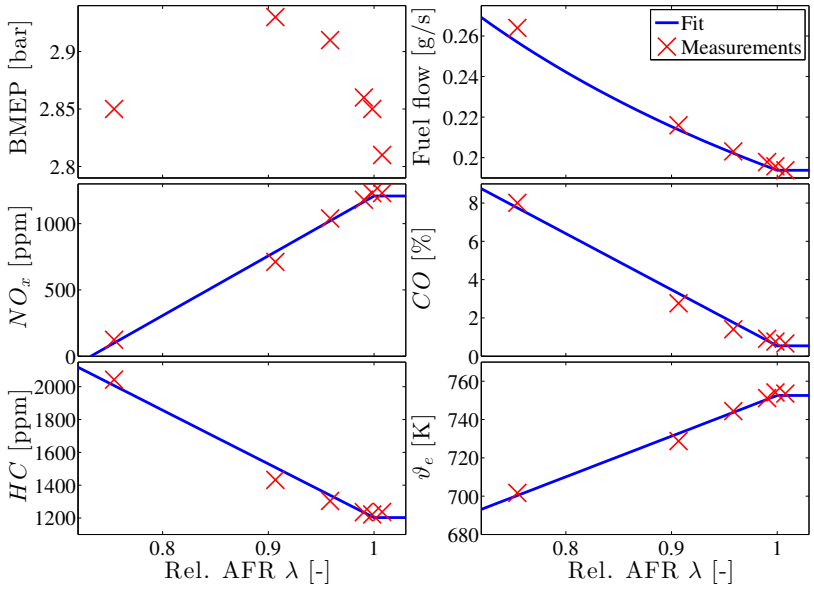

Figure 4.4: Steady-state measurements in SI combustion mode at 1800 RPM (red crosses) and fit (solid blue) at varying dilution. Top left: Engine load. Top right: Fuel mass flow. Center left and right: Engine-out NO_x and CO emissions, respectively. Bottom left: Engine-out HC emissions. Bottom right: Engine-out exhaust gas temperature.

functions are used to fit conversion efficiency to the measurements shown in Fig. 4.5.[2]

$$\eta_{NO_x,\lambda}(\lambda) = 1 - \exp\left(-\left(\frac{\lambda - 1.02}{0.013}\right)^5\right) \tag{4.2}$$

$$\eta_{CO,\lambda}(\lambda) = 1 - \exp\left(-0.6247 \cdot \left(\frac{\lambda - 0.85}{0.1}\right)^{4.581}\right) \tag{4.3}$$

$$\eta_{HC,\lambda}(\lambda) = 1 - \exp\left(-0.0637 \cdot \left(\frac{\lambda - 0.82}{0.08}\right)^{5.1265}\right) \tag{4.4}$$

[2]Under lean AFR conditions the TWC is ineffective in converting NO_x, leading to equal pre- and post-cat NO_x values. However, due to measurement errors the post-cat concentration may appear slightly larger than the pre-cat one, leading to negative conversion efficiencies. Therefore, for such cases zero conversion was assumed.

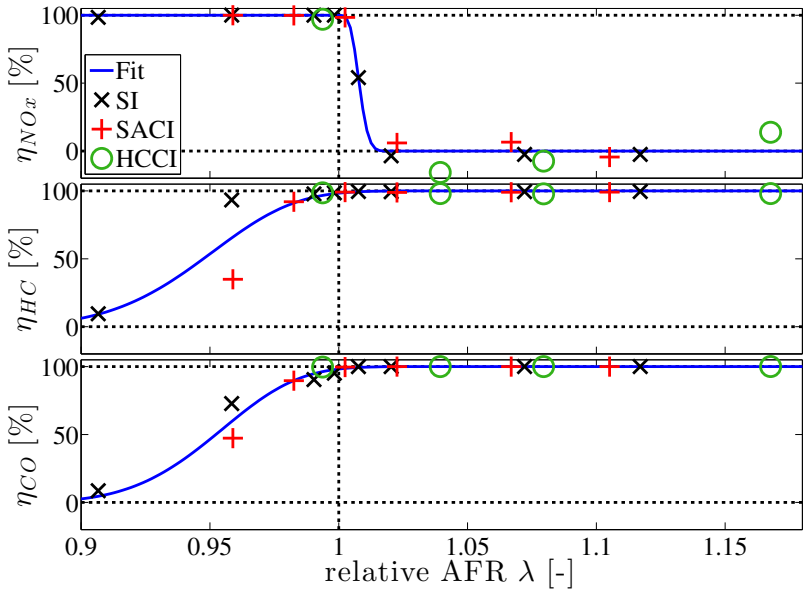

Figure 4.5: TWC NO_x conversion efficiency measurements at 1800 RPM and fit (solid blue). SI (black cross), SACI (red plus), HCCI (green circle).

In addition, similar Wiebe functions are used to approximate the light-off behavior of the TWC, as function of TWC brick temperature ϑ_b:

$$\eta_{NO_x,\vartheta_b}(\vartheta_b) = 1 - \exp\left(-\left(\frac{\vartheta_b - 573}{100}\right)^5\right) \tag{4.5}$$

$$\eta_{CO,\vartheta_b}(\vartheta_b) = 1 - \exp\left(-\left(\frac{\vartheta_b - 493}{140}\right)^5\right) \tag{4.6}$$

$$\eta_{HC,\vartheta_b}(\vartheta_b) = 1 - \exp\left(-\left(\frac{\vartheta_b - 463}{120}\right)^5\right). \tag{4.7}$$

Finally, the total conversion efficiencies are computed as follows:

$$\eta_{NO_x}(\lambda, \vartheta_b) = \min\left\{0.9990, \eta_{NO_x,\lambda} \cdot \eta_{NO_x,\vartheta_b})\right\} \tag{4.8}$$

$$\eta_{CO}(\lambda, \vartheta_b) = \min\left\{0.9986, \eta_{CO,\lambda} \cdot \eta_{CO,\vartheta_b})\right\} \tag{4.9}$$

$$\eta_{HC}(\lambda, \vartheta_b) = \min\left\{0.9976, \eta_{HC,\lambda} \cdot \eta_{HC,\vartheta_b})\right\}. \tag{4.10}$$

The functions are saturated at the maximum measured conversion efficiencies.

The conversion efficiencies are used to determine the flow rates at the TWC outlet:

$$\dot{n}_{NO_x,out} = \dot{n}_{NO_x,in} \cdot (1 - \eta_{NO_x}) \tag{4.11}$$

$$\dot{n}_{CO,out} = \dot{n}_{CO,in} \cdot (1 - \eta_{CO}) \tag{4.12}$$

$$\dot{n}_{HC,out} = \dot{n}_{HC,in} \cdot (1 - \eta_{HC}) \tag{4.13}$$

4.3 TWC Temperature Dynamics

To get an idea about the influence of low temperature HCCI exhaust on the TWC's performance a low-order brick temperature model is described and briefly validated in the following section. An overview on TWC temperature modeling can be found in [132]. The model distinguishes between the temperature of the gas phase ϑ_g and the brick temperature ϑ_b. However, similar to [133, 134], the model shown here is even more simplified by being 0-dimensional. This leads to the two following state equations:

$$\epsilon_c V_c \rho_g c_{v,g} \frac{d\vartheta_g}{dt} = \dot{m}_{exh} c_{p,g} (\vartheta_{g,in} - \vartheta_g) - \dot{Q}_c \tag{4.14}$$

$$m_c c_s \frac{d\vartheta_b}{dt} = \dot{Q}_c + \dot{Q}_r - \dot{Q}_a \tag{4.15}$$

where ϵ_c denotes the volume fraction of the TWC filled with exhaust gas, V_c the volume of the TWC, c_s the specific heat capacity of the solid phase, and m_c the mass of the TWC. Furthermore, the density ρ_g and the specific heat capacity $c_{v,g}$ of the exhaust gas are functions of incoming gas temperature $\vartheta_{g,in}$ and its composition. as mentioned above, the composition is approximated as described by Heywood, chapter 4 [130]. The heat flows from gas to brick and brick to ambient, $\dot{Q}_c$, $\dot{Q}_a$, respectively, are defined as

$$\dot{Q}_c = \alpha_c A_{geo} V_c (\vartheta_g - \vartheta_b) \tag{4.16}$$

$$\dot{Q}_a = A_{cat} U_{cat} (\vartheta_b - \vartheta_a) \tag{4.17}$$

with α_c and U_{cat} heat transfer coefficients, A_{cat} the TWC surface area, and A_{geo} $[\mathrm{m}^2/\mathrm{m}^3]$ the specific geometric catalytic surface, defined as $A_{geo} = 4\sqrt{\epsilon_c \cdot \frac{cpsi}{0.0254^2}}$ in [135]. The heat losses to the environment are based on conduction and free convection coefficients, h_{cond} and h_{conv}, respectively, with $U_{cat} = \left(h_{cond}^{-1} + h_{conv}^{-1}\right)^{-1}$. Similar to [136], the heat generated by the exothermic reactions in the TWC is approximated by

assuming only the three overall reactions:

$$NO + CO \rightarrow \frac{1}{2}N_2 + CO_2 \tag{4.18}$$

$$CO + \frac{1}{2}O_2 \rightarrow CO_2 \tag{4.19}$$

$$H_aC_b + (b + \frac{a}{4})O_2 \rightarrow bCO_2 + \frac{a}{2}H_2O. \tag{4.20}$$

As in [136], HC are modeled as 86% propene and 14% methane. Of course this is a very simplifying assumption, since the oxidation rates of hydrocarbons, especially methane, vary strongly with composition and are focus on ongoing research [137]. However, for this application such a simple model was deemed sufficient. This results in the following terms for the reaction enthalpies:

$$\Delta h_{r,1} = h_{NO} + h_{CO} - \left(\frac{1}{2}h_{N_2} + h_{CO_2}\right) \tag{4.21}$$

$$\Delta h_{r,2} = h_{CO} + \frac{1}{2}h_{O_2} - h_{CO_2} \tag{4.22}$$

$$\Delta h_{r,3,a} = h_{C_3H_6} + 4.5h_{O_2} - (3h_{CO_2} + 3h_{H_2O}) \tag{4.23}$$

$$\Delta h_{r,3,b} = h_{CH_4} + 2h_{O_2} - (h_{CO_2} + 2h_{H_2O})\,. \tag{4.24}$$

Using the TWC's conversion efficiencies, the reaction rates of the three reactions are approximated, resulting in the total heat produced $\dot{Q}_r$:

$$\dot{Q}_{r,1} = \Delta h_{r,1} \cdot \eta_{NO_x} \cdot \dot{n}_{NO_x,in} \tag{4.25}$$

$$\dot{Q}_{r,2} = \Delta h_{r,2} \cdot (\eta_{CO} \cdot \dot{n}_{CO,in} - \eta_{NO_x} \cdot \dot{n}_{NO_x,in}) \tag{4.26}$$

$$\dot{Q}_{r,3} = (0.86 \cdot \Delta h_{r,3,a} + 0.14 \cdot \Delta h_{r,3,b}) \cdot \eta_{HC} \cdot \dot{n}_{HC,in} \tag{4.27}$$

$$\dot{Q}_r = \dot{Q}_{r,1} + \dot{Q}_{r,2} + \dot{Q}_{r,3}. \tag{4.28}$$

The steady-state data, described above and shown in Fig. 4.6, was used to find parameters h_{cond} and α_{cat}. Parameters m_c and c_s are based on assumptions and values in literature. The parameters of the TWC temperature model are listed in Table 4.1. A validation of the TWC temperature model is shown in Fig. 4.7. Chassis dynamometer data of engine exhaust temperature and exhaust composition in SI-only combustion are used as input to the model. As can be seen the simulation generally underpredicts the brick temperature by up to 40 °C. The match, however, between the simulated and measured TWC brick temperatures is acceptable for purposes here, especially in terms of the dynamics.

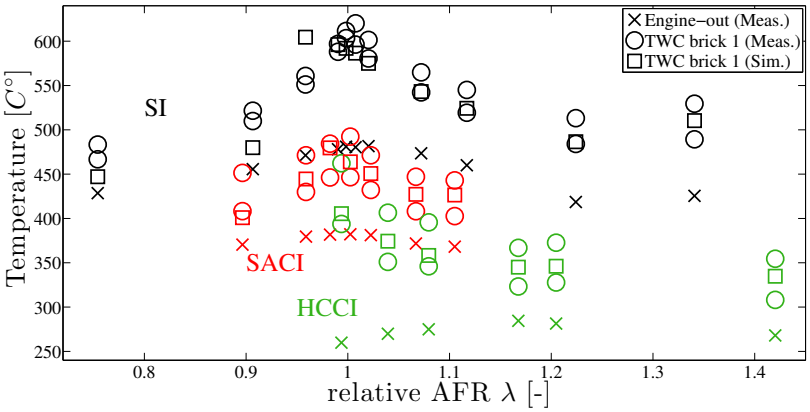

Figure 4.6: Steady-state experiments and simulation of TWC brick 1 temperature for SI (black), SACI (red), and HCCI (green) combustion, over relative AFR. Engine-out exhaust gas temperature (cross), brick temperature measurements and (square) and simulations (circle). The brick temperature is measured at two locations.

Table 4.1: TWC temperature model parameters

Name	**Symbol**	**TWC 1**	**TWC 2**
Specific geometric catalytic surface	A_{geo}	$3.45 \cdot 10^3\,\mathrm{m^2/m^3}$	$2.82 \cdot 10^3\,\mathrm{m^2/m^3}$
TWC volume	V_c	$1.29 \cdot 10^{-3}\,\mathrm{m^3}$	$1.05 \cdot 10^{-3}\,\mathrm{m^3}$
Gas volume fraction	ϵ_c	0.8	
Catalyst mass	m_c	0.45 kg	0.3 kg
Specific heat capacity of TWC	c_s	800 J/kgK	
Heat transfer gas - solid	α_c	140 W/m²K	
Outer surface area of TWC	A_{cat}	0.0492 m²	0.0492 m²
Heat conductivity of TWC wall	h_{cond}	0.5 W/m²K	

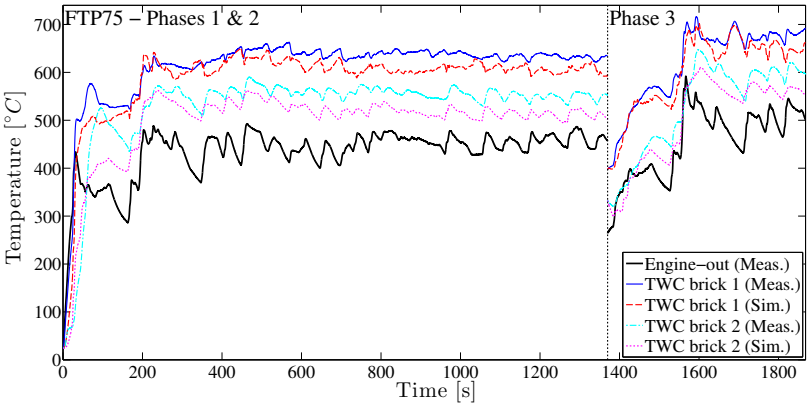

Figure 4.7: Measurements and simulation of TWC brick temperatures during the three phases of the FTP75 drive cycle. Measured engine-out exhaust (black), brick 1 measured (solid blue) and simulated (dashed red), brick 2 measured (dash-dotted cyan) and simulated (dotted magenta).

4.4 Oxygen Storage Dynamics

This section covers the modeling and parameterization of the TWC's oxygen storage dynamics.

4.4.1 Experimental Setup

"The sensors used for the experiments are also shown in Fig. 4.1. In addition to the wide-range λ-sensor in front of the first TWC, two additional ones were placed in between the two and after the second catalyst, respectively. Furthermore, the NO_x emissions were measured using Cambustion CLD500 fast-NO_x analyzers with a response time T_{10-90} of 10 ms. The space velocity was approximately $13,000\,\mathrm{hr}^{-1}$.

SI/HCCI combustion mode switches require sophisticated control strategies. At the time of the experiments the two-stage cam profile system and the control strategy were under development. Ideally a full switch would have been carried out during the experiments, including switches from low to high lift cams. Instead, by using variable valve timing and a stoichiometric or rich AFR, an extension strategy was tested with a switch to SACI combustion mode. In this mode SI combustion conditions are approached, nevertheless they consist of both flame propagation and some autoignition. Further information about spark-assisted compression ignition can be found in Sec. 1.2 and [48, 65]. More details about the experimental setup and results are described in [129]." [2]

4.4.2 Transient Mode Switch Experiments

"Combustion mode switch experiments were conducted by [129] at different levels of dilution. In this dissertation the data is used to characterize the two TWCs and their OSC. The combustion mode was switched between lean HCCI at $\lambda = \{1.06, 1.16, 1.34\}$ and rich SACI at $\lambda = \{0.9, 0.98\}$. The engine speed was kept constant at 1800 RPM and the load moved between 2-3 bar BMEP. During the combustion mode switches actuators settings such as intake and exhaust valve timing, injected fuel mass, and start of injection (SOI), were linearly moved between the steady-state settings during 1 s." [2] In addition, as discussed in the previous chapter, a complete mode switch to SI would involve switching the lift of the cams. It must be noted that, even though this is a representative mode switch strategy, the parameterization of the mode switch model is based on the closed-loop SI/HCCI switch and can be found in Sec. 4.5.

"Experimental results of one particular run are shown in Fig. 4.8. As can be seen the OSC delays the breakthrough of λ after the mode switches. As soon as the storage is full and λ_{post} switches to lean the conversion efficiency drops to zero and the NO_x post-cat is equal to NO_x pre-cat. During the mode switches spikes in NO_x levels occur beyond their steady-steady values. The reason is the mode switch control strategy, that favors NO_x production during the switch by allowing larger fuel amounts together with lean AFR. Post-cat NO_x continuously decreases to 0 ppm as the OSC is being depleted and the TWC's NO_x conversion efficiency gradually increases. In addition, it is possible that the increased oxygen partial pressure during the lean phase lead to filling of storage sites, that are difficult to reach under conditions closer to stoichiometry [129]. Comparing these experimental results to examples published in literature, e.g., [138, 139], a difference is apparent after the switch from SACI to HCCI at $t = 30$ s. After the pre-cat AFR is changed from rich to lean, mid- and post-cat λ values are expected to show a fast response until they reach stoichiometry. Instead they exhibit a slow response. One possible explanation for this behavior might be the storage of hydrocarbons on the TWC during extensive rich operation. The hydrocarbons might get desorbed during the succeeding lean phase, leading to a rich post-cat λ." [2]

4.4.3 Model

"Modeling the chemical reactions occurring in a catalyst accurately requires detailed kinematic models [140–142]. Nevertheless several approaches can be found in literature introducing simplifications to the system to make it more feasible for control-purposes. Those simplified models are either phenomenological and oxygen storage-dominated [143,144] or based on reduced chemical relationships [138,145,146]. They try to estimate the relative oxygen storage level, one of the most important states for aftertreatment control. In this dissertation the approach shown in [3,147] is applied. In an effort to obtain an initial estimate of the fuel penalties due to emission constraints, the simple oxygen storage model was applied at all loads and speeds, extrapolating the behavior of the local conditions used for tuning the model.

In the following section the implementation of the model in this dissertation is briefly repeated. A block diagram of the model is shown in Fig. 4.9. The relative oxygen storage level Θ is the only state. Inputs are exhaust mass flow $\dot{m}_{exh}$, incoming NO_x concentration and relative AFR λ_{in}. Outputs are outgoing NO_x concentration and relative AFR λ_{out}.

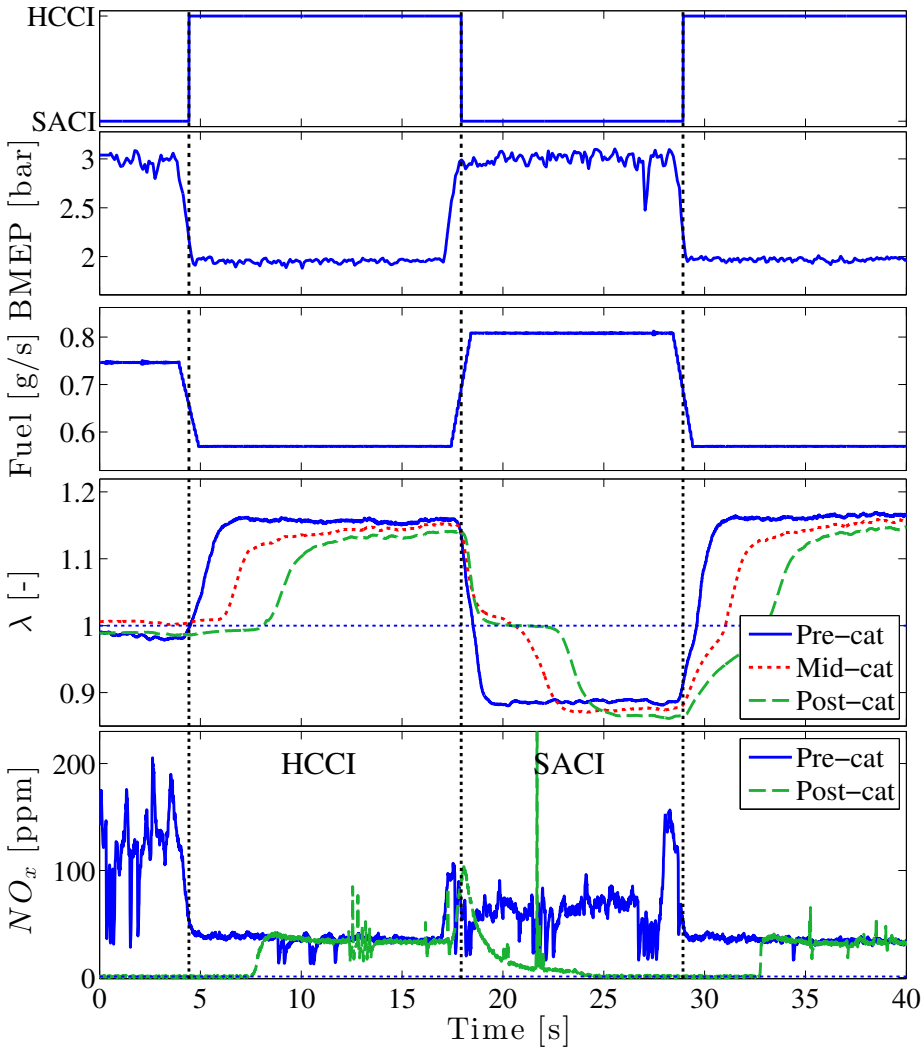

Figure 4.8: Combustion mode switch experiment between rich SACI ($\lambda = 0.9$) and lean HCCI ($\lambda = 1.16$). Top: Combustion mode based on EVC position. The center of the linear cam phasing of 1 s represents the mode switch (dashed black). Second and third: BMEP and fuel mass flow command respectively. Fourth: Pre-cat AFR measurements (solid blue), mid-cat (dashed green) and post-cat (dotted red). Bottom: NO_x measurements pre-cat (solid blue) and post-cat (dotted green). [2]

The function $f_\rho(\Theta, \lambda_{in})$ regulates how fast the OSC can be filled and lies between 0 and 1. In short, an empty storage can be filled faster than a full one, vice versa for depletion. The functions f_L and f_R represent the fraction of oxygen being adsorbed

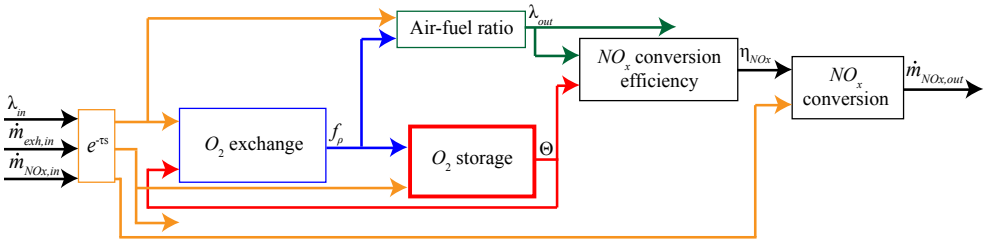

Figure 4.9: Block diagram of the TWC model, introduced by [3].

from and released to the feed gas, respectively:

$$f_L(\Theta) = \frac{1 - e^{p_L \Theta}}{e^{p_L} - 1} + 1 \tag{4.29}$$

$$f_R(\Theta) = \frac{e^{-p_R \Theta} - 1}{e^{-p_R} - 1} \tag{4.30}$$

$$f_\rho(\Theta, \lambda_{in}) = \begin{cases} f_L(\Theta) & \lambda_{in} \geq 1 \\ f_R(\Theta) & \lambda_{in} < 1. \end{cases} \tag{4.31}$$

Parameters p_L and p_R determine the shape of those functions. They were chosen so that the simulated behavior of pre- and post-cat λ matches the one in the experiments." [2] The mass flow $\dot{m}_{exh}$ is input to the state equation for Θ. From mass balance output λ_{out} can be easily derived in (4.33):

$$\dot{\Theta} = \begin{cases} \frac{0.23}{C}(1 - \frac{1}{\lambda_{in}}) \cdot \dot{m}_{exh} \cdot f_\rho(\Theta, \lambda_{in}) & 0 \leq \Theta \leq 1 \\ 0 & \text{else} \end{cases} \tag{4.32}$$

$$\lambda_{out} = \lambda_{in} - f_\rho(\Theta, \lambda_{in}) \cdot (\lambda_{in} - 1). \tag{4.33}$$

4.4.4 Validation

The six unknown parameters C_1, C_2, $p_{L,1}$, $p_{L,2}$, $p_{R,1}$, and $p_{R,2}$ "were found by matching the model to the transient mode switch experiments at the different conditions for λ. The results are shown in Tab. 4.2. The model was validated with additional experimental data sets at the same operating conditions. Figure 4.10 shows the comparison of the model to one of these experiments. Steady-state map values for BSFC and engine-out λ and NO_x at same speed / load conditions were used as inputs. Durations and behavior of λ during filling and depletion of the OSCs are very com-

Table 4.2: OSC model parameters

	TWC 1		TWC 2	
Storage Capacities	C_1	0.7 g	C_2	0.4 g
Adsorption	$p_{L,1}$	6.6	$p_{L,2}$	4.5
Release	$p_{R,1}$	8.1	$p_{R,2}$	6.5
PI	$K_{p,OSC}$	0.08	$K_{i,OSC}$	25 s

parable. It can also be seen that both the steady-state NO_x values match as well as the instant where the OSC is full and the conversion efficiency drops. As expected by the model construction, this simplified model is not able to reproduce the roll-off in post-cat NO_x at $t = 18\,\mathrm{s}$ but shows an instantaneous drop to zero. In addition, since steady-state maps are used here the NO_x spikes during rich-to-lean transitions are not recreated. Another disagreement can be seen at $t = 30\,\mathrm{s}$ when λ_{Post} steps to stoichiometry immediately, instead of following the slow response of the measurement. This model is only parameterized and validated for medium loads and speeds. However, for this work it is only required to approximate the oxygen storage dynamics within the HCCI load range and for that purpose this model is considered to be accurate enough." [2]

4.4.5 Estimation

"It is not necessary to solely rely on the model to detect a depleted or full oxygen storage. The very accurate switching-type sensor, located in between the two catalysts, provides feedback as soon as the AFR switches from lean to rich and vice versa. A model-based closed loop estimation approach shown by [148, 149] is adapted and integrated. The structure of the estimator is shown in Fig. 4.11." [2]

The wide-range oxygen sensor in front of the first catalyst is modeled as a first-order system with a time constant $\tau_s = 0.15\,\mathrm{s}$. In reality these sensors are also prone to biases and noise which are neglected here:

$$\tilde{\lambda}_{pre} = \frac{1}{1 + \tau_s \cdot s} \lambda_{pre}. \tag{4.34}$$

Figure 4.12 shows the λ-voltage characteristic of the implemented switching-type sensor. The following equation, described in [107], translates the sensors voltage output U_λ into an oxygen storage estimation $\tilde{\Theta}_1'$ by simply interpolating the signal in a narrow

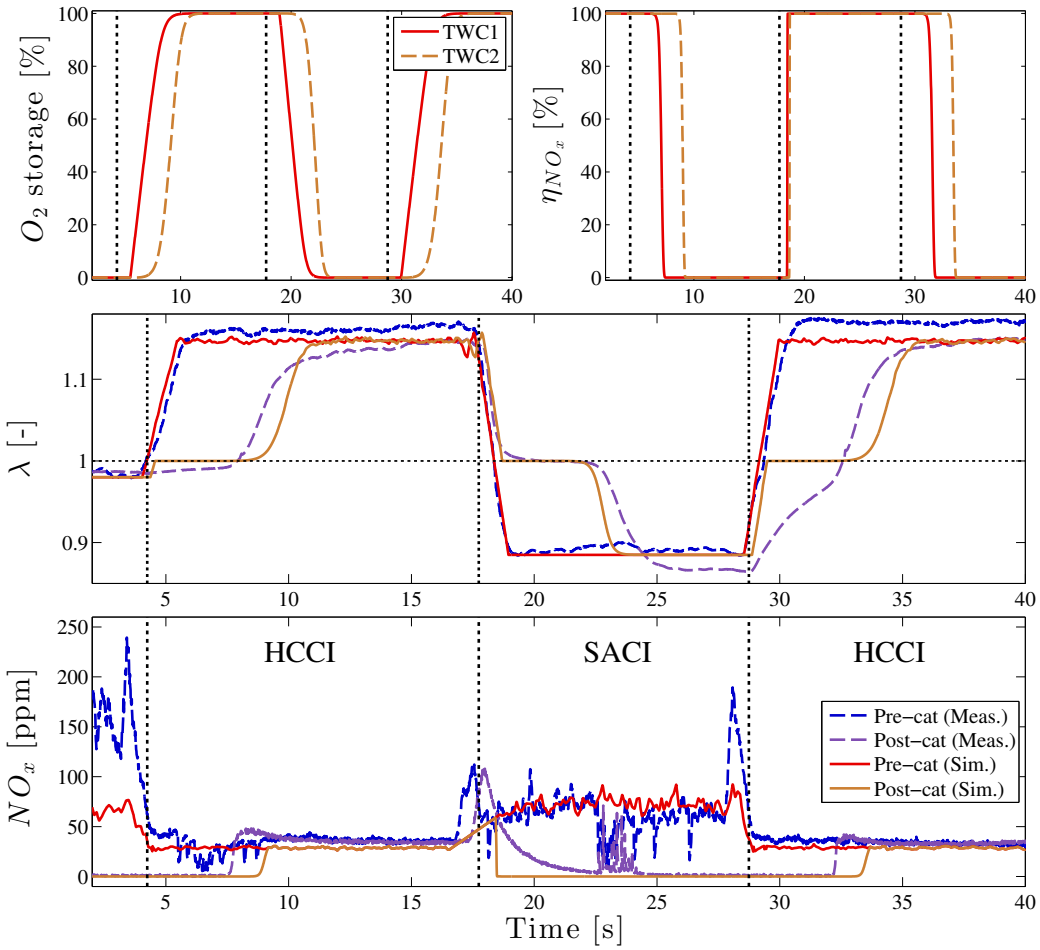

Figure 4.10: Validation of the aftertreatment model with a different experimental data set at same conditions as in Fig. 4.8. Top: Left and right plots of the OSC level and NO_x conversion efficiency, respectively, for the two TWCs. Center and Bottom: Relative AFR λ and NO_x, respectively. Pre-cat and post-cat measurements (dashed dark and light blue, respectively). Pre-cat and post-cat simulation (solid red and orange, respectively). [2]

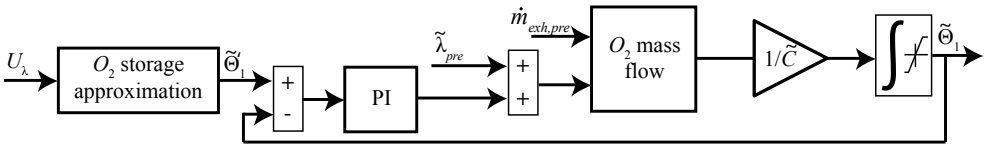

Figure 4.11: Block diagram of the OSC estimator. [2]

range around stoichiometry:

$$\tilde{\Theta}'_1 = \begin{cases} 1 & U_\lambda < 0.2\,\mathrm{V} \\ 1 - (U_\lambda - 0.2)/0.5 & 0.2\,\mathrm{V} \le U_\lambda \le 0.7\,\mathrm{V} \\ 0 & 0.7\,\mathrm{V} < U_\lambda. \end{cases} \tag{4.35}$$

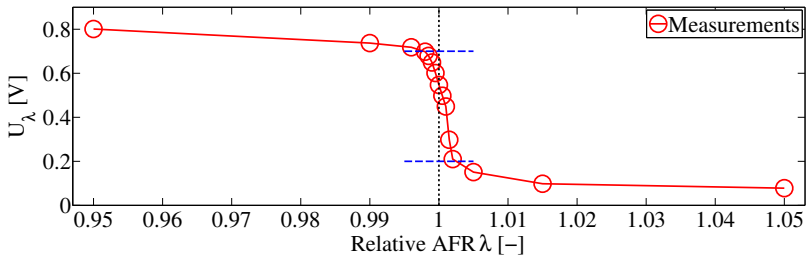

Figure 4.12: Switching-type sensor voltage - AFR characteristic.

Whenever λ_{mid} is close to stoichiometry, $\tilde{\Theta}_1'$ is compared with the estimated $\tilde{\Theta}_1$ the determine a correctional input $\Delta\lambda$. The integrator of the PI controller resets as soon as the gas composition deviates from stoichiometry:

$$\Delta\lambda = \begin{cases} \mathrm{PI}(\tilde{\Theta}_1' - \tilde{\Theta}_1) & 0.2\,\mathrm{V} \leq U_\lambda \leq 0.7\,\mathrm{V} \\ 0 & \text{else.} \end{cases} \tag{4.36}$$

The leads to the state equation for $\tilde{\Theta}_1$:

$$\dot{\tilde{\Theta}}_1 = \frac{0.23 \cdot \dot{m}_{exh,e}}{\tilde{C}} \cdot \left(1 - \frac{1}{\tilde{\lambda}_{pre} + \Delta\lambda}\right). \tag{4.37}$$

This model is almost equal to the one used as plant, only differing from the play model with parameter $\tilde{C}_1 = 0.85\,\mathrm{g}$ and missing function ρ, to incorporate some model uncertainty. To observe a realistic plant, a parameter adaptation scheme as described by [149] is required to lead to good performance over the entire operating range.

4.5 Extension of Combustion Mode Switch Model

The combustion mode switch model is described in detail in Sec. 3.3. In the following section the model is extended to allow rich operation in SI mode and account for the emissions during the mode switch. The modified flow diagram can be seen in Fig. 4.13.

4.5.1 Mode Switch Scheduling

In the extended model R_{TWC} is incorporated, output of the applied depletion strategy, as described in Sec. 4.6. Further an additional input to the mode switch u_{ri} is defined, which determines when to operate in rich SI mode.

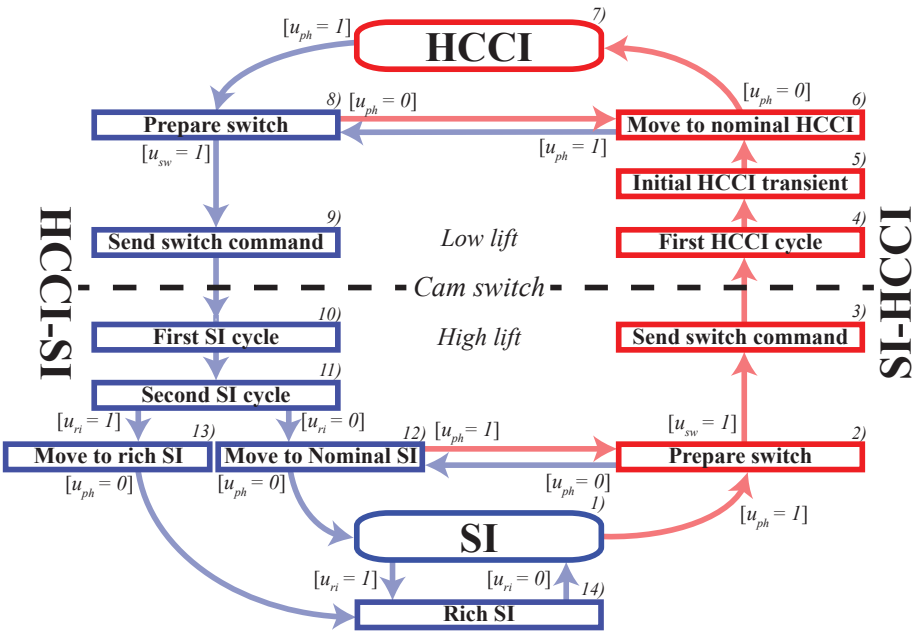

Figure 4.13: Extension of finite-state combustion mode switch model shown in Fig. 3.5. The model includes states under rich operating conditions to deplete the TWC's OSC. The finite states i are enumerated from 1 through 14. The model is subject to three control inputs u_{ph}, u_{sw}, and u_{ri}.

- In SI mode ($M = 1$), the state of the TWC, represented by R_{TWC} needs to allow a mode switch to HCCI. Therefore equation (3.7) is modified to:

$$u_{ph} = \begin{cases} 1 & R_{in} = \text{HCCI and } R_{TWC} = \text{HCCI} \\ 0 & \text{else.} \end{cases} \tag{4.38}$$

  Alternatively rich SI operation can be requested as well:

$$u_{ri} = \begin{cases} 1 & R_{TWC} = \text{rich SI} \\ 0 & \text{else.} \end{cases} \tag{4.39}$$

- During the SI-HCCI mode switch, $M \in (2-6)$, as well as in nominal HCCI mode, $M = 7$, (3.9) is modified to include the TWC constraints:

$$u_{ph} = \begin{cases} 0 & (R_{act} = \text{SI and } R_{in} = \text{SI}) \text{ or } R_{TWC} \neq \text{HCCI} \\ 1 & \text{else.} \end{cases} \tag{4.40}$$

  Therefore a mode switch back to SI can be initiated, e.g., in case of a drop in TWC temperature.
- At the beginning of the HCCI-SI switch, $M = 8$, the cams remain in prepared conditions as long as either both $R_{out,1}$ and $R_{out,2}$ or R_{TWC} demand SI mode.

Therefore equations (3.13) and (3.14) are extended such as:

$$u_{ph} = \begin{cases} 0 & R_{out,1} = \text{HCCI and } R_{out,2} = \text{HCCI and } R_{TWC} = \text{HCCI} \\ 1 & \text{else} \end{cases} \tag{4.41}$$

$$u_{sw} = \begin{cases} 1 & (R_{out,1} = \text{SI and } R_{out,2} = \text{SI}) \text{ or } R_{TWC} \neq \text{HCCI} \\ 0 & \text{else.} \end{cases} \tag{4.42}$$

- As mentioned in Sec. 3.3, upon entering high lift conditions, $M \in (10, 11)$, the engine will be operated rich to enable the TWC to reduce the increased levels of NO_x. This results in relatively high fuel penalties. After the first two SI-cycles, depending on R_{TWC}, it is decided to either continue to deplete the OSC, $M \in (13, 14)$ or to operate at stoichiometry, $M \in (12, 1)$. Alternatively, another switch to HCCI can be initiated. Therefore (3.15) is extended to:

$$u_{ri} = \begin{cases} 1 & R_{TWC} = \text{rich SI} \\ 0 & \text{else.} \end{cases} \tag{4.43}$$

$$u_{ph} = \begin{cases} 1 & R_{in} = \text{HCCI and } R_{TWC} = \text{HCCI} \\ 0 & \text{else.} \end{cases} \tag{4.44}$$

4.5.2 Fuel, Emissions, etc.

In the following paragraphs engine-out emissions, relative AFR, and exhaust gas temperature are defined for the different stages of the combustion mode switch. In addition the definitions for the fuel flow need to be extended to account for the additional states of the mode switch. Figures 4.14 and 4.15 show exemplary mode switches including the trajectories of some of the mentioned variables for visualization.

Fuel

As mentioned in Sec. 4.2 the fuel penalty due to rich operation is approximated to be linearly proportional to inverse of the relative AFR λ_e. During the reduction of the intake manifold pressure with rich AFR, $M = 13$, this penalty is added to the fuel penalty due to the modified EVC timing:

$$d_{13} = d_{12} + (\frac{1}{\lambda_e} - 1) \tag{4.45}$$

$$d_{14} = \frac{1}{\lambda_e} - 1. \tag{4.46}$$

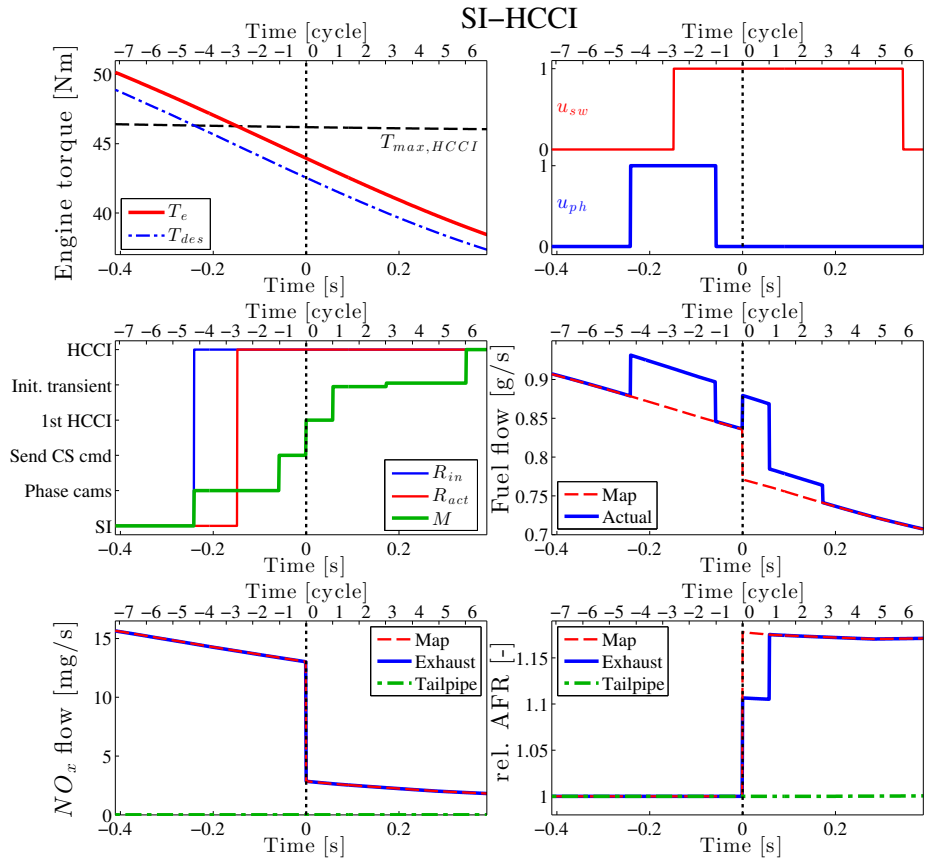

Figure 4.14: Exemplary SI-HCCI mode switch during simulation of the FTP75 drive cycle. The variables are plotted over time (bottom-axis) and engine cycles (top-axis). Engine speed is 2500 RPM.

The computation of the fuel flow from equation (3.6) is changed to incorporate the two additional finite states:

$$\dot{m}_f = \begin{cases} f_{f,SI}(\omega_e, T_e) & M = 1 \\ f_{f,HCCI}(\omega_e, T_e) & M = 7 \\ f_{f,SI}(\omega_e, T_e) \cdot (1 + d_i) & M \in (2, 3, 10 - 14) \\ f_{f,HCCI}(\omega_e, T_e) \cdot (1 + d_i) & M \in (4 - 6, 8, 9). \end{cases} \tag{4.47}$$

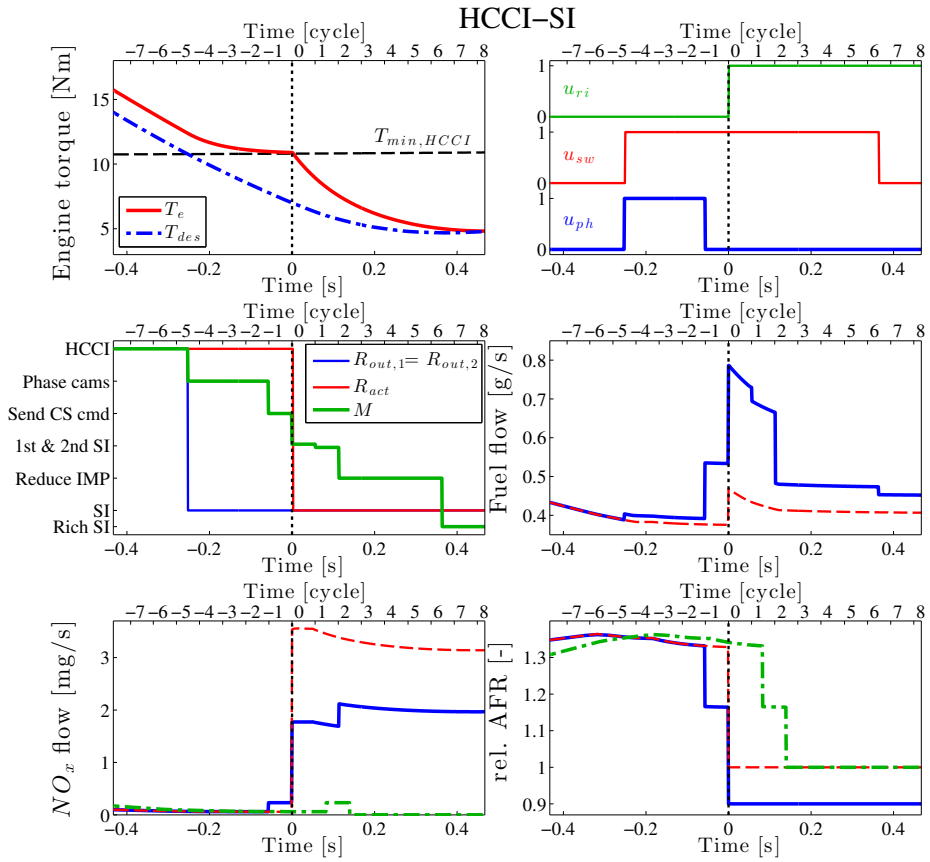

Figure 4.15: Exemplary HCCI-SI mode switch during simulation of the FTP75 drive cycle. The variables are plotted over time (bottom-axis) and engine cycles (top-axis). Engine speed is 2500 RPM.

Air-Fuel Ratio

The relative AFR during the mode switch is chosen as follows:

$$\lambda_e = \begin{cases} 1 & M \in (1-3, 12) \\ f_{\lambda,HCCI}(\omega_e, T_e) & M \in (5-8) \\ 0.9 & M \in (10, 11, 13, 14) \\ 0.6 \cdot f_{\lambda,HCCI}(\omega_e, T_e) + 0.4 & M = 4 \\ 0.5 \cdot f_{\lambda,HCCI}(\omega_e, T_e) + 0.5 & M = 9. \end{cases} \tag{4.48}$$

As can be seen in nominal SI mode as well as during preparation of the SI-HCCI mode switch the AFR is assumed to be exactly stoichiometric. In finite states, associated with low lift conditions, the AFR is determined using the steady-state map $f_{\lambda,HCCI}$. Exceptions are the last SI cycle and last HCCI cycle during the switches, where the

AFR is interpolated between stoichiometry and the HCCI map value. Finally, as discussed in Sec. 3.3, the applied mode switch strategy includes periods of rich operation immediately after the cam switch to allow OSC depletion.

Emissions

The engine-out NO_x emissions are determined by steady-state maps $f_{NO_x,SI}$ and $f_{NO_x,HCCI}$. The lack of oxygen in rich modes leads to a reduction in NO_x, shown in Fig. 4.4:

$$d_{r,NO_x}(\lambda_e = 0.9) = 0.63. \tag{4.49}$$

In addition, due to the low combustion temperature it is assumed that during the last HCCI cycle only small quantities of NO_x are produced. This assumption has the following impact: As can be seen in the example in Fig. 4.15, if the OSC is full this NO_x breaks through and reaches the tailpipe. However, the NO_x produced during the succeeding engine cycles are being reduced, since the engine is operated under rich conditions. Therefore, in this simulation the amount of NO_x in $M \in (10, 11)$ is not very relevant.

$$\dot{m}_{NO_x,e} = \begin{cases} f_{NO_x,SI}(T_e, \omega_e) & M \in (1-3, 12) \\ f_{NO_x,HCCI}(T_e, \omega_e) & M \in (4-8) \\ 0.05 \cdot f_{NO_x,SI}(T_e, \omega_e) + 0.95 \cdot f_{NO_x,HCCI}(T_e, \omega_e) & M = 9 \\ 0.5 \cdot f_{NO_x,SI}(T_e, \omega_e) & M \in (10, 11) \\ f_{NO_x,SI}(T_e, \omega_e) \cdot d_{r,NO_x} & M \in (13, 14) \end{cases} \tag{4.50}$$

Exhaust Gas Temperature

The engine exhaust gas temperatures are subject to first-order dynamics, as described in Sec. 2.2.4. It is assumed that the dynamics during the mode switch are too fast to affect exhaust gas temperature. Therefore the associated map for the forcing term $\bar{\vartheta}_{g,e}$ switches instantaneously, modifying equation (2.36) to:

$$\bar{\vartheta}_{g,e} = \begin{cases} f_{\vartheta,SI}(T_e, \omega_e) & M \in (1-3, 10-12) \\ f_{\vartheta,HCCI}(T_e, \omega_e) & M \in (4-9). \end{cases} \tag{4.51}$$

4.6 Depletion Strategies

To maximize fuel economy it is necessary to remain in the HCCI combustion mode for as long as possible while minimizing the total mode switch fuel penalty. On the other hand, running lean HCCI eventually fills up the OSC and stops the conversion of NO_x. Therefore the OSC must be depleted when returning to SI combustion by running the engine rich to avoid breakthroughs of the unacceptably high engine-out NO_x during SI operation. Of course, running rich SI leads to an additional penalization of fuel economy.

However, catalyst oxygen storage depletion might already be necessary before the operating regime of HCCI is left. To begin with, even though the NO_x emissions in HCCI are very low, summed up over an entire drive cycle they might be too high to fulfill very restrictive emissions requirements without aftertreatment. Furthermore, if NO_x spikes occur during HCCI to SI mode switches it is necessary to have some remaining OSC to maintain conversion efficiency during the switch. For those reasons the aftertreatment system could not only lead to a fuel economy penalty due to depletion but also because of premature cancellation of residences in HCCI mode.

Three depletion strategies are investigated in terms of fuel economy and NO_x emissions. They offer different alternatives to define R_{TWC}. A comparison of the strategies at an illustrative drive cycle situation is depicted in Fig. 4.16.

4.6.1 Strategy 0: No Oxygen Storage Dynamics (*NoO*)

The first option is more of an assumption than a strategy. Here it is assumed that the TWC does not exhibit any OSC dynamics. Specifically this means that during a mode switch from SI to HCCI the OSC fills up immediately, therefore not reducing any NO_x in HCCI. On the other hand, during a HCCI-SI mode switch the OSC is automatically depleted without requiring rich operation and therefore NO_x conversion efficiencies are restored instantaneously. For that reason in the definition of R_{TWC} only TWC temperature is considered:

$$R_{TWC} = \begin{cases} \text{stoich. SI} & \vartheta_{b,1} < \vartheta_{min} \\ \text{HCCI} & \text{else} \end{cases} \tag{4.52}$$

This is the baseline case, resulting in the same fuel economy values as presented in Chap. 3.

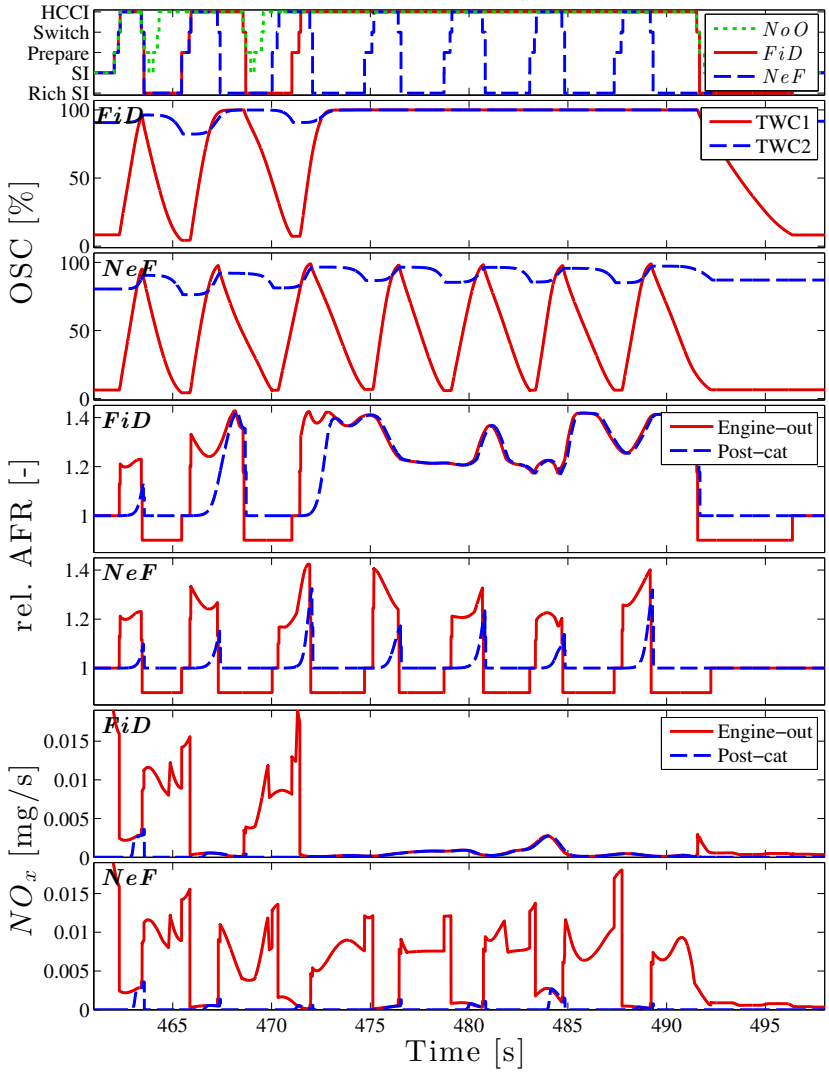

Figure 4.16: Comparison of depletion strategies *FiD* and *NeF* at an example time interval during the FTP75 drive cycle. Top: Currently active combustion mode. Intermediate modes from Fig. 3.5 summarized as Prepare and Switch. *NoO* (dotted green), *NeF* (dashed blue), and *FiD* strategy (solid red). Second and third: Comparison of OSC trajectories for the two strategies, TWC 1 (red) and TWC 2 (blue). Fourth and fifth: λ. Sixth and seventh. NO_x engine-out (red) and tail pipe (blue).

4.6.2 Strategy 1: Fill & Deplete after Mode Switch (*FiD*)

This strategy offers a compromise between fuel economy and emissions. A transition to rich SI is only demanded if the OSC is estimated to be full and the HCCI regime

is left, i.e., the cam switch to high lift already occured:

$$R_{TWC} = \begin{cases} \text{rich SI} & \tilde{\Theta} \geq 0.9 \text{ and } M \in (1-3, 10-13) \\ \text{stoich. SI} & \vartheta_{b,1} < \vartheta_{min} \\ \text{HCCI} & \text{else.} \end{cases} \tag{4.53}$$

Once $R_{TWC} = \text{HCCI}$ is commanded the engine remains in depletion mode until the OSC is empty:

$$R_{TWC} = \begin{cases} \text{rich SI} & \tilde{\Theta} > 0.1 \\ \text{stoich. SI} & \vartheta_{b,1} < \vartheta_{min} \\ \text{HCCI} & \text{else.} \end{cases} \tag{4.54}$$

As soon as this is the case, a mode switch back to HCCI becomes feasible again. This strategy leads to a fuel penalty due to the rich operation. However, it should not substantially reduce the total time spent in HCCI mode.

4.6.3 Strategy 2: Never Fill Oxygen Storage (*NeF*)

This strategy prohibits a completely full OSC to ensure conversion of potential engine-out NO_x spikes during mode switches. In any state M a depletion is demanded as soon as the OSC is full:

$$R_{TWC} = \begin{cases} \text{rich SI} & \tilde{\Theta} \geq 0.9 \\ \text{stoich. SI} & \vartheta_{b,1} < \vartheta_{min} \\ \text{HCCI} & \text{else.} \end{cases} \tag{4.55}$$

Again, the engine is operated rich until the OSC is detected to be depleted, as in equation (4.54). This strategy leads to the largest penalization in fuel economy due to the cancellation of residences in HCCI and the more frequent depletion phases. On the other hand, it should result in the lowest emissions.

4.7 Supervisory Strategies

The supervisory strategies used to control the SI/HCCI mode switching are described in detail in Sec. 3.4. In this chapter, two of these strategies are applied. The supervisor without any prediction *NoP* does not require any changes to incorporate the

different depletion strategies. The hypothetical *PeP* strategy, based on perfect load and speed prediction as well as a mode switching policy found with dynamic programming (DP), is used as benchmark. The *PeP* strategy requires modifications since the depletion of the OSC impacts the efficiency benefit of each residence in HCCI mode and therefore the optimal mode switching policy μ^*.

The DP algorithm, described in Sec. 3.4, is extended here to include the relative OSC Θ as additional state, discretized into 100 segments. Again the drive cycle simulation results, assuming instantaneous mode switches, were used for the calculation, sampled at 20 Hz. The state transitions for Θ from one time step to another are defined as:

$$\Delta\Theta_{SI} = 0 \tag{4.56}$$

$$\Delta\Theta_{HCCI} = \frac{0.23}{C_1} \int_t^{t+t_s} \dot{m}_{exh,e} \left(1 - \frac{1}{\lambda_{HCCI}}\right) dt \tag{4.57}$$

$$\Delta\Theta_{rich} = \frac{0.23}{C_1} \int_t^{t+t_s} \dot{m}_{exh,e} \left(1 - \frac{1}{0.9}\right) dt \tag{4.58}$$

for SI, HCCI, and rich operation, with sampling time t_s. Of course the associated depletion strategy applies. The resulting policy $\mu^*(t, \Theta)$ denotes which HCCI visitations are beneficial for fuel economy.

4.8 Drive Cycle Results

The depletion strategies introduced above are applied in the simulation of FTP75, HWFET, and US06 drive cycles and compared to the SI-only case. First the results for fuel economy and NO_x emissions are analyzed. Then the influence of temperature is discussed.

4.8.1 Fuel Economy

Fuel economy and other results are plotted in Fig. 4.17. In addition to comparing the performance of the three depletion strategies, also instantaneous mode switches as well as the supervisory strategies without prediction and with perfect prediction are applied, *NeF* and *PeP*, respectively, as discussed in the previous section.

It can be seen that the fuel penalties due to mode switches and depletion have significant impact on fuel economy. Even if instantaneous mode switches or per-

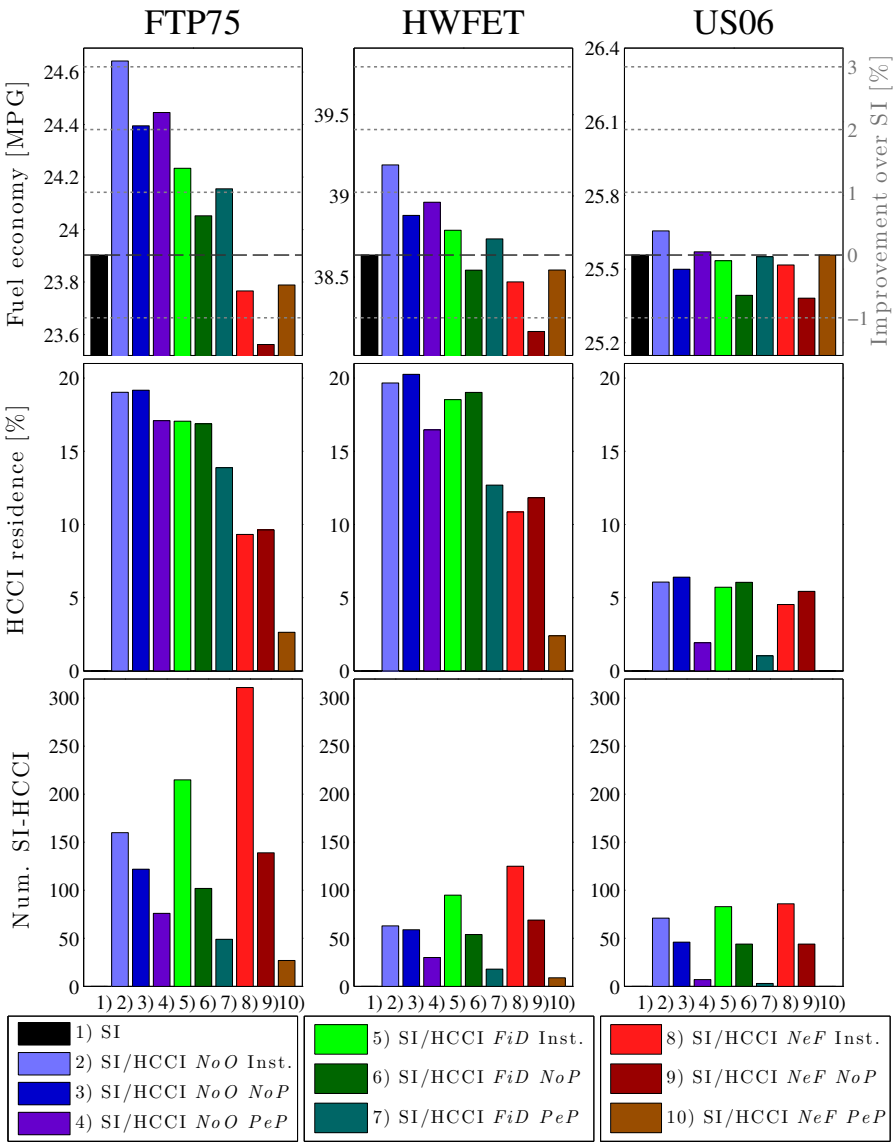

Figure 4.17: Drive cycle simulation results for FTP75 (left column), HWFET (center column), and US06 (right column). Top row: Fuel economy in MPG. Middle row: Total residence time in HCCI mode relative to drive cycle duration. Bottom row: Number of cam switches in SI-HCCI direction. Three different oxygen storage depletion strategies are compared, *NoO* (blue), *FiD* (green), and *NeF* (red), for instantaneous (light) and penalized mode switches using the *NoP* and *PeP* strategies (dark).

fect knowledge are assumed, it is apparent that the potential fuel economy benefits from using HCCI vanish as soon as lean-rich cycling and succeeding OSC depletion phases are required. Compared to the *NoP* strategy, *PeP* is able to improve performance significantly, sometimes outperforming the instantaneous switches. However, for FTP75 and HWFET and the *NeF* depletion strategy, *PeP* still results in a worse

fuel economy than SI-only. Therefore, the mode switching policy found, using dynamic programming assuming simplified mode switching and TWC dynamics, is not accurate enough for those cases. As can be seen, the *PeP*-strategy reduces the time spent in HCCI virtually to zero. It can be concluded that residences in HCCI are basically never beneficial for fuel economy, especially if the *NeF* strategy is applied.

4.8.2 NO_x Emissions

The results for NO_x emissions are shown in Fig. 4.18. Since the *PeP*-strategy is only hypothetical it is omitted here. As expected, the SI-only case leads to the highest **engine-out** NO_x. However, overall the difference between the strategies is relatively small, since SI is in any case the predominant mode. This might change if NO_x spikes during mode switches need to be considered. Those would especially increase the average engine-out NO_x for the *NeF* strategy, due to the high number of mode switches.

The SI-only case leads to the lowest **tailpipe** NO_x results due to the assumption of exactly stoichiometric combustion and close-to-perfect TWC conversion efficiency. Shown is the LEV II SULEV limit of $20\,{}^{\mathrm{mg}}/_{\mathrm{mi}}$ average tailpipe NO_x emission during the FTP75 drive cycle. As can be seen, all the results are far higher than this limit. However, a large fraction of tailpipe NO_x emissions during the FTP75 drive cycle are the result of the engine cold start during the first phase, when the TWC's temperature is below light-off. This amount of NO_x could be reduced by tuning the cold start strategy, which is beyond the scope of this dissertation. To have a chance at passing low emissions regulations, it needs to be ensured that the HCCI operation does not lead to significant additional tailpipe NO_x. As can be seen, the *NoO* strategy without any oxygen storage dynamics leads to the highest NO_x emissions. The use of the *FiD* depletion strategy leads to a reduction in tailpipe NO_x emissions since now the OSC dynamics are considered, being able to convert the initial NO_x in each HCCI residence. However, as can be seen even though in this analysis a TWC with generous OSC is considered, it is unable to maintain NO_x conversion efficiency for significant amount of time while operating lean. The resulting NO_x due to HCCI operation alone is still as high as the SULEV limit. In case of the *NeF* strategy the amount of additional NO_x is smaller, since less time is spent in HCCI mode while the OSC is being depleted more often. This, however, leads to prohibitive fuel penalties as discussed above.

"The quantitative results need to be treated with caution. As mentioned a large

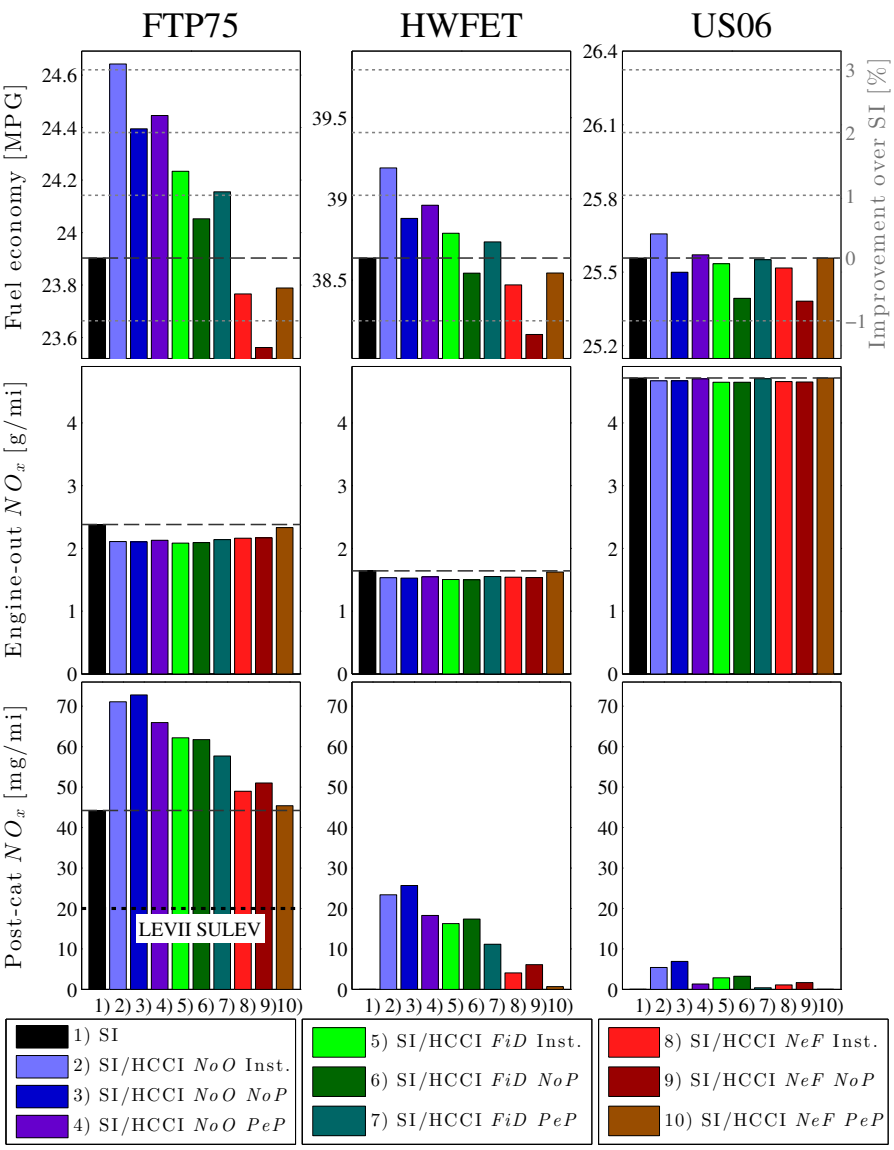

Figure 4.18: Drive cycle simulation results for FTP75 (left column), HWFET (center column), and US06 (right column). Top row: Fuel economy. Middle row: Engine-out NO_x per distance. Bottom row: Tailpipe NO_x per distance. Three different oxygen storage depletion strategies are compared, NoO (blue), FiD (green), and NeF (red), for instantaneous (light) and penalized mode switches using the NoP strategy (dark). Results are compared to LEV II SULEV limit 20 $^{\text{mg}}/_{\text{mi}}$ (dotted black).

number of assumptions and simplifications were applied in the process. The oxygen storage model is very simple, neglects temperature, composition, non-equilibrium effects, etc. and was only locally parameterized. If operating conditions are found under which the OSC could be depleted at lower fuel cost, the penalty of lean-rich cycling would decrease. In addition, the performance of HCCI could be more fuel beneficial than stated, if its operating regime can be enlarged and its engine-out emissions at

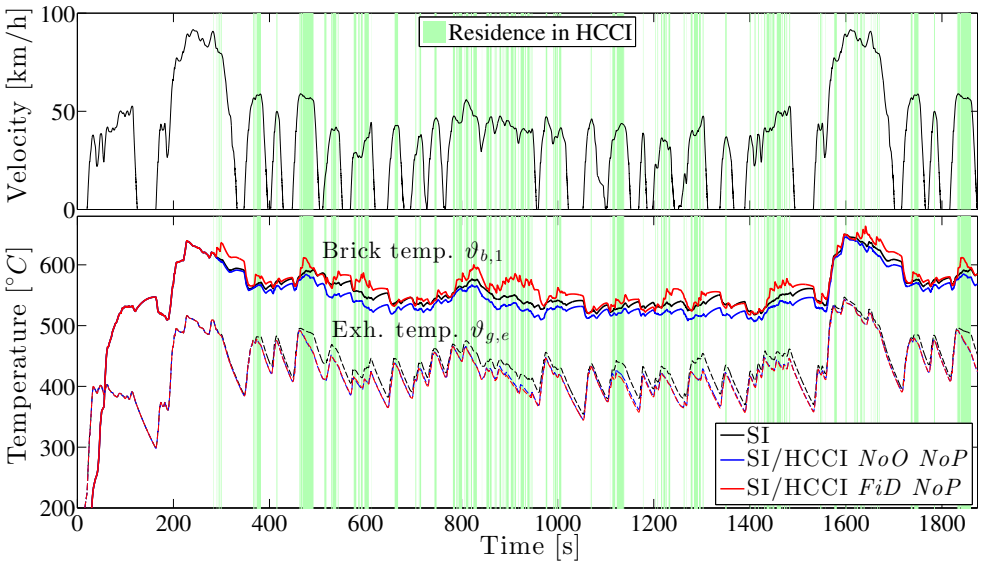

Figure 4.19: Temperature trajectories during simulation of the FTP75 drive cycle. Top: Velocity. Bottom: TWC brick temperature (thick) and engine exhaust gas temperature (thin). SI-only (black), supervisory strategy *NoP* with depletion strategy *NoO* (blue) and *FiD* (red). Green backgrounds represent residence in HCCI mode, specifically at low-lift.

higher loads reduced. This would extend the duration per stay in HCCI mode. Also, if it is possible to conduct a combustion mode switch in a shorter amount of time and with lower fuel and NO_x penalties than assumed here, a higher number of mode switches would have a less harmful effect on overall fuel economy." [2] However, many effects which potentially increase NO_x have also not been considered. For example transient effects and possible NO_x spikes generally lead to an increase in engine-out NO_x. Furthermore, imperfect AFR-control and deviations from stoichiometry in SI mode result in a decrease in conversion efficiency. In addition, it always have to be kept in mind that large quantities of NO_x are being produced during engine cold start. Finally, the LEV II SULEV limit does not only consider NO_x by itself but $NO_x + NMOG$, which is even more stringent. Together with the large penalty in fuel economy it can be concluded that a TWC aftertreatment system with large OSC is not suited for low emissions in a SI/HCCI multimode context and requires significant engine rich operation that reduces fuel efficiency.

4.8.3 Influence of Temperature

As discussed in [11], subjecting the TWC to low HCCI exhaust gas temperatures for extended periods of time can lead to cool-down of the TWC. This in turn results in a decrease in its conversion efficiency for HC and CO emissions. For that reason the previously discussed results include simulation of the TWC temperature. The resulting trajectories for exhaust temperature $\vartheta_{g,e}$ and brick temperature of the close-coupled TWC $\vartheta_{b,1}$ during FTP75 are shown in Fig. 4.19. The baseline SI-only case is compared to the multimode engine applying the supervisory strategy without prediction NoP. In addition, it is distinguished between no OSC dynamics NoO and OSC depletion FiD. Note that the applied TWC temperature model is strongly simplified by only including two dynamic states. However, this section should give an idea about how strong the influence of temperature on HCCI's performance is.

As can be seen in Fig. 4.19, the difference in exhaust temperature between the SI-only and the SI/HCCI cases is always smaller than 35 °C and therefore HCCI operation results only in a small reduction in $\vartheta_{g,e}$. The reason is the very short uninterrupted residence time in HCCI mode. In consequence, in case of NoO also the drop in TWC brick temperature is small and far away from light-off temperature. In addition, when looking at the FiD case it can be seen that depleting the OSC actually results in an increase in brick temperature. This is due to the large amount of engine-out HC and CO emissions during rich operation, resulting in exothermic oxidation reactions in the TWC brick. Therefore it is concluded here, that with the given multimode engine hardware, residence time in HCCI mode is too short to result in problematic cooling of the TWC. However, for a more detailed and final analysis a TWC model of higher order needs to be applied.

4.9 Summary

This chapter discusses the interaction between a SI/HCCI multimode engine and a TWC aftertreatment system in terms of drive cycle fuel economy and NO_x emissions. The use of a TWC is desirable due to its relatively low cost. The TWC hardware used in this study is designed to have a generous oxygen storage capacity to allow extended NO_x conversion while operating under lean HCCI conditions. The dynamics of the TWC's oxygen-storage are captured with a phenomenological model and parameterized with mode switching experiments. It is seen that a great fuel penalty arises from the requirement of depleting the catalyst's oxygen storage by running the

engine rich.

Three illustrative TWC depletion strategies are compared, each targeting a different trade-off between fuel economy and emissions. The first strategy assumes no oxygen storage dynamics, as has been done in prior SI/HCCI fuel economy studies. The second strategy depletes a full oxygen storage after each residence in HCCI regime. The third strategy is even more stringent by forcing a mode switch back to SI as soon the oxygen storage is full. It is shown that subsequent depletion of the oxygen storage negates the fuel economy benefits gained during efficient HCCI operation. Furthermore, low emissions standards for NO_x are not robustly secured.

An additional interaction between HCCI combustion and TWC is caused by the exhaust temperature. It was seen in previous work that prolonged low temperature HCCI combustion leads to a decrease in TWC brick temperature, resulting in an unacceptable drop in HC conversion efficiency. To account for this interaction in this study, a simple two-state TWC temperature model is presented and validated with drive cycle experiments. It is seen, that with the applied multimode engine and its small HCCI regime, low temperature operation is too short and interrupted too frequently to have a significant effect on TWC temperature. In addition, running the engine rich to deplete the oxygen storage results in large quantities of HC and CO being oxidized in the TWC. This exothermic reaction results in a temperature increase and reduces HCCI's cooling effect.

Chapter 5

Multimode Combustion in a Mild HEV

The majority of the contributions presented in following chapter have been submitted in [102] as well as in [100] and [101]:

IFAC Control Engineering Practice
submitted, *Multimode Combustion in a Mild HEV*
Part 1: Supervisory Control and Synergies and
Part 2: Three-Way Catalyst Considerations
S. Nüesch and A.G. Stefanopoulou.

A new generation of mild hybrid electric vehicles (HEV) are based on 48 V-systems that rely on relatively small electric motors and batteries. Such vehicles are shown to offer significant benefits in fuel economy [150], due to their start/stop and regenerative braking capabilities. Concurrently, due to the low voltage and the small sizes of electric machine and battery, the cost of this architecture is relatively low. Furthermore, due to increasing numbers of comfort and safety features in the vehicle, electric auxiliary load demands are predicted to exceed the limits of the current 12 V-standard, making a widespread switch to a 48 V-standard even more probable.

As discussed in Chap. 3, a major disadvantage of the SI/HCCI multimode engine is the small HCCI operating regime, which leads to short residence times in the beneficial mode, as well as a large number of combustion mode switches. One way to address this issue is the integration of the multimode engine in a HEV. The electric motor as second power source offers more freedom in choosing the engine's operating point. Therefore, the residence time in HCCI mode can potentially be extended significantly while reducing the need for mode switching. Different HEV architectures in combination with advanced combustion modes have been discussed in previous simulation studies [90–93]. When comparing the fuel economy of different HEV ar-

chitectures, Delorme et al. [90] concluded that, the higher the level of hybridization, the smaller the synergy between the multimode engine and the electric system.

The following chapter discusses the multimode engine operation in a mild HEV. The combination of a SI/HCCI multimode engine and 48 V mild HEV could offer significant fuel economy synergies at relatively low cost. The work presented here exceeds previous work on this topic by taking into account the dynamics and penalties associated with combustion mode switching. The mode switching affects the final fuel economy result, and it also needs to be considered in the supervisory control strategy of the HEV. In the following chapter, four alternative implementations of supervisory strategies are presented and analyzed in terms of fuel economy benefits, synergies, and NO_x emissions. Furthermore, the study in Chap. 4, concerning the interaction between multimode engine and TWC is continued. In two case studies, modifications to the system hardware and the mode switching strategy are introduced and their impact on fuel economy and NO_x emissions is discussed.

5.1 Mild HEV Model

The model of the conventional vehicle[1] is described in Chap. 2. The following section extends this model to a mild HEV. This includes the models for electric motor and battery, as well as the corresponding control strategy equivalent consumption minimization strategy (ECMS).

5.1.1 Integrated Starter-Generator (ISG)

In this dissertation the electric motor used is a belt-driven integrated starter-generator (ISG). The ISG with a maximum continuous power of 5 kW boost and 14 kW regeneration represents a small e-machine as seen upcoming in 48 V-systems. A belt-ratio of $\gamma_b = 2.5$ is used to connect engine and ISG. The efficiency map f_m of the belt-driven ISG is based on steady-state data. It is used to compute the electric power of the

[1] Conventional vehicle is here defined as a vehicle only using an ICE-based powertrain without any electric hybridization.

motor $P_{m,el}$ as a function of mechanical power P_m and ω_m:

$$\omega_m = \gamma_b \cdot \omega_e \tag{5.1}$$

$$P_m = T_m \cdot \omega_m \tag{5.2}$$

$$P_{m,el} = f_m(P_m, \omega_m). \tag{5.3}$$

As described in Sec. 2.2.2, in case of the conventional vehicle the ISG simply operates as alternator to deliver power for electric auxiliaries. In case of the mild HEV the ISG offers additional functionalities for start/stop operation, torque assist, and regenerative braking. The ISG dynamics are modeled as a first-order system, as shown in equation (2.30). The control input to the ISG is the corresponding torque command u_m. While for the conventional vehicle u_m was computed based on the electric auxiliary power, here it is defined as the sum of the individual commands for each of the ISG's functionalities:

$$u_m = u_{m,al} + u_{m,c} + u_{m,r} \tag{5.4}$$

with $u_{m,al}$ to satisfy the alternator load, $u_{m,c}$ for torque assist, and $u_{m,r}$ for regenerative braking. The three functionalities are described in more detail in the following paragraphs.

Electric Auxiliaries

To satisfy the power demand of the electric auxiliaries $u_{m,al}$ is defined as:

$$u_{m,al} = -\frac{f_m^{-1}(\omega_m, P_{al})}{\omega_m}. \tag{5.5}$$

See Sec. 2.2.2 for more details on the alternator-operation of the ISG.

Torque Assist

The optimal torque-split between engine and ISG is computed by the ECMS, described in Sec. 5.1.3. Due to this optimization in general $u_e \neq T_{des}$, resulting in torque gaps which need to be filled by the ISG. The time constant of the ISG τ_m is an order of magnitude faster than time constant of the engine τ_e. In addition, the goal is to compare the performance of the HEV powertrain to the conventional vehicle without changing the combined response of engine and ISG. For that reason the time

constant of the engine is used to filter the desired driver torque T_{des} and to compute $\widetilde{T}_e$, which represents the virtual engine torque the driver expects, if he was used to the torque response of the conventional vehicle and SI-only engine:

$$\frac{d}{dt}\widetilde{T}_e = \frac{1}{\tau_e}(T_{des} - \widetilde{T}_e). \tag{5.6}$$

The ISG is used to compensate for the gap between virtual and actual engine torque, $\widetilde{T}_e$ and T_e, respectively. The associated torque command to the ISG $u_{m,c}$ is defined as:

$$u_{m,c} = \frac{1}{\gamma_b}(\widetilde{T}_e - T_e). \tag{5.7}$$

This definition automatically also applies when compensating for torque gaps, e.g., due to torque saturations at the limits of the HCCI regime (5.23).

Regenerative Braking

The model of the regular friction brake is described in Sec. 2.1.3. If regenerative braking is inactive, $u_{m,r} = 0$, and the nominal computation of u_b is used. Regenerative braking is activated if the brake pedal u_b is pressed while the clutch pedal $u_c = 0$. If active the ISG is used to generate as much power as possible while matching the brake torque demand:

$$u_{m,r} = \max\{-\frac{u_b \cdot T_{b,max}\eta_g}{\gamma_b\gamma_{fdr}\gamma_g}, T_{m,min} - u_{m,al} - u_{m,c}\}. \tag{5.8}$$

The limit of the regenerative braking operation depends thereby on the maximum generation torque of the ISG $T_{m,min}$ as well as the torque demands of the electric auxiliaries and the torque assist. The net braking torque on the wheels is maintained by reducing the value of the torque command u_b accordingly, resulting in an overwritten command $\hat{u}_b$:

$$\hat{u}_b = -\frac{u_b T_{b,max} + u_{m,r}\gamma_b\gamma_{fdr}\gamma_g}{\eta_g T_{b,max}(n_{t,n} + n_{t,d})} \tag{5.9}$$

The regenerative braking events during the three drive cycles are highlighted in Fig. 5.1.

5.1.2 Battery

The total power drawn from the battery consists of the auxiliary load P_{al} and the ISG $P_{m,el}$:

$$P_b = P_{al} + P_{m,el}. \tag{5.10}$$

The battery is described by an equivalent circuit model with I_c and U_c, cell current and voltage, respectively [107].

$$U_c = U_{OC}(\xi) - \zeta_i(\xi, I_c) \cdot I_c \tag{5.11}$$

$$I_c = \frac{P_b}{n_s n_p U_c} \tag{5.12}$$

The battery consists of $n_p = 1$ cells in parallel and $n_s = 14$ in series, each cell with a capacity of $Q_c = 5\,\mathrm{Ah}$. The open-circuit voltage U_{OC} and the internal resistance ζ_i are implemented as look-up tables based on steady-state data. They are functions of the battery's state-of-charge (SOC) ξ and, in case of ζ_i, the direction of I_c. The battery's only state SOC is modeled assuming coulomb-counting [107]:

$$3600\,\mathrm{s/h} \cdot Q_c \frac{d}{dt}\xi = -I_c. \tag{5.13}$$

The influence of battery temperature on U_{OC} and R_i is neglected.

5.1.3 Adaptive ECMS

The equivalent consumption minimization strategy (ECMS) is a widely applied method to achieve the close-to-optimal fuel economy of a HEV while maintaining battery SOC [107]. Due to its low computational complexity it can implemented to run in real-time. At each time step the torque split between engine and ISG is determined which minimizes the instantaneous equivalent power consumption:

$$J(x_T) = P_f(x_T) + \alpha \cdot P_c(x_T) \tag{5.14}$$

$$x_T^* = \arg\min_{x_T \in X} \; J(x_T). \tag{5.15}$$

The argument of the minimization is engine torque x_T, constrained to the space of admissible controls X, which is mainly based on the limits of the current combustion

mode M, SI or HCCI, and the limits of the ISG:

$$X = \{x_T \mid T_{min}(M) \leq x_T \leq T_{max}(M) \text{ and } \ldots \tag{5.16}$$

$$T_{m,min} \leq \hat{T}_m(x_T) \leq T_{m,max}\}. \tag{5.17}$$

$P_f(x_T)$ and $P_c(x_T)$ are the power released by the burned fuel and by the battery cells, respectively, as a function of engine torque. Co-state α represents the equivalence factor, used to compare the two power sources and thereby maintaining SOC close to its reference. $\hat{T}_m(x_T)$ is the required motor torque to fulfill the driver's demand as function of argument x_T.

Equivalence Factor

Various approaches are described in literature on how to determine the equivalence factor α. Onori and Serrao [151] compare several adaptive methods, in which α is defined as a function of battery SOC ξ. In this paper the approach by Chasse et al. [152] is used, in which a PI controller modifies α to track a reference SOC ξ_{ref}, in this case $\xi_{ref} = 50\%$:

$$\alpha = K_{p,ECMS} \cdot (\xi_{ref} - \xi) + \underbrace{K_{i,ECMS} \cdot \int (\xi_{ref} - \xi) dt}_{\alpha_I}. \tag{5.18}$$

The closed-loop system was linearized to tune the controller gains $K_{p,ECMS} = 20$ and $K_{i,ECMS} = 0.5$.

Similar to [153] the drive cycles were simulated repeatedly to ensure the final SOC to be close to the initial SOC. The drive cycle trajectories of motor power P_m, equivalence factor, and SOC are plotted in Fig. 5.1.

Computation of Equivalent Power

The chemical power of the fuel is computed using the steady-state maps of the two combustion modes:

$$P_f(x_T) = H_f \cdot \dot{m}_f(x_T, M) \tag{5.19}$$

$$\dot{m}_f(x_T, M) = \begin{cases} f_{SI}(x_T, \omega_e) & M = \text{SI} \\ f_{HCCI}(x_T, \omega_e) & M = \text{HCCI} \end{cases} \tag{5.20}$$

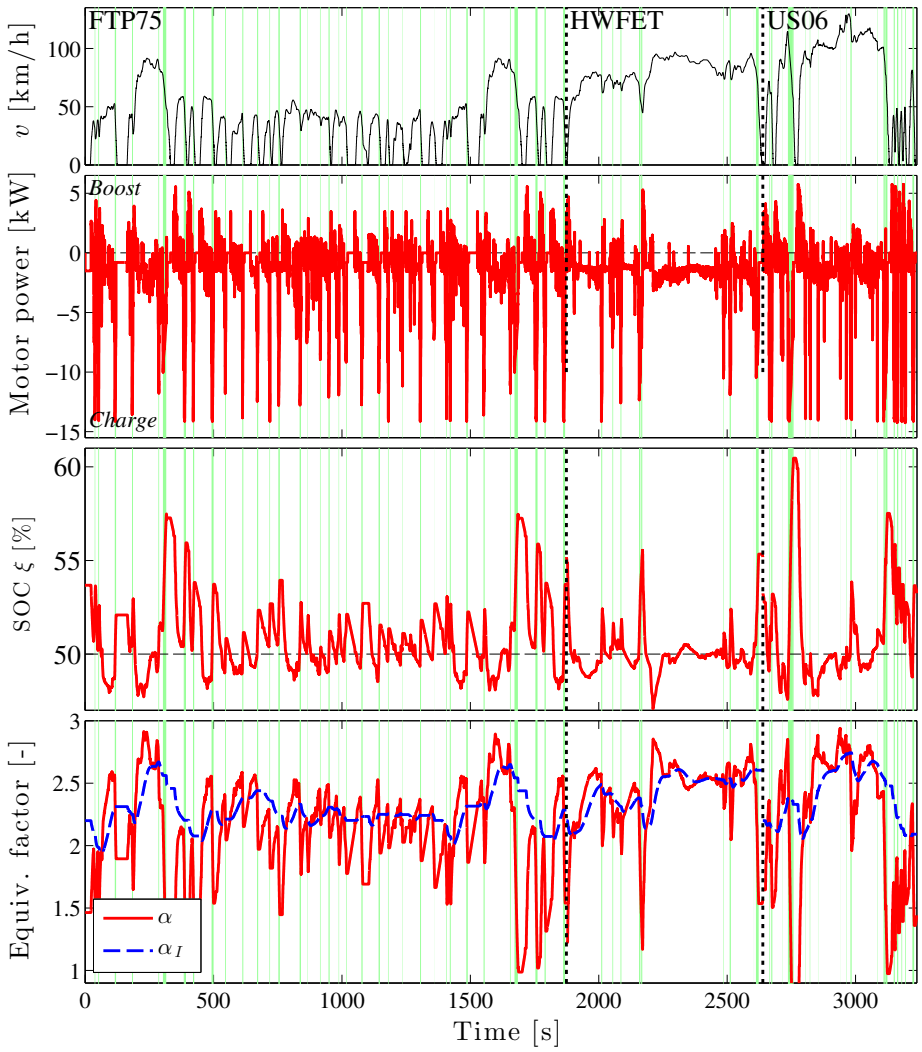

Figure 5.1: Trajectories of the SI-only HEV during the simulation of the three drive cycles. Top: Velocity v. Second: Motor power P_m. Third: Battery SOC ξ. Bottom: Equivalence factor α (solid red) and its integral part α_I (dashed blue). Time periods allowing for regenerative braking are highlighted green.

with lower heating value of gasoline H_f. The gap between desired torque T_{des} and engine torque argument x_T needs to be compensated by the ISG. The resulting motor torque argument $\hat{T}_m(x_T)$ is constrained by the limits of the ISG via space X and takes into account the load demanded by the electric auxiliaries $u_{m,al}$, as defined in Sec. 5.1.1.

$$\hat{T}_m(x_T) = u_{m,al} + \frac{1}{\gamma_b}(T_{des} - x_T) \tag{5.21}$$

Equations (5.2) - (5.10) are applied to compute current in the battery cells $\hat{I}_c(x_T)$ from $\hat{T}_m(x_T)$. Ultimately, the power released by the battery cells $P_c(x_T)$ follows as:

$$P_c(x_T) = n_p \cdot n_s \cdot \hat{I}_c(x_T) \cdot U_{OC}(\xi). \tag{5.22}$$

5.1.4 Engine Torque Command

In case of the conventional vehicle, equation (3.17) was used to compute engine torque command u_e from desired torque T_{des}. However, when simulating the HEV, the optimum engine torque x_T^*, the result of the ECMS described in Sec. 5.1.3, needs to be considered in the corresponding function:

$$u_e = f_{sat}(x_T^*, M). \tag{5.23}$$

5.2 Supervisory Control Strategies

The ECMS, described in Sec. 5.1.3, controls the torque-split between engine and ISG for the mild HEV with a SI-only engine. However, if a multimode engine is used, the selection of the combustion mode represents an additional degree of freedom. As discussed in Chap. 3, associated mode switching dynamics and penalties need to be considered in the control strategy. Therefore, on top of the nominal ECMS a supervisory controller is required, which makes the mode switching decision. In the following section four supervisory control strategies for SI/HCCI mode switching in a mild HEV are described. The first strategy can be applied in both the conventional vehicle and the mild HEV. The remaining three strategies rely on the torque assist by the ISG. An exemplary residence in HCCI mode is shown in Fig. 5.2 to compare the four supervisors. The discretization within the ECMS computation results in the steplike behavior in engine torque T_e. The block diagrams of the supervisors are depicted in Fig. 5.3.

5.2.1 Strategy 1: No Prediction (*NoP*)

The first supervisory control strategy *NoP* is discussed in detail in Sec. 3.4 and is here used as baseline. It prepares the SI-HCCI mode switch as soon as T_{des} enters the HCCI regime, as can be seen in Fig. 5.2 at $t = 378.6\,\mathrm{s}$. The cams are switched to low

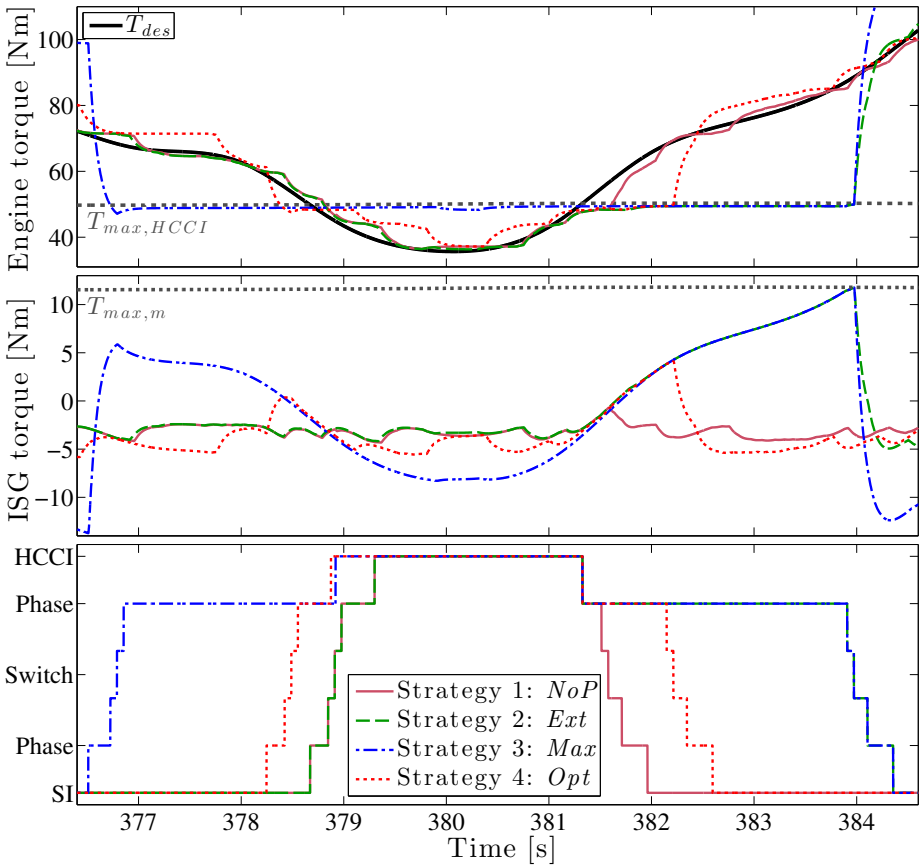

Figure 5.2: Exemplary residence in HCCI mode during the HWFET cycle to compare the four supervisory strategies *NoP* (solid brown), *Ext* (dashed green), *Max* (dash-dotted blue), and *Opt* (dotted red). Top: Engine torque with desired torque T_{des} (solid black). Middle: ISG torque T_m. Bottom: Combustion mode M.

lift once the valves reach their switching positions and T_e enters the HCCI regime. Conversely, in the HCCI-SI direction the mode switch is prepared when T_{des} exits the HCCI regime, in Fig. 5.2 at $t = 381.3\,\mathrm{s}$. The cam switch to high lift is initiated, if T_{des} still lies outside the HCCI boundaries by the time the valves reach their switching position.

The *NoP* strategy can be used in the conventional vehicle, as done in Chap. 3, and in the HEV. As can be seen in Fig. 5.2, when applied in the mild HEV, this strategy does not attempt to extend the residence time in HCCI mode. However, additional benefits in fuel economy are possible, since ECMS exploits high efficiency areas within the HCCI regime. Depending on the applied vehicle, conventional or hybrid electric, the commanded engine load u_e is determined by (3.17) or (5.23), respectively.

As described in Sec. 3.5, $T_{min,HCCI}$ and $T_{max,HCCI}$ could be altered to modify $R_{out,2}$ with the goal to trade-off drivability with fuel economy. Alternatively, also dis-

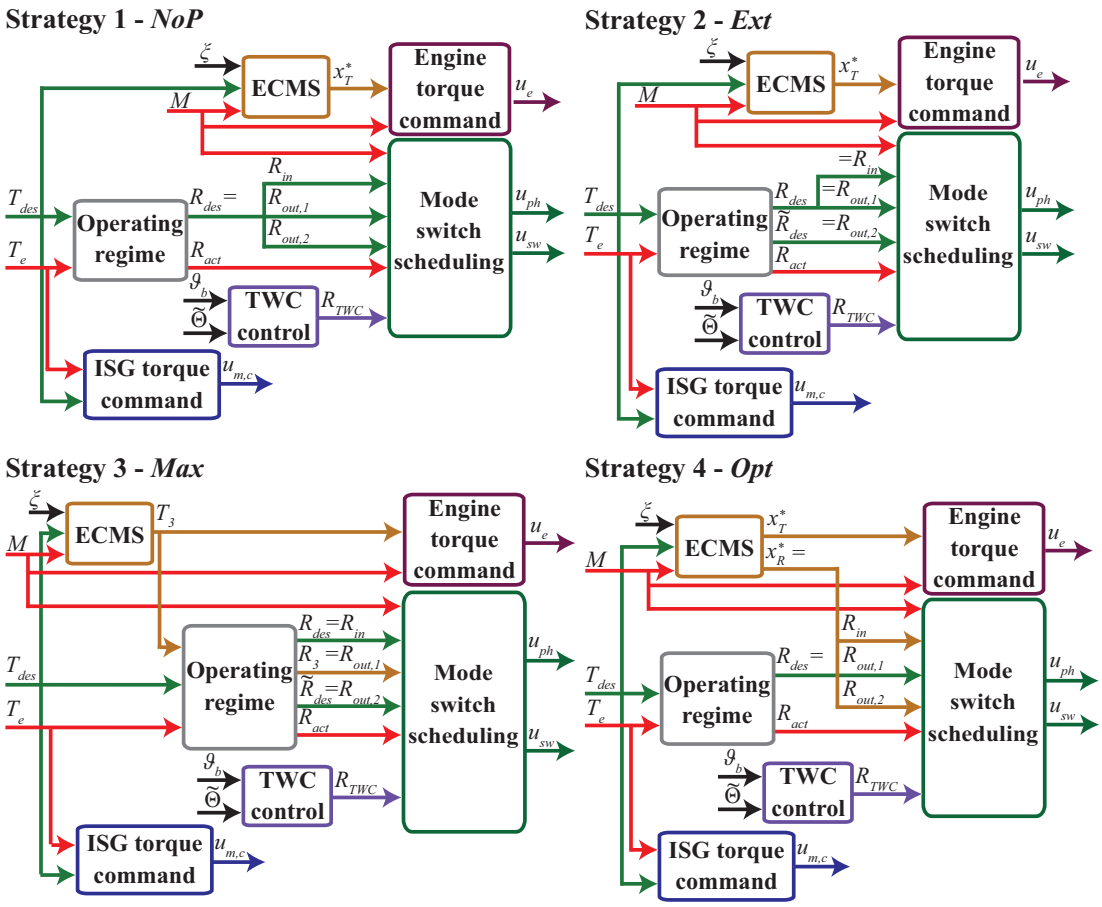

Figure 5.3: Block diagrams of the four supervisory control strategies.

cussed in Sec. 3.5, prediction could be used to improve the controller's performance by anticipating upcoming entries and exits of the HCCI regime.

5.2.2 Strategy 2: Extended Stay (*Ext*)

The second supervisory strategy *Ext* aims to improve fuel economy by extending the residence time in HCCI while reducing the number of mode switches. The ISG is used to create a virtual HCCI regime, which is composed of the actual HCCI limits and the ISG's torque range:

$$\widetilde{T}_{min,HCCI} = T_{min,HCCI} + \gamma_b \cdot (T_{max,m} - u_{m,al}) \tag{5.24}$$

$$\widetilde{T}_{max,HCCI} = T_{max,HCCI} - \gamma_b \cdot (u_{m,al} - T_{min,m}). \tag{5.25}$$

The virtual HCCI regime accounts for the ISG torque required to power the electric auxiliaries $u_{m,al}$. As in strategy *NoP* a mode switch from SI to HCCI is commanded if

T_{des} enters the HCCI regime. However, in case of strategy *Ext*, if T_{des} exits the actual HCCI regime the engine torque command u_e saturates at the HCCI limits while the ISG is used to bridge the gap between engine torque T_e and desired torque T_{des}. At the same time the valves are phased to their target switching position. Therefore, once the desired torque exits the virtual HCCI regime, the cam switch command can be sent and the HCCI-SI mode switch executed immediately, shown in Fig. 5.2 at $t = 384\,\mathrm{s}$.

$$R_{in} = R_{out,1} = R_{des} = f_R(T_{des}, T_{min,HCCI}, T_{max,HCCI}) \tag{5.26}$$

$$R_{out,2} = \tilde{R}_{des} = f_R(T_{des}, \widetilde{T}_{min,HCCI}, \widetilde{T}_{max,HCCI,m}) \tag{5.27}$$

Remaining at a valve position, which allows an immediate switch while still being in the virtual HCCI regime, has the advantage of a minimum delay in total propulsion torque once the driver desires to accelerate. The disadvantage, on the other hand, is a small reduction in engine efficiency since over prolonged time HCCI mode is operated with under conditions different from their nominal setpoint.

Similar to the SI-only case, with strategy *Ext* the torque command to the engine u_e is determined by ECMS and x_T^* (5.23).

5.2.3 Strategy 3: Maximum Stay (*Max*)

The strategy above is modified to extend the residence time in the HCCI regime even further. Strategy *Max* uses the ISG to both delay switches from HCCI to SI and also shift the engine load to the HCCI regime preemptively, shown in Fig. 5.2 at $t = 376.7\,\mathrm{s}$. If T_{des} enters a band above and below the actual HCCI regime, the load is forced into the regime. The lower band was chosen between $T_{min,HCCI}$ and $0\,\mathrm{Nm}$. The width of the upper band is determined by parameter $\Delta T \in (0\,\mathrm{Nm}, \gamma_b(T_{max,m} - u_{m,al}))$. The smaller the value of ΔT the more aggressive the strategy. Strategy *Ext* can be implemented by selecting $\Delta T = \gamma_b(T_{max,m} - u_{m,al})$. Here $\Delta T = 15\,\mathrm{Nm}$ was chosen. The intermediate torque command T_3 follows then as:

$$T_3 = \begin{cases} T_{min,HCCI} & 0 < T_{des} < T_{min,HCCI} \\ T_{max,HCCI} & T_{max,HCCI} < T_{des} < \tilde{T}_{max,HCCI} - \Delta T \\ x_T^* & \text{else.} \end{cases} \tag{5.28}$$

The mode switch in HCCI-SI direction is controlled in the same fashion as in strategy *Ext*:

$$R_{in} = R_3 = f_R(T_3, T_{min,HCCI}, T_{max,HCCI}) \tag{5.29}$$

$$R_{out,1} = R_{des} = f_R(T_{des}, T_{min,HCCI}, T_{max,HCCI}) \tag{5.30}$$

$$R_{out,2} = \tilde{R}_{des} = f_R(T_{des}, \widetilde{T}_{min,HCCI}, \widetilde{T}_{max,HCCI}). \tag{5.31}$$

This strategy requires modification of the engine torque to move to the HCCI regime. Therefore, here the torque command u_e is based on T_3 instead of x_T^*:

$$u_e = f_{sat}(T_3, M). \tag{5.32}$$

5.2.4 Strategy 4: Optimal Stay (*Opt*)

Instead of making a rule-based decision about when to enter or exit HCCI mode, as done in the supervisors shown above, strategy *Opt* integrates this decision into the ECMS control structure.

Equation (5.15) is replaced with the following minimization to determine the optimal torque split x_T^* together with the currently optimal combustion mode x_R^*:

$$J(x_T, x_R) = P_f(x_T, x_R) + \alpha \cdot P_c(x_T) \tag{5.33}$$

$$(x_T^*, x_R^*) = \arg \min_{x_T \in X, x_R \in \{\text{SI,HCCI}\}} J(x_T, x_R) \tag{5.34}$$

with the space of admissible controls X now a function of x_R:

$$X(x_R) = \{x_T \mid T_{min}(x_R) \leq x_T \leq T_{max}(x_R) \text{ and } \ldots \tag{5.35}$$

$$T_{m,min} \leq \hat{T}_m(x_T) \leq T_{m,max}\}. \tag{5.36}$$

The computation of the chemical power of the fuel is modified as well to incorporate

the fuel penalties of the mode switches:

$$P_f(x_T, x_R) = H_f \cdot \dot{m}_f(x_T, x_R, M) \tag{5.37}$$

$$\dot{m}_f(x_T, \text{SI}, M) = \begin{cases} f_{SI}(x_T, \omega_e) & M = \text{SI} \\ f_{SI}(x_T, \omega_e) \cdot (1 + \bar{d}_{HCCI-SI}) & M = \text{HCCI} \end{cases} \tag{5.38}$$

$$\dot{m}_f(x_T, \text{HCCI}, M) = \begin{cases} f_{HCCI}(x_T, \omega_e) & M = \text{HCCI} \\ f_{HCCI}(x_T, \omega_e) \cdot (1 + \bar{d}_{SI-HCCI}) & M = \text{SI} \end{cases} \tag{5.39}$$

Equation (5.38) is used to compute the fuel consumption of remaining in SI and switching to SI from HCCI mode, (5.39) vice versa. $\bar{d}_{SI-HCCI}$ and $\bar{d}_{HCCI-SI}$ represent the total penalties in terms of fuel flow for the SI-HCCI and HCCI-SI mode switches, respectively, and are calculated as follows:

$$\bar{d}_{SI-HCCI} = \frac{1}{\tau_{SI-HCCI}} \cdot \left(\sum_{i \in (2-6)} d_i \cdot \Delta t_i \right) \tag{5.40}$$

$$\bar{d}_{HCCI-SI} = \frac{1}{\tau_{HCCI-SI}} \cdot \left(\sum_{i \in (8-12)} d_i \cdot \Delta t_i \right). \tag{5.41}$$

As can be seen these penalties represent the total fuel penalty divided by tuning parameters $\tau_{SI-HCCI}$ and $\tau_{HCCI-SI}$. These parameters can be interpreted as the average durations between the mode switches. Larger values of $\tau_{SI-HCCI}$ and $\tau_{HCCI-SI}$ encourage and smaller values prevent mode switching. Their optimal choice depends on the applied drive cycle. Here $\tau_{SI-HCCI} = 1\,\text{s}$ and $\tau_{HCCI-SI} = 6\,\text{s}$ were chosen.

Therefore, the switches to and from HCCI are ultimately determined by the ECMS output x_R^*, rather than from any load command. In Fig. 5.2 the SI-HCCI and HCCI-SI switches can be seen at $t = 378.4\,\text{s}$ and $t = 382.3\,\text{s}$, respectively. In addition, similar to strategies *Ext* and *Max* the HCCI-SI mode switch is prepared if T_{des} leaves the HCCI regime:

$$R_{in} = R_{out,2} = x_R^* \tag{5.42}$$

$$R_{out,1} = f_R(T_{des}, T_{min,HCCI}, T_{max,HCCI}). \tag{5.43}$$

The engine torque command u_e is computed by (5.23), similar to strategies *NoP* and *Ext*.

5.3 Drive Cycle Characteristics

The visitation frequencies of different engine load/speed conditions during the three drive cycles are shown in Fig. 5.4 for the conventional vehicle applying supervisory strategy *NoP* and the HEV using strategy *Opt*. As can be seen, ECMS in SI mode reduces high load operation by shifting the operating conditions to lower loads. Furthermore, the plots show the effect of the mode switching supervisors and strategy *Opt* in particular. The supervisory strategies shift frequently visited operating conditions from the extended HCCI regime into the actual HCCI regime. Thereby they create bands above and below the HCCI regime where the engine barely operates. At the same time, in case of the HEV the distribution of visitations within the HCCI regime is less homogeneous and more concentrated at the load boundaries compared to the conventional vehicle. These results are attributed to short excursions of T_{des} from the HCCI regime which are being compensated for by the ISG while the engine torque is held close to the boundaries.

General characteristics of the three drive cycles are presented in Table 5.1. As can be seen in Fig. 5.1, the FTP75 velocity profile incorporates substantially more time spent at vehicle standstill than the other two drive cycles. This relates directly to the high fuel savings of 4.5% due to start/stop operation. With values below 1% the corresponding results for the HWFET and US06 are significantly smaller. In addition to significant vehicle standstill, the FTP75 drive cycle also exhibits generally lower velocities than the HWFET and US06, as well as less aggressive accelerations than the US06. Those three characteristics are the reason why the FTP75 exhibits a low desired torque, averaged over time, of 22 Nm. This directly relates to the distribution of T_{des}, which spends about 20% of time in the HCCI regime during the FTP75 and the HWFET and only 7% during the US06. If the HCCI regime is extended by the ISG all those numbers more than double to 46%, 64%, and 31% for the FTP75, HWFET, and US06, respectively. The effect is especially strong for the HWFET since its torque distribution is highly concentrated above the HCCI regime at around 70-80 Nm, as can also be seen in Fig. 5.4. In case of the US06 cycle the time spent in the extended HCCI regime is significantly larger than the time spent in the regular regime. However, with only 31% of time it is still relatively low. In contrast to the other drive cycles, the US06 cycle's region of highly visited engine conditions lies at very high torques beyond the extended HCCI regime.

Finally, a large difference between the drive cycles is the amount energy harvested with regenerative braking. This difference can be seen qualitatively in Fig. 5.1 and

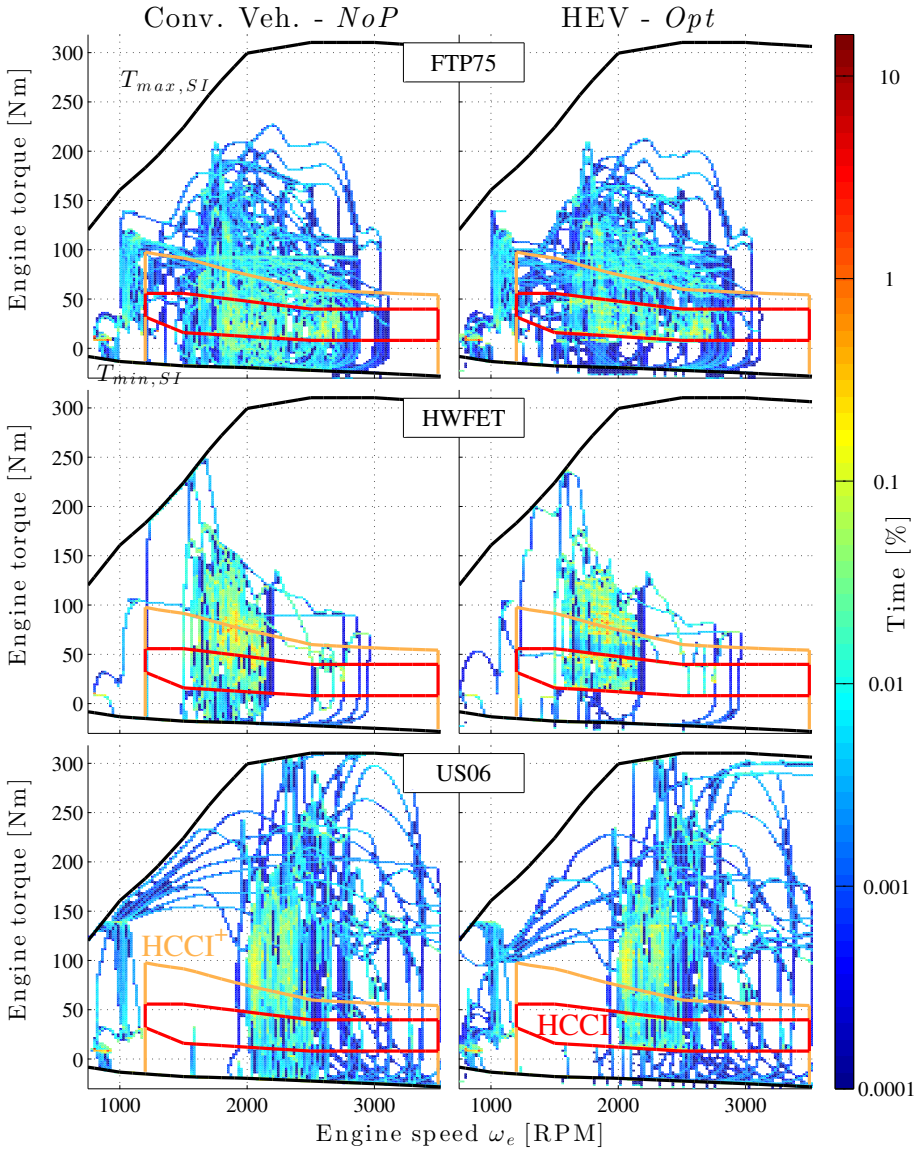

Figure 5.4: Operating regimes of the multimode engine and visitation frequencies of load/speed conditions. Top: FTP75. Middle: HWFET. Bottom: US06. Compared are the conventional vehicle applying strategy *NoP* (left) with the mild HEV using strategy *Opt* (right). Limits of SI and HCCI in black and red, respectively and HCCI regime extended by ISG (HCCI$^+$) in orange.

quantitatively by computing the average energy regenerated per distance travelled. As can be seen, the FTP75 cycle with 66 J/m achieves the highest amount of regeneration and the HWFET, with only a handful braking events and 14 J/m the lowest.

The gains due to start/stop operation, together with the available battery energy from regenerative braking, directly relates to the fuel economy benefit of the mild HEV with SI-only combustion. Here the FTP75 results in 8.7% fuel economy

Table 5.1: Drive cycle characteristics.

	FTP75	**HWFET**	**US06**
Fuel economy benefit			
- from start/stop	4.5%	0.11%	0.82%
- from start/stop & ECMS	8.7%	1.8%	3.8%
Mean desired torque	22 Nm	62 Nm	70 Nm
Mean regenerative braking energy	66 J/m	14 J/m	52 J/m
Fraction of time desired torque spent			
- in HCCI regime	19.8 %	20.4 %	7.3 %
- in extended HCCI regime	45.8 %	63.6 %	31.0 %

improvement, half of which is due to start/stop. With less battery energy available to reduce the engine load and fewer start/stop events, the US06 results in 3.8% improvement. Finally, the gains during the HWFET are even lower with 1.8%, due to virtually no start/stop operation and almost negligible regeneration.

5.4 Fuel Economy Benefits & Synergies

In the following section, the fuel economy results for the three drive cycles, shown in Fig. 5.5, are discussed. Similar to Chap. 3 it is distinguished between the penalized mode switch model and instantaneous mode switches. Here it is focused on the effect of hybridization and its synergies with the different supervisory strategies in terms of fuel economy. The results discussed here assume an ideal aftertreatment system, which does not require any depletion.

In the case of the HEV and the FTP75 drive cycle, all four supervisory control strategies lead to noticeable improvements in fuel economy. Strategy *NoP*, however, does not benefit from the hybridization. Its associated relative improvements of 3.0% and 2.0% for instantaneous and penalized mode switches, respectively, are very similar to the ones seen with the conventional vehicle. This is not surprising since strategy *NoP* does not attempt to exploit the torque assist capabilities to improve the HCCI performance. On the other hand, strategies *Ext*, *Max*, and *Opt* result in improvements over the SI-only HEV of approximately 5.7% and 4.2% for instantaneous and penalized mode switches, respectively. The performance of the three supervisors is very similar in case of the FTP75, all being able to take advantage of the synergies between SI/HCCI multimode operation and the torque assist from the ISG, which al-

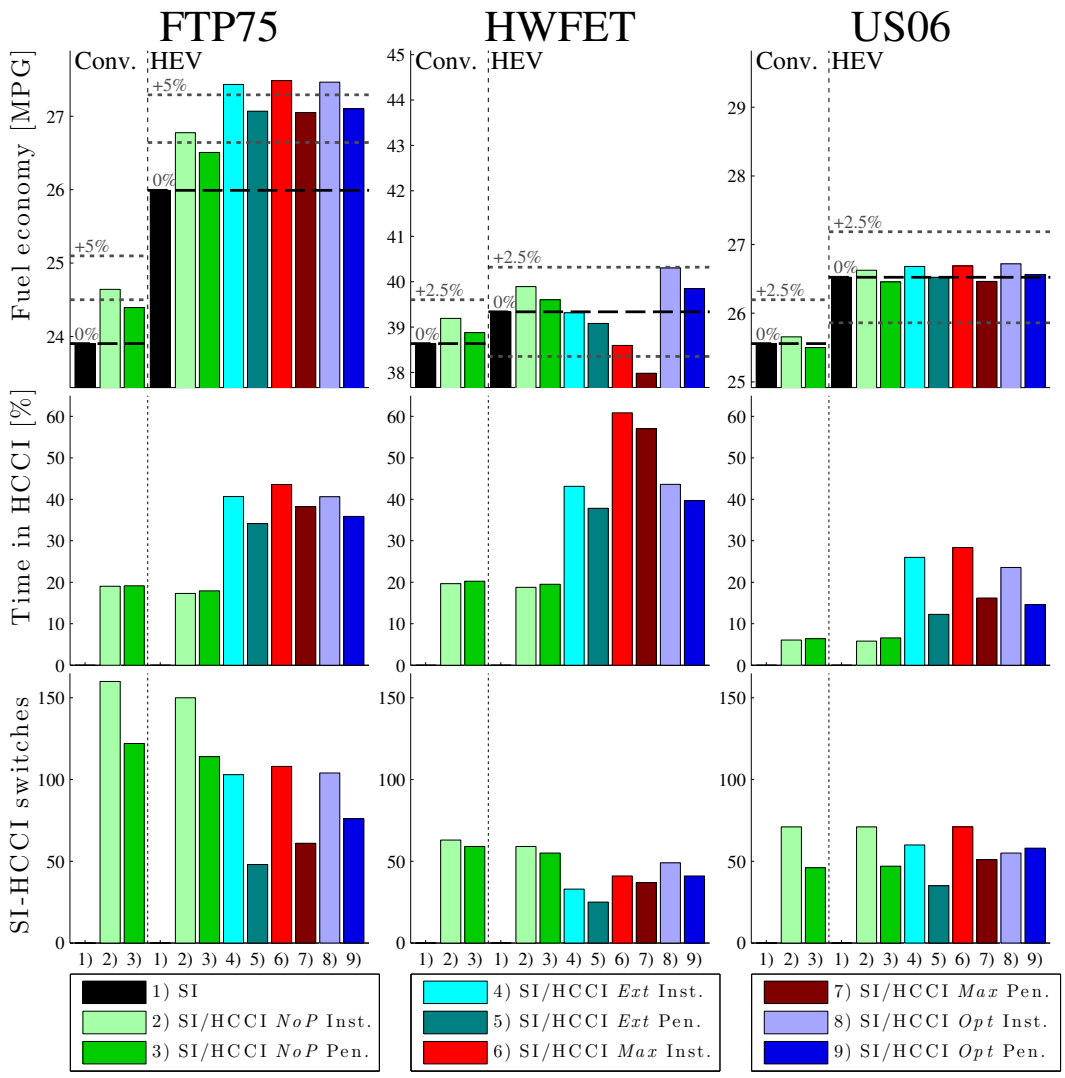

Figure 5.5: Drive cycle results assuming an ideal aftertreatment system, which does not require any depletion. Results for FTP75 (left column), HWFET (center column), and US06 (right column) cycles. Plotted are fuel economy (top row), fraction of time spent in HCCI combustion (center row), and number of cam switches from SI to HCCI (bottom row). Conventional vehicle (bars on the left) and mild HEV (bars on the right) with results shown for the SI-only engine (black bars) as well as the SI/HCCI multimode engine applying the four supervisory strategies. Mode switches are assumed instantaneous (green bars) and penalized (blue bars).

lows longer residence time in HCCI combustion while performing fewer fuel-expensive mode switches. Meanwhile, the optimal strategy *Opt* performs only marginally better than *Ext* and *Max*. As discussed above and shown in Fig. 5.1, the FTP75 drive cycle results in a desired load that is evenly distributed within the extended HCCI regime, with residences in HCCI being regularly interrupted by regenerative braking events.

Therefore, the HCCI operation does not significantly affect the battery's SOC and it can be concluded that a simple mode switch supervisory strategy is sufficient to achieve high fuel economy benefits from HCCI.

The fuel economy results for the HWFET, however, show a different pattern. Here the optimal strategy *Opt* clearly shows the best performance and again higher relative improvements than strategy *NoP* and the conventional vehicle. It can be seen that strategies *Ext* and *Max* result in reductions in fuel economy, despite 40-60% of time spent in HCCI mode. As discussed above, for a majority of the HWFET drive cycle, the cruise condition lies at loads right above the HCCI regime. A large amount of electric power is required to shift the engine load down to HCCI for extended periods of time. At the same time, opportunities to charge the battery are very sparse. This leads to the poor performance of strategies *Ext* and *Max*. Supervisory strategy *Opt* resolves this issue by returning to SI if at a certain SOC the fuel economy benefits of remaining in HCCI mode are lower than the required battery power to do so.

Finally, the results for the US06 drive cycle show barely any improvement from using HCCI combustion. With the ISG's torque-assist, penalized mode switches, and strategies *Ext*, *Max*, and *Opt* the total residence time in the HCCI regime doubles compared to the conventional vehicle, from 6% to 14%. This is, however, still small, leading to very limited improvements even when assuming instantaneous mode switches. The residence time in HCCI per cam switch is short as well, resulting in a larger impact of the mode switch penalties. The reason for this low visitation time of the HCCI regime is the fact that a majority of the engine's operating conditions during the US06 cycle are located at relatively high loads. At these conditions they are not in reach of the ISG and cannot be consistently shifted to the HCCI regime. However, while all the other strategies result in negative fuel economy benefits, strategy *Opt* still achieves at least a neutral result.

In general, it can be concluded that two effects are required to successfully exploit the synergies between torque assist in a mild HEV and multimode combustion. First, regular regeneration events and therefore large quantities of available battery energy are required to allow to shift the engine operation into the HCCI regime for significant periods of time. The consequence of a lack of such events was seen in case of the HWFET, where the SOC-constraint required switches back to SI mode even though a residence in HCCI would have been possible. Second, due to the ISG's limitation the desired torque T_{des} is required lie close to the HCCI regime. Otherwise, as seen in case of the US06 cycle, the beneficial HCCI regime cannot be exploited.

In addition, it can be seen that the characteristics of the drive cycle and the as-

sociated distribution in desired torque determines if SOC represents an important constraint for the SI/HCCI mode switching decision. If the driver's load requirement is located around the extended HCCI regime, including significant residence time at very low loads as seen in the FTP75, the ECMS uses the ISG equally for torque assist and charging. Therefore, the SOC does not need to be specifically considered in the mode switch decisions to achieve high fuel economy improvements. However, if the driver continuously requires loads that are located slightly above the HCCI regime, as seen in the HWFET, the ISG is preferably used as torque-assist to compensate for short excursions from the HCCI regime to higher loads. This leads to a significant reduction in SOC, which needs to be accounted for in the mode switching decision. Finally, if the average load demand is so high that the ISG is unable shift it to the HCCI regime, HCCI combustion cannot be used for a significant amount of time anyway, therefore removing any significance of SOC on the mode switch decision.

5.5 Three-Way Catalyst Considerations

As shown in Fig. 5.5, the combination of hybridization and multimode combustion leads to significant total residence time in HCCI mode. This needs to be considered in the design and operation of the aftertreatment system. In the following section, the TWC model described in Chap. 4 is included in the analysis to see impact on fuel economy, NO_x, and TWC temperature. The two supervisory strategies *NoP* and *Opt* are applied to control the mode switching decision. Similar to the results in Sec. 5.4 it is distinguished between instantaneous and penalized mode switches. To control the oxygen storage of the TWC, two depletion strategies, described in more detail in Sec. 4.6, are applied. The first strategy *NoO* assumes that the TWC's OSC does not exhibit any dynamics, i.e., it fills instantaneously when HCCI mode is entered and it returns to a depleted state as soon as stoichiometric SI is reached. Therefore, this strategy does not incur any fuel penalty from depletion and results in the same fuel economy values as presented in Fig. 5.5. On the other hand, it also does not have the OSC to buffer the NO_x breakthrough when entering HCCI. The second strategy *FiD* includes OSC dynamics and depletion penalty and assumes depletion of the OSC after a mode switch from HCCI to SI.

5.5.1 Catalyst Temperature

The influence of low temperature HCCI exhaust gas on TWC brick temperature in case of the conventional vehicle is discussed in Sec. 4.8. It is seen that residences in HCCI mode are generally too short to have a significant effect on TWC temperature. However, since residence times in HCCI mode are extended due to the ISG's torque assist, this cool-down effect might be amplified. Therefore the trajectories of exhaust and brick temperatures during the simulation of the FTP75 drive cycle with the mild HEV are shown in Fig. 5.6. Similar to Fig. 4.19 for both the conventional vehicle as well as the mild HEV three cases are compared: An SI-only engine and a multimode engine with and without OSC depletion, *NoO* and *FiD*, respectively.

As can be seen, the mild HEV exhibits an average reduction in exhaust gas temperature $\vartheta_{g,e}$ of approximately 23 °C compared to the conventional vehicle, due to overall lower engine load. The mild HEV allows for significantly longer residence time in HCCI mode, resulting in an additional decrease in exhaust temperature by in average 27 °C, especially during the time period of 800-1000 s. This in turn translates into an average drop in TWC brick temperature $\vartheta_{b,1}$ of 15 °C. However, also in case of the HEV, it can be seen that the requirement of running rich might counteract this effect and lead to a small temperature rise. The resulting average drop in brick temperature compared to SI-only is only 6 °C instead of 15 °C.

As can be seen, the use of the simple 0D-catalyst model does also in case of the mild HEV not suggest a TWC temperature drop below light-off. For that reason, upon engine warm-up the TWC's temperature did not act as a constraint and the breakthrough of HC and CO was not relevant in this study. However, in reality it is possible that the spatial temperature dynamics play a role. Specifically the front-end of the TWC is directly subjected to relatively cold HCCI exhaust gas. This, in turn, could result in an additional drop in temperature in this part of the catalyst and potentially lead to partial cool-down of the brick. For more confidence in this area a more detailed model and additional experimental data would be required. However, Kulzer et al. [11] have shown a control strategy that ensures high TWC temperature with only limited impact on fuel economy.

5.5.2 Fuel Economy & NO_x emissions

The drive cycle results for fuel economy and tailpipe NO_x emissions are shown in Fig. 5.7. Note that since results for the NO_x emissions are based on steady-state

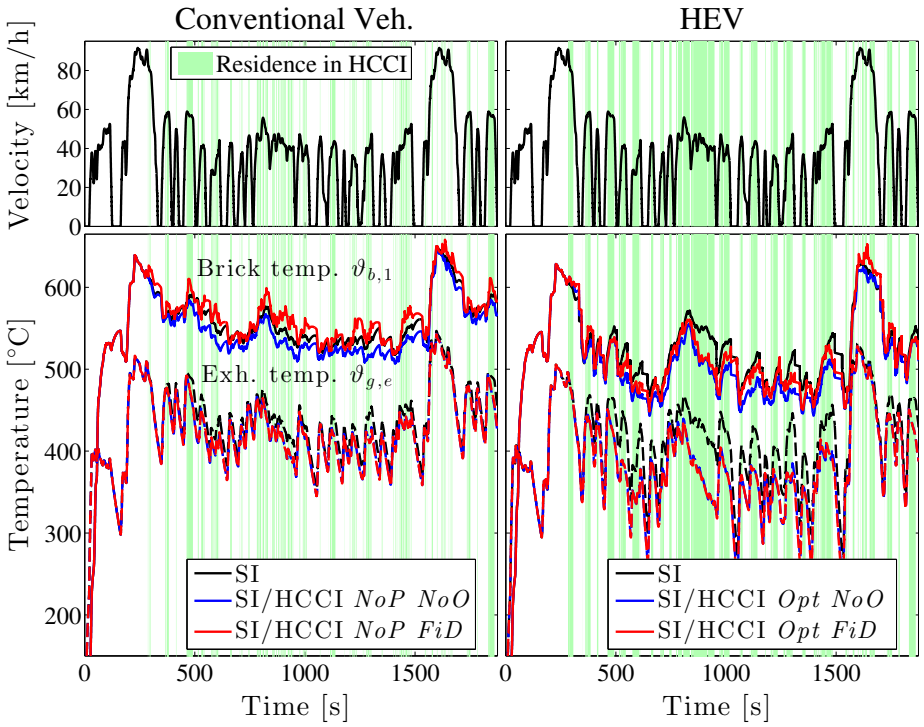

Figure 5.6: Trajectories of the conventional vehicle (left) and the HEV (right) during the FTP75 drive cycle, periods in HCCI mode highlighted light green. Top: Velocity v. Bottom: TWC brick temperature $\vartheta_{b,1}$ (solid) and engine exhaust gas temperature $\vartheta_{g,e}$ (dashed), SI-only (black), without OSC dynamics *NoO* (blue), and with OSC depletion *FiD* (red).

data, the absolute numbers need to be treated with caution and are in reality generally higher due to transient dynamics and imperfect AFR control.

The FTP75 drive cycle is subjected to engine and TWC cold start. During the first 30 s of the drive cycle the TWC's temperature lies below light-off, as can be seen in Fig. 5.6. This leads to the relatively high tailpipe NO_x results. However, upon reaching nominal temperatures, the applied model assumes perfect AFR control and NO_x conversion in stoichiometric SI mode. For that reason, NO_x in the SI-only cases during the HWFET and US06 cycles is equal to zero.

As can be seen for the FTP75 and the HWFET drive cycles, extended residence time in HCCI corresponds to long periods of NO_x breakthrough. The NO_x accumulates to significant amounts, which would pose a problem for low emissions certification. Since during the US06 cycle HCCI combustion is only rarely used, even in case of the mild HEV, the resulting NO_x emissions are relatively low.

Furthermore, the impact of the OSC dynamics can be seen clearly. For all the drive cycles and both vehicles, the requirement of depleting the OSC leads to a sig-

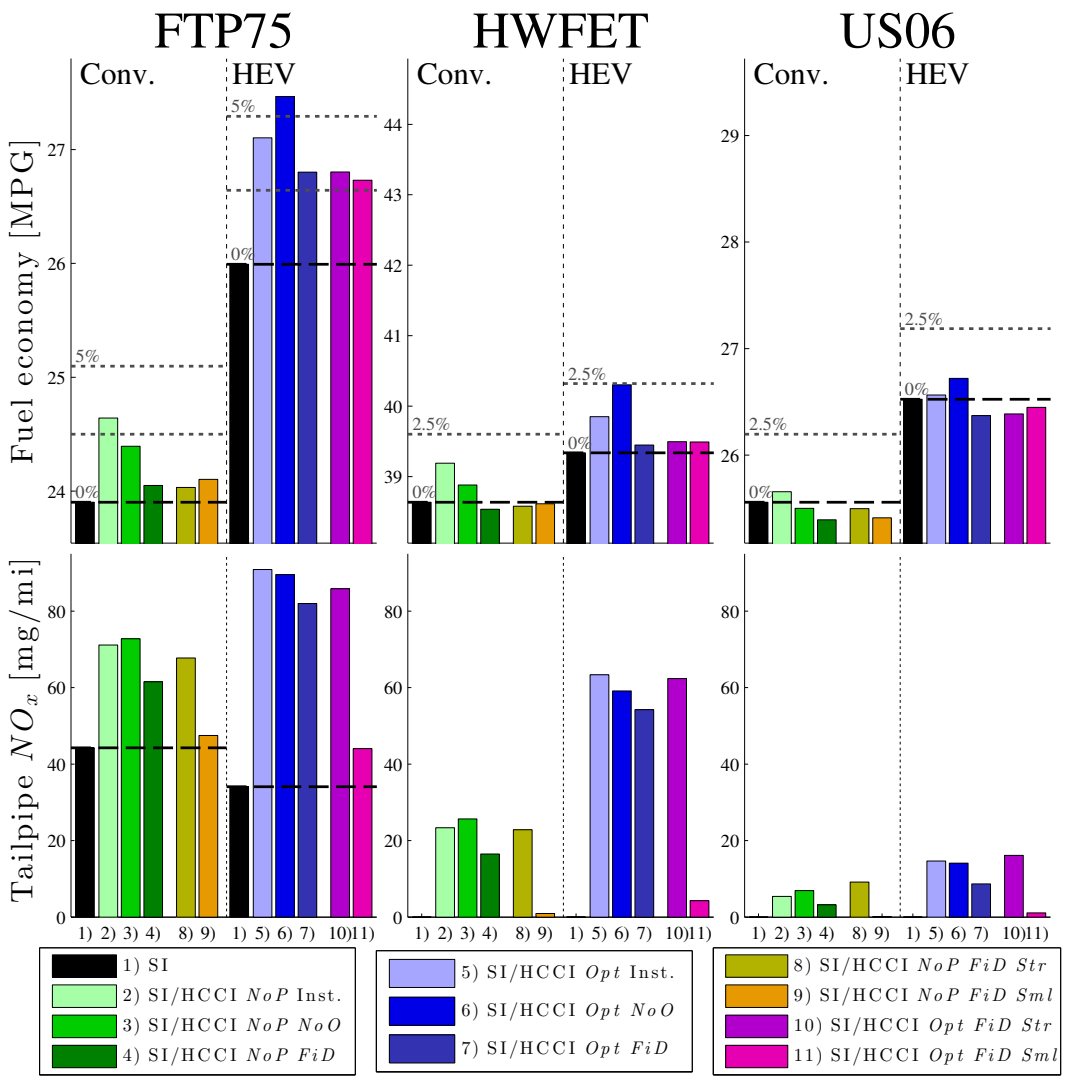

Figure 5.7: Drive cycle results assuming a TWC, which requires OSC depletion. Results for FTP75 (left column), HWFET (center column), and US06 (right column) cycles. Plotted are fuel economy (top row) and average tailpipe NO_x (bottom row). Conventional vehicle (bars on the left) and mild HEV (bars on the right) applying the supervisory strategies *NoP* and *Opt*, respectively. Results shown for the SI-only engine (black bars) as well as the SI/HCCI multimode engine (colored bars). Mode switches are assumed instantaneous (light color) or penalized without TWC depletion *NoO* (medium color) and penalized with OSC depletion *FiD* (dark color). Additional results are shown for case study *Str* with modified HCCI-SI mode switch and case study *Sml* with reduced OSC capacity and HCCI regime.

nificant drop in fuel economy. For the conventional vehicle, the depletion negates all of HCCI's efficiency benefits. On the other hand, in case of the HEV and the FTP75 cycle still more than 2.5% improvement in fuel economy is achieved, despite the OSC depletion. However, hybridization does not lead to a noticeable improvement for the

other drive cycles. Focusing on the NO_x emissions, it can be seen that the delay in NO_x breakthrough due to the OSC does not lead to a significant reduction in tailpipe NO_x.

5.5.3 Case Studies

The following section discusses two case studies which apply small modifications in HCCI-SI control strategy and hardware to the original mode switch parameterization, as presented in Chap. 3 and 4. The results of the case studies and their impact on fuel economy and NO_x emissions are presented in Fig. 5.7 and denoted *Str* and *Sml*.

Case Study 1: Stratified HCCI-SI Switch (*Str*)

The first case study *Str* discusses a potential variation in the HCCI-SI mode switch control strategy. As discussed in Sec. 4.5 the original control strategy attempts rich SI operation from right after the cam switch to high lift. The goal of this procedure is avoid breakthroughs in NO_x by enabling the TWC to convert the high levels of engine-out NO_x during SI combustion as fast as possible. The downside of this strategy, however, is a substantial fuel penalty during the first two SI engine cycles. Of course this results in a trade-off between fuel economy and NO_x emissions. In this case study an alternative strategy is tested, in which the first two engine cycles after the cam switch are run in stratified lean SI combustion, comparable to the mode switch strategy presented by Tian et al. [76]. In this case the correct amount of fuel is injected to match the torque request while not constraining AFR in SI mode. Detailed HCCI-SI mode switch simulations of this strategy have shown a relative AFR of approximately $\lambda = 1.7$ during the first and $\lambda = 1.2$ during the second SI cycle. Fuel penalties of 1.07 and 1.06 and engine-out NO_x slightly lower than nominal SI were assumed. The final assumption states that after those two lean SI cycles the engine can be operated either at stoichiometry or rich, if the OSC needs to be depleted. The original and modified parameters can be found in Table 5.2. An exemplary HCCI-SI mode switch is shown in Fig. 5.8 to compare this parameterization with the original one.

The results are shown in Fig. 5.7. As can be seen for both vehicle configurations as well as all three drive cycles, the resulting improvements in fuel economy are almost negligible, while the tailpipe NO_x emissions, however, are noticeably increased. Of course this result depends on the applied assumptions and parameters.

Table 5.2: Modified mode switch model parameters for case study *Str*

	State i	FP d_i	Δt_i	λ_i	$NO_{x,i}$
Org	10 (SI)	68%	1 cyc	0.9	$0.5NO_{x,SI}$
	11 (SI)	60%	1 cyc	0.9	$0.5NO_{x,SI}$
Sml	10 (SI)	7%	1 cyc	1.7	$0.8NO_{x,SI}$
	11 (SI)	6%	1 cyc	1.2	$0.9NO_{x,SI}$

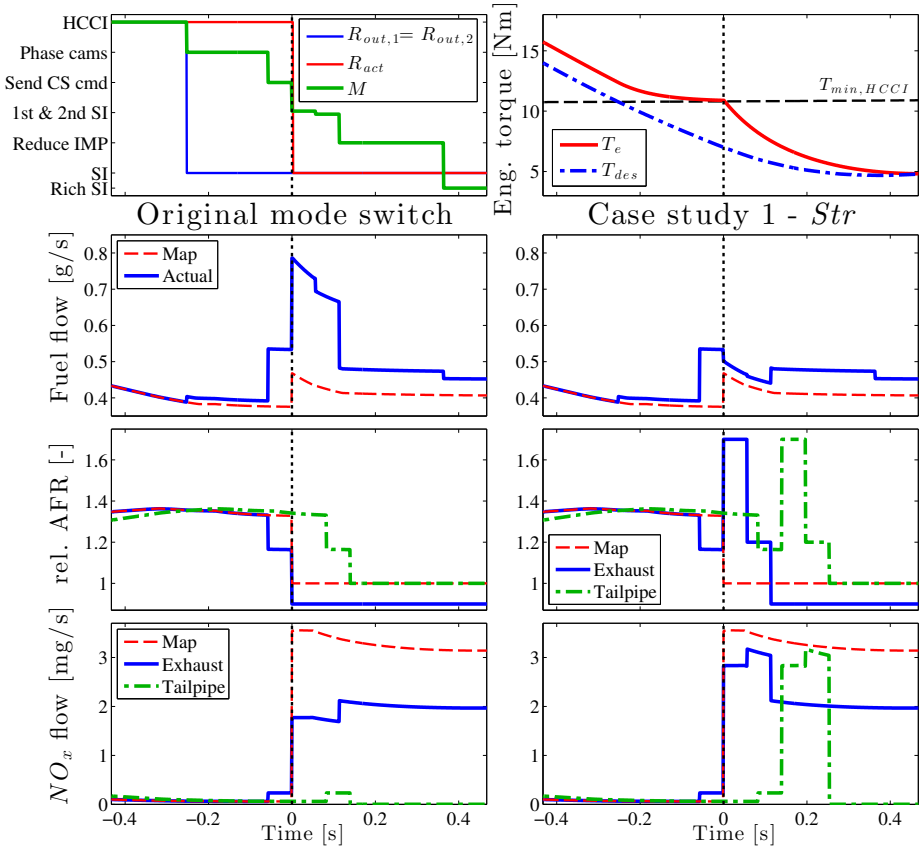

Figure 5.8: Exemplary HCCI-SI mode switch, similar to Fig. 4.16. Lower six plots to compare the original (left) with the parameterization of case study 1 (right).

Case Study 2: Small HCCI Regime with small OSC (*Sml*)

The second case study *Sml* discusses two hardware modifications. First of all, even if a TWC with generous OSC is used, this storage fills up too fast to lead to a substantial reduction in tailpipe NO_x. This can be seen in Fig. 5.7 when comparing the results of penalized mode switch with and without OSC dynamics. However, it requires a large quantity of fuel to deplete the full OSC. Therefore the usage of a TWC with a small rather than a large OSC might actually be desirable, thereby assuming that in

SI-combustion AFR-control is accurate enough.

Second of all, it can be seen that extended operation in HCCI mode results in significant amounts of tailpipe NO_x, since the TWC's OSC is full for a substantial amount of time. In case of the HEV this effect is even enhanced. However, as shown in Fig. 4.3, while HCCI engine-out NO_x is very low in the bottom half of the HCCI regime, it reaches significant values towards higher loads. At the same the engine often operates at those higher loads, as seen in Fig. 5.4. This is especially true in case of the HEV when the driver desires a torque higher than the maximum HCCI load while the ISG compensates for the difference. Finally, as also seen in Fig. 4.3, efficiency benefits from using HCCI compared to SI at these higher loads are relatively small.

Therefore simulations were run, assuming only the lower half of the HCCI regime combined with a TWC offering only a quarter of the original OSC. The associated results are shown in Fig. 5.7. As can be seen the fuel economy of this modified configuration is almost equal or greater than the original results. In addition, tailpipe NO_x originating from HCCI operation is significantly reduced.

5.6 Summary

This chapter discusses the application of SI/HCCI multimode combustion in a mild HEV. Four supervisory mode switching control strategies are introduced. "The baseline strategy does not utilize torque assist for HCCI operation. Two rule-based strategies extend and maximize the residence time in HCCI without taking into account the battery's SOC. Finally, the optimal strategy incorporates the mode switching decision and associated penalties into the ECMS. The strategies are analyzed in terms of fuel economy benefits and synergies over the FTP75, HWFET, and US06 drive cycles. It is shown that the FTP75 drive cycle, which exhibits a low average load demand and a high number of regenerative braking events, offers many possibilities to operate in HCCI mode while the battery can be recharged. As a result the rule-based and the optimal strategies produce almost equal fuel economy benefits and show great synergies between the electric motor and the multimode engine. Conversely, the HWFET displays an average load demand right above the HCCI regime and virtually no regeneration events. This leads to extended periods of time during which torque assist can be used to facilitate HCCI operation. However, for the rule-based strategies, this translates into substantial battery discharge, which

is harmful for overall fuel economy. Therefore, in such a case battery SOC needs to be incorporated into the mode switching decision. Finally, the aggressive US06 cycle results in a load demand which is too high and can rarely be achieved by HCCI together with the ISG. As a result, there are no significant synergies between mild HEV and SI/HCCI multimode engine despite several battery regeneration events over the course of the drive cycle." [100]

The vehicle model is extended with a TWC aftertreatment system to incorporate TWC brick temperature and oxygen storage capacity. "It is shown that the extended residence time in HCCI due to the ISG's torque assist reduces the amount of fuel spent on depleting the OSC. Based on a simple 0D-temperature model for the TWC, operation in HCCI mode does not lead to a significant drop in TWC brick temperature compared to the HEV with SI-only engine. In fact, the requirement of running rich to deplete the OSC leads exothermic reactions partially compensating for the cold HCCI exhaust gas. However, the prolonged HCCI operation results in extended periods of time under which the TWC is unable to reduce NO_x, leading to substantial tailpipe emissions." [101]

"Two case studies are presented. In the first study, the parameterization of the mode switch model is modified to describe a HCCI-SI switch under stratified instead of stoichiometric or rich SI conditions. This reduces the fuel penalty of the HCCI-SI mode switch; however, it does result in additional tailpipe NO_x. Based on the assumed parameters, it is shown that over the course of a drive cycle this strategy leads to a visible increase in NO_x while the fuel economy stays essentially the same. The second case study evaluates the impact of a smaller HCCI regime and a smaller OSC. Even a generous OSC fully oxidizes rapidly under lean HCCI conditions and is therefore unable to maintain NO_x conversion in a significant way. Thus, it is suggested, that a TWC with smaller OSC is preferable, since its depletion requires less fuel. Furthermore, the attempt to push the HCCI regime to higher loads gives rise to an increase in combustion temperature and therefore engine-out NO_x. Constraining the HCCI regime to conditions exhibiting ultra-low NO_x emissions reduces the associated breakthrough substantially. Due to the ISG's torque assist, even this smaller HCCI regime can be utilized for significant periods of time. Simultaneously, the fuel savings originating from the smaller OSC compensates for reduced HCCI residence time." [101]

Chapter 6

Conclusions and Future Work

6.1 Results and Conclusions

Multimode combustion engines, specifically those based on spark-ignition (SI) and homogeneous charge compression ignition (HCCI) combustion, have been a focus of research for several years and have shown great potential for high fuel efficiency and low emissions. In the past decade several drive cycle simulation studies of vehicles equipped with SI/HCCI engines promised significant improvements in fuel economy at relatively low cost, making them a competitive alternative to hybrid electric vehicles (HEV).

However, these prior assessments were based on optimistic assumptions and did not incorporate essential dynamics of the SI/HCCI engine system. The studies applied engine maps based on simulations, which offered a large HCCI regime, thereby resulting in long residence times in this efficient mode. Furthermore, switches between the combustion modes and their inherent dynamics and penalties were consistently neglected. Finally, all these studies in part or fully excluded both emissions and drivability from their scope. This dissertation presented a comprehensive simulation methodology to assess the performance of a SI/HCCI multimode engine in terms of drive cycle fuel economy and emissions. Various supervisory control strategies were described and analyzed. The more realistic assessment of the SI/HCCI technology led to simulation results that show less potential than promised in prior work.

First, a novel finite-state model for combustion mode switching dynamics and fuel penalties was introduced, parameterized, and integrated within the vehicle model. Discrete switching between combustion modes represents an interesting modeling problem and decision process, especially since such switches exhibit fuel penalties. In this work it was shown that some visitations of the HCCI regime are too short to result in an overall fuel economy benefit. Also, every mode switch requires a certain

amount of time to prepare, which may lead to delays and torque response with noticeable jerk. It was demonstrated that prediction of the driver's torque demand could improve the performance of the supervisory controller by avoiding or anticipating mode switches, which are harmful for fuel economy or drivability. Simulation results were presented to compare a SI/HCCI to a SI-only engine. For the FTP75 drive cycle improvements in fuel economy of 3% and 2% are achieved, assuming ideal and realistic mode switches, respectively. Among a large number of properties, the size of the feasible HCCI regime has the most significant impact on HCCI's fuel economy benefits. A larger regime results in longer residence times and fewer mode switches, which in turn leads to higher fuel economy. The limits of the HCCI regime, determined by factors such as pressure rise rates, misfires, and fuel efficiency, are not easy to predict in simulation and the resulting maps need to be treated with caution.

Second, this work has demonstrated that the applied aftertreatment system directly affects the performance of the multimode engine. The claim about the cost-effectiveness of the SI/HCCI technology is significantly based on the assumption that it can be used in combination with a relatively inexpensive three-way catalytic converter (TWC) to pass stringent future emissions regulations. Cooling of the TWC due to low temperature HCCI exhaust gas has been studied in the past. In this work this effect is only significant if the residence time in the HCCI regime is of a certain duration. Conversely, the interaction between HCCI and the TWC's oxygen storage capacity (OSC), which has been neglected in the past, was examined here. The previous assumption was that a generous OSC would avoid NO_x breakthroughs under lean HCCI conditions. This work has shown that even a large OSC is oxidized rapidly, resulting in relatively long periods of time during which the TWC is unable to convert NO_x, thereby releasing it into the atmosphere. It is important to note that, while HCCI combustion exhibits ultra-low levels of engine-out NO_x emissions at lower loads, where dilution is high and temperature low, towards higher loads NO_x emissions may be prohibitive to wish to satisfy future regulations without treatment. For that reason the level of engine-out NO_x emissions further constrains the size of the HCCI regime. Furthermore, the requirement of depleting the OSC before operating in the nominal SI mode produces excessive fuel penalties, canceling most of HCCI's efficiency benefits. It can be concluded that a TWC with a large OSC is not an appropriate aftertreatment choice for a vehicle equipped with a SI/HCCI engine.

Finally, the multimode engine was integrated in a mild HEV. Upcoming 48 V-type HEVs are expected to offer fuel economy improvements during city driving at relatively low system cost. For that reason it was evaluated, if the SI/HCCI capabilities

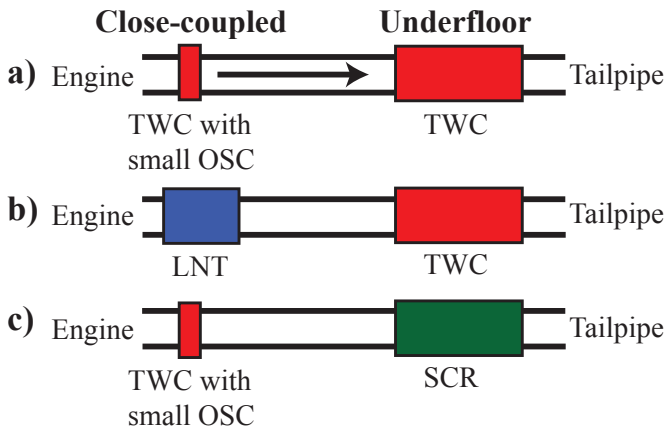

Figure 6.1: Potential aftertreatment systems for SI/HCCI multimode engine. a) TWC. b) LNT/TWC. c) Passive SCR

offer the potential to improve the fuel economy of such a HEV even further. In fact, it was seen that the ability of the electric motor to provide torque-assist allows significant extension of the operation in the HCCI mode. Optimal supervisory controllers were compared to rule-based strategies that do not take the battery's state-of-charge (SOC) into account. The FTP75 drive cycle exhibits on average relatively low load and multiple time periods allowing for regenerative braking. Under those conditions, using SI/HCCI instead of the SI-only engine offers great synergies independent of the specific control strategy, resulting in a fuel economy improvement of 3.5%, including mode switching penalties. However, during highway driving, SOC is a constraint that needs to be considered in the supervisory strategy, mainly due to the lack of regenerative braking periods. In addition, it was seen that a mild HEV with small HCCI regime and a TWC with small OSC might have the potential for a fuel efficient system at acceptable cost.

6.2 Future Work and Open Challenges

The next step towards the realization of a SI/HCCI multimode engine is the practical implementation of supervisory control strategies. The combustion mode switch controller and the supervisors need to be tested in engine-in-the-loop or vehicle-in-the-loop environments to see the actual impact mode switching has on vehicle fuel economy, emissions, and drivability. A detailed emissions analysis is required to quantify the exact exhaust characteristics during mode switches.

After concluding that the TWC with generous OSC is unsuited for a SI/HCCI

multimode engine, alternative aftertreatment systems need to be evaluated. Three potential configurations are sketched in Fig. 6.1. As suggested here, the most simple alternative is a close-coupled TWC with very small to negligible OSC, which can be depleted efficiently. A second, underfloor TWC can be used for redundancy. The depletion of the second TWC can be scheduled at more convenient times. However, the breakthrough in NO_x while operating in the HCCI mode remains a disadvantage of this configuration. The second option is a lean NO_x trap (LNT), which is commercially applied in Diesel engines. LNT's store O_2 and NO_x [154] and require periodic bursts of rich operation to convert the NO_x they accumulate [155]. If a TWC is placed downstream of the LNT, this rich operation is not necessary while in SI mode. In addition, due to the low HCCI NO_x concentration the LNT does not need to be regenerated as frequently as in the case of Diesel applications, which reduces the associated fuel penalty. However, the LNT needs to be regenerated before a mode switch to HCCI is performed. Furthermore, even in the SI mode the LNT requires high temperature regeneration to avoid sulfur poisoning, which results in an additional fuel penalty. Finally, LNTs are expensive due their high precious metal loading. The third potential system is denoted passive selective catalytic reduction (SCR) and is a configuration discussed for lean gasoline engines [156, 157]. The SCR catalyst requires ammonia (NH_3) to reduce NO_x. Instead of relying on urea-injection as in nominal SCR systems, this configuration generates the NH_3 using a close-coupled TWC at slightly rich SI conditions [158]. The downstream SCR catalyst then stores the NH_3 until required in the HCCI mode. Since HCCI NO_x is low, not much NH_3 is required to convert NO_x, which limits the need for rich operation. Furthermore, a SCR catalyst is generally cheaper than a LNT. However, this system, consisting of two combustion modes and two different catalysts, is very complex and and its interactions might be difficult to control. The challenge that all these systems share is that they depend on some sort of regeneration or depletion to maintain high conversion efficiency. In addition, they all exhibit chemical storage dynamics and are constrained to certain temperature ranges. Therefore, they require assessments of the full vehicle system, similar to the one performed in this work.

Finally, the analysis and optimization of other properties of the vehicle system were left for future work. Different engine design variables, e.g., the compression ratio, are subject of a trade-off in fuel efficiency between the SI and HCCI modes, which will greatly affect the vehicle's performance and overall fuel economy. The transmission design and the choice of gear ratios, in combination with multimode combustion, needs to be evaluated in more detail. This includes evaluating the combination of

multimode combustion with automatic, dual-clutch, or continuously variable transmission hardware. Furthermore, multimode combustion can be applied in different engine and vehicle sizes. Finally, besides SI/HCCI other multimode concepts exist, which need to be evaluated and analyzed over the course of a drive cycle. Examples are SI and spark-assisted compression ignition (SACI) engines or the combination of conventional diesel with reactivity controlled compression ignition (RCCI) combustion. Finally, conceptually similar to combustion mode switching might be the decision to perform cylinder deactivation in variable displacement engines. The author believes that the presented methodology provides a good starting ground to perform such future assessments.

Appendices

Appendix A

EPA Fuel Economy & Emissions Standards

The following section summarizes the EPA fuel economy and emissions regulation, applied in this work. The information is based on the final rule for revisions to the fuel economy label for the 2013 model year [159]. This summary only considers light-duty, gasoline-fueled internal combustion engine (ICE) powered vehicles. The fuel economy FE in miles-per-gallon (MPG) of such a vehicle over a given drive cycle is officially calculated the following way:

$$FE = \frac{5174 \cdot 10^4 \cdot CWF \cdot SG}{(CWF \cdot m_{HC} + 0.429 \cdot m_{CO} + 0.273 \cdot m_{CO_2}) \cdot (0.6 \cdot SG \cdot H_f + 5471)} \quad \text{(A.1)}$$

with m_{HC}, m_{CO}, and m_{CO_2} the measured emissions over the drive cycle in $^{\mathrm{g}}/_{\mathrm{mi}}$. H_f net heating value by mass of fuel and SG special gravity of the fuel. However, in this work the calculation of FE is simplified to

$$FE = \frac{0.6214 \cdot 10^{-3} \cdot s_v}{264.17 \cdot V_f} = \frac{0.6214 \cdot 10^{-3} \cdot s_v \cdot \rho_f}{264.17 \cdot 10^{-3} \cdot m_f} \quad \text{(A.2)}$$

with s_v the travelled distance in m, V_f the fuel volume consumed in m^3, m_f the fuel mass consumed in g, and ρ_f the density of the fuel in $\mathrm{kg/m}^3$. The density of the gasoline used in this work is $\rho_f = 743\,^{\mathrm{kg}}/_{\mathrm{m}^3}$.

A.1 Drive Cycles

In this work the following EPA drive cycles are used: Federal Test Procedure (FTP75), Highway Fuel Economy Test (HWFET), and the supplemental US06 drive cycles. Details on the drive cycle regulations can be found in [4, 160]. Some details are summarized in Tab. A.1.

FTP75 represents city driving with several accelerations as well as idling periods. Its velocity profile is shown in Fig. A.1. The drive cycle is separated into three phases. The first phase is the cold start transient phase with the engine starting at ambient temperature. After the second phase, called the stabilized phase, the engine is stopped for ten minutes, called hot soak. Finally the third phase, denoted as the hot transient phase, is started, with the same velocity profile as for the first phase. To calculate the fuel economy of the total FTP75 drive cycle FE_{FTP75} in MPG, the

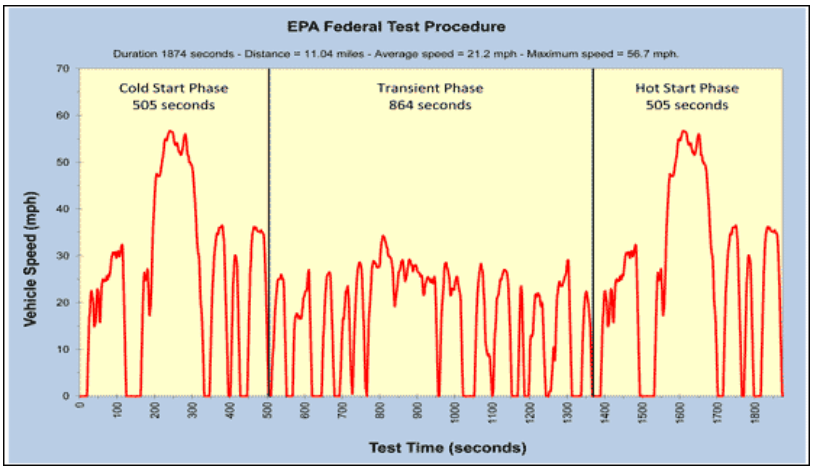

Figure A.1: FTP75 Drive Cycle [4]

three individual phases have to be added up as follows:

$$FE_{FTP} = \frac{0.6214 \cdot 10^{-3}}{264.17} \cdot \left(0.43 \cdot \frac{V_{f,1} + V_{f,2}}{s_{v,1} + s_{v,2}} + 0.57 \cdot \frac{V_{f,2} + V_{f,3}}{s_{v,2} + s_{v,3}} \right)^{-1}. \tag{A.3}$$

Therefore this assumes, that 43% of the time a vehicle is launched cold and 57% of time warm.

HWFET represents highway driving under 60 mph. Its velocity profile is shown in Fig. A.2.

US06 represents aggressive city and highway driving. Its velocity profile is shown in Fig. A.3.

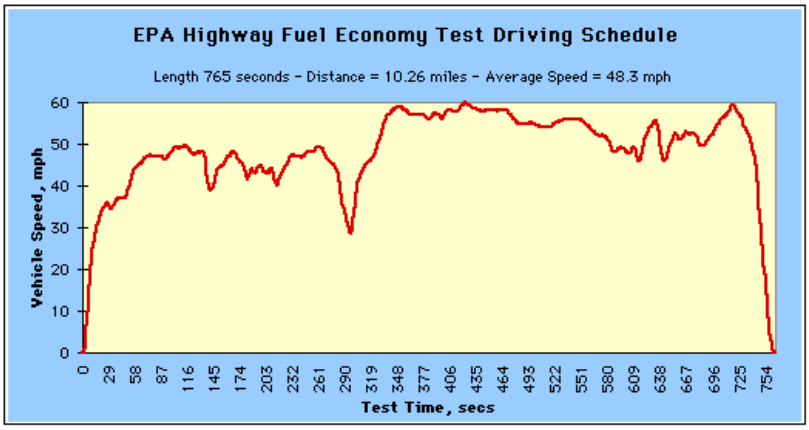

Figure A.2: HWFET Drive Cycle [4]

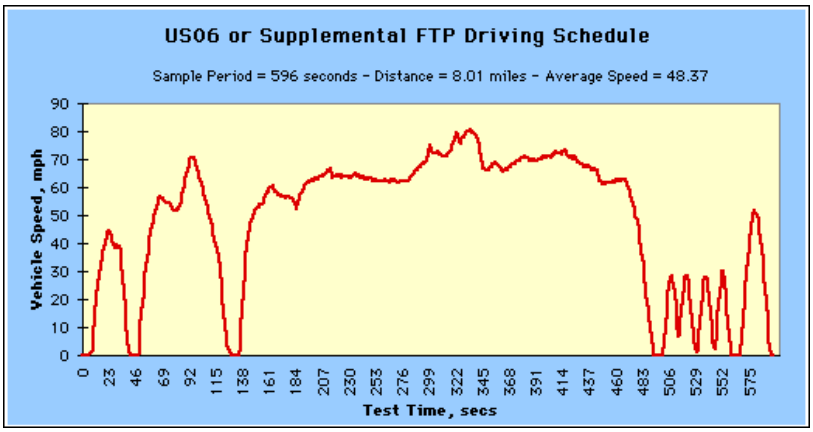

Figure A.3: US06 Drive Cycle [4]

Table A.1: Summary of Drive Cycles

	Duration [s]	**Distance [mi]**
FTP75	1874	11.04
- Phase 1	505	
- Phase 2	864	
- Phase 3	505	
HWFET	765	10.26
US06	594	8.01

A.2 Velocity Tolerance

Based on the regulation [161] the driver has to follow the reference velocity v_{ref} as closely as possible. However, the driver needs to remain within a velocity tolerance band with the following main characteristics:

- The upper limit is 2 mph higher than the highest point on the trace within 1 s of the given time.
- The lower limit is 2 mph lower than the lowest point on the trace within 1 s of the given time.
- Speed variation greater than the tolerances (such as may occur during gear changes and braking spikes) are acceptable, provided they occur for less than 2 s on any occasion.

Appendix B
Publications

B.1 Journal Publications

1. S. Nüesch, A.G. Stefanopoulou, L. Jiang, and J. Sterniak, "Fuel Economy of a Multimode Combustion Engine with Three-Way Catalytic Converter", *Journal of Dynamic Systems, Measurement, and Control, Vol. 137, May, 2015.* [2]
2. S. Nüesch, P. Gorzelic, L. Jiang, J. Sterniak, and A.G. Stefanopoulou, "Accounting for Combustion Mode Switch Dynamics and Fuel Penalties in Drive Cycle Fuel Economy", *International Journal of Engine Research, May, 2015.* [96]
3. S. Nüesch and A.G. Stefanopoulou, "Multimode Combustion in a Mild HEV. Part 1: Supervisory Control and Synergies", *IFAC Control Engineering Practice, 2016, submitted for revision.* [100]
4. S. Nüesch and A.G. Stefanopoulou, "Multimode Combustion in a Mild HEV. Part 2: Three-Way Catalyst Considerations", *IFAC Control Engineering Practice, 2016, submitted for revision.* [101]

B.2 Conference Publications

5. S. Nüesch, E. Hellström, L. Jiang, and A.G. Stefanopoulou, "Influence of Transitions Between SI and HCCI Combustion on Driving Cycle Fuel Consumption", *In Proc. of European Control Conference, July, 2013, 1976-1981.* [94]
6. S. Nüesch, E. Hellström, L. Jiang, and A.G. Stefanopoulou, "Mode Switches Among SI, SACI, and HCCI Combustion and Their Influence on Drive Cycle Fuel Economy", *In Proc. of American Control Conference, June, 2014, 849-854.* [95]
7. S. Nüesch, A.G. Stefanopoulou, L. Jiang, and J. Sterniak, "Methodology to Evaluate the Fuel Economy of a Multimode Combustion Engine with Three-Way Catalytic Converter", *In Proc. of ASME Dynamic Systems and Control Conference, October, 2014, DSCC2014-6146.* [99]
8. S. Nüesch, J. Sterniak, L. Jiang, and A.G. Stefanopoulou, "On Beneficial Mode Switch Decisions Based on Short-term Engine Load Prediction", *In Proc. of IFAC E-COSM, August, 2015, 159-166.* [98]

9. S. Nüesch and A.G. Stefanopoulou, "Is it Economical to Ignore the Driver? A Case Study on Multimode Combustion", *In Proc. of ASME Dynamic Systems and Control Conference, October, 2015, DSCC2015-9875.* [97]
10. S. Nüesch and A.G. Stefanopoulou, "Mild HEV with Multimode Combustion: Benefits of a Small Oxygen Storage", *In Proc. of IFAC Advances in Automotive Control, June, 2016, submitted.* [102]

Bibliography

[1] H. Yilmaz, L. Jiang, and O. Miersch-Wiemers, "DOE vehicle technologies program review - ACCESS," 2014. [Online]. Available: http://energy.gov/sites/prod/files/2014/07/f17/ace066_yilmaz_2014_o.pdf

[2] S. Nüesch, L. Jiang, J. Sterniak, and A. Stefanopoulou, "Fuel economy of a multimode combustion engine with three-way catalytic converter," *Journal of Dynamic Systems, Measurement, and Control*, vol. 137, 2015.

[3] E. Brandt, Y. Wang, and J. Grizzle, "Dynamic modeling of a three-way catalyst for SI engine exhaust emission control," *Control Systems Technology*, vol. 8, no. 5, pp. 767–776, 2000.

[4] *Dynamometer Drive Schedules*. [Online]. Available: http://www.epa.gov/nvfel/testing/dynamometer.htm

[5] *Light-Duty Automotive Technology, Carbon Dioxide Emissions, and Fuel Economy Trends: 1975 Through 2014*, October 2014. [Online]. Available: http://www.epa.gov/fueleconomy/fetrends/1975-2014/420r14023a.pdf

[6] *Fact Sheet: NHTSA and EPA Set Standards to Improve Fuel Economy and Reduce Greenhouse Gases for Passenger Cars and Light Trucks for Model Years 2017 an Beyond*. [Online]. Available: http://www.nhtsa.gov/staticfiles/rulemaking/pdf/cafe/CAFE_2017-25_Fact_Sheet.pdf

[7] *Summary of Fuel Economy Performance*, June 2014. [Online]. Available: http://www.nhtsa.gov/staticfiles/rulemaking/pdf/cafe/June_2014_Summary_Report.pdf

[8] J. German, *Policy Update: Tier 3 Motor Vehicle Emission and Fuel Standards (Final Rule)*, March 2014. [Online]. Available: http://www.theicct.org/us-tier-3-vehicle-emissions-and-fuel-quality-standards-final-rule

[9] *Transitions to Alternative Vehicles and Fuels*. The National Academies Press, 2013. [Online]. Available: http://www.nap.edu/download.php?record_id=18264#

[10] *Interim Joint Technical Assessment Report: Light-Duty Vehicle Greenhouse Gas Emission Standards and Corporate Average Fuel Economy Standards for Model Years 2017-2025*, September 2010. [Online]. Available: http://www.epa.gov/oms/climate/regulations/ldv-ghg-tar.pdf

[11] A. Kulzer, J.-P. Hathout, C. Sauer, R. Karrelmeyer, W. Fischer, and A. Christ, "Multi-mode combustion strategies with CAI for a GDI engine," in *SAE*, no. 2007-01-0214, 2007.

[12] A. Cairns and H. Blaxill, "The effects of combined internal and external exhaust gas recirculation," in *SAE*, no. 2005-01-0133, 2005.

[13] J. Farrell and J. Stevens, "Second law analysis of high efficiency low emission gasoline engine concepts," in *SAE*, no. 2006-01-0491, 2006.

[14] J. Dec and M. Sjöberg, "A parametric study of HCCI combustion - the sources of emissions at low loads and the effects of GDI fuel injection," in *SAE*, no. 2003-01-0752, 2003.

[15] F. Zhao, T. Asmus, D. Assanis, J. E. Dec, J. Eng, and P. Najt, *Homogeneous Charge Compression Ignition (HCCI) Engines - Key Research and Development Issues*. SAE International, March 2003, no. PT-94.

[16] F. E. Zhao, *HCCI and CAI Engines for the Automotive Industry*. Woodhead Publishing Limited and CRC Press LLC, 2007.

[17] M. Yao, Z. Zheng, and H. Liu, "Progress and recent trends in homogeneous charge compression ignition (HCCI) engines," *Progress in Energy and Combustion Science*, vol. 35, no. 5, pp. 398–437, October 2009.

[18] M. Alperstein, W. Swim, and P. Schweitzer, "Fumigation kills smoke - improves diesel," *SAE Transactions*, vol. 66, pp. 574–595, 1958.

[19] M. Noguchi, Y. Tanaka, T. Tanaka, and Y. Takeuchi, "A study on gasoline engine combustion by observation of intermediate reactive products during combustion," in *SAE*, no. 790840, 1979.

[20] S. Onishi, S. Hong Jo, K. Shoda, P. Do Jo, and S. Kato, "Active thermo-atmosphere combustion (ATAC) - a new combustion process for internal combustion engines," in *SAE*, no. 790501, 1979.

[21] P. Najt and D. Foster, "Compression-ignited homogeneous charge combustion," in *SAE*, no. 830264, 1983.

[22] R. Thring, "Homogeneous-charge compression ignition (HCCI) engines," in *SAE*, no. 892068, 1989.

[23] C.-J. Chiang and A. Stefanopoulou, "Sensitivity analysis of combustion timing of homogeneous charge compression ignition gasoline engines," *Journal of Dynamic Systems, Measurement, and Control*, vol. 131, pp. 014 506–1 – 014 506–5, January 2009.

[24] J. Yang, T. Culp, and T. Kenney, "Development of a gasoline engine system using HCCI technology - the concept and the test results," in *SAE*, no. 2002-01-2832, 2002.

[25] G. Haraldsson, P. Tunestål, B. Johansson, and J. Hyvönen, "HCCI closed-loop combustion control using fast thermal management," in *SAE*, no. 2004-01-0943, 2004.

[26] M. Christensen, A. Hultqvist, and B. Johansson, "Demonstrating the multi fuel capability of a homogeneous charge compression ignition engine with variable compression ratio," in *SAE*, no. 1999-01-3679, 1999.

[27] G. Haraldsson, P. Tunestål, and B. Johansson, "HCCI combustion phasing in a multi cylinder engine using variable compression ratio," in *SAE*, no. 2002-01-2858, 2002.

[28] J. Willand, R.-G. Nieberding, G. Vent, and C. Enderle, "The knocking syndrome - its cure and its potential," in *SAE*, no. 982483, 1998.

[29] L. Koopmans and I. Denbratt, "A four stroke camless engine, operated in homogeneous charge compression ignition mode with regular gasoline," in *SAE*, no. 2001-01-3610, 2001.

[30] H. Song and C. Edwards, "Optimization of recompression reaction for low-load operation of residual-effected HCCI," in *SAE*, no. 2008-01-0016, 2008.

[31] D. Law, D. Kemp, J. Allen, G. Kirkpatrick, and T. Copland, "Controlled combustion in an IC-engine with a fully variable valve train," in *SAE*, no. 2001-01-0251, 2001.

[32] D. Law and J. Allen, "On the mechanism of controlled auto ignition," in *SAE*, no. 2002-01-0421, 2002.

[33] P. Wolters, W. Salber, J. Geiger, M. Duesmann, and J. Dilthey, "Controlled auto ignition combustion process with an electromechanical valve train," in *SAE*, no. 2003-01-0032, 2003.

[34] P. Caton, H. Song, N. Kaahaaina, and C. Edwards, "Residual-effected homogeneous charge compression ignition with delayed intake-valve closing at elevated compression ratio," *International Journal of Engine Research*, vol. 6, pp. 399–419, 2005.

[35] A. Babajimopoulos, P. Challa, L. G.A., and D. Assanis, "Model-based assessment of two variable cam timing strategies for HCCI engines: Recompression vs. rebreathing," in *Proc. of ICES*, no. ICES2009-76103, May 2009.

[36] J.-O. Olsson, P. Tunestål, and B. Johansson, "Closed-loop control of an HCCI engine," in *SAE*, no. 2001-01-1031, 2001.

[37] F. Agrell, B. Ångström, Ericsson, J. Wilander, and J. Linderyd, "Integrated simulation and engine test of closed loop HCCI control by aid of variable valve timings," in *SAE*, no. 2003-01-0748, 2003.

[38] ——, "Transient control of HCCI through combined intake and exhaust valve actuation," in *SAE*, no. 2003-01-3172, 2003.

[39] G. Shaver, "Cycle-to-cycle control of HCCI engines," in *Proc. of IMECE*, no. IMECE2003-41966, 2003.

[40] J. Souder, J. H. Mack, J. Hedrick, and R. Dibble, "Microphones and knock sensors for feedback control of HCCI engines," in *Proc. of ICEF*, no. ICEF2004-960, 2004.

[41] C. Chiang and A. Stefanopoulou, "Control of thermal ignition in gasoline engines," in *Proc. of ACC*, June 2003, pp. 3847–3852.

[42] N. Killingsworth, S. Aceves, D. Flowers, and M. Krstic', "Extremum seeking tuning of an experimental HCCI engine combustion timing controller," in *Proc. of ACC*, July 2007, pp. 3665–3670.

[43] J. Bengtsson, P. Strandh, R. Johansson, P. Tunestål, and B. Johansson, "Model predictive control of homogeneous charge compression ignition (HCCI) engine dynamics," in *International Conference on Control Applications*, October 2006.

[44] N. Ravi, H.-H. Liao, A. Jungkunz, A. Widd, and J. Gerdes, "Model predictive control of HCCI using variable valve actuation and fuel injection," *Control Engineering Practice*, vol. 20, pp. 421–430, 2012.

[45] N. Ravi, H.-H. Liao, A. Jungkunz, C.-F. Chang, H. Song, and J. Gerdes, "Modeling and control of an exhaust recompression HCCI engine using split injection," *Journal of Dynamic Systems, Measurement, and Control*, vol. 1134, pp. 011 016–1 – 011 016–12, January 2012.

[46] S. Jade, E. Hellström, J. Larimore, A. Stefanopoulou, and L. Jiang, "Reference governor for load control in a multicylinder recompression HCCI engine," *Control Systems Technology*, vol. 22, 2014.

[47] G. Shaver, J. Gerdes, and M. Roelle, "Physics-based closed-loop control of phasing, peak pressure and work output in HCCI engines utilizing variable valve actuation," in *Proc. of ACC*, June 2004, pp. 150–155.

[48] L. Manofsky, J. Vavra, D. Assanis, and A. Babajimopoulos, "Bridging the gap between HCCI and SI: Spark-assisted compression ignition," in *SAE*, no. 2011-01-1179, 2011.

[49] J. Eng, "Characterization of pressure waves in HCCI combustion," in *SAE*, no. 2002-01-2859, 2002.

[50] J. Hyvönen, G. Haraldsson, and B. Johansson, "Supercharging HCCI to extend the operating range in a multi-cylinder VCR-HCCI engine," in *SAE*, no. 2003-01-3214, 2003.

[51] J.-O. Olsson, P. Tunestål, and B. Johansson, "Boosting for high load HCCI," in *SAE*, no. 2004-01-0940, 2004.

[52] D. Polovina, D. McKenna, J. Wheeler, J. Sterniak, O. Miersch-Wiemers, A. Mond, and H. Yilmaz, "Steady-state combustion development of a downsized multi-cylinder engine with range extended HCCI/SACI capability," in *SAE*, no. 2013-01-1655, 2013.

[53] J. Dec, "A computational study of the effects of low fuel loading and EGR on heat release rates and combustion limits in HCCI engines," in *SAE*, no. 2002-01-1309, 2002.

[54] T. Urushihara, K. Kiraya, A. Kakuhou, and T. Itoh, "Expansion of HCCI operating region by the combination of direct fuel injection, negative valve overlap and internal fuel reformation," in *SAE*, no. 2003-01-0749, 2003.

[55] T. Aroonsrisopon, P. Werner, J. Waldman, V. Sohm, D. Foster, T. Morikawa, and M. Iida, "Expanding the HCCI operation with the charge stratification," in *SAE*, no. 2004-01-1756, 2004.

[56] H. Yun, N. Wermuth, and P. Najt, "Development of robust gasoline HCCI idle operation using multiple injection and multiple ignition (MIMI) strategy," in *SAE*, no. 2009-01-0499, 2009.

[57] E. Hellström, J. Larimore, S. Jade, A. Stefanopoulou, and L. Jiang, "Reducing cyclic variability while regulating combustion phasing in a four-cylinder HCCI engine," *Control Systems Technology*, vol. 22, no. 3, pp. 1190–1197, May 2014.

[58] S. Jade, J. Larimore, E. Hellström, A. Stefanopoulou, and L. Jiang, "Controlled load and speed transitions in a multicylinder recompression HCCI engine," *Control Systems Technology*, 2015.

[59] M. Weinrotter, E. Wintner, K. Iskra, T. Neger, J. Olofsson, H. Seyfried, M. Aldén, M. Lackner, F. Winter, A. Vressner, A. Hultqvist, and B. Johansson, "Optical diagnostics of laster-induced and spark plug-assisted HCCI combustion," in *SAE*, no. 2005-01-0129, 2005.

[60] J. Hyvönen, G. Haraldsson, and B. Johansson, "Operating conditions using spark assisted HCCI combustion during combustion mode transfer to SI in a multi-cylinder VCR-HCCI engine," in *SAE*, no. 2005-01-0109, 2005.

[61] H. Santoso, J. Matthews, and W. Check, "Managing SI/HCCI dual-mode engine operation," in *SAE*, no. 2005-01-0162, 2005.

[62] T. Urushihara, K. Yamaguchi, K. Yoshizawa, and T. Itoh, "A study of a gasoline-fueled compression ignition engine - expansion of the HCCI operation range using SI combustion as a trigger of compression ignition," in *SAE*, no. 2005-01-0180, 2005.

[63] N. Kalian, H. Zhao, and C. Yang, "Effects of spark-assistance on controlled auto-ignition combustion at different injection timings in a multicylinder direct-injection gasoline engine," *International Journal of Engine Research*, vol. 10, pp. 133–148, 2009.

[64] J. Szybist, E. Nafzinger, and A. Weall, "Load expansion of stoichiometric HCCI using spark assist and hydraulic valve actuation," in *SAE*, no. 2010-01-2172, 2010.

[65] G. Lavoie, J. Martz, M. Wooldridge, and D. Assanis, "A multi-mode combustion diagram for spark assisted compression ignition," *Combustion and Flame*, vol. 157, pp. 1106–1110, 2010.

[66] D. Reuss, T.-W. Kuo, V. Natarajan, and V. Sick, "Experimental metric for identifying origins of combustion variability during spark-assisted compression ignition," *International Journal of Engine Research*, vol. 9, pp. 409–434, 2008.

[67] C. Daw, K. Edwards, R. Wagner, and J. Green, "Modeling cyclic variability in spark-assisted hcci," *Journal of Engineering for Gas Turbines and Power*, vol. 130, pp. 052 801–1 – 052 801–6, 2008.

[68] J. Larimore, E. Hellström, J. Sterniak, L. Jiang, and A. Stefanopoulou, "Experiments and analysis of high cyclic variability at the operational limits of spark-assisted HCCI combustion," in *Proc. of ACC*, June 2012.

[69] L. Koopmans, H. Ström, S. Lundgren, O. Backlund, and I. Denbratt, "Demonstrating a SI-HCCI-SI mode change on a Volvo 5-cylinder electronic valve control engine," in *SAE*, no. 2003-01-0753, 2003.

[70] G. Shaver, M. Roelle, and J. Gerdes, "Modeling cycle-to-cycle dynamics and mode transitions in HCCI engines with variable valve actuation," *Control Engineering Practice*, vol. 14, pp. 213–222, 2006.

[71] C. Daw, R. Wagner, K. Edwards, and J. Green, "Understanding the transition between conventional spark-ignited combustion and HCCI in a gasoline engine," *Proc. of the Institution of Mechanical Engineers, Part D: Journal of Automobile Engineering*, vol. 31, pp. 2887–2894, 2007.

[72] Y. Zhang, H. Xie, N. Zhou, T. Chen, and H. Zhao, "Study of SI-HCCI-SI transition on a port fuel injection engine equipped with 4VVAS," in *SAE*, no. 2007-01-0199, 2007.

[73] H. Kakuya, S. Yamaoka, K. Kumano, and S. Sat, "Investigation of a SI-HCCI combustion switching control method in a multi-cylinder gasoline engine," in *SAE*, no. 2008-01-0792, 2008.

[74] A. Widd, R. Johansson, P. Borgqvist, P. Tunestål, and B. Johansson, "Investigating mode switch from SI to HCCI using early intake valve closing and negative valve overlap," in *SAE*, no. 2011-01-1775, 2011.

[75] N. Milovanovic, D. Blunder, S. Gedge, and J. Turner, "SI-HCCI-SI mode transition at different engine operating conditions," in *SAE*, no. 2005-01-0156, 2005.

[76] G. Tian, Z. Wang, Q. Ge, J. Wang, and S. Shuai, "Control of a spark ignition homogeneous charge compression ignition mode transition on a gasoline direct injection engine," *Proc. of the Institution of Mechanical Engineers, Part D: Journal of Automobile Engineering*, vol. 221, pp. 867–875, 2007.

[77] A. Cairns and H. Blaxill, "The effects of two-stage cam profile switching and external EGR on SI-CAI combustion transitions," in *SAE*, no. 2007-01-0187, 2007.

[78] N. Kalian, H. Zhao, and J. Qiao, "Investigation of transition between spark ignition and controlled auto-ignition combustion in a V6 direct-injection engine with cam profile switching," *Proc. of the Institution of Mechanical Engineers, Part D: Journal of Automobile Engineering*, vol. 222, pp. 1911–1926, 2008.

[79] H. Wu, N. Collings, S. Regitz, J. Etheridge, and M. Kraft, "Experimental investigation of a control method for SI-HCCI-SI transition in a multi-cylinder gasoline engine," in *SAE*, no. 2010-01-1245, 2010.

[80] T. Nier, T. Kulzer, and R. Karrelmeyer, "Analysis of the combustion mode switch between SI and gasoline HCCI," in *SAE*, no. 2012-01-1105, 2012.

[81] N. Ravi, M. Jagsch, J. Oudart, N. Chaturvedi, D. Cook, and A. Kocic, "Closed-loop control of SI-HCCI mode switch using fuel injection timing," in *Proc. of DSCC*, no. DSCC2013-3785, October 2013.

[82] P. Gorzelic, P. Shingne, M. J., A. Stefanopoulou, J. Sterniak, and L. Jiang, "A low-order HCCI model extended to capture SI-HCCI mode transition data with two-stage cam switching," in *Proc. of DSCC*, no. DSCC2014-6275, October 2014.

[83] S. Zhang and G. Zhu, "Model-based mode transition control between SI and HCCI combustion," in *Proc. of DSCC*, no. DSCC2014-6148, 2014.

[84] X. Yang and G. Zhu, "SI and HCCI combustion mode transition control of an HCCI capable SI engine," *Control Systems Technology*, vol. 21, no. 5, pp. 1558–1569, September 2013.

[85] P. Gorzelic, "Modeling and model-based control of multi-mode combustion engines for closed-loop SI/HCCI mode transitions with cam switching strategies," Ph.D. dissertation, University of Michigan, May 2015.

[86] *GM's HCCI program makes steady progress*, July 2009. [Online]. Available: http://articles.sae.org/6635/

[87] T. Ma, H. Zhao, J. Li, and N. Ladommatos, "Experimental investigation of controlled auto-ignition (CAI) combustion in a 4-stroke multi-cylinder gasoline engine and drive cycle simulations," in *Proc. of IFP International Congress*, 2001, pp. 115–124.

[88] E. Ortiz-Soto, D. Assanis, and A. Babajimopoulos, "A comprehensive engine to drive-cycle modelling framework for the fuel economy assessment of advanced engine and combustion technologies," *International Journal of Engine Research*, vol. 13, pp. 287–304, 2012.

[89] J. Wheeler, D. Polovina, V. Fresnel, O. Miersch-Wiemers, A. Mond, J. Sterniak, and H. Yilmaz, "Design of a 4-cylinder GTDI engine with part-load HCCI capability," in *SAE*, no. 2013-01-0287, 2013.

[90] A. Delorme, A. Rousseau, T. Wallner, E. Ortiz-Soto, A. Babajimopoulos, and D. Assanis, "Evaluation of homogeneous charge compression ignition (HCCI) engine fuel savings for various electric drive powertrains," in *The 25th World Battery, Hybrid and Fuel Cell Electric Vehicle Symposium & Exhibition*, November 2010.

[91] B. Lawler, E. Ortiz-Soto, R. Gupta, H. Peng, and Z. Filipi, "Hybrid electric vehicle powertrain and control strategy optimization to maximize the synergy with a gasoline HCCI engine," in *SAE*, no. 2011-01-0888, 2011.

[92] K. Ahn, J. Whitefoot, A. Babajimopoulos, E. Ortiz-Soto, and P. Papalambros, "Homogeneous charge compression ignition technology implemented in a hybrid electric vehicle: System optimal design and benefits analysis for a power-split architecture," *Proc. of the Institution of Mechanical Engineers, Part D: Journal of Automobile Engineering*, vol. 227, pp. 87–98, 2012.

[93] A. Solouk, M. Shahbakhti, and M. Mahjoob, "Energy management and control of a hybrid electric vehicle with an integrated low temperature combustion (LTC) engine," in *Proc. of DSCC*, no. DSCC2014-6286, October 2014.

[94] S. Nüesch, E. Hellström, L. Jiang, and A. Stefanopoulou, "Influence of transitions between SI and HCCI combustion on driving cycle fuel consumption," in *Proc. of ECC*, 2013, pp. 1976–1981.

[95] ——, "Mode switches among SI, SACI, and HCCI combustion and their influence on drive cycle fuel economy," in *Proc. of ACC*, 2014, pp. 849–854.

[96] S. Nüesch, P. Gorzelic, L. Jiang, J. Sterniak, and A. Stefanopoulou, "Accounting for combustion mode switch dynamics and fuel penalties in drive cycle fuel economy," *International Journal of Engine Research*, 2015.

[97] S. Nüesch and A. Stefanopoulou, "Is it economical to ignore the driver? A case study on multimode combustion," in *Proc. of DSCC*, no. DSCC2015-9875, 2015.

[98] S. Nüesch, J. Sterniak, L. Jiang, and A. Stefanopoulou, "On beneficial mode switch decisions based on short-term engine load prediction," in *Proc. of IFAC E-COSM*, 2015.

[99] S. Nüesch, L. Jiang, J. Sterniak, and A. Stefanopoulou, "Methodology to evaluate the fuel economy of a multimode combustion engine with three-way catalytic converter," in *Proc. of DSCC*, no. DSCC2014-6146, 2014.

[100] S. Nüesch and A. Stefanopoulou, "Multimode combustion in a mild HEV. Part 1: Supervisory control and synergies," *Control Engineering Practice*, 2016, submitted.

[101] ——, "Multimode combustion in a mild HEV. Part 2: Three-way catalyst considerations," *Control Engineering Practice*, 2016, submitted.

[102] ——, "Mild HEV with multimode combustion: Benefits of a small oxygen storage," in *Proc. of IFAC AAC*, 2016, submitted.

[103] H. Yilmaz, *2012 DOE Merit Review - ACCESS*, 2012, accessed 2/2015. [Online]. Available: http://www1.eere.energy.gov/vehiclesandfuels/pdfs/merit_review_2012/adv_combustion/ace066_yilmaz_2012_o.pdf

[104] *Annual Merit Review Results Report - Advanced Combustion Engine Technologies*, 2014. [Online]. Available: http://energy.gov/eere/vehicles/downloads/2014-annual-merit-review-results-report-advanced-combustion-engine

[105] *Cost, Effectiveness and Deployment of Fuel Economy Technologies for Light-Duty Vehicles*, 2015. [Online]. Available: http://www8.nationalacademies.org/onpinews/newsitem.aspx?RecordID=21744

[106] L. Glielmo, L. Iannelli, V. Vacca, and V. Vasca, "Gearshift control for automated manual transmissions," *Mechatronics*, vol. 1, pp. 17–26, 2006.

[107] L. Guzzella and A. Sciarretta, *Vehicle Propulsion Systems, Introduction to Modeling and Optimization*. Springer, 2007.

[108] R. Rajamani, *Vehicle Dynamics and Control*. Springer, 2012.

[109] L. Ericsson and L. Nielsen, *Modeling and Control of Engines and Drivelines*. John Wiley & Sons, 2014.

[110] V. Petrushov, "Improvement in vehicle aerodynamic drag and rolling resistance determination from coast-down tests," *Proc. of Institution of Mechanical Engineers, Part D: J. Automobile Engineering*, vol. 212, no. 5, pp. 369–380, 1998.

[111] H. Pacejka, E. Bakker, and L. Nyborg, "Tyre modelling for use in vehicle dynamics studies," in *SAE*, no. 870421, 1987.

[112] D. McMahon, J. Hedrick, and S. Shladover, "Vehicle modelling and control for automated highway systems," in *ACC*, 1990, pp. 297–303.

[113] The MathWorks, Inc., *Using Simulink and Stateflow in Automotive Applications*, 1998.

[114] R. Eichhorn, M. Boot, and C. Luijten, "Throttle loss recovery using variable geometry turbine," *SAE International*, no. 2010-01-1441, 2010.

[115] H. Wi, Y. Lee, J. Park, J. Lee, and K. Park, "Effects of FTP-75 mode vehicle fuel economy improvement due to types of power steering system," *International Journal of Automotive Technology*, vol. 10, pp. 771–776, 2009.

[116] W. Yu and D. Williams, "Energy saving analysis of power steering system by varying flow design," in *SAE*, no. 2007-01-4216, 2007.

[117] Z. Gao, J. Conklin, C. Daw, and V. Chakravarthy, "A proposed methodology for estimating transient engine-out temperature and emissions from steady-state maps," *International Journal of Engine Research*, vol. 11, pp. 137–151, 2010.

[118] M. Roelle, G. Shaver, and J. Gerdes, "Tackling the transition: A multi-mode combustion model of SI and HCCI for mode transition control," in *Proc. of IMECE*, 2004, pp. 329–336.

[119] T. Matsuda, W. H., T. Kono, T. Nakamura, and T. Urushihara, "A study of a gasoline-fueled HCCI engine - mode changes from SI combustion to HCCI combustion," in *SAE*, no. 2008-01-0050, 2008.

[120] P. Gorzelic, E. Hellström, L. Jiang, and A. Stefanopoulou, "Model-based feedback control for an automated transfer out of SI operation during SI to HCCI transitions in gasoline engines," in *Proc. of DSCC*, 2012, pp. 359–367.

[121] X. Yang, G. Zhu, and X. Chen, "Air-to-fuel ratio regulation during SI to HCCI combustion mode transition using LQ tracking control," in *Proc. of ACC*, 2012, pp. 2054–2059.

[122] Z. Ren and G. Zhu, "Modeling and control of an electric variable valve timing system for SI and HCCI combustion mode transition," in *ACC*, 2011, pp. 979–984.

[123] X. Yang, G. Zhu, and Z. Sun, "A control oriented SI and HCCI hybrid combustion model for internal combustion engines," in *Proc. of DSCC*, 2010, pp. 657–664.

[124] H. List and P. Schoeggl, "Objective evaluation of vehicle driveability," in *SAE*, no. 980804, 1998.

[125] X. Wei and G. Rizzoni, "Objective metrics of fuel economy, performance and drivability - a review," in *SAE*, no. 2004-01-1338, 2004.

[126] C. Shin, J. Choi, S. Cha, and W. Lim, "An objective method of driveability evaluation using a simulation model for hybrid electric vehicles," *International Journal of Precision Engineering and Manufacturing*, vol. 15, no. 2, pp. 219–226, February 2014.

[127] F. Posada, A. Bandivadekar, and J. German, "Estimated cost of emission control technologies for light-duty vehicles Part 1 - Gasoline," in *SAE*, no. 2013-01-0534, 2013.

[128] ——, "Estimated cost of emission control technologies for light-duty vehicles Part 2 - Diesel," in *SAE*, no. 2013-01-0539, 2013.

[129] Y. Chen, V. Sima, W. Lin, J. Sterniak, and S. Bohac, "Fuel efficiency and NOx reduction from multi-mode combustion with three-way catalysts," in *Proc. of ASME ICED Fall Technical Conference*, 2014.

[130] J. B. Heywood, *Internal Combustion Engine Fundamentals*. McGraw-Hill, 1988.

[131] L. Eriksson, "Mean value models for exhaust system temperatures," in *SAE*, no. 2002-01-0374, 2002.

[132] L. Guzzella and C. Onder, *Introduction to Modeling and Control of Internal Combustion Engine Systems*. Springer, 2010.

[133] P. R. Sanketi, J. K. Hedrick, and T. Kaga, "A simplified catalytic converter model for automotive coldstart control applications," in *Proc. of ASME IMECE*, 2005.

[134] D. Kum, H. Peng, and N. K. Kucknor, "Supervisory control of parallel hybrid electric vehicles for fuel and emissions reduction," *Journal of Dynamic Systems, Measurement, and Control*, vol. 133, pp. 061 010–1–061 010–10, 2011.

[135] P. Kiwitz, "Model-based control of catalytic converters," Ph.D. dissertation, ETH Zurich, November 2012.

[136] B. T. Shaw, G. D. Fischer, and J. K. Hedrick, "A simplified coldstart catalyst thermal model to reduce hydrocarbon emissions," in *Proc. of IFAC 15th Triennial World Congress*, 2002.

[137] T. V. Johnson, "Review of vehicular emissions trends," in *SAE*, no. 2015-01-0993, 2015.

[138] D. Tsinoglou, G. Koltsakis, and J. Peyton Jones, "Oxygen storage modeling in three-way catalytic converters," *Industrial & Engineering Chemistry Research*, vol. 41, pp. 1152–1165, 2002.

[139] J. Peyton Jones, "Modeling combined catalyst oxygen storage and reversible deactivation dynamics for improved emissions prediction," in *SAE*, no. 2003-01-0999, 2003.

[140] F. Aimard, S. Li, and M. Sorine, "Mathematical modeling of automotive three-way catalytic converters with oxygen storage capacity," *Control Engineering Practice*, vol. 4, no. 8, pp. 1119–1124, 1996.

[141] K. Ohsawa, N. Baba, and S. Kojima, "Numerical prediction of transient conversion characteristics in a three-way catalytic converter," in *SAE*, no. 982556, 1998.

[142] P. Kumar, T. Gu, K. Grigoriadis, M. Franchek, and V. Balakotaiah, "Spatio-temporal dynamics of oxygen storage and release in a three-way catalytic converter," *Chemical Engineering Science*, vol. 111, pp. 180–190, 2014.

[143] J. Peyton Jones, J. Roberts, and P. Bernard, "A simplified model for the dynamics of a three-way catalytic converter," in *SAE*, no. 2000-01-0652, 2000.

[144] K. Muske and J. Peyton Jones, "Estimating the oxygen storage level of a three-way automotive catalyst," in *Proc. of ACC*, vol. 5, 2004, pp. 4060–4065.

[145] P. Kiwitz, C. Onder, and L. Guzzella, "Control-oriented modeling of a three-way catalytic converter with observation of the relative oxygen level profile," *Journal of Process Control*, vol. 22, no. 6, pp. 984–994, 2012.

[146] P. Kumar, I. Makki, J. Kerns, K. Grigoriadis, M. Franchek, and V. Balakotaiah, "A low-dimensional model for describing the oxygen storage capacity and transient behavior of a three-way catalytic converter," *Chemical Engineering Science*, vol. 73, pp. 373–387, 2012.

[147] G. Fiengo, J. Grizzle, J. Cook, and A. Karnik, "Duel-UEGO active catalyst control for emissions reduction: Design and experimental validation," *Control Systems Technology*, vol. 13, no. 5, pp. 722–736, 2005.

[148] E. Shafai, C. Roduner, and H. Geering, "Indirect adaptive control of a three-way catalyst," in *SAE*, no. 961038, 1996.

[149] M. Ammann, H. Geering, C. Onder, C. Roduner, and E. Shafai, "Adaptive control of a three-way catalytic converter," in *Proc. of ACC*, vol. 3, 2000, pp. 1561–1566.

[150] A. Rick and B. Sisk, "A simulation based analysis of 12V and 48V microhybrid systems across vehicle segments and drive cycles," in *SAE*, no. 2015-01-1151, 2015.

[151] S. Onori and L. Serrao, "On adaptive-ECMS strategies for hybrid electric vehicles," in *Proc. of RHEVE*, December 2011, pp. 1–7.

[152] A. Chasse, G. Corde, A. Del Mastro, and F. Perez, "Online optimal control of a parallel hybrid with after-treatment constraint integration," in *Proc. of VPPC*, September 2010, pp. 1–6.

[153] H. Borhan, A. Vahidi, A. M. Philipps, M. L. Kuang, I. V. Kolmanovsky, and S. Di Cairano, "MPC-based energy management of a power-split hybrid electric vehicle," *Control Systems Technology*, vol. 20, no. 3, pp. 593–603, May 2012.

[154] M. Canova, S. Midlam-Mohler, A. Soliman, Y. Guezennec, and G. Rizzoni, "Control-oriented modeling of NOx aftertreatment systems," in *SAE*, no. 2007-24-0106, 2007.

[155] M. F. Hsieh, M. Canova, and J. Wang, "Model predictive control approach for AFR control during lean NOx trap regenerations," in *SAE*, no. 2009-01-0586, 2009.

[156] W. Li, K. L. Perry, K. Narayanaswamy, C. H. Kim, and P. Najt, "Passive ammonia SCR system for lean-burn SIDI engines," in *SAE*, no. 2010-01-0366, 2010.

[157] V. Y. Prikhodko, J. E. Parks, J. A. Pihl, and T. J. Toops, "Ammonia generation over TWC for passive SCR NOx control for lean gasoline engines," in *SAE*, no. 2015-01-1505, 2015.

[158] K. Ramanathan, C. S. Sharma, and C. H. Kim, "Global kinetics for ammonia formation and oxidation reactions in a commercial three-way catalyst," *Industrial & Engineering Chemistry Research*, vol. 51, pp. 1198–1208, 2012.

[159] *Federal Register, Vol. 76, No. 129 from July 6, 2011, Part II.* [Online]. Available: http://www.epa.gov/otaq/carlabel/regulations.htm

[160] *Federal Test Procedure Revisions.* [Online]. Available: http://www.epa.gov/otaq/sftp.htm

[161] *EPA Urban Dynamometer Driving Schedule.* [Online]. Available: http://www.ecfr.gov/cgi-bin/text-idx?SID=12b6ecb62f8c323b909bcba1a7f239eb&node=se40.19.86_1115_678&rgn=div8